UNIVERSITY OF SOUTHAMPTON

FACULTY OF PHYSICAL AND APPLIED SCIENCES

OPTOELECTRONICS RESEARCH CENTRE

Optical Microfiber Sensors

by

George Y. Chen

A thesis submitted in partial fulfillment for the degree of

Doctor of Philosophy

October 2013

UNIVERSITY OF SOUTHAMPTON
FACULTY OF PHYSICAL AND APPLIED SCIENCES
OPTOELECTRONICS RESEARCH CENTRE

Doctor of Philosophy

Optical Microfiber Sensors

By George Y. Chen

Abstract

The technology and applications of optical fibers have progressed very rapidly in recent years. Fiber-optic sensors have been commercially successful and well established in various industries from biomedical to defense. They exhibit many advantages over their electrical counterparts, including higher responsivity, higher detection bandwidth, higher temperature performance, better immunity to electromagnetic interference, all-dielectric composition, greater environmental ruggedness and distributed sensing capability. However, the physical dimensions and the minimum bend radius of the optical fiber sets a lower limit on the final package size. In applications where the working space is stringent or where physical intrusion must be minimized, it becomes highly desirable to develop ultra-compact sensors that can maintain the level of performance despite the miniaturization. The recent emergence of optical microfibers has opened up a new era of technological innovations. Microfibers have the potential to solve the problem with its range of enabling properties, including large evanescent field, strong optical confinement, bend insensitivity, low stiffness and high configurability. This thesis focuses on the innovative development of relatively unexplored areas of microfiber-based sensing as well as the envisioning of performance-enhancing techniques that can shape the on-going development of such sensors. In particular, extensive advancement was made in light of the simple demonstration of a novel current sensor with potentially gigahertz detection bandwidth. This includes the development of the resonator design to achieve higher compactness, and the first reported fabrication of the spun optical microfiber to counter the effects of linear birefringence. Well established and successfully proven sensing configurations such as the flexural disc and air-backed mandrel were adopted to create miniaturized microfiber-based accelerometers and microphones, with potential responsivity enhancements of at least one order of magnitude.

Table of contents

Abstract 3
Declaration of authorship 9
Acknowledgements 10
List of abbreviations 11
List of figures 13
List of tables 19
1. Introduction 20
1.1 Scope and objectives 21
1.2 Thesis outline 21
2. Background of optical microfiber and nanofiber-based sensors 23
2.1 Introduction 23
2.2 Fabrication 24
2.2.1 Flame-brushing technique 24
2.2.2 Modified flame-brushing technique 25
2.2.3 Self-modulated taper-drawing 25
2.2.4 Acid-etching technique 26
2.2.5 Direct drawing from the bulk 27
2.2.6 Self-assembly from silica nanoparticles 27
2.2.7 Electro-spinning from a glass-forming melt 28
2.3 Optical and mechanical properties 30
2.3.1 Mode propagation 30
2.3.2 Optical confinement 31
2.3.3 Evanescent field 32
2.3.4 Propagation loss 33
2.3.5 Bend loss 34
2.3.6 Mechanical strength 34
2.3.7 Dispersion 34
2.3.8 Nonlinearity 34
2.4 Sensing parameters 35
2.4.1 Responsivity of sensor 35
2.4.2 Resolution or sensitivity of detection system 35
2.4.3 Sensitivity of measurand 35
2.4.4 Response time 35
2.4.5 Detection bandwidth 36
2.4.6 Dynamic range 36
2.4.7 Repeatability 36
2.4.8 Reproducibility 36

2.4.9 Stability 36
2.4.10 Practicality 36
2.4.11 Compactness 36
2.5 Sensors overview 37
2.5.1 Refractive index sensors 41
2.5.2 Chemical and bio-chemical sensors 52
2.5.3 Temperature sensors 56
2.5.4 Current sensors 59
2.5.5 Displacement/strain sensors 60
2.5.6 Bend/curvature sensors 63
2.5.7 Roughness sensors 63
2.5.8 Acceleration sensors 64
2.5.9 Force/pressure sensors 66
2.5.10 Rotation sensors 67
2.5.11 Acoustic sensors 67
2.5.12 Electric field sensors 68
2.5.13 Magnetic field sensors 68
2.5.13 Conclusions 69
2.6 References 70
3. Temperature sensing with optical microfiber 80
3.1 Resonance shift detection schemes 80
3.2 Sliding microfiber coil resonator temperature sensor for inspection of electrical wires 81
3.2.1 Introduction 81
3.2.2 Theory 82
3.2.3 Fabrication 84
3.2.4 Experimental setup 86
3.2.5 Simulations 87
3.2.6 Experimental results 88
3.2.7 Conclusion 91
3.3 References 92
4. Current sensing with optical microfiber 94
4.1 Faraday Effect 94
4.1.1 Introduction 94
4.1.2 Fiber-optic polarization rotation detection schemes 98
4.1.3 Birefringence 102
4.1.4 Noise sources 102
4.1.5 High Verdet constant materials 102
4.2 High detection bandwidth microfiber coil current sensors 105
4.2.1 Introduction 105

4.2.2 Theory 106
4.2.3 Fabrication 110
4.2.4 Experimental setup and results 110
4.2.5 Further demonstration 111
4.2.6 Conclusion 111
4.3 Resonantly enhanced Faraday rotation in microfiber coil resonators 113
4.3.1 Introduction 113
4.3.2 Theory 113
4.3.3 Fabrication 115
4.3.4 Experimental setup 116
4.3.5 Simulations 119
4.3.6 Experimental results 122
4.3.7 Conclusion 128
4.4 Passive and active stabilization techniques for microfiber coil resonators 129
4.4.1 Introduction 129
4.4.2 Theory of chirped microfiber coil resonators 129
4.4.3 Simulations 132
4.4.4 Theory of PZC-wound microfiber coil resonators 135
4.4.5 Fabrication 136
4.4.6 Experimental setup 137
4.4.7 Simulations 138
4.4.8 Experimental results 139
4.4.9 Conclusion 140
4.5 Spun optical microfiber for high performance current sensing 142
4.5.1 Introduction 142
4.5.2 Theory 144
4.5.3 Fabrication 146
4.5.4 Simulations 148
4.5.5 Fiber characterization 152
4.5.6 Experimental setup 154
4.5.7 Experimental results 155
4.5.8 Conclusion 156
4.6 Efficient Faraday rotation in birefringent microfiber loop resonators 158
4.6.1 Introduction 158
4.6.2 Simulations 159
4.6.3 Conclusion 164
4.7 Birefringence treatment of non-ideal optical microfiber coils for continuous Faraday rotation 165
4.7.1 Introduction 165
4.7.2 Simulations 165

4.7.3 Conclusion 168
4.8 References 169
5. Acceleration sensing with optical microfiber 173
5.1 Interferometry 173
5.1.1 Introduction 173
5.1.2 Fiber-optic interferometer types 174
5.1.3 Phase demodulation 181
5.1.4 Signal fading 183
5.1.5 Noise sources 183
5.2 Compact flexural disc-based acceleration sensor 186
5.2.1 Introduction 186
5.2.2 Theory 187
5.2.3 Fabrication 191
5.2.4 Experimental setup 194
5.2.5 Simulations 197
5.2.6 Experimental results 204
5.2.7 Conclusion 207
5.3 References 209
6. Acoustic sensing with optical microfiber 212
6.1 Polarimetric interferometry 212
6.2 Compact air-backed mandrel-based acoustic sensor 213
6.2.1 Introduction 213
6.2.2 Theory 213
6.2.3 Fabrication 216
6.2.4 Experimental setup 217
6.2.5 Simulations 220
6.2.6 Experimental results 221
6.2.7 Conclusion 224
6.3 Development of tapering rig for fabricating long optical microfibers 225
6.3.1 Introduction 225
6.3.2 Tapering setup 225
6.3.3 Tapering procedure 226
6.3.4 Experimental results 227
6.3.5 Conclusion 228
6.4 References 229
7. Summary, Discussion and Conclusion 230
7.1 Summary 230
7.2 Discussions 233
7.2.1 Advantages of optical microfibers and nanofibers 233

7.2.2 Challenges and practical issues (future work) 233
7.3 Conclusion 236
7.4 References 238
List of publications 239
A.1 Journal publications 239
A.2 Conference publications 241
A.3 Book chapters 241

Declaration of authorship

I, *George Y. Chen*,

declare that the thesis entitled

'*Optical Microfiber Sensors*'

and the work presented in it are my own. I confirm that:

- this work was done wholly or mainly while in candidature for a research degree at this University;
- where any part of this thesis has previously been submitted for a degree or any other qualification at this University or any other institution, this has been clearly stated;
- where I have consulted the published work of others, it is always clearly attributed;
- where I have quoted from the work of others, the source is always given. With the exception of such quotations, this thesis is entirely my own work;
- I have acknowledged all main sources of help;
- where the thesis is based on work done by myself jointly with others, I have made clear exactly what was done by others and what I have contributed myself;
- parts of this work have been published as:

Refer to Appendex A: List of publications

Signed:

Date: 25/10/2013

Acknowledgements

It would not have been possible to write this doctoral thesis without the help and support of the kind people around me, to only some of whom it is possible to give particular mention here.

Above all, I am deeply indebted to my supervisor, Dr. Trevor P. Newson, for the patience and guidance he showed me throughout the course of my PhD study. His profound knowledge of both optics and electronics has been invaluable to me. Not only did he give me the freedom to explore on my own, but he was always there to help when I encountered difficulties. One simply could not wish for a better or friendlier supervisor.

Progress in this work would not have been possible without the help of the following individuals/groups:

Dr. Gilberto Brambilla – who provided me with countless opportunities and fruitful discussions in the area of optical microfibers. In particular, he gave me the chance to use his fabrication facilities, which I see as a pivotal step in the development of my research. I also had the pleasure of working alongside his friendly and helpful group of fellow PhD students.

Dr. Mohammad Belal – for his generous support especially at the beginning of my PhD study. He is a great colleague who often went out of his way to help me with my research.

The ORC – during this work I have collaborated with many colleagues for whom I have great regard, and I wish to extend my warmest thanks to all those who have helped me.

I would also like to express my gratitude for the financial support provided by the British Engineering & Physical Sciences Research Council (EPSRC).

Last but not least, my utmost gratitude to my wife Qiongyue and son Phillip, my parents and in-laws, for their love and support.

List of abbreviations

ABM	Air-backed mandrel
AC	Alternating-current
BD	Balanced detector
BIF	Bend-insensitive fiber
CT	Current transformer
DC	Direct-current
DOP	Degree of polarization
DR	Dynamic range
EDFA	Erbium-doped fiber amplifier
EMI	Electromagnetic interference
ER	Extinction ratio
FBG	Fiber Bragg grating
FD	Flexural disc
FFT	Fast Fourier Transform
FPI	Fabry–Perot interferometer
FRM	Faraday rotator mirror
FSR	Free spectral range
FUT	Fiber under test
FWHM	Full-width at half-maximum
LPG	Long period grating
LS	Loudspeaker
MC	Optical microfiber coil
MCR	Optical microfiber coil resonator
MI	Mach–Zehnder interferometer
MKR	Optical microfiber knot resonator
MLR	Optical microfiber loop resonator
MNF	Optical micro/nanofiber
MZI	Michelson interferometer
OFDR	Optical frequency-domain reflectometry
OM	Optical microfiber
ON	Optical nanofiber
OPD	Optical path difference
OPL	Optical path length
OR	Operating range
OSA	Optical spectrum analyzer
PBS	Polarization beam splitter
PC	Polarization controller
PCF	Photonic crystal fiber
PD	Photodetector/photoreceiver
PDL	Polarization-dependent loss
PM	Polarization-maintaining
PMC	Polarization-maintaining circulator
PMF	Polarization-maintaining fiber
PMMA	Poly(methyl methacrylate)
PSD	Power spectral density
PZC	Piezo-electric ceramic
PZT	Piezo-electric transducer

Q	Quality (usually associated with Q-factor)
RH	Relative humidity
RI	Refractive index
RIU	Refractive index unit
SG	Signal generator
SMF	Single-mode fiber
SNR	Signal-to-noise ratio
SOM	Spun optical microfiber
SOP	State of polarization
TBP	Time-bandwidth product
TLS	Tunable laser source
UV	Ultraviolet
WLI	White-light interferometer/interferometry

List of figures

Figure 1. Schematic diagram of a micro/nanofiber. 24
Figure 2. Schematic diagram of the flame-brushing technique. 25
Figure 3. Schematic diagram of self-modulated taper-drawing. 26
Figure 4. Schematic diagram of the acid-etching technique. 26
Figure 5. Schematic diagram of direct drawing from bulk. 27
Figure 6. Schematic diagram of self-assembly from silica nanoparticles. 28
Figure 7. Schematic diagram of electro-spinning from glass-forming melt. 28
Figure 8. Dependence of the mode field diameter on the V number of a micro/nanofiber [23]. 32
Figure 9. Dependence of the power fraction propagating in the evanescent field on the wavelength-to-radius ratio in different refractive index surroundings [23]. 33
Figure 10. Schematic diagrams of common non-resonator-type micro/nanofiber arrangements. 39
Figure 11. Schematic diagrams of the optical microfiber (a) loop resonator, (b) knot resonator, and (c) coil resonator. The evanescent field couples power between different sections of the same fiber. The directions of light propagation and coupling are shown as arrows. 41
Figure 12. Schematic diagram of the optical microfiber grating based on a micro-structured rod. Inset: cross-section of the support rod. 43
Figure 13. Schematic diagram of the embedded microfiber loop resonator. The packaging thickness is controlled such that the evanescent field can overlap into the surrounding analyte. 46
Figure 14. (a) Schematic diagram of the microfiber coil resonator sensor, and (b) a photograph of the packaged sample. 48
Figure 15. Schematic diagram of the coated optical nanofiber for bio-chemical sensing. 52
Figure 16. Schematic diagram of the functionalized optical nanofiber tip for selective bio-chemical sensing. 53
Figure 17. Schematic diagram of an optical microfiber coupled to a micro-sphere for biological detection. 55
Figure 18. (a) Photograph of a packaged microfiber coil resonator, and (b) a close-up view on the optical microfiber coiled around the support rod. 58
Figure 19. Schematic diagram of the microfiber loop resonator being modulated in diameter by displacements. 62
Figure 20. Schematic diagram of the optical microfiber interacting with a cylindrical surface to detect non-uniformities. 64
Figure 21. Schematic diagram of the microfiber knot resonator embedded in magnetic fluid. 69
Figure 22. Illustration of how optical resonators respond to changes in the optical path length. 80
Figure 23. Schematic diagram of the microfiber coil resonator-based thermometer sliding along an electrical wire to measure the local temperature. 82

Figure 24. Side cross-sectional view of the microfiber coil resonator sensor with a heating element inside. 83

Figure 25. Schematic diagram of the existing tapering rig setup. A computer controls the initial position and differential velocities of the two translation platforms. 84

Figure 26. Schematic diagram of the existing coiling rig setup. Both the rotation and translation stages are controlled by a computer. 86

Figure 27. Transmission spectrum of the packaged microfiber coil resonator compared to the original SMF-28. Inset: individual pair of resonances associated with the polarized light in the two orthogonal axes arising from linear birefringence. 86

Figure 28. Schematic diagram of the experimental setup. 87

Figure 29. Simulated wavelength shift of the microfiber coil resonator sensor for a 1 °C change in temperature. 88

Figure 30. Characterization of the heating element, with a linear fit. Note: error bars are plotted behind the markers. 89

Figure 31. Measured temperature responsivity with an average linear fit (dashed line), compared with the theoretical prediction (solid line). 90

Figure 32. Schematic diagram of the Faraday Effect. 95

Figure 33. Schematic of the microfiber interrogated by a solenoid to determine the value of $\mu_r V_{eff}$. The curved sections of microfiber outside the solenoid are not drawn. 98

Figure 34. Setup of the basic polarimeter. 99

Figure 35. Setup of the Sagnac interferometer. 100

Figure 36. Setup of the in-line reflection polarimeter. 101

Figure 37. Setup of the polarization diversity polarimeter. 101

Figure 38. Schematic diagram of the microfiber coil sensor head. 106

Figure 39. Schematic diagram of the time-varying current-induced magnetic field imposed on light propagating through the microfiber coil. 108

Figure 40. Simulated broadening of the (a) current pulse shape, as seen in the (b) optical response, by an amount equal to the difference in transit time. 109

Figure 41. Measured optical signal responding to a fast current pulse (400 data points with 10-point moving-average). 111

Figure 42. Schematic diagram of the microfiber coil resonator sensor head being interrogated by current. The directions of light propagation and coupling are shown as arrows. The arrows in dashed-circles represent the Faraday rotation. 114

Figure 43. Analysis of E_x and E_y for a small Faraday rotation. 114

Figure 44. Sensor interrogation using (a) a transformer to generate AC, and (b) a packaged microfiber coil resonator to sense the current via the Faraday Effect. 116

Figure 45. Schematic diagram of the experimental setup. TLS: tunable laser source, PMF: polarization-maintaining fiber, PMC: polarization-maintaining circulator, SMF: single-mode fiber, PC: polarization controller, MCR: microfiber coil resonator, CT: current transformer, SG: signal generator, FRM: Faraday rotator mirror, PBS: polarization beam splitter, PD: photodetector/photoreceiver, BD: balanced detector, OSC: digital oscilloscope. 117

Figure 46. Simulated transmission and Faraday rotation spectra of the microfiber coil resonator ($N = 3$, $r = 0.5$ mm, $n_{core} = 1.45$, $n_{clad} = 1.373$, $\mu_0 = 4\pi\times10^{-7}$, $\mu_r = 1$, $V = 0.54$ rad/T.m, $I = 7.9$ A, $\kappa = 5523$ m^{-1}, $\alpha = 69$ m^{-1}, $\Delta n = 7.7\times10^{-5}$). 122

Figure 47. Measured double-pass transmission spectra of the microfiber coil resonator for X and Y-polarized light, with no current signal. 123

Figure 48. Measured current responsivity (λ_R) at a signal frequency of 30 Hz with a linear fit (dashed line), compared with the theoretical prediction (solid line). For no current or small current-induced signals with SNR < 1, the noise-equivalent rotation based on the measured noise amplitude was plotted instead. 124

Figure 49. Optical signal at (a) λ_0 (b) λ_M and (c) λ_R in response to current signal modulated at I = 7.9 A, f = 30 Hz. 125

Figure 50. Simulated relationship between the initial differential phase and the double-pass Faraday rotation. 126

Figure 51. Simulated relationship between the extinction ratio and the enhancement factor. 127

Figure 52. Effect of thermally induced resonance shift on the transmission spectrum of a (a) 3-turn microfiber coil resonator, and a (b) 12-turn chirped microfiber coil resonator. The two dots compare the output power before and after the shift, when initially operating at the resonant wavelength. 130

Figure 53. Configurations of the chirped microfiber coil resonator with (a) individual turns, and (b) paired turns. 130

Figure 54. For a 3-turn microfiber coil resonator: simulated effect on the resonance shape when (a) the coupling coefficient is varied with no chirping (Δn = 0), and (b) the chirp is varied with a fixed coupling coefficient (κ = 5410 m^{-1}). 132

Figure 55. For a 12-turn regular microfiber coil resonator: simulated effect on the resonance shape when the coupling coefficient is varied with no chirping (Δn = 0), at (a) full scale, and (b) enlarged selection around resonance. 133

Figure 56. For a 12-turn chirped microfiber coil resonator: simulated effect on the resonance shape when the chirp is varied with a fixed coupling coefficient (κ = 5410 m^{-1}), at (a) full scale, and (b) enlarged section around resonance. 134

Figure 57. (a) Simulated spectral width as a function of resonance extinction ratio for 12-turn regular and chirped microfiber coil resonators, and (b) the broadening factor in spectral width for a range of extinction ratios. 134

Figure 58. (a) Schematic diagram of the microfiber coil resonator attached to the Teflon-coated piezo-electric ceramic disc, and (b) an illustration of the physical deformation under piezo-electric and Poisson effects. 135

Figure 59. Schematic diagram showing the cross-sectional view of the Teflon-coated piezo-electric ceramic disc coiled with optical microfiber, from (a) the side, and (b) the top. 136

Figure 60. Schematic diagram of the experimental setup. 138

Figure 61. Simulated wavelength shift of the microfiber coil resonator when 100 V is applied across the electrodes of the piezo-electric ceramic disc. 139

Figure 62. (a) Normalized power spectra showing spectral shift with different voltages, and (b) the measured voltage responsivity with a linear fit (dashed line) compared with the theoretical prediction (solid line). 140

Figure 63. Schematic diagram of the spun microfiber with a constant spin rate Φ along fiber axis z. 144

Figure 64. Side view of (a) a side-polished fiber, and (b) the waist of a tapered fiber. 146

Figure 65. Schematic diagram of the newly developed tapering and spinning rig setup. A computer controls the initial position and differential velocities of the two translation platforms and the rotator module. 147

Figure 66. Simulated relationship between the effective linear birefringence and the packaged linear birefringence with $\Delta n_{eff} = n_x - n_y$ (where n_x = 1.45). 148

Figure 67. Simulated effective linear birefringence as a function of spin rate, for different intrinsic linear birefringence with L = 1 cm. 149

Figure 68. Simulated effective linear birefringence as a function of fiber length, for different spin rates with $\Delta n_{int} = 1\times10^{-2}$. 150

Figure 69. Simulated relationships between (a) differential phase, and (b) Faraday efficiency, with increasing distance along the optical fiber. 151

Figure 70. Simulated normalized current responsivity with varying values of beat length and spin pitch. 152

Figure 71. Transmission spectra of spun microfibers with (a) $\Phi = 0$ rad/cm, (b) $\Phi = 8\pi$/cm, and (c) $\Phi = 16\pi$/cm, each fabricated from a 2 μm diameter hi-bi microfiber with L_{OM} = 10 mm and $\Delta n_{int} = 3.23\times10^{-3}$ 153

Figure 72. Photograph of a packaged sample. The microfiber coil sensor head was embedded in polymer on a glass slide. 154

Figure 73. Schematic diagram of the experimental setup. TLS: tunable laser source, PMF: polarization-maintaining fiber, PMC: polarization-maintaining circulator, SMF: single-mode fiber, PC: polarization controller, MC: optical microfiber coil, CT: current transformer, SG: signal generator, FRM: Faraday rotator mirror, PBS: polarization beam splitter, PD: photodetector/photoreceiver, BD: balanced detector, OSC: digital oscilloscope. 155

Figure 74. Measured current responsivity for spun and unspun microfibers at a signal frequency of 30 Hz, with average linear fits. 156

Figure 75. Dependence of Faraday efficiency ($\eta = \theta/\theta_{ideal}$) on differential phase. 159

Figure 76. Schematic diagram of a microfiber loop resonator-based current sensor. The directions of light propagation and coupling are shown as arrows. The arrows in dashed-circles represent the Faraday rotation. 159

Figure 77. Transmission spectra of microfiber loop resonators, with (a) zero birefringence, (b) a small/moderate birefringence-induced resonance separation, and (c) a large birefringence-induced resonance separation. 160

Figure 78. Roundtrip phase analysis for microfiber loop resonators operating at the resonant wavelength, with (a) zero birefringence, (b) X-eigenmode on-resonance with large birefringence-induced resonance separation ($L_B = 4L_C$), and (c) Y-eigenmode on-resonance with large birefringence-induced resonance separation ($L_B = 4L_C$). The initial phase (coupled in light) and final phase (prior to coupling back in) are labeled inside rectangles that represent the M^{th} and N^{th} roundtrip of the eigenmode in the fast- and slow-axes respectively. 161

Figure 79. Schematic diagram of the birefringence modulation technique operating at selective regions along the microfiber coil. The directions of light propagation and coupling are shown as arrows. The arrows in dashed-circles represent the Faraday rotation. 166

Figure 80. Simulations of birefringence modulation in a microfiber coil (λ = 1550 nm, $\mu_0 = 4\pi\times10^{-7}$, $\mu_r = 1$, I_{DC} = 10 A, V = 0.54 rad/T.m, r = 0.5 mm) to rectify the direction of Faraday rotation for an efficient build-up of current responsivity over fiber length. The impact of changing (a) the local birefringence, is reflected in (b) the differential phase, (c) the Faraday efficiency, and (d) the total Faraday rotation. 167

Figure 81. Schematic diagram of the fiber-optic Mach–Zehnder interferometer. 175

Figure 82. Schematic diagram of the fiber-optic Michelson interferometer. 176

Figure 83. Schematic diagram of the fiber-optic Fabry–Perot interferometer. 177

Figure 84. Schematic diagram of the fiber-optic white light interferometer. 178

Figure 85. Schematic diagram of the fiber-optic Sagnac interferometer. 179

Figure 86. Schematic diagram of the fiber-optic passive ring resonator. 180

Figure 87. Different magnitudes of phase-induced optical power modulation along an interference fringe. 181

Figure 88. Schematic diagram of a fiber-optic interferometer with feedback control. 182

Figure 89. (a) Schematic diagram of the equivalent force/pressure imposed on the flexural disc resulting from acceleration, and (b) the top view of the disc showing radial strain translating into axial strain on the optical microfiber. 187

Figure 90. Schematic diagram of the displacements in a flexing disc. 189

Figure 91. Schematic diagram of two possible optical microfiber arrangements on the surface of a flexural disc. 191

Figure 92. Proposed automated winding technique for long microfibers. The arrows indicate the direction of motion. 194

Figure 93. Schematic diagram of the experimental setup. TLS: tunable laser source, SMF: single-mode fiber, PZT: piezo-electric transducer, FRM: Faraday rotator mirror. 195

Figure 94. Example fringe analysis for the Fabry–Perot reference interferometer. 197

Figure 95. Simulated relationship between the fiber length and the acceleration responsivity, for different fiber diameters at r = 12 mm. 198

Figure 96. Simulated relationship between the distance from the disc center and the acceleration responsivity, for different fiber diameters at L = 5 mm. 199

Figure 97. Simulated relationship between the disc radius and the detection bandwidth for different fiber diameters. 200

Figure 98. Simulated acceleration responsivities and detection bandwidths of microfiber and bend-insensitive fiber-based flexural discs of varying sizes. 201

Figure 99. Schematic diagram showing the side cross-sectional structure of the optical microfiber loop embedded in polymer and attached to the disc. 201

Figure 100. Simulated relationship between the fiber length and the double-pass phase change for different fiber diameters. 203

Figure 101. Measured acceleration responsivity of Samples 1 and 2 at a signal frequency of 500 Hz with linear fits (dashed lines), compared with the theoretical prediction (solid lines). For no acceleration or small acceleration-induced signals with SNR < 1, the noise-equivalent phase based on the measured noise amplitude was plotted instead. Note: error bars may be obscured by the markers. 204

Figure 102. Measured frequency response for acceleration responsivities. 205

Figure 103. Measured frequency response for acceleration sensitivities. 207

Figure 104. Schematic diagram of the simple polarimeter. The arrows indicate: the polarization azimuth of the input light (yellow), the axes of the birefringent fiber (dotted green), and the polarization azimuth of the analyzer (purple). 212

Figure 105. (a) Working principle of the air-backed mandrel bound with a microfiber coil, and (b) a schematic diagram of the construction. 214

Figure 106. (a) Photograph of the UV-curing process of the polymer coating, and (b) the resulting sensor fixed on a glass slide for testing. 217

Figure 107. Schematic diagram of the experimental setup. TLS: tunable laser source, PMF: polarization-maintaining fiber, PMC: polarization-maintaining circulator, SMF: single-mode fiber, PC: polarization controller, ABM: air-backed mandrel, PBS: polarization beam splitter, BD: balanced detector, OSC: digital oscilloscope, SG: signal generator, LS: loudspeaker with power amplifier. 218

Figure 108. Measured acoustic responsivity at a signal frequency of 70 Hz with a linear fit (dashed line), compared with the theoretical prediction (solid line). For no acoustic or small acoustic-induced signals with SNR < 1, the noise-equivalent phase based on the measured noise amplitude was plotted instead..... 221

Figure 109. Measured frequency response for acoustic responsivities and sensitivities. 222

Figure 110. Optical and loudspeaker drive signals at the frequency of 1562.5 Hz. The temporal offset is due to the time delay for the acoustic signal to reach the sensor. 223

Figure 111. Schematic diagram of the newly developed tapering rig setup. 226

Figure 112. Photograph showing the tapering rig inside the enclosure. Inset: side-view of the micro-heater with the optical fiber positioned in the center of the cavity..... 226

Figure 113. Measured and ideal fiber taper diameter profiles. 227

Figure 114. Transmission spectra of the optical microfiber compared to the original SMF-28. 228

List of tables

Table 1. Comparison of best-reported performances in each micro/nanofiber design category for micro-fluidic-based refractive index sensing. 50

Table 2. Comparison of best-reported performances in each micro/nanofiber design category for humidity sensing. 52

Table 3. Comparison of best-reported performances in each micro/nanofiber design category for temperature sensing. 58

Table 4. Comparison of best-reported performances in each micro/nanofiber design category for current sensing. 60

Table 5. Comparison of best-reported performances in each micro/nanofiber design category for displacement sensing. 63

Table 6. Comparison of best-reported performances in each micro/nanofiber design category for acceleration sensing. 65

Table 7. Comparison of best-reported performances in each micro/nanofiber design category for force sensing. 67

Table 8. Verdet constants, refractive indices and attenuation for a selection of glasses 103

Table 9. Verdet constants, refractive indices and attenuation for a selection of polymers. . 104

Table 10. Summary of contributions to current sensing using optical microfiber technology. 237

Chapter 1

1. Introduction

In the past few decades, fiber-optic sensors have seen an immense rise in applications which has attracted a great deal of attention from both research institutions and industries Fiber-optic sensor technology offers the possibility of sensing different measurands such as RI, bio-chemical, temperature, current, displacement/strain, bend/curvature, roughness, acceleration, force/pressure, rotation, acoustic, electric field and magnetic field in harsh and remote locations. Information about the measurand is typically conveyed by a modulation in power, phase, polarization or wavelength of the received light.

Indeed, fiber-optic sensors have been the subject of an intense research and development effort. The most important and well-known applications in terms of commercial value are the fiber-optic gyroscope and hydrophone. They have been extensively studied and optimized over the years, offering unprecedented reliability and the benefit of being very low cost. The growing interest in fiber-optic technology stems from its inherent benefits of high responsivity, high detection bandwidth, high temperature performance, excellent immunity to electromagnetic interference (EMI), all-dielectric composition, environmental ruggedness and distributed-sensing capability. These advantages of fiber-optic sensors over their electrical equivalents make them popular in a wide range of applications such as manufacturing processes, quality control systems and medical diagnostics.

Optical microfibers and nanofibers (MNF) are a new lineage of optical fiber that confine light due a refractive index (RI) difference between the solid core and the external medium cladding. The fraction of light that propagates in the cladding depends on the ratio of the fiber diameter to the wavelength of light. It has now been a decade since the first experiments on low-loss MNFs were conducted by Tong *et al* [1]. Interest in this early work quickly mushroomed out to laboratories worldwide, generating a thriving research community which has sustained a strong focus on this technology through the 2000s to the present time. The motivation behind this on-going research is to establish micro- and nano-scale optical fibers as a new sensor

technology which can create devices that are extremely small size, ultra-light weight and have the potential to be manufactured at low cost.

1.1 Scope and objectives

This thesis is based on the development of optical microfiber (OM)-based temperature, current, acceleration and acoustic sensors. The main objective of this research is to design and implement novel sensor heads that exhibit at least one order of magnitude improvement in compactness, responsivity, detection bandwidth and response time. When integrated with the appropriate detection system, the improvement in responsivity can yield a superior sensitivity to the measurand. Such devices are to be theoretically modeled, fabricated, characterized and tested in-house. Although optical nanofibers (ON) have the potential to surpass OMs in terms of performance, their fragility currently limits the extent of their use. The key topics underlying this work can be summarized as follows:

- To develop an understanding of the theory and experimental design of interferometric and polarimetric-based sensors, as well as the fundamental properties and fabrication methods of MNFs.
- To generate ideas for novel sensors and performance enhancing techniques.
- To provide theoretical and experimental demonstrations of OM-based temperature, current, acceleration and acoustic sensors.

1.2 Thesis outline

The work carried out in this thesis is based on the author's own research. Use of any material from other sources is clearly referenced. This thesis is divided into seven chapters. Chapter 2 introduces the background of MNF technology, including the fabrication techniques, waveguide properties, sensing parameters, and an overview of prominent MNF-based sensors reported in literature. Chapter 3 describes the resonant wavelength shift detection schemes that are typically employed for resonator-based temperature sensing, before presenting the theoretical and experimental demonstrations of a sliding microfiber coil resonator (MCR)-based thermometer for the rapid inspection of insulation faults along electrical wires.

Chapter 4 focuses on the core subject of this thesis, namely current sensing using OMs. Firstly, a range of polarization rotation detection schemes are compared to identify their merits and demerits. Lessons learnt from this critical analysis are used to select, combine and develop the most promising schemes to be exploited. To begin with, the compactness and gigahertz detection bandwidth capability of OM-based current sensors are introduced. This is followed by a short study on the possible materials for improving the performance of the sensor head. Next, the resonance ability of the sensor head is demonstrated both theoretically and experimentally for responsivity enhancement. To solve the stability issues of the resonator, techniques based on RI chirping (passive) and piezo-electric tuning (active) are discussed. To further refine the sensor head, the problem of birefringence is considered by first critically appreciating the previous contributions relating to eliminating bend- and packaging-induced birefringence, before presenting a solution in the form of spun optical microfiber (SOM). The fabrication details and characterization results are followed by current sensing trials. Moreover, the means to achieve efficient Faraday rotation in both birefringent and non-birefringent optical microfiber loop resonators (MLRs) is theoretically analyzed. Lastly, a novel post-fabrication technique is proposed as an alternative to SOM for countering the birefringence-induced reduction in the responsivity of MC-based current sensors.

Chapter 5 initially explores the existing range of interferometers and phase demodulation schemes to identify their pros and cons, before discussing issues such as drifting, ambiguity, signal fading and noise. The benefits of combining OM with interferometry for acceleration sensing are then presented, with the experimental demonstrations of a flexural disc (FD) accelerometer supported by simulations. Similarly, Chapter 6 briefly describes the polarimetric variant of interferometry, before exploring the benefits of using OM for acoustic sensing. A compact air-backed mandrel (ABM) microphone is presented to further illustrate the potential of OM-based sensors. This sensor design can be modified for operating underwater as a hydrophone. In addition, the development and testing of a new tapering rig specialized for making long fiber tapers is reported. The aim is to deliver sufficient lengths of OM to realize the full potential of OM-based sensors. Finally, Chapter 7 concludes the thesis with a summary of results and a discussion on future work aimed at overcoming challenges and scaling the performance of OM-based sensors.

Chapter 2

2. Background of optical microfiber and nanofiber-based sensors

The field of optical MNF sensing has witnessed an explosion of activity since they were first introduced a decade ago. Rapid advances in MNF-based sensors have been driven by prospective powerful industries such as automotive, biomedical and defense, with increasing demands for highly responsive/sensitive, high detection bandwidth, fast response, highly selective, non-intrusive, compact, light and robust sensors that can perform in-situ measurements at remote and harsh environments. A diverse range of MNF-based sensors have been developed for measuring RI, bio-chemical, temperature, current, displacement/strain, bend/curvature, roughness, acceleration, force/pressure, rotation, acoustic, electric field and magnetic field. Therefore, it is imperative to review the sensors and techniques developed so far in order to comprehend the current status and future opportunities. This chapter provides an introduction to MNFs in terms of the fabrication techniques, optical and mechanical properties, sensing parameters, and an overview of MNF-based sensors.

2.1 Introduction

MNFs are the uniform waists of biconical fiber tapers, with diameters comparable to the wavelength of light. MNFs are usually manufactured by heating and stretching [2] regular-sized optical fibers whose diameter are often in excess of 100 μm. The result is a biconical taper that provides a smooth, lossless connection to other fiberized components. By controlling the pull rate during the fabrication process, the taper diameter profile can be fine-tuned to suit the application [3, 4]. Optical materials other than silica have been used to manufacture MNFs, including phosphate [5], tellurite [5], lead silicate [6], bismuthate [6], chalcogenide glasses [7], and a variety of polymers [8–11]. The remarkable optical and mechanical properties exhibited by MNFs make them an excellent platform for optical sensors.

2.2 Fabrication

Applications of MNFs have previously been limited because of the difficulties in fabricating low-loss sub-micron structures. With the development of computer-controllable tapering rigs, it is now possible to manufacture precise and sub-wavelength tapers. The most conventional way to reduce the fiber diameter is to taper it. Optical fiber tapers are made by stretching a heated fiber, forming a structure comprising a narrow stretched filament (i.e. the taper waist) each end of which is linked to an un-stretched fiber by a conical section (i.e. the taper transition), as shown in Figure 1. In the down-taper transition, the mode confinement changes from a core-cladding to a cladding-surrounding interface. That is, the original core disappears and the original cladding becomes the new core, with the external medium being the new cladding. If the transition is adiabatic [12, 13], the optical loss of the transition regions is negligible.

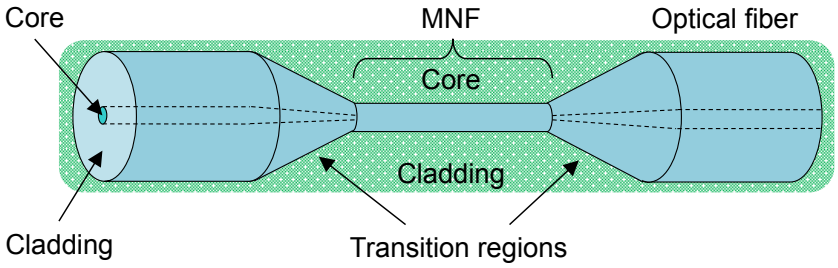

Figure 1. Schematic diagram of a micro/nanofiber.

In the following sections, the fabrication techniques are either classified as top-down or bottom-up. Bottom-up techniques grow MNFs from a seed of a few nanometers. Top-down techniques manufacture MNFs by reducing the size of macroscopic samples, and thus can provide much longer MNFs.

2.2.1 Flame-brushing technique

The flame-brushing technique was initially developed for manufacturing fiber tapers and fused couplers. The basic idea involves a moving small flame under the optical fiber that is being stretched, as shown in Figure 2. Both the burner and the optical fiber ends are fixed onto stages and controlled by a computer. By fine-tuning the pull rate and the flame movement, the taper shape can be tailored to a high degree of accuracy. Moreover, it has been known to provide the longest MNFs (e.g. 110 mm)

[14] with the lowest measured loss (e.g. 0.015 dB/mm) [15]. Finally, the flame-brushing technique enables both ends of the MNF to be pigtailed to standard optical fiber. This feature is extremely important for practical applications, where connectivity and system integration are highly essential.

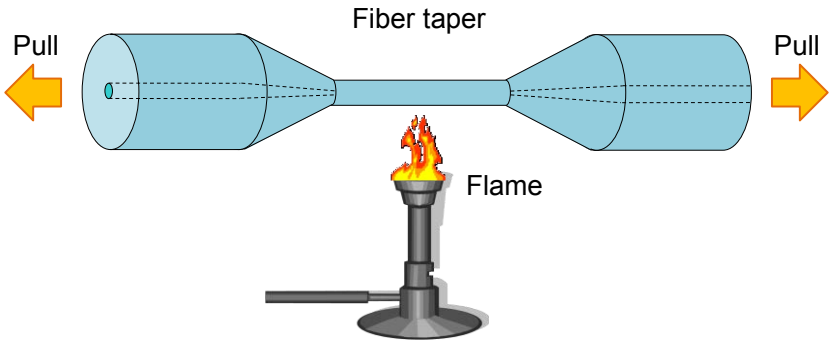

Figure 2. Schematic diagram of the flame-brushing technique.

2.2.2 Modified flame-brushing technique

The modified flame-brushing technique replaces the flame by a ceramic micro-heater [6] or a sapphire capillary tube heated by a CO_2 laser beam [16]. In the center of the micro-heater is a heating element whose temperature can be set by tuning the current level. For the sapphire tube/CO_2 laser approach, the temperature is controlled by varying the focus of the laser beam onto the sapphire tube. The modified flame-brushing technique provides more flexibility than the original technique due to the adjustable temperature range. This technique can be applied to manufacture MNFs from a wide range of low softening-temperature glasses. For silica optical fibers, this technique can fabricate MNFs with much lower OH content compared with those manufactured by the flame-brushing technique, which generates water vapor as combustion by-product [6].

2.2.3 Self-modulated taper-drawing

This technique begins with the tapering of a standard optical fiber to a diameter of several micrometers using the conventional flame-brushing technique. Then, the taper waist is broken into two halves with one end wrapped around a hot sapphire rod, and the other end bent and further drawn to a sub-micron diameter. The sapphire tip shown in Figure 3 is heated with a flame at a distance from the optical fiber, in order to maintain a steady temperature distribution. Initially, to draw a thick wire

would require a relatively large force. Coincidentally, the center of bending occurs at the thicker part of the taper, which will produce a tensile force to stretch the optical fiber. As the taper length increases and the waist diameter decreases, the bend loosens and the center of bending moves towards the thinner end of the taper. This results in smaller forces for drawing thinner wires, which helps to keep the taper from breaking under unpredictable drawing conditions. Although this approach involves a complex fabrication procedure and a relatively high loss (at least one order of magnitude higher than the other techniques), the so-called self-modulated taper-drawing technique is capable of providing extremely small diameter MNFs [17].

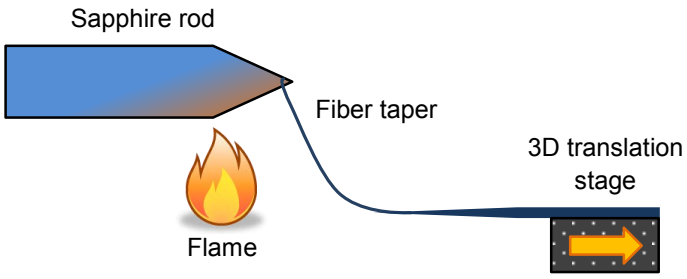

Figure 3. Schematic diagram of self-modulated taper-drawing.

2.2.4 Acid-etching technique

Etching techniques are mostly used to create or modify MNF tips rather than uniform waists. To initiate the etching process, an acid droplet-filled dish is raised by a translation stage to immerse a standard optical fiber, as shown in Figure 4. The droplet shape, position, immersion depth and time allowed the length and diameter of the waist region to be tailored for the intended application. As for creating biconical tapers, optical losses less than 0.1 dB/mm have been demonstrated [18].

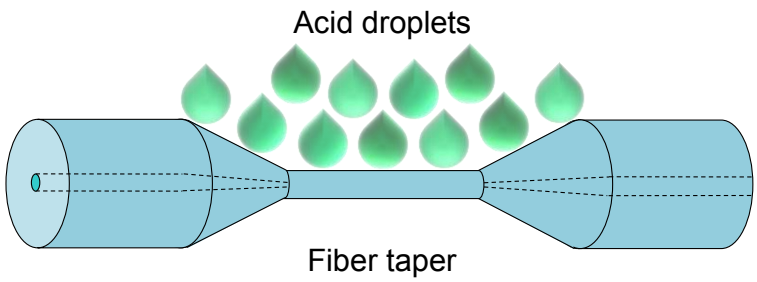

Figure 4. Schematic diagram of the acid-etching technique.

2.2.5 Direct drawing from the bulk

For optical materials that are unavailable in fiber form, it is possible to manufacture MNFs straight from the bulk material [5]. In this approach, a small hot sapphire rod shown in Figure 5 is brought into contact with the bulk glass for a localized softening. Then the sapphire rod is promptly moved away, drawing a glass strand with micrometer/sub-micron diameter. This technique is extremely flexible and does not require expensive equipment, but the MNF uniformity and diameter are difficult to control.

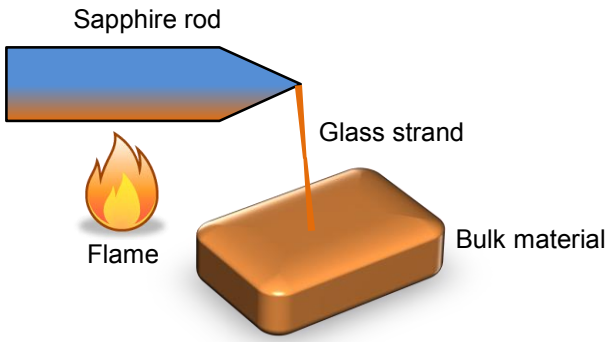

Figure 5. Schematic diagram of direct drawing from bulk.

2.2.6 Self-assembly from silica nanoparticles

In a rather different approach, uniform OMs can be created by evaporative self-assembly [19]. The process initiates from a colloidal silica dispersion of nanoparticles with a small amount of NH_4^+ ions to prevent aggregation in the solution. OM formation shown in Figure 6 occurs as a consequence of rising stresses during the evaporation of the immobilized drop. These stresses arise due to the van der Waals forces that bind nanoparticles together into a closely packed structure. During the course of drying, the constriction of the so-called coffee-stain effect leads to inward-directional stress around the ring. This packing-in effect counteract the stresses. As the self-assembly propagates following the evaporation front, the rapid build-up of radial stresses leads to fractures. Although stresses are temporary relieved, they build up again and the fractured planes act as seeds for further fracturing. The maintenance of this cycle forms the basis for the fabrication of OMs.

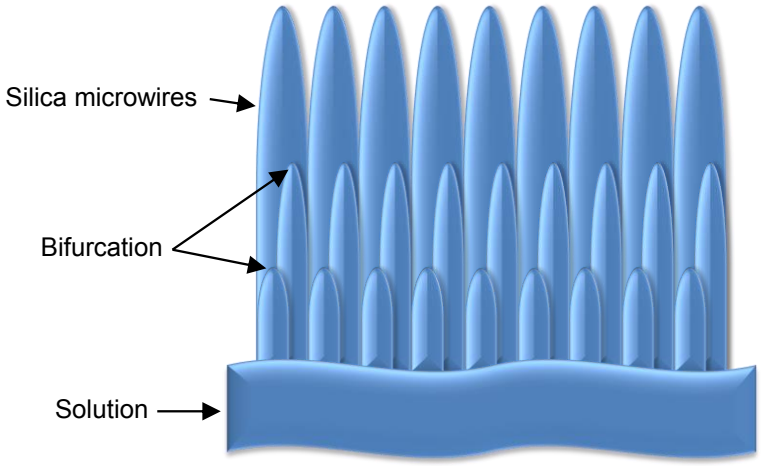

Figure 6. Schematic diagram of self-assembly from silica nanoparticles.

2.2.7 Electro-spinning from a glass-forming melt

To-date, the direct production of sub-micron diameter glass fibers has relied on mechanical drawing techniques. Electro-spinning [20] is a popular technique which has been known for decades for its ability to produce sub-micron diameter fibers from a wide range of polymer solutions. Part of the attraction is its simplicity to implement. Figure 7 shows that by applying a voltage to the solution and charging its surface, a liquid jet is ejected from the surface to form nanometer-diameter continuous glass fibers [21].

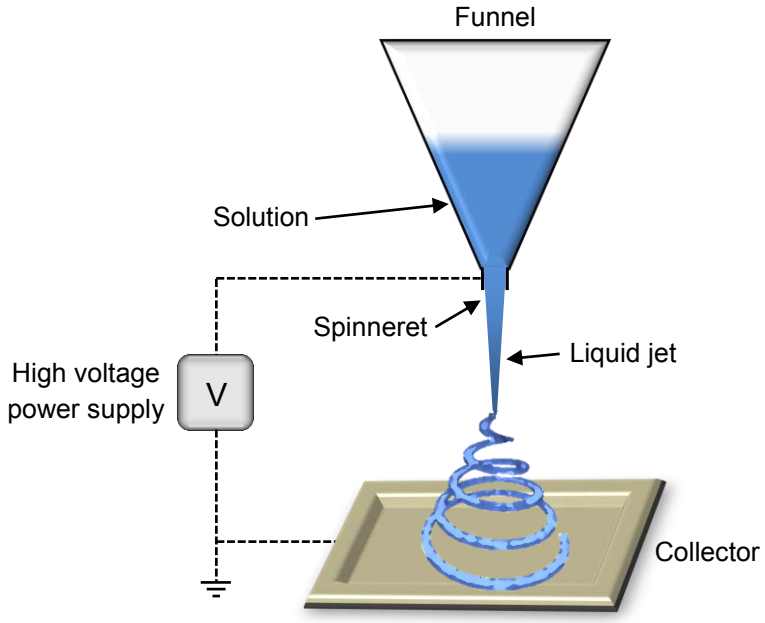

Figure 7. Schematic diagram of electro-spinning from glass-forming melt.

To summarize the various fabrication methods, one should consider using the modified flame-brushing technique if the application requires long length and low loss. Due to the tunable processing temperature, more fabricators are choosing the modified version over the original. If the emphasis is on producing the smallest possible diameter OM, the self-modulated taper-drawing is the best choice. If the material happens to be in a non-fiber form, one can choose between direct drawing from the bulk, self-assembly from nanoparticles (silica only), or electro-spinning from a glass-forming melt. For a non-precise OM geometry, the first method is the simplest and quickest to carry out. The second method is still in the early stages of development, so the control over the OM geometry is unlikely to be optimized. The third method is well established and therefore it may serve as the ideal candidate.

2.3 Optical and mechanical properties

This section introduces the unique optical and mechanical properties of MNFs, including mode propagation, evanescent field, optical confinement, propagation loss, bend loss, mechanical strength, dispersion and nonlinearity.

2.3.1 Mode propagation

In MNFs, light is guided by the cladding-surrounding interface rather than by the core-cladding interface for two reasons. Firstly, the original core after tapering is more than one order of magnitude smaller than the wavelength of light. Secondly, the RI difference at the cladding-surrounding (e.g. air) interface can be up to 100 times larger than the RI difference at the core-cladding interface. Therefore, the core has a marginal influence on the guiding properties and can be neglected. As light propagates, the effective index decreases monotonically along the down-taper transition, and the mode becomes guided by the cladding-surrounding interface. For the rest of this thesis, the cladding will be considered as the core of the MNF.

Since the weakly guiding approximation is not valid as a result of the large RI difference between the cladding and its surrounding medium, the exact eigenvalue equation is used for the propagation constant (β) of various hybrid and transverse modes [22].

For HE_{vm} and EH_{vm} modes:

$$\left[\frac{J_v'(U)}{UJ_v(U)}+\frac{K_v'(W)}{WK_v(W)}\right]\cdot\left[\frac{J_v'(U)}{UJ_v(U)}+\frac{n_{sur}^2K_v'(W)}{n_{MNF}^2WK_v(W)}\right]=\left(\frac{v\beta}{kn_{MNF}}\right)^2\cdot\left(\frac{V}{UW}\right)^4 \qquad (2.1)$$

where the β solutions are denoted with two indices v and m. v originates from the detailed calculations of the fields and describes the azimuthal dependence. m denotes the m^{th} root of the eigenvalue equation. J_v is the v^{th} order Bessel function of the first kind and K_v is the v^{th} order modified Bessel function of the second kind. n_{MNF} and n_{sur} are the refractive indices of the MNF and its surrounding medium respectively.

For TE_{0m} modes:

$$\frac{J_1(U)}{UJ_0(U)}+\frac{K_1(W)}{WK_0(W)}=0 \qquad (2.2)$$

For TM_{0m} modes:

$$\frac{n_{MNF}^2 J_1(U)}{U J_0(U)} + \frac{n_{sur}^2 K_1(W)}{W K_0(W)} = 0 \tag{2.3}$$

where $U = r \cdot \sqrt{k_0^2 n_{MNF}^2 - \beta^2}$, $W = r \cdot \sqrt{\beta^2 - k_0^2 n_{sur}^2}$,
$V = \sqrt{U^2 + W^2} = k_0 \cdot r \cdot \sqrt{n_{MNF}^2 - n_{sur}^2}$, $k_0 = \frac{2\pi}{\lambda}$,

k_0 is the propagation constant of light in free-space. r is used to denote the core radius and corresponds to the core-cladding interface from the center in standard optical fibers, and likewise the cladding-surrounding interface from the center in MNFs.

2.3.2 Optical confinement

MNFs can confine light to the diffraction limit for lengths that are only limited by loss. As shown in Figure 8, when r starts to decrease, the V number decreases and light becomes more tightly confined until the mode field diameter (ω) reaches a minima (A). For smaller V, the core-cladding interface does not confine light anymore and the spot size expands into the cladding, causing ω to reach a maxima (B). By further reducing V, light is then guided only by the cladding-surrounding interface. ω decreases until it reaches a minima around $V \approx 2$ (C), before increasing again. The region below $V < 2$ is typical of MNFs, where ω can be much greater than r and a large fraction of the power resides in the evanescent field. For $V < 0.6$, ω can continue to expand until it becomes orders of magnitude larger than r.

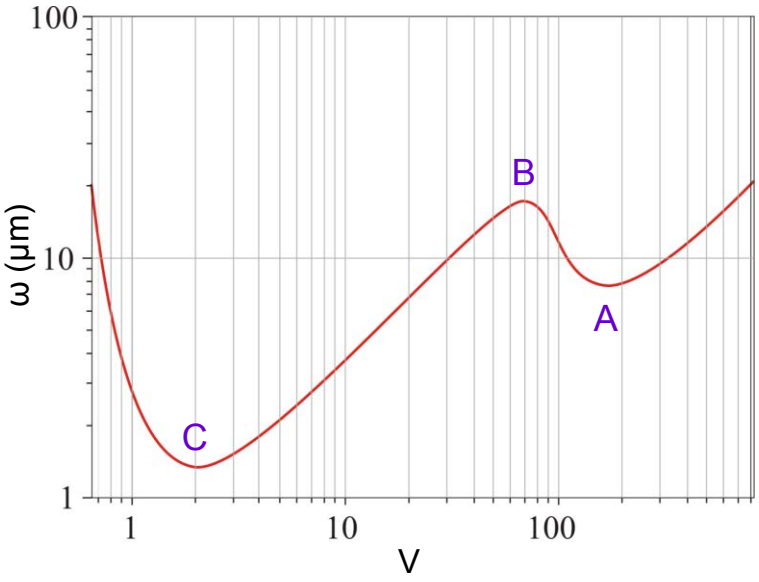

Figure 8. Dependence of the mode field diameter on the V number of a micro/nanofiber [23].

2.3.3 Evanescent field

When $V \ll 1$, a large portion of the optical power resides in the evanescent field outside the MNF. The extension of the evanescent field and the fraction of power (η_{EF}) propagating in it depend on the λ/r ratio and can be obtained from the component of the Poynting vector along the direction of the beam propagation S_z [22]:

$$\eta_{EF} = \frac{\int_{out} S_z \mathrm{d}A}{\int_{in} S_z \mathrm{d}A + \int_{out} S_z \mathrm{d}A} = \frac{\int_r^{\infty} S_z \mathrm{d}A}{\int_0^r S_z \mathrm{d}A + \int_r^{\infty} S_z \mathrm{d}A} \tag{2.4}$$

where $\int_{in} S_z \mathrm{d}A$ and $\int_{out} S_z \mathrm{d}A$ are over the MNF cross-sectional area (A) inside and outside the MNF respectively. Figure 9 shows the nonlinear dependence of η_{EF} on the λ/r ratio for silica MNFs (i.e. RI of n = 1.444) with different surrounding RI. When the surrounding medium is air, η_{EF} reaches 0.5 at λ/r = 4, meaning that half of the power is propagating outside the MNF when its radius is a quarter of the wavelength of light. η_{EF} increases with increasing surrounding RI for the same λ/r ratio. Therefore, to enhance the evanescent field, low-loss polymers can be used to embed (i.e. submerse) the MNF. To improve the η_{EF} even further, hollow MNFs have been proposed [24]. A large evanescent field is particularly important in

resonators, where a significant fraction of the propagating power needs to interact with surrounding medium.

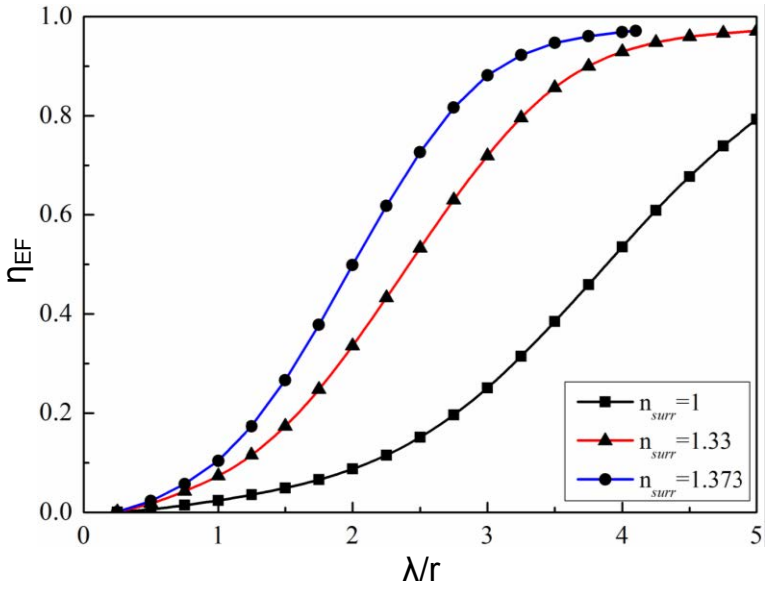

Figure 9. Dependence of the power fraction propagating in the evanescent field on the wavelength-to-radius ratio in different refractive index surroundings [23].

2.3.4 Propagation loss

The greatest contributions to loss come from surface roughness, diameter non-uniformity, and impurities associated with the MNF and its surrounding medium [25]. The loss increases for decreasing MNF diameter, regardless of the fabrication technique. This can be explained by the stronger interaction between the field intensity of the guided light and the surface of thinner MNFs. A theory of non-adiabatic intermodal transitions was developed to investigate what is the smallest MNF which can still transmit light [26, 27]. The guided mode was found to vanish at a threshold value of what is approximately one order of magnitude smaller than the wavelength of light. The propagation loss is also time-dependent [28] and a high temperature treatment is necessary to restore the loss to its near-initial condition [14]. MNFs with smaller diameters were found to degrade faster in air and this was attributed to the formation of cracks at the surface as a consequence of water absorption [14]. A method of reducing the time-related degradation was demonstrated by embedding MNFs in low-RI materials such as Teflon (n = 1.315) [29].

2.3.5 Bend loss

MNFs have excellent mechanical properties which allow them to be bent and manipulated without inducing physical damage. Due to the large RI contrast between silica and air, bend radii of the order of micrometers can be readily achieved with relatively low bend-induced loss (e.g. <1 dB for 90° turn with a bend radius of 5 μm in an air-clad 530 nm diameter silica MNF [30]). This gives rise to highly compact devices with complex geometry.

2.3.6 Mechanical strength

Although MNFs have very small dimensions, they possess an extraordinarily high strength due to the smaller flaw size of surface imperfections. The tensile ultimate strength of MNFs fabricated by the modified flame-brushing technique was found to be much higher than those made by the self-modulated taper-drawing technique [17].

2.3.7 Dispersion

MNFs have a remarkable potential for tailoring the dispersion properties, to a greater extent via the waveguide contribution rather than the material contribution. By controlling the MNF diameter it is possible to move the zero-dispersion to a shorter wavelength [31]. Furthermore, since a considerable fraction of the mode can propagate outside the MNF's physical boundary, its dispersion properties can also be modified by changing the surrounding medium (e.g. using transparent liquids).

2.3.8 Nonlinearity

The optical nonlinearity (γ) of a MNF is at its maximum when ω reaches its minimum in the high confinement region ($V \approx 2$ in Figure 8). While standard optical fibers such as the telecom single-mode fiber (SMF-28) have $\gamma \approx 10^{-3}$ $W^{-1}m^{-1}$, γ in silica MNFs are about seventy times larger due to the inverse relationship between the effective γ and ω. By producing MNFs from highly nonlinear materials (e.g. lead silicate, bismuth silicate and chalcogenide glasses), γ can be up to five orders of magnitude larger than that of SMF-28 [6]. This makes them superior hosts for observing nonlinear effects.

2.4 Sensing parameters

The performance of sensors is typically conveyed by a set of parameters including responsivity, resolution, sensitivity, response time, detection bandwidth and operating range. There are also non-numerical parameters such as repeatability, reproducibility, stability, practicality and compactness.

2.4.1 Responsivity of sensor

The responsivity of the sensor head describes the change in the detected parameter as a result of a change in the measurand. For example, in the case of refractometric sensors a change in the RI, measured in units of RIU, is very often understood in terms of a wavelength shift relative to an initial wavelength. This detection parameter is measured in nanometers, yielding the responsivity in nm/RIU.

2.4.2 Resolution or sensitivity of detection system

The resolution or sensitivity of the detection system denotes the smallest observable change in the parameter (e.g. wavelength or phase) used for detection. The resolution or sensitivity is related to the precision with which the measurement is made, and thus it is governed by the specifications of the detection system. For example, the phase sensitivity is usually based on the phase of the noise-equivalent signal.

2.4.3 Sensitivity of measurand

The sensitivity of the measurand represents the smallest value of the measurand that can be detected by the sensor. It is calculated by dividing the resolution/sensitivity of the detection system by the responsivity of the sensor.

2.4.4 Response time

Response time (T_R) is sometimes defined as the time taken for the detection parameter to rise from 10–90% of its final value, or to fall from 90–10% of its initial value. In this case, it is governed solely by the time delay of the sensing mechanism rather than that of the electro-optic system. In other cases, such as this thesis, T_R is associated with the time delay of the sensing mechanism plus the transit time of light to reach the photoreceiver. The excess delay of the electronics/software/firmware is not included, because it depends much on the user settings (e.g. averaging).

2.4.5 Detection bandwidth

Detection bandwidth (B_w) is the maximum signal frequency of the measurand that can be detected without significant fading or distortion (e.g. ±3 dB response).

2.4.6 Dynamic range

Dynamic range (DR) is the range of values of the parameter that can be measured by the sensor head, and hence by definition a large DR is highly desirable.

2.4.7 Repeatability

Repeatability provides an indication of the agreement between the measured performances of the same sensor head taken under the same experimental conditions at different times. The repeatability reflects the life-time of the sensor head.

2.4.8 Reproducibility

Reproducibility is based on the agreement between the measured performances of different sensor heads taken under the same experimental conditions. A good reproducibility is essential for the mass production of a qualified sensor.

2.4.9 Stability

Stability is associated with the susceptibility of the sensor head to external effects such as temperature, vibrations or EMI. A good stability ensures accurate measurements over a long period of time.

2.4.10 Practicality

Practicality is about how viable it is for the sensing system to be transported from a laboratory to real measurement environments. For example, if the sensor head needs to be redesigned or refabricated for each measurement then it is not practical.

2.4.11 Compactness

Compactness is one of the key considerations for a sensor. For sensing systems that allow remote interrogation, the size and weight of the detection system is not as important as those of the sensor head. A small footprint allows easier deployment and minimizes intrusion in the measurement environment.

2.5 Sensors overview

This section introduces some of the MNF-based sensors reported to-date for the measurement of RI, bio-chemical, temperature, current, displacement, bend/curvature, roughness, acceleration, force, rotation, acoustic, electric field and magnetic field.

Non-resonator-type (i.e. no closed-loop interference) MNF-based sensors come in many different forms, as illustrated by Figure 10. The straight MNF shown in Figure 10(a) is a common configuration that exploits the strong evanescent field of the guided modes to interact with its surrounding medium [32]. The measured effect is usually a direct change in power or an indirect change in power from a change in phase of the transmitted light. The straight MNF is either connected to standard optical fiber pigtails or evanescently coupled to single-ended fiber tapers shown in Figure 10(b). To enhance the responsivity to certain measurands, the surface of the MNF shown in Figure 10(c) can be functionalized to respond to specific chemical or biological species [33]. Fiber Bragg gratings (FBG) [34] illustrated in Figure 10(d) or long period gratings (LPG) [35] can be inscribed on the straight MNF that undergo a spectral shift in response to a change in the ambient conditions.

Figure 10(e) shows that two strands of MNF can be manipulated to form a Mach–Zehnder interferometer (MZI) [36] that features high responsivity to the phase difference between the sensing and reference arms. Alternatively, abrupt tapered sections can be exploited for modal interferometry in the configuration of either MZI [37] (Figure 10(f)) or Michelson interferometer (MI) [38] (Figure 10(g)). Modal interferometry can also be realized with LPGs on a single MNF [39], and polarimetric interferometry is possible with rectangular MNFs that have highly birefringent fiber axes [40]. The MNF tip shown in Figure 10(h) is widely established as a sensor head for probing and manipulating atoms and molecules [41]. The sub-wavelength cross-section of the tip facilitates minimally invasive analysis of extremely small areas. Lastly, MNF in an uncoupled helical coil illustrated in Figure 10(i) can be employed for detecting rotations in the state of polarization (SOP) induced by variations in the local magnetic field [42].

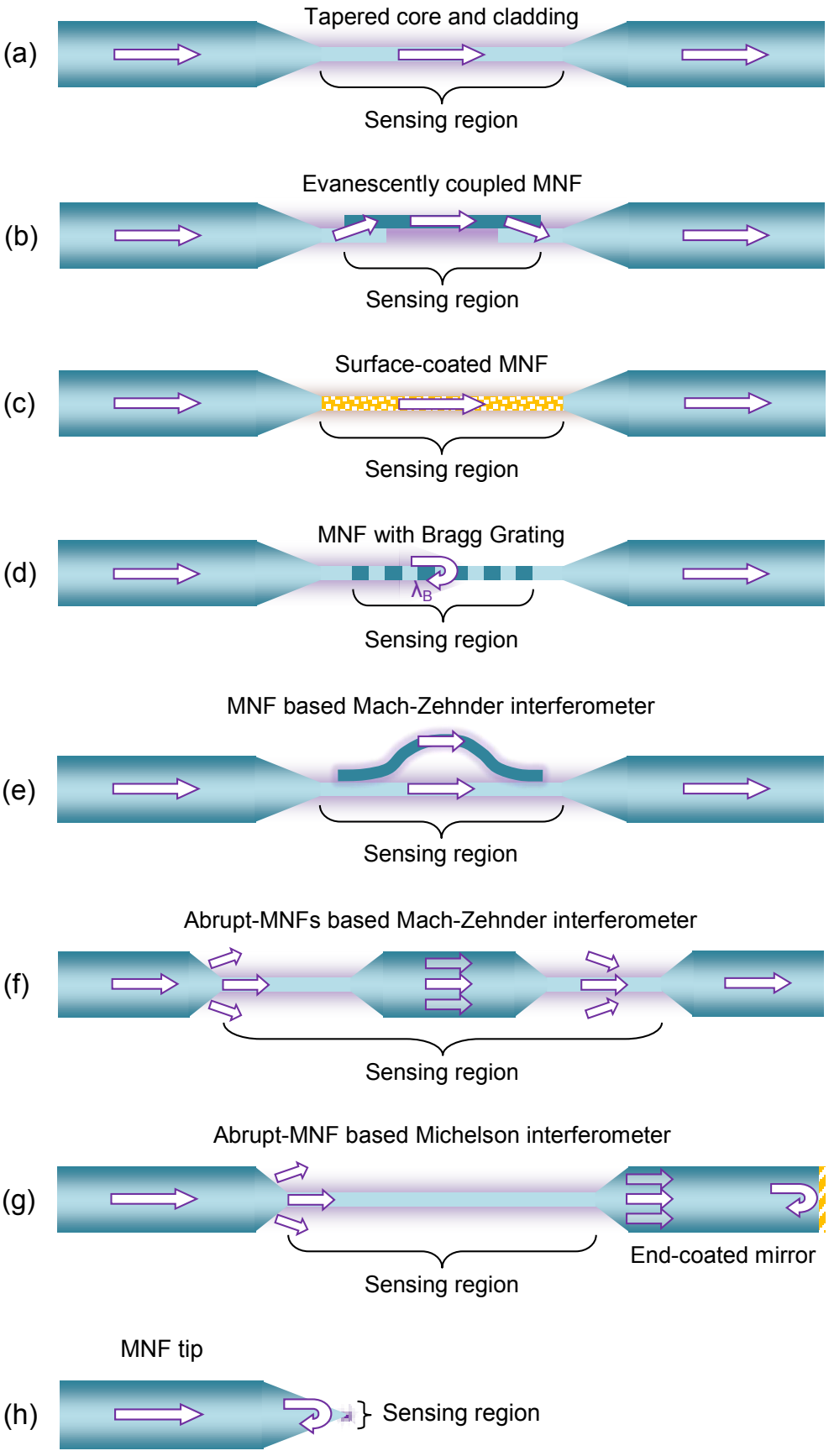
(a)
Tapered core and cladding
Sensing region
(b)
Evanescently coupled MNF
Sensing region
(c)
Surface-coated MNF
Sensing region
(d)
MNF with Bragg Grating
λ_B
Sensing region
(e)
MNF based Mach-Zehnder interferometer
Sensing region
(f)
Abrupt-MNFs based Mach-Zehnder interferometer
Sensing region
(g)
Abrupt-MNF based Michelson interferometer
Sensing region
End-coated mirror
(h)
MNF tip
Sensing region

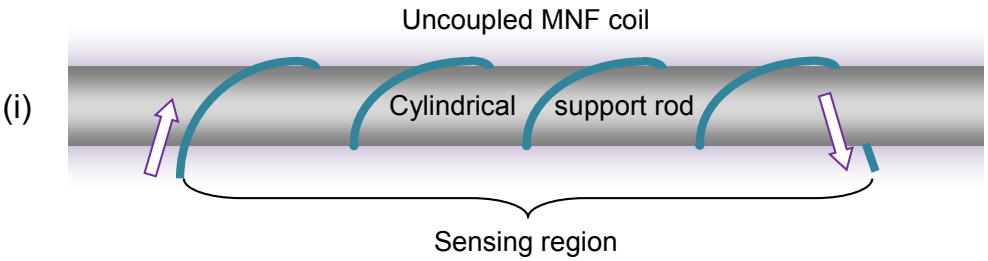

Figure 10. Schematic diagrams of common non-resonator-type micro/nanofiber arrangements.

Resonator-type MNF-based sensors comprise all sensors which exploit resonant structures. MNFs (mostly OMs) have been used to manufacture homogeneous resonant sensors in the arrangements of loop, knot and coil. Coiling an OM onto itself allows the guided modes in adjacent turns to evanescently overlap and couple, thereby creating compact resonators with predicted Q-factors as high as ~10^9. These resonators have many advantages including small size and low fabrication cost that have attracted much interest to develop them as optical sensors. A variety of configurations has been reported in the literature, and they are described in the following paragraph.

The MLR shown in Figure 11(a) is the simplest form of the homogeneous (all-OM) micro-resonator. Fabrication begins with manufacturing the OM and bending it into a self-coupling loop [43]. Translation and/or rotation stages can be used to adjust the loop to the desired size. The resulting MLRs show strong self-coupling due to the close proximity of the waveguide with itself at the coupling region, with Q-factors of the order of 10^5. The geometrical shape of the MLR is maintained by electrostatic and van der Waals interactions at the point of coupling, meaning it suffers from a limited stability strongly dependent on the environmental conditions [44, 45]. Embedding the MLR in polymer has been the preferred solution to provide long term-stability, though it can considerably modify the transmission spectrum [46]. Fusing the loop contact points with a CO_2 laser [47, 48] has been proposed. Although this technique has generally negative effects relating to the Q-factor, resonators with $Q > 10^5$ have nonetheless been demonstrated [48]. The Q-factor is defined as 2π times the ratio of the stored energy to the energy dissipated per oscillation cycle. Or equivalently, the ratio of the resonant wavelength to the full-width at half-maximum (FWHM) linewidth of the resonance shape. Similarly, CO_2

lasers have also been deployed to splice together different silica [49] and soft glass [50] OMs. An alternative approach to increase the MLR long-term stability relies on the use of a copper support rod to preserve its geometry [51]. Critical coupling (i.e. coupling coefficient optimized based on propagation loss to attain maximum interference visibility) has been demonstrated by tuning the resonator with thermal effects induced by current flowing in the conducting rod, achieving a Q-factor up to 4000 and an extinction ratio (ER) of 30 dB [52].

The optical microfiber knot resonator (MKR) shown in Figure 11(b) can be fabricated by forming a simple knot to couple adjacent OM sections. This design requires less alignment precision than the MLR and benefits from improved stability. Q-factors of up to 57000 and finesses of 22 have been achieved [53]. The Q-factor and spectral properties can be tuned by changing the knot radius and tightness [54].

The MCR shown in Figure 11(c) is a 3-dimensional resonator consisting of self-coupled adjacent loops in a helix arrangement [16]. The theoretical Q-factor is of the order of 10^9, competing with those achieved using whispering-gallery mode (WGM) resonators [55–57]. MCRs were first experimentally demonstrated in 2007 [58], and subsequently implemented in various applications [59-65]. The highest Q-factor experimentally achieved in an MCR (Q = 470,000 [66]) is still a few orders of magnitude smaller that the theoretical maximum. Fabrication involves coiling an OM around a support rod of mm/cm scale diameter using a translation stage that controls the pitch between the turns of the MCR and a rotation stage to adjust the rotation angle of the winding. Post-fabrication, the resonator can be packaged in polymer to improve its life-time by preventing the ingress of dust and moisture. The multi-turn MCR transmission can be analyzed during fabrication to identify the eigenmodes present [67].

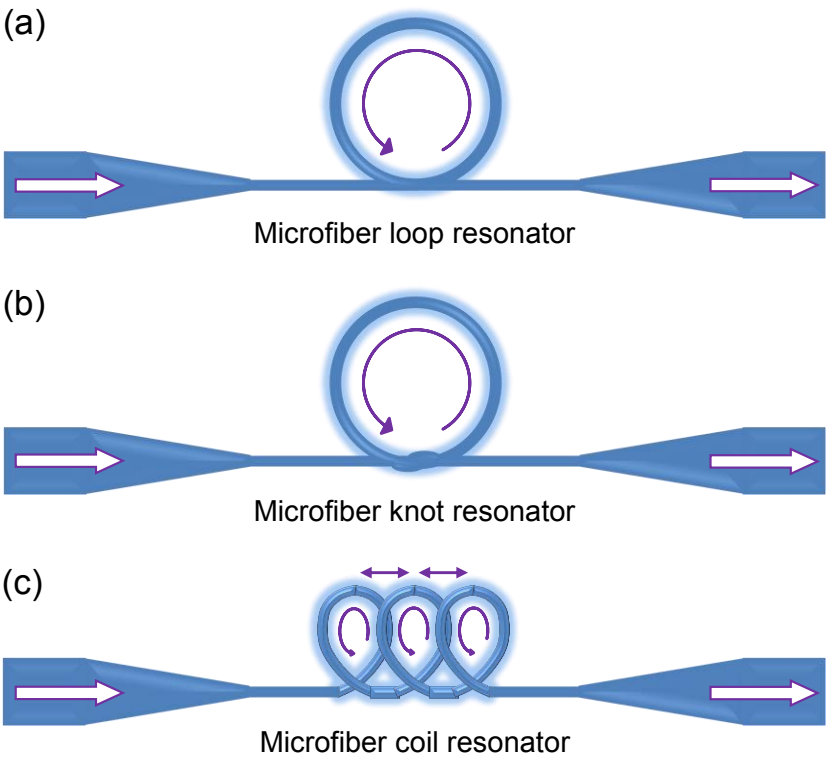

Figure 11. Schematic diagrams of the optical microfiber (a) loop resonator, (b) knot resonator, and (c) coil resonator. The evanescent field couples power between different sections of the same fiber. The directions of light propagation and coupling are shown as arrows.

A large number of resonant sensors utilize a single OM to excite or collect light from high-Q resonators such as micro-rings [68, 69], micro-spheres [70, 71], micro-toroids [72, 73], micro-capillaries [74, 75] or bottle resonators [76, 77], which are classified as heterogeneous. By matching the propagation constants of the mode in the OM and the micro-resonator, coupling efficiencies in excess of 90% have been demonstrated [78]. Evanescent sensing in these types of high-Q resonators has been used to monitor chemical and biological elements positioned in proximity of the resonator surface.

2.5.1 Refractive index sensors

RI sensing is a prominent subject of optical sensing that has a broad range of uses, including the inspection of concentration levels in aqueous solutions and quality control in the monitoring of food engineering processes [79]. The compact form of MNF-based sensors makes sensing RI in micro-fluidic channels and humidity environments highly feasible and robust.

2.5.1.1 Micro-fluidic-based sensors

The first experiments with straight MNFs to confirm its applicability for RI sensing began as early as 1986, when Lacroix *et al* [32] studied the transmitted core-mode power as a function of external RI with varying taper lengths. In 2005, Polynkin *et al* [80] reported a simple MNF-based RI sensor consisting of a sub-micron diameter optical fiber taper immersed in a transparent curable soft polymer. Liquid analyte surrounded the 3 cm length MNF waist, making the absorption loss sensitive to the RI difference between the polymer and the liquid. The sensitivity was estimated to be 5×10^{-4} RIU. Recently, a highly sensitive RI sensor based on a tapered multimode fiber, rather than the conventional single-mode fiber, was demonstrated by Wang *et al* [81]. The MNF diameter and length were 30 μm and 675 μm respectively. The device was able to achieve a responsivity of at least 1900 nm/RIU and sensitivity of 5.23×10^{-6} RIU within the RI range of n = 1.33–1.44.

Miniaturized refractometric sensors based on tapered photonic crystal fiber (PCF) have shown higher responsivity than regular PCFs. Qiu *et al* [82] investigated, both theoretically and experimentally, the RI sensing properties of PCFs with different diameters, achieved using acid-etching instead of tapering. The maximum responsivity obtained was 750 nm/RIU, 5 times higher than that of the un-etched version. An enhancement factor of up to 100 times can be expected by optimizing the etching process to achieve thinner and more uniform PCF-MNFs.

One of the first metal-clad MNFs for RI sensing based on the concept of exciting surface plasmon modes was introduced by Díez *et al* [33]. A thin layer of gold was evaporated on a MNF of 30 μm diameter and 40 mm length, with the different surface plasmon modes excited by the fiber modes. A sharp loss occurs when the propagation constant of the guided mode matches with that of a surface plasmon mode. Hence, surface plasmon waves are strongly dependent on the RI surrounding the surface. Monzón-Hernández *et al* [83] have studied different hybrid surface plasmon modes that are excited and supported by a semi-cylindrical metallic shell (25 nm thick gold layer) around the MNF (27.5 μm diameter, 4 mm length). The transmission spectrum of the device exhibits multiple resonance peaks, three of which are simultaneously monitored. The measured responsivity was remarkably

high at 127500 nm/RIU for RI between n = 1.44–1.454. A sensitivity of 7×10^{-7} RIU can be obtained, assuming a wavelength resolution of 10 pm.

The combination of FBGs and MNFs was first reported by Liang *et al* [34]. A single etched MNF (6 μm diameter) with FBG and another MNF (3 μm) with a pair of FBGs forming a Fabry–Perot interferometer (FPI) was compared. In both cases, the resonant wavelength shift is proportional to the external RI. Due to the narrower resonance spectral shape of the latter configuration, a sensitivity of 1.4×10^{-5} RIU was attained. Xu *et al* [84] proposed a method of manufacturing gratings by wrapping a MNF around a micro-structured rod, as shown in Figure 12. By exploiting the large evanescent field of MNFs, the holes in the rod can be exploited as micro-fluidic channels for RI sensing. This method avoids post-processing thin MNFs and enables design flexibility. By designing the air hole size and position in the micro-structured rod, RI chirping can also be realized. The expected responsivity of the device was 103 nm/RIU, but is yet to be experimentally realized.

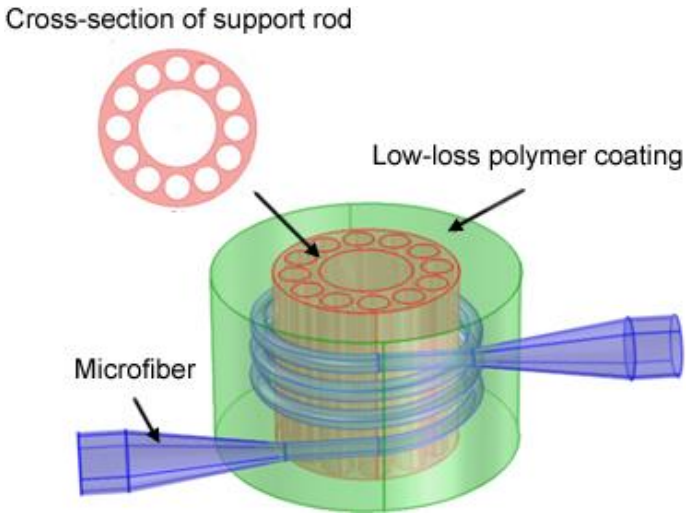

Figure 12. Schematic diagram of the optical microfiber grating based on a micro-structured rod. Inset: cross-section of the support rod.

Wang *et al* [85] modeled a MNF where the external RI affects only the central segment of the grating. Due to the stop-band degeneracy and rapid emergence of spectral modes when an effective phase shift occurs, a highly responsive sensor can be realized. A sensitivity of 2.5×10^{-6} RIU was estimated for this design, which is an order of magnitude better than non-phase-shifted FBGs. The performance of FBG based MNFs as RI sensors was studied by Liang *et al* [86]. Attributes such as the

MNF radius, grating period and temperature cross-sensitivity were investigated theoretically. It was predicted that a 400 nm radius MNF FBG sensor has a maximum responsivity of 1200 nm/RIU in the RI range of n = 1.3–1.39. Moreover, a sensitivity of 8.3×10^{-6} RIU can be achieved using their design. The fabrication and characterization of a LPG-based MNF RI sensor has been reported by Allsop *et al* [35]. The sensor response comes in the form of a spectral feature that splits and separates with increasing external RI. A series of gratings were inscribed on a 25 μm diameter MNF using a frequency-doubled argon ion laser with a point-by-point writing technique. The grating periods varied from 250–500 μm and the length of all grating samples was 5 cm. The resulting devices yielded a sensitivity of 8.5×10^{-5} RIU in the RI range of n = 1.33–1.335.

It is possible to employ a pair of LPGs with a tapered section in between to form an in-line MZI. Ding *et al* [39] presented such a design that operates by partially coupling light to and from a cladding-mode providing interference with the core-guided mode. A KrF excimer laser with a point-by-point grating writing technique was used to fabricate gratings with a period of 414 μm, in order to excite a cladding-mode of the ninth order for high responsivity. A sensitivity of 5.8×10^{-6} RIU can be achieved assuming the measurement system has a spectral resolution of 1 pm.

A compact MNF-based modal interferometer was proposed and demonstrated by Salceda-Delgado *et al* [87]. An abrupt taper of 10 μm diameter and 30 mm uniform waist length was created with such geometry that allowed the fundamental mode to excite a higher-order mode during the down-taper. The modes recombine interferometrically when they enter the up-taper transition. The minimum sensitivity was 3.7×10^{-6} in the RI range of n =1.33–1.428. As with all interferometers, the length of the sensing region influences the responsivity.

An in-line MNF-based MI was first reported by Tian *et al* [38], using a 500 nm thick gold coated end facet to reflect the core-mode and the abrupt-taper-induced cladding-mode that beats together at the tapered section. The MNF has a diameter of 40 μm and uniform waist length of 734 μm. A change in the external RI produces a phase difference between the two paths of the modal interferometer that results in a wavelength shift of the interference fringes. The minimum detectable RI variation was 5.1×10^{-4}. Tian *et al* [37] also created an in-line MZI by concatenating two

MNFs together. This design utilizes one abrupt taper to couple light from the core into the cladding, and a closely followed second abrupt taper to couple the cladding-mode back to the core. The pairs of MNFs were of 40 μm diameter and 707 μm length. The responsivity to RI changes was measured to be 17.1 nm/RIU.

An ultra-sensitive RI sensor was demonstrated by Li *et al* [40], which utilizes the polarimetric interference of a rectangular, 3.29 μm diameter and 32.15 mm length MNF. The broadband light splits into two orthogonal axes at the highly birefringent MNF and recombines at a coupler. The measured responsivity was 18987 nm/RIU around n = 1.33. The high responsivity was due not only to the RI-induced birefringence variation but also to its dispersive properties. The device can detect a RI variation as small as 5.27×10^{-7} for a wavelength resolution of 10 pm. High linear birefringence that can be created post-fabrication inside a MNF by milling a slot to break the circular geometry was proposed and modeled by Kou *et al* [88]. By inserting the fiberized slot waveguide inside a fiber-loop mirror configuration, a responsivity as high as 5×10^{4} nm/RIU was predicted.

Tapered optical fiber tips are simple yet effective at sensing RI variations within small detection volumes. Tai *et al* [89] presented a metal-free sub-wavelength tip that responds to RI changes in the external medium via an optical power modulation. The numerical aperture of the sensor head was 0.12, obtaining a power change of 8000%/RIU in the RI range of n = 1.3–1.4. Kou *et al* [90] also developed a metal-dielectric-hybrid MNF probe with milled-gratings replacing the micro-cavity. The 2 mm length tip was coated with a 30 nm thick layer of gold by magnetron sputtering. The gold surface provides relatively low absorption in the infrared and exhibits inertness to oxidation when exposed in air. The resulting responsivity was 125 nm/RIU for RI in the range of n = 1.3739–1.3577.

A tunable RI sensor in the form of a 2×2 poly(trimethylene terephthalate) MNF coupling splitter was implemented by Zhu *et al* [91]. The compact structure was assembled by twisting two flexible 440-nm-diameter MNFs. The sensor consisted of two input branches, a twisted coupling region and two output branches. The highest measured responsivity was 26.96 mW/RIU for n = 1.3321–1.3565, and a minimum sensitivity of 1.85×10^{-7} RIU. A hybrid device integrating a MKR in a Sagnac loop reflector was proposed for RI and temperature sensing by Lim *et al* [92]. The

fabricated MNF diameters varied from 3 μm to 8 μm, and the sensing regions ranged from 0.5 mm to 2 mm in diameter. The RI responsivity was 30.49 nm/RIU in the RI range of n = 1.334–1.348, and the temperature responsivity was 20.6 pm/°C from 30 °C to 130 °C.

Resonant sensors have also been used to monitor RI. The working principle of resonant refractometric sensors is quite simple. The embedded OM resonator has a considerable fraction of its mode propagating in the fluidic channel, thus any change in the analyte RI results in a shift in the resonant wavelength with an approximately linear dependence. Shi *et al* [93] created a theoretical model for the MLR and optimized its structural parameters including the OM radius, the loop radius and the length of coupling region for higher responsivity, wider DR, and lower sensitivity. Simulations indicated sensitivities as low as 10^{-5} RIU. However, as MLRs rely on electrostatic surface charges to preserve their geometry, long-term stability is likely to be an issue as practical devices. Embedded MLRs, such as the one shown in Figure 13, were demonstrated by Xu *et al* [94]. Sensitivities of the order of 10^3 nm/RIU have been predicted for a MNF radius of 300 nm.

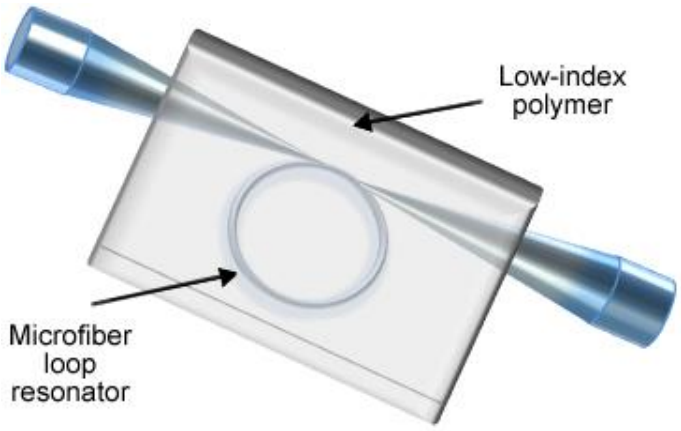

Figure 13. Schematic diagram of the embedded microfiber loop resonator. The packaging thickness is controlled such that the evanescent field can overlap into the surrounding analyte.

Guo *et al* [51] reported a MLR refractometric sensor which was manufactured with the aid of a copper support rod. By tuning the coupling coefficient to compensate for the circulation loss, critical coupling and a Q-factor of 4000 was achieved for a 2.4 μm diameter OM. This MLR has a robust structure for sensing RI in liquids and the flexibility of obtaining critical coupling within a broad spectral range. Moreover, it

showed high responsivity and high stability for sensing in both low- and high-concentration solutions. By performing measurements around the wavelengths of λ = 1.55 µm and λ = 1.22 µm, sensitivities of 1.1×10^{-4} RIU and 1.8×10^{-5} RIU were obtained in a low-concentration ethanol solution and high-concentration glycerol solution respectively. Responsivities were 17.8 nm/RIU and 110 nm/RIU for high index-contrast and low index-contrast sensing respectively.

A MZI coupled micro-ring experimentally demonstrated by Wang *et al* [68] showed a high responsivity as well as a large DR. A very large quasi-free spectral range (>120 nm) was achieved with 400–500 nm diameter MNF rings. The measured responsivity was as high as 111 nm/RIU in a DR range of n = 1–1.538.

A miniature polarimetric interferometer consisting of a twisted, highly birefringent OM loop was developed by Sun *et al* [95]. The transmission spectral characteristics were governed by the birefringence and the twist degree of the OM, with OM diameters of 5.4–6 µm. The structure exhibited a high responsivity of 24373 nm/RIU in the RI range of n = 1.355–1.3586, and excellent temperature stability of better than 5 pm/°C.

MKRs fabricated from multimode OMs have also been used as refractometric sensors by Pal *et al* [96]. A MKR of <1 mm diameter was made from etched fibers. The highest responsivity of 172 nm/RIU was observed at n = 1.370. Although MCRs have a more complex structure and they require a considerably more sophisticated fabrication procedure than other OM resonators, they have nonetheless been explored for numerous sensing applications.

Refractometric sensors based on embedded MCR have been proposed [97] and demonstrated by Xu *et al* [60]. Due to the 3-dimensional geometry, MCRs have an intrinsic channel that can be exploited for micro-fluidic applications. An OM with 50 mm length and 2.5 µm diameter of the uniform waist region was fabricated and wrapped 5 times around a 1 mm diameter poly(methyl methacrylate) (PMMA) rod. The entire structure was repeatedly coated with Teflon resin to form a protective layer. The embedded MCR was then carefully treated with acetone to remove the support rod, which took 1–2 days at room temperature to be completely dissolved. Finally, a micro-fluidic channel of ~1 mm diameter was fabricated. Figure 14 shows the schematic and photograph of the MCR structure. The working principle relates to

the overlap between the analyte and the evanescent field of the mode propagating in the OM. Any change in the analyte RI is reflected as a resonant wavelength shift due to the change in effective index. The wavelength shift is particularly affected by the wavelength/OM diameter ratio and the coating thickness between the OM and the fluidic channel. For optimized designs, responsivities up to 700 nm/RIU and sensitivities of the order of 10^{-7} have been predicted [97]. Experimental demonstration was carried out by inserting the MCR in solutions of isopropanol and methanol. The resonant wavelength underwent a red shift for increasing analyte refractive indices and a responsivity of 40 nm/RIU was reported [60]. The inferior experimental achievement was reportedly due to the lack of smoothness of the internal wall surface and the large OM diameter used.

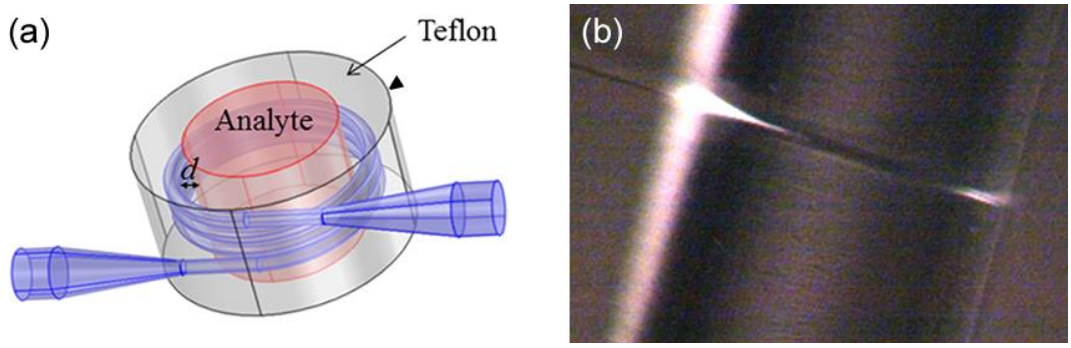

Figure 14. (a) Schematic diagram of the microfiber coil resonator sensor, and (b) a photograph of the packaged sample.

Micro-capillaries have been used as refractometric sensors and liquid-core ring-resonators with Q-factors larger than 10^5 have been demonstrated by White *et al* [74]. The liquid flowing in the micro-fluidic channel has a higher RI than that of the surrounding polymer, and the confined modes in the high RI core are excited by an external waveguide via resonant tunneling. A responsivity of 17 nm/RIU was achieved. The sensitivity to RI changes in capillaries of submicron wall-thickness was larger than other reported optical micro-cavities [98]. Responsivities of exceeding 100 nm/RIU for water and a maximum of 390 nm/RIU were achieved.

To summarize, a multitude of MNF-based sensors have been developed for micro-fluidic-based RI sensing. Table 1 lists some of the most prominent achievements. Although the different sensing mechanisms of the various works produce RI responsivity in different units, the RI sensitivity is the common parameter to

compare. From the table, the twisted MNF sensor [85] exhibits the best performance. Moreover, MNF-based sensors appear to out-perform top RI sensors employing regular-sized specialty fibers such as PCF [99].

MNF configuration	Responsivity	Sensitivity	Refractive index range	Reference
Straight MNF	1900 nm/RIU	5.23×10^{-6} RIU	1.33–1.44 RIU	Wang *et al* [81]
Coated MNF	127500 nm/RIU	7×10^{-7} RIU	1.44–1.454 RIU	Monzón-Hernández *et al* [83]
MNF Bragg grating	N/A	2.5×10^{-6} RIU	–	Wang *et al* [85]
	1200 nm/RIU	8.3×10^{-6} RIU	1.3–1.39 RIU	Liang *et al* [86]
Interferometric MNF	18987 nm/RIU	5.27×10^{-7} RIU	~1.3 RIU	Li *et al* [40]
	5×10^{4} nm/RIU	–	–	Kou *et al* [88]
MZI coupled micro-ring	111nm/RIU	–	1–1.538 RIU	Wang *et al* [68]
MNF tip	8000%/RIU	–	1.3–1.4 RIU	Tai *et al* [89]
	125 nm/RIU	–	1.3577–1.3739 RIU	Kou *et al* [90]
Twisted MNF	26.96 mW/RIU	1.85×10^{-7} RIU	1.3321–1.3565 RIU	Zhu *et al* [91]
	24373 nm/RIU	–	1.355–1.3586 RIU	Sun *et al* [95]
OM loop resonator	17.8 nm/RIU (high index-contrast), 110 nm/RIU (low index-contrast)	1.1×10^{-4} RIU (ethanol), 1.8×10^{-5} RIU (glycerol)	1.40–1.43 RIU	Guo *et al* [51]
OM knot resonator	172 nm/RIU	–	~1.370 RIU	Pal *et al* [96]
OM coil resonator	40 nm/RIU	–	1.49–1.51 RIU	Xu *et al* [60]

MNF with micro-capillaries	17 nm/RIU	–	1.33–1.5 RIU	White *et al* [74]
Standard PCF	8500 nm/RIU	2.02×10^{-6} RIU	1.33–1.44 RIU	Sun *et al* [99]

Table 1. Comparison of best-reported performances in each micro/nanofiber design category for micro-fluidic-based refractive index sensing.

2.5.1.2 Humidity-based sensors

MNF-based humidity sensors typically operate on RI changes in its external coating in response to variations in ambient humidity. The stability of the composite fiber structure varies depending on the coating material. Externally induced effects such as thermal expansion can cause shear stress to build-up along the fiber-coating interface, which will ultimately result in delamination above a certain threshold. Corres *et al* [100] have coated a MNF with humidity-sensitive nano-film using poly-diallyldimethyl ammonium chloride and the polymeric Dye R-478 as the polycation-polyanion pair that overlap each other at the molecular level to produce a homogeneous optical material. The optimization of the humidity response was further studied [101] by tuning the coating type, coating thickness, dimensions of the taper and the light source. A variation of 16 dB in optical transmittance was achieved with a responses time of 300 ms for changes in relative humidity (RH) from 75–100% RH [102].

An alternative humidity-sensitive material is the agarose gel, as shown by Bariáin *et al* [103]. A mixture of agarose powder dissolved in water was heated and then deposited on a MNF of 25 μm diameter and 0.1 mm uniform waist length. A variation of up to 6.5 dB of the optical transmittance was recorded with RH changes between 30% and 80% that lead to increased leakage of light into the cladding layer. Gelatin is another material sensitive to humidity changes. Zhang *et al* [104] exploited this effect by coating a 680 nm diameter, 8 mm length MNF with an 80 nm thick layer of gelatin. The sensor displayed a 10 dBm change in optical transmittance with a DR of 9–94% RH, with T_R = 70 ms.

A humidity sensor based on tapered PCF filled with moisture-sensitive polymer was proposed by Li *et al* [105]. Theoretical results show the loss varies from 0.063 dB/cm to 75.847 dB/cm when the RH changes from 0% RH to 95% RH. The silica MKR has showed a responsivity of 12 pm/10% RH within a DR of 14–60% RH.

Wang *et al* [69] fabricated micro-rings assembled with polyacrylamide (PAM) OMs of 2–3 μm diameter for humidity sensing. These OMs absorb water molecules and inflate monotonically with increasing humidity, resulting in resonant wavelength shifts. Responsivities as high as 490 pm/% RH and response times of T_R = 120 ms were recorded within a DR of 5–71% RH. Humidity sensors based on silica/polymer MKRs were reported by Wu *et al* [106]. The silica MKR sensor (1.2 μm diameter, Q-factor of 15000) factor showed a responsivity of 12 pm/10% RH within a DR of 15–60% RH. The polymer MKR sensor (2.1 μm diameter, Q-factor of 20000) achieved a responsivity of 88 pm/10%-RH from 17–95% RH, with T_R < 0.5 s.

Table 2 summarizes the top-performing sensors from each design category for humidity sensing. Although the sensitivity information is not available for comparison, it is clear that the responsivity of the OM ring resonator [69] surpasses the other MNF-based designs with by far the largest wavelength shift. However, compared to the top-tier humidity sensors using a regular-sized coated optical fiber [107], MNFs are less responsive due to the smaller surface area exposed to the measurand. Sensing the level of humidity in an environment does not usually face space restrictions, therefore the compact size of MNFs offer no advantages.

MNF configuration	**Responsivity**	**Sensitivity**	**Relative humidity range**	**Reference**
Coated MNF	16 dB/25% RH	–	75–100% RH	Corres *et al* [102]
PCF MNF	12 pm/10% RH	–	14–60% RH	Li *et al* [105]
OM ring resonator	490 pm/1% RH	–	5–71% RH	Wang *et al* [69]
OM knot resonator	88 pm/10% RH	–	17–95% RH	Wu *et al* [106]
Standard	1.08 nm/1% RH	–	20–80% RH	Hernáez *et al*

coated fiber				[107]

Table 2. Comparison of best-reported performances in each micro/nanofiber design category for humidity sensing.

2.5.2 Chemical and bio-chemical sensors

There has been a rapid development of optical sensors for the detection of chemicals and biological materials of environmental and biomedical interest. The emergence of MNF-based devices gave rise to the ability to interrogate samples in the microscopic size regime with minimized intrusion, greater stability and shorter response times. In the following section, sensors are categorized primarily by their sensing mechanism.

2.5.2.1 Surface absorption and fluorescence-based sensors

The strong optical confinement and prominent evanescent field of guided light in MNFs give rise to ultra-sensitive surface spectroscopy of molecules in close vicinity of the MNF waist region. Using the guided mode for both excitation and fluorescence collection, Stiebeiner *et al* [108] performed spectroscopic measurements on 3,4,9,10-perylenetetracarboxylic dianhydride molecules at ambient conditions shown in Figure 15, using MNFs with waist diameter down to 100 nm and lengths of 1–10 mm. Fine-tuning of the transmission band of MNFs allow for further optimization on the surface spectroscopy of organic molecules. A systematic study of the influence of the taper profile parameters on the transmission properties of MNFs as well as the loss mechanisms was also undertaken by Stiebeiner *et al* [3].

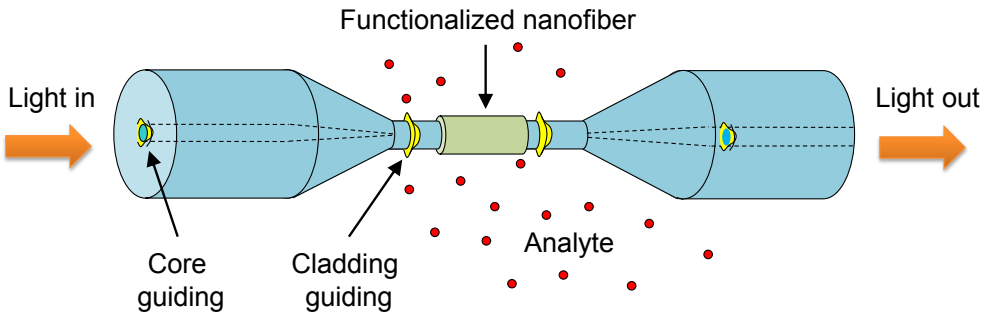

Figure 15. Schematic diagram of the coated optical nanofiber for bio-chemical sensing.

Nayak *et al* [109] demonstrated efficient coupling of atomic fluorescence to the guided mode of a MNF. It was reported that the fluorescence of a very small number of atoms could be detected around MNFs with diameters of 100–1000 nm and 40 mm length. Likewise, they also confirmed that the fluorescence excitation spectrum reflects the effect of the van der Waals interaction between atoms and the MNF surface. Moreover, Nayak *et al* [110] discovered that single atoms around the MNF reveal a very prominent spectral feature, where the excitation spectrum splits into two peaks with a separation smaller than the natural linewidth. A full understanding of this effect is yet to be achieved.

MNF tip sensors facilitate sensitive and selective means to monitor cellular microenvironments at the single cell level. Tan *et al* [41] were amongst the first to realize this vast potential. A thousand-fold probe miniaturization, a million-fold sample reduction and a hundred-fold shorter response time (T_R < 20 ms) was achieved over regular optical fibers (100–200 um diameter) by combining MNF tips with near-field photo-polymerization. The wide variety of medical uses at the cellular level was discussed by Vo-Dinh *et al* [111]. In their report, MNF tips of 30–50 nm diameters shown in Figure 16 were covalently bound with antibodies that are selective to target analyte molecules. The sensor head was excited by light launched into its fiber pigtail and the resulting evanescent field at the MNF tip was used to excite target molecules bound to the antibody molecules. The fluorescence emission from the analyte molecules was then collected and analyzed via a microscope to determine the presence of biochemical targets inside single cells.

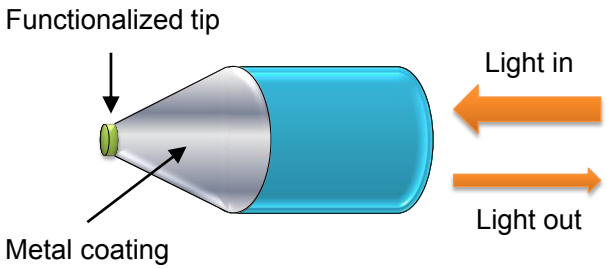

Figure 16. Schematic diagram of the functionalized optical nanofiber tip for selective bio-chemical sensing.

An in-line absorption sensor was fabricated with an embedded MCR by Lorenzi *et al* [112]. The sensor was tested by measuring the optical absorption of an aqueous solution of synthetic dye, Brilliant Blue FCF (1.3×10^5 $M^{-1}cm^{-1}$ at λ = 630 nm), with

concentration ranging from 6 μM up to 0.18 mM. The measurements were taken while the analyte flowed through the tube enclosed by the MCR. The experimental results have been interpreted as a function of analyte concentration. Low concentrations of flowing analyte show losses in agreement with a modified Beer-Lambert law and higher concentration reached a limit of the measured losses arising from absorption mechanisms.

The simulations of the sensing performance of ring resonator chemical vapor sensors based on a four-layer Mie model have been carried out by Sun *et al* [113]. Two ring resonator configurations were investigated, where a vapor sensitive polymer layer was coated on either the interior or exterior surface of a fused silica cylindrical ring resonator. Due to the interaction between the polymer and the vapor analyte, the change in RI and polymer layer thickness lead to a spectral shift in the resonant wavelength. The RI responsivity and thickness responsivity were studied as a function of the polymer coating thickness, external RI, ring resonator size, wall thickness, resonant mode order and polarization. This study provides an insight into the WGM interaction with vapor molecules and enables sensor optimization for various applications.

Optical micro-spheres have also been widely used for biological detection. A micro-sphere resonator with Q-factor of 2×10^6 shown in Figure 17 was used as a biosensor and its responsivity was measured via the adsorption of bovine serum albumin dissolved in phosphate buffered saline on the micro-sphere bathed in phosphate buffered saline solution. Vollmer *et al* [114] showed that microspheres can likewise be used to detect streptavidin binding to biotin.

Toroidal micro-resonators can provide extremely high Q, thus they have an obvious application in optical sensing. Such structures have been used for distinguishing chemically similar species. The Q-factor in heavy water (D_2O) is different from that in common water (H_2O), since H_2O has a stronger absorption than D_2O. By monitoring the Q-factor, concentrations of 0.00001% of D_2O in H_2O have been detected by Armani *et al* [72].

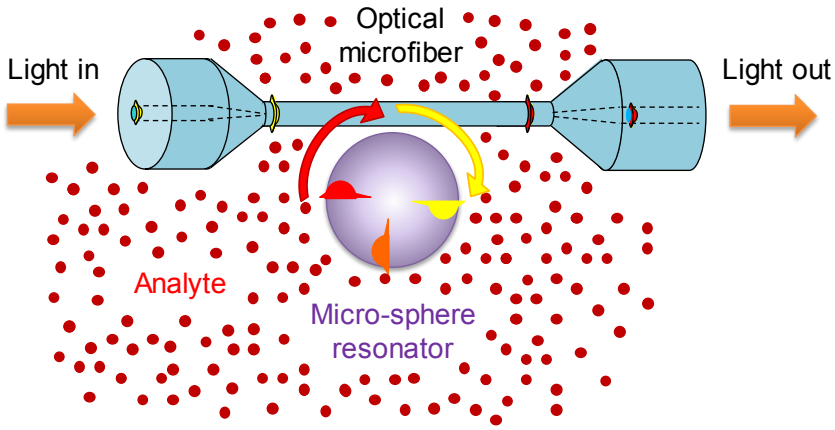

Figure 17. Schematic diagram of an optical microfiber coupled to a micro-sphere for biological detection.

2.5.2.2 Gas-based sensors

One of the first demonstrations of using MNFs for sensing gaseous elements was an oxygen sensor by Rosenzweig *et al* [115]. The working principle is based on the fluorescence quenching of tris-(1,10-phenanthroline)ruthenium(II) chloride in the presence of oxygen or dissolved oxygen. The Ru compound was implanted in an acrylamide polymer attached to a silanized 0.1–0.5 μm diameter MNF tip by photo-initiated polymerization. The minimum sample volume required for measurements was 100 fL. An absolute sensitivity of 1×10^{-17} M was achieved with response times under 1 s.

Functionalized polymer MNFs for gas detection were reported by Gu *et al* [10], which include PMMA, polystyrene, polyacrylamide, and polyaniline/polystyrene nanowires. A 250 nm diameter polyaniline/polystyrene MNF for sensing NO_2 was fabricated from a polymer-blend solution. It was found from the spectral absorption that the oxidation degree of the MNF increases with the concentration of NO_2. A sensitivity below 0.1 ppm and T_R = 7 s has been achieved. For sensing NH_3, a 270 nm diameter bromothymol-blue doped PMMA was used as the sensor head. As the NH_3 gas diffuses into the MNF, the bromothymol-blue reacts with NH_3 and changes from acidic form to basic form, resulting in evident absorption of the probing light. A sensitivity of better than 14 ppm has been demonstrated with T_R = 1.8 s.

Unlike RI sensors, no comparison can be made between the various chemical and bio-chemical sensors due to the different measurands involved.

2.5.3 Temperature sensors

Over the past few decades, temperature sensing has matured into a profound technology which has been successfully deployed in many industrial sectors, including ecological monitoring, fire detection, leakage detection, oil and gas exploration, plant and process monitoring, power cable and transmission line monitoring, storage tanks and vessels, and structural health monitoring. The compactness of MNF-based structures in conjunction with its excellent immunity to EMI has attracted considerable interest in recent years.

A simple modal interferometer was constructed by Zhu *et al* [116], by coating the waist region of a MNF (4 mm length uniform, 8 mm total) with a high thermo-optic coefficient material. The ambient temperature has a great influence on the RI of the coating film and thus the interference pattern. The optical response was studied under different MNF diameters varying from 1.6 μm to 20 μm and a temperature DR of –20 °C to 80 °C. An in-line MZI was conceived by Lu *et al* [117], using two cascaded MNFs to excite and recombine the cladding mode with the core mode. The MNFs were of 65 μm diameter and 525 μm length. The highest responsivity obtained was 77 pm/°C between 20–60 °C. Ji *et al* [118] proposed a multiplexed optical temperature sensing system using MNFs with FPGs as end reflectors. Experimental results showed a responsivity of 9.7 pm/°C between 20–70 °C.

Ding *et al* [119] demonstrated a compact MNF coupler tip capable of sensing temperature up to 1283 °C with a 2-dimensional resolution of <200 μm. The device exploited the temperature dependence of intermodal coupling in the coupler uniform waist region, exhibiting a responsivity of 11.96 pm/°C and sensitivity of 0.836 °C when the wavelength resolution is 10 pm.

An experimental investigation on tapered PCF coated with a layer of liquid crystal was presented by Rajan *et al* [120]. Several in-line interferometers were fabricated by tapering a small section of PCF by collapsing the air holes and thinning down the collapsed region to micron-scale. Temperature tuning of the spectral response of the tapered interferometers with different waist diameters coated with high- and low-RI liquid crystal materials were carried out.

In the case of MLRs, the positions of the transmission resonances are very sensitive to variations in the effective RI and circumferential length of the micro-ring, which are affected by the surrounding temperature. A temperature sensor has been reported by Sumetsky *et al* [45] in a free-standing MLR, which has a larger interfacial contact area with the ambient environment than a micro-ring resonator mounted on a substrate. By monitoring the changes in the transmitted power at a wavelength near resonance, temperature variations of 0.4 °C were measured with a fast response time of T_R = 3 ms due to the extremely low thermal mass. The temperature sensitivity of this temperature sensor could be as small as 0.1 mK.

MKRs have been reported for temperature sensing by Wu *et al* [121]. An MgF_2 crystal plate was adopted as substrate and various sized sensing knots were covered by a thin MgF_2 slab to stabilize it against environmental fluctuations. A thermally induced resonant wavelength shift resulting in a responsivity of 52 pm/°C was recorded in the range 30–700 °C with $T_R \approx 1$ ms for a silica sensor MKR. A polymer-based MKR sensor showed a responsivity of 266 pm/°C within 20-80 °C and T_R = 5 ms. Better performance is anticipated by improving the Q-factor of the MKR. More recently, the same research group presented theoretically and experimentally a high precision and multi-point temperature sensor, by cascading two MKRs and measuring the shift difference between the first and second-order resonance peaks [122].

MCRs embedded in the Teflon in Figure 18 with opposite thermo-optic coefficients were proposed and demonstrated as a temperature-insensitive device by Chen *et al* [123]. By coiling 3 turns of OM of 3 μm diameter, a responsivity of <6 pm/°C was achieved in the room temperature range. It was found that responsivity can be optimized by tuning the OM diameter. Chen *et al* [124] also showed the temperature sensing capability of Teflon-embedded MCRs with a demonstration using OM of 4–5 μm diameter and 14 μm length, coiled around a PMMA rod of 2 μm diameter. The responsivity to temperature was observed to be 80 pm/°C.

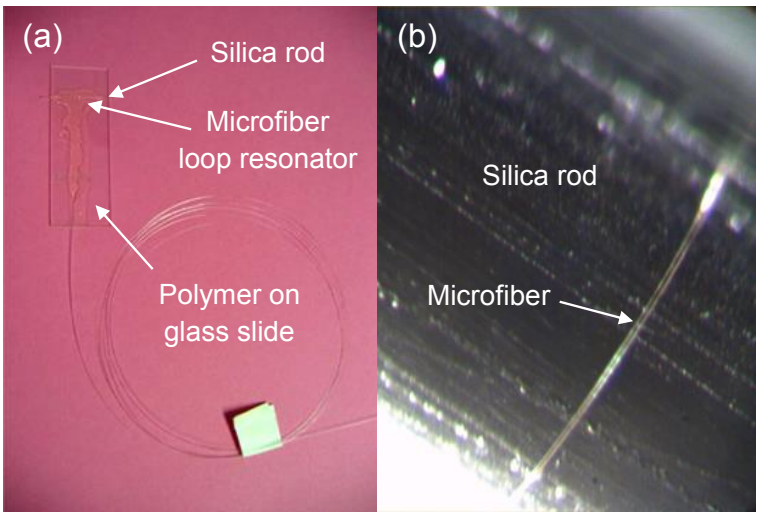

Figure 18. (a) Photograph of a packaged microfiber coil resonator, and (b) a close-up view on the optical microfiber coiled around the support rod.

Table 3 compares the top-performing sensors from each design category for temperature sensing. From the reported responsivities, the OM knot resonator [121] offers the largest response to changes in temperature with the largest dynamic range. In comparison to the best temperature sensors employing regular-sized specialty fibers such as PCF [125], MNF-based sensors are a step behind in all areas except compactness.

MNF configuration	**Responsivity**	**Sensitivity**	**Temperature range**	**Reference**
Interferometric MNF	77 pm/°C	–	20–60 °C	Lu *et al* [117]
MNF coupler tip	11.96 pm/°C	0.836 °C	–	Ding *et al* [119]
OM knot resonator	266 pm/°C	–	20–80 °C	Wu *et al* [121]
OM coil resonator	80 pm/°C	–	–	Chen *et al* [124]
Standard PCF	1.4 nm/°C	–	20–600 °C	Rao *et al* [125]

Table 3. Comparison of best-reported performances in each micro/nanofiber design category for temperature sensing.

2.5.4 Current sensors

There are well known advantages in using fiber-optic current sensors over conventional current transformers. Due to the dielectric nature of optical fibers, its sensors have the robustness to take measurements in high voltage or high magnetic induction noise fields, and have excellent immunity to saturation effects that otherwise may limit conventional current transformers. In addition, fiber-optic current sensors exhibit a linear responsivity over a wide detection bandwidth. This allows them to detect transient electrical faults, inspect noise on direct current (DC) lines for the monitoring of partial discharges during automatic control, and protect high power equipment and vital electrical components. Their compactness, lightweight and potential availability at low cost makes them an attractive choice as sensors. The shorter optical path length (OPL) of coiled MNFs can host a higher detection bandwidth compared to regular-sized fiber coils with the same number of turns (i.e. same responsivity), which are also much bulkier due to the larger minimum bend radius.

Belal *et al* introduced coiled MNFs as compact current sensors, by wrapping a MNF around a conductive wire to form an optical microfiber coil (MC). Alternating current (AC) can be detected by either a polarimetric technique via the Faraday Effect [42], or by tracking thermally induced phase shifts when incorporated into the sensing arm of a MZI [126]. For the former configuration, a current responsivity of 16.8 μrad/A for a DR of 0–19 A and a sensitivity of 0.04 A/$\sqrt{\text{Hz}}$ was achieved with 25 turns. The detection bandwidth was predicted to be in the gigahertz regime. For the latter configuration, the measured responsivity was 1.28×10^{-4} rad/A^2 at 50 Hz between 0–120 A_{rms}. In both cases, the MNF was of 5 μm diameter, 10 cm length, and the responsivity was expected to increase with the number of MNF turns.

By wrapping MLR around a copper rod, the resonant wavelength can be tuned by applying a current through the copper rod. For a MLR with Q-factor of 4000, an approximately linear dependence of wavelength shift on the current was demonstrated by Guo *et al* [52] with a slope of 26.5 pm/A between 0–1.6 A. Using similar principles, Lim *et al* [127] achieved current sensing by wrapping a MKR around a copper rod. The wavelength shift was measured to be linearly proportional

to the square of the current and a maximum tuning slope of 51.3 pm/A^2 between 0–2 A was obtained.

Table 4 compares the top-performing sensors from each design category for current sensing. It is difficult to judge the best from the different forms of reported responsivities. The OM coil and loop resonator gives a linear responsivity, whereas the interferometric MNF and OM knot resonator exhibits a response proportional to the electrical power rather than the current. The middle 3 entries are all based on thermal effects, and hence their detection bandwidths are considerably lower than the gigahertz capabilities of the OM coil. In comparison to Faraday Effect-based current sensors employing standard fiber coils made from silica [128], the limited fabrication length of MNFs resulted in inferior responsivity and thus lower sensitivity.

MNF configuration	**Responsivity**	**Sensitivity**	**Current range**	**Reference**
OM coil	16.8 µrad/A	0.04 A/$\sqrt{\text{Hz}}$	0–19 A	Belal *et al* [42]
Interferometric MNF	1.28×10^{-4} rad/I^2 at 50 Hz	–	0–120 A_{rms}	Belal *et al* [126]
OM loop resonator	26.5 pm/A	–	0–1.6 A	Guo *et al* [52]
OM knot resonator	51.3 pm/A^2	–	0–2 A	Lim *et al* [127]
Standard spun fiber coil	–	0.1 mA_{rms} /$\sqrt{\text{Hz}}$	0–450 A_{rms}	Payne *et al* [128]

Table 4. Comparison of best-reported performances in each micro/nanofiber design category for current sensing.

2.5.5 Displacement/strain sensors

This category of sensors can be found in a wide variety of industrial applications including semiconductor processing, assembly of disk drives, precision thickness measurements, machine tool metrology and assembly line testing. The aforementioned characteristics of MNF-based structures enable such optical sensors to operate in confined spaces.

The bending effects in MNFs were experimentally investigated by Arregui *et al* [129] to yield a set of design rules for implementing displacement sensors. In their work, the MNF diameters ranged from 22 μm to 66 μm. It was found that narrower waist diameters lead to a higher spatial resolution, while wider waist diameters enabled a broader measurement range. A locally bent MNF bimodal interferometer was presented by Luo *et al* [130] as a displacement sensor, based on spectral shifts resulting from the beating between the fundamental mode and the first excited higher-order mode. The MNF diameter was carefully chosen at 1.92 μm such that the thermo-optic coefficients of the two modes are equal, leading to temperature-insensitive measurements. The responsivity to micro-displacements was 102 pm/μm with a DR of 0–20 g. Ji *et al* [118] demonstrated the feasibility of a multiplexed optical displacement sensing system using cascaded MNF-Bragg-gratings. The fiber taper of each sensing branch acted as sensor head to provide a displacement-induced curvature-dependent bend loss. The FBG provided the end-reflection that identified the particular sensor head with a unique Bragg wavelength. The resulting optical signals were then distinguished by their wavelength and the displacement in each case was proportional to the individual peak power. Experimental results showed a responsivity of 0.11 dB/μm for displacements within a DR of 0–400 μm.

As previously mentioned, the MLR transmission spectrum is strongly dependent on the loop size. As a result, they have been exploited as displacement sensors by Martinez-Rios *et al* [131]. Figure 19 shows one of the loop pigtails attached to a moving surface. The principle of operation is based on the interaction between the fundamental cladding mode propagating through the OM waist and the excited higher-order cladding modes when the OM is deformed to form a loop. The notch wavelength resonances shift as a function of the loop diameter. A responsivity of 0.116 nm/μm has been achieved in a displacement DR of 0–3.125 mm and the maximum wavelength shift was 360.93 nm. Alternatively, a responsivity of 2.7 nW/μm was recorded when the measurements were carried out around a center wavelength of λ = 1280 nm with a low-power light-emitting diode of 100 nm bandwidth and a Ge-based photodetector (PD).

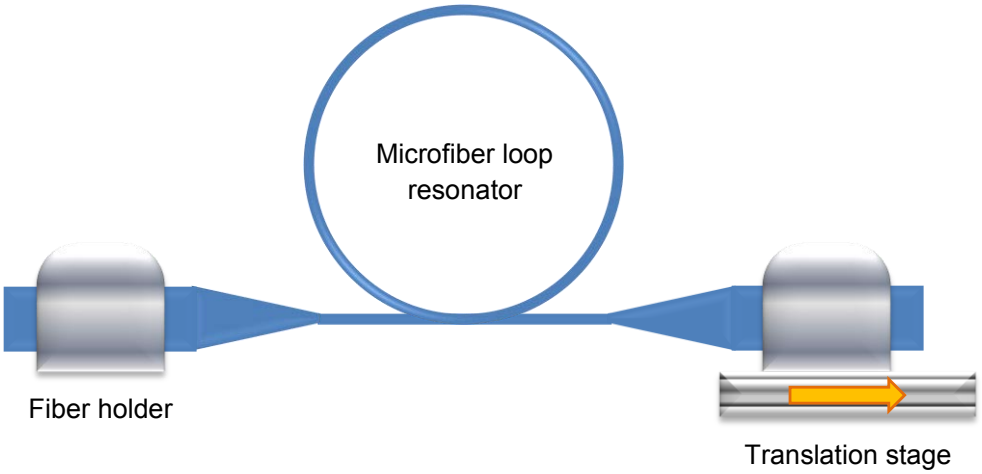

Figure 19. Schematic diagram of the microfiber loop resonator being modulated in diameter by displacements.

A micro-ball lens structure fabricated at the cleaved tip of a MNF coupler was demonstrated for displacement measurements by Jasim *et al* [132]. The diameter of the MNF and micro-ball measures 40 µm and 102 µm respectively. The device operates on the interference between the reflected beams from the micro-ball lens and the reflector, with an increased Q-factor for larger displacements.

Table 5 compares the top-performing sensors from each design category for displacement sensing. From the reported responsivities, the OM loop resonator [131] and the MNF Bragg grating [118] are the most responsive in terms of wavelength shift and optical power modulation. However, it is difficult to compare the performance against a top-performing non-MNF displacement sensor comprising of an extrinsic FP [133], due to the lack of a common parameter. Nevertheless, it is expected that the low stiffness of MNFs do not offer any advantages for measuring displacements, due to the irrelevance of force/strain.

MNF configuration	**Responsivity**	**Sensitivity**	**Displacement range**	**Reference**
Interferometric MNF	102 pm/µm	–	0–20 g	Luo *et al* [130]
MNF Bragg grating	0.11 dB/µm	–	0–400 µm	Ji *et al* [118]
OM loop resonator	0.116 nm/µm	–	0–3.125 mm	Martinez-Rios *et al* [131]

Standard FP	–	2.2 nm	2–5000 nm	Seat *et al* [133]

Table 5. Comparison of best-reported performances in each micro/nanofiber design category for displacement sensing.

2.5.6 Bend/curvature sensors

Bend or curvature sensors have various uses in the areas of mechanical engineering, robotic arms, structural health monitoring and turbulence sensing. With excellent immunity to EMI and compact size, the advantages of MNF-based devices are clear.

A compact curvature sensor based on concatenating two MNFs of 60 μm diameter has been demonstrated by Monzon-Hernandez *et al* [134]. When the device is bent, the symmetry of the straight taper is lost and light from the first taper excites cladding modes. In the second taper, a fraction of light guided by the cladding modes couples back to the fundamental mode, producing an interference pattern in the transmission spectrum. A vector bend sensor was proposed by Zhang *et al* [135], consisting of a lateral-offset splicing joint and an up-taper formed through an excessive fusion splicing method. The diameter and length of the expanded section are 168 μm and 280 μm respectively, with a lateral-offset of 6.5 μm. At the first lateral-offset fusion-splicing joint, the input light is split into fundamental core and cladding modes. The cladding modes couples back into the core when propagating through the up-taper, forming a MZI due to the phase difference between the core and cladding modes. For concave bending, the RI experienced by the mode propagating in the optical fiber increases in the region close to the inner side of fiber axis, while the RI decreases in the region close to outer side. For convex bending, the cladding modes will experience a longer propagation path than the core mode. For a curvature DR from –3 m^{-1} to 3 m^{-1}, the bend responsivities at 1463.86 nm and 1548.41 nm are 11.987 nm/m and 8.697 nm/m respectively.

2.5.7 Roughness sensors

The detection and minimization of surface and bulk non-uniformities of MNFs are of prime importance for reducing their optical loss during fabrication. These sensing techniques can be extended for quality control of standard and special types of optical fibers.

Birks *et al* [136] devised and tested a simple way of measuring the diameter uniformity of optical fibers. The proposed method shown in Figure 20 uses a MNF as the probe, which translates across small distances along the fiber under test (FUT) and periodically touches it for discrete measurements. At these points, the MNF transmission spectrum exhibits WGM resonances that shift in wavelength depending on the OPL or the effective radius of the local region of fiber. A 1.6 μm diameter sensor taper was tested on target fibers that have been tapered to a notional uniform diameter of 19.7 μm over a length of ~10 mm. Diameter variations of less than one part in 10^4 (i.e. 2 nm) were reported to be measurable. Scanning MNF surface and bulk distortions with sub-nanometer accuracy was developed by Sumetsky *et al* [137]. Their method employs a partially stripped SMF as a probe that slides perpendicularly along a MNF transmitting the fundamental mode. Since the OPL of the WGM is constant, variations in the transmittance at a single wavelength is analyzed instead. This depends on the amount of light absorbed by the probe, which is controlled by the coupling coefficient that is related to the distance from the probe and thus the local diameter of the MNF. Hence, by measuring variations in the transmittance of the probe output, the uniformity of the MNF can be determined. Sumetsky *et al* [138] also improved upon the first demonstration by Birks *et al*, to reach a sensitivity of angstrom-scale.

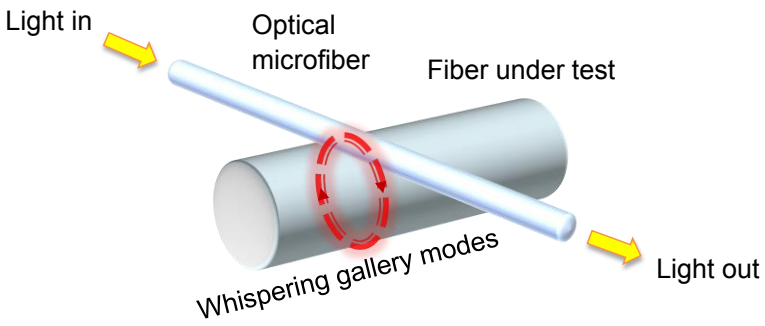

Figure 20. Schematic diagram of the optical microfiber interacting with a cylindrical surface to detect non-uniformities.

2.5.8 Acceleration sensors

Accelerometers are well established in the commercial landscape. They are employed in earthquake monitoring, guidance systems, inertial navigation, platform stabilization, vibration monitoring in portable electronics, machinery, vehicles and vessels. Such optical sensors are highly desirable since they are unaffected by EMI

from static electricity, strong magnetic fields and surface potentials. MNF-based devices can operate in very confined spaces and this gives them an advantage in many applications.

A MNF-based vibration sensor based on an optical trapping mechanism was proposed by Wang *et al* [139]. A polystyrene micro-sphere with a diameter of 10 µm was used as the mass block, enclosed in a sensing cavity filled with RI-matching liquid. Two MNFs were inserted such that vibration-induced location variations of the micro-sphere will change the amount of light collected by the MNF tips. A detection bandwidth of 15–1000 Hz was demonstrated in the preliminary results.

High Q-factor MLRs and MKRs have also been demonstrated as accelerometers by Hou *et al* and Wu *et al* [140, 141] with a DR of 0–20 g. The resonators were individually fixed on to the surface of a cantilever beam and attached to a micro-machined silicon proof-mass. The MLR-based sensor (1 µm diameter, 250 µm loop diameter) provided a responsivity of 624.7 mV/g, while the MKR-based sensor (1.1 µm diameter, 386 µm knot diameter) reached a slightly higher performance of 654.7 mV/g.

Table 6 compares the top-performing sensors from each design category for acceleration sensing. Judging from the reported responsivities, the OM knot resonator [141] holds a slight advantage over the OM loop resonator [140]. However, compared to the best traditional accelerometers using standard optical fiber [142], the performance is vastly inferior.

MNF configuration	**Responsivity**	**Sensitivity**	**Acceleration range**	**Reference**
OM loop resonator	624.7 mV/g	–	0–20 g	Wu *et al* [140]
OM knot resonator	654.7 mV/g	–	0–20 g	Wu *et al* [141]
Standard fiber with compliant mandrel	10500 rad/g	1 ng/$\sqrt{\text{Hz}}$	–	Gardner *et al* [142]

Table 6. Comparison of best-reported performances in each micro/nanofiber design category for acceleration sensing.

2.5.9 Force/pressure sensors

Force sensors have gathered much attention over the years and have established its role in many fields such as biomechanics, civil engineering, fluid-flow measurements, motor sport, process monitoring and control. For standard optical fiber-based sensors, the responsivity tends to scale inversely with the fiber cross-sectional area. Therefore, it is possible to increase force responsivity by using MNFs instead. The small dimensions of MNFs can also minimize the intrusiveness when taking sensitive measurements.

A FBG inscribed along the uniform waist of a MNF has been demonstrated by Wieduwilt *et al* [143]. The force-induced axial strain produced a shift in the Bragg wavelength, inducing a responsivity of 1900 nm/N for a 3.5 μm diameter, 8 mm length MNF. Forces as small as 25 μN could be measured with this sensor. Wang *et al* [144] proposed combining MNFs with an optical frequency-domain reflectometry (OFDR) technique to create a high responsivity and high resolution force sensor. The cross-correlation wavelength shift in the uniform waist region of the MNF is related to the RI change of the fundamental mode. The force responsivity was significantly improved due to its reduced diameter. A force responsivity of 620.83 nm/N and sensitivity of 6.35 μN was demonstrated with a spatial resolution of 3.85 mm for a MNF of 6 μm diameter, which is about 500 times higher than that of its SMF equivalent.

Table 7 compares the top-performing sensors from each design category for force sensing. By directing comparing the sensitivities, the MNF with OFDR [144] has the best sensitivity despite featuring a lower responsivity. The sensitivity is more important than the responsivity because it is a derivative of the former that takes into account the limits of the detection system to determine the minimum detectable quantity of the measurand. Unlike displacement sensors, the low stiffness advantage of MNF-based force sensors can be exploited for an advantage over their standard optical fiber counterparts [145].

MNF configuration	Responsivity	Sensitivity	Force range	Reference
MNF Bragg grating	1900 nm/N	25 μN	–	Wieduwilt *et al* [143]

MNF with OFDR	620.83 nm/N	6.35 μN	–	Wang *et al* [144]
Standard D-fiber with FBG	255.9 pm/N.mm	–	0–1.9 N/mm	Dennison *et al* [145]

Table 7. Comparison of best-reported performances in each micro/nanofiber design category for force sensing.

2.5.10 Rotation sensors

Rotation sensors have numerous applications, notably in inertial navigation systems, control, stabilization, and positioning systems. Although both mechanical and optical techniques exist for rotation sensing, the latter was found to provide higher responsivities and lower drift rates. Micro-resonators are advantageous in the sense that they can enhance the responsivity without enlarging the size of the device.

Rotation sensors and gyroscopes with enhanced responsivities have been predicted for MCR-based structures by Scheuer *et al* [65]. The interplay of slow-light and conventional propagation effects leads to an improvement in responsivity. The resonsivity enhancement increases rapidly as the loss is decreased. Simulations estimated that for a lossless MCR, the responsivity to rotation could be improved by four orders of magnitude with respect to the case of non-optimized standard optical fiber gyroscopes with similar parameters. However, a later theoretical analysis by Digonnet *et al* [146] revealed that gyroscopes made from MCRs are actually less sensitive than standard resonant fiber-optic gyroscopes consisting of a single loop. The responsivity is proportional to the total group delay of light through the structure and the maximum achievable group delay is limited in the same manner by loss.

2.5.11 Acoustic sensors

The commercial use of acoustic sensing spans several decades, and it is one of the most successful applications in the field of fiber-optic sensors. Rapid advances in this area have been driven by increasing demands from industries such as defense. The acoustic signatures of tanks, aircrafts, helicopters and submarines can be tracked, improving battlefield awareness and surveillance. MNF-based devices are less intrusive and easier to deploy, making them an attractive choice.

A simple vibration sensor based on a non-adiabatic MNF was shown by Xu *et al* [147]. The environmental vibrations were detected by demodulating the transmission loss of the 22 μm diameter MNF. The sensing system displayed a wide frequency response, ranging from a few hertz to tens of kilohertz.

2.5.12 Electric field sensors

Optical electric field sensors have attracted the attention of several industrial segments due to the fact that they can act as dielectric receiver antennas. MNF-based sensor probes have an excellent performance as field receivers compared to metal-based electric field probes due to their excellent immunity to EMI. Such low-invasive and noise-rejecting qualities exhibit the ideal way of detecting of localized electric field distributions. Moreover, these sensors offer reduced power consumption and smaller size than their conventional electronic counterparts.

Veilleux *et al* [148] have demonstrated control over the transmission of a MNF using a layer of electric-field-tunable liquid crystal (Merck ZLI-1800-100). The MNF was of 15 μm diameter and 5 mm length. When the voltage applied between two electrodes changed from 0 V to 350 V, the external RI changed from n = 1.33 to 1.48. Such a device could be adapted into a compact electric field optical sensor.

2.5.13 Magnetic field sensors

Magnetic field sensors have coexisted alongside electric field sensors due to their duality transformations. Fidelity, compactness and configurability are the most important parameters for a good magnetic field sensor design. Thus, magnetic field sensing with MNF devices has inherent advantages when it comes to meeting these requirements. The broad range of possible applications includes automotive, navigation, proximity sensors, spatial and geophysical research, transducers for micro-actuators, traffic counting and vehicle detection.

A MKR was demonstrated as a magnetic field sensor by Li *et al* [149]. The device shown in Figure 21 was submersed in a magnetic fluid (Ferrotec EMG509) that can be modulated to influence the effective index and thus the resonant wavelength of the MKR. A linear responsivity of 0.3 pm/Oe up to 300 Oe and a sensitivity of 10 Oe were reported.

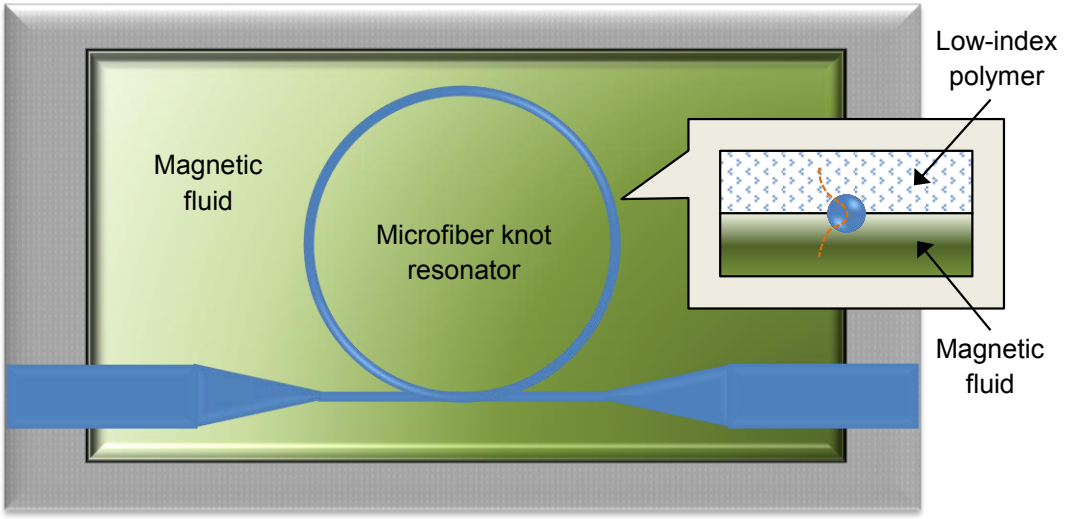

Figure 21. Schematic diagram of the microfiber knot resonator embedded in magnetic fluid.

2.5.13 Conclusions

MNF-based sensors is a rapidly growing field. MNFs exhibit many desirable characteristics such as large evanescent field, strong optical confinement, bend insensitivity, low stiffness and high configurability. The resulting sensors hold numerous advantages over their standard optical fiber counterparts, including higher responsivity, higher detection bandwidth, faster response, higher selectiveness, lower intrusiveness, smaller size and lighter weight. With sensing areas spanning RI, bio-chemical, temperature, current, displacement/strain, bend/curvature, roughness, acceleration, force/pressure, rotation, acoustic, electric field and magnetic field, the future of MNF technology looks exceptionally promising. There is no doubt that new applications will continue to arise from the development of MNF-based sensors.

Several areas encompassed by the existing range of MNF sensors remain relatively unexplored and the sensors in development are potentially competitive with their traditional counterparts, particularly for current, acceleration and acoustic. It will be the primary interest of this thesis to develop the current sensor and the preceding chapters will explore different means to detect current, using sensing mechanisms such as thermal effects and the Faraday Effect.

2.6 References

1. L. Tong, R. R. Gattass, J. B. Ashcom, S. He, J. Lou, M. Shen, I. Maxwell, and E. Mazur, "Subwavelength-diameter silica wires for low-loss optical wave guiding", Nature, vol. 426, pp. 816–819, 2003.

2. G. Brambilla, "Optical fibre nanowires and microwires: a review", J. Opt., vol. 12, no. 4, pp. 043001, 2010.

3. A. Stiebeiner, R. Garcia-Fernandez, and A. Rauschenbeutel, "Design and optimization of broadband tapered optical fibers with a nanofiber waist", Opt. Express, vol. 18, no. 22, pp. 22677–22685, 2010.

4. T. A. Birks and Y. W. Li, "The shape of fiber tapers", J. Lightwave Technol., vol. 10, no. 4, pp. 432–438, 1992.

5. L. Tong, L. Hu, J. Zhang, J. Qiu, Q. Yang, J. Lou, Y. Shen, J. He, and Z. Ye, "Photonic nanowires directly drawn from bulk glasses" Opt. Express, vol. 14, no. 1, pp. 82–87, 2006.

6. G. Brambilla, F. Koizumi, X. Feng, and D. J. Richardson, "Compound-glass optical nanowires", Electron. Lett., vol. 41, no. 7, pp. 400–402, 2005.

7. E. C. Mägi, L. B. Fu, H. C. Nguyen, M. R. E. Lamont, D. I. Yeom, and B. J. Eggleton, "Enhanced Kerr nonlinearity in sub-wavelength diameter As_2Se_3 chalcogenide fiber tapers", Opt. Express, vol. 15, no. 16, pp. 10324–10329, 2007.

8. S. A. Harfenist, S. D. Cambron, E. W. Nelson, S. M. Berry, A. W. Isham, M. M. Crain, K. M. Walsh, R. S. Keynton, and R. W. Cohn, "Direct drawing of suspended filamentary micro- and nanostructures from liquid polymers", Nano Lett., vol. 4, no. 10, pp. 1931–1937, 2004.

9. A. S. Nain, J. C. Wong, C. Amon, and M. Sitti, "Drawing suspended polymer micro-/nanofibers using glass micropipettes", Appl. Phys. Lett., vol. 89, no. 18, pp. 183105–7, 2006.

10. F. Gu, L. Zhang, X. Yin, and L. Tong, "Polymer single-nanowire optical sensors", Nano Lett., vol. 8, no. 9, pp. 2757–2761, 2008.

11. X. Xing, Y. Wang, and B. Li, "Nanofiber drawing and nanodevice assembly in poly(trimethylene terephthalate)", Opt. Express, vol. 16, no. 14, pp. 10815–10822, 2008.

12. J. D. Love and W. M. Henry, "Quantifying loss minimisation in single-mode fibre tapers", Electron. Lett., vol. 22, no. 17, pp. 913–914, 1986.

13. J. D. Love, W. M. Henry, W. J. Stewart, R. J. Black, S. Lacroix, and F. Gonthier, "Tapered single-mode fibers and devices: 1. adiabaticity criteria", IEE Proceedings J. Optoelectronics, vol. 138, no. 5, pp. 343–354, 1991.

14. G. Brambilla, F. Xu, and X. Feng, "Fabrication of optical fibre nanowires and their optical and mechanical characterization", Electron. Lett., vol. 42, no. 9, pp. 517–519, 2006.

15. G. Brambilla, V. Finazzi, and D. Richardson, "Ultra-low-loss optical fiber nanotapers", Opt. Express, vol. 12, no. 10, pp. 2258–63, 2004.

16. M. Sumetsky, “Optical fiber microcoil resonator”, Opt. Express, vol. 12, no. 10, pp. 2303–2316, 2004.

17. L. Tong, J. Lou, Z. Ye, G. T. Svacha, and E. Mazur, “Self-modulated taper drawing of silica nanowires”, Nanotech., vol. 16, no. 9, pp. 1445–1448, 2005.

18. E. Zhang, “Hydrofluoric acid flow etching of low-loss subwavelength-diameter biconical fiber tapers”, Opt. Express, vol. 18, no. 21, pp. 22593–22598, 2010.

19. M. Naqshbandi, J. Canning, M. Nash, and M. J. Crossley, “Controlling the fabrication of self-assembled microwires from silica nanoparticles”, OFS-22, pp. 842182-1–4, 2012.

20. Z. Huang, Y. Zhang, M. Kotaki, and S. Ramakrishna, “A review on polymer nanofibers by electrospinning and their applications in nanocomposites”, Compos. Sci. Technol., vol. 63, no. 15, pp. 2223–2253, 2003.

21. M. Praeger, E. Saleh, A. Vaughan, W. J. Stewart, and W. H. Loh, “Fabrication of nanoscale glass fibers by electrospinning”, Appl. Phys. Lett., vol. 100, no. 6, pp. 063114-1–3, 2012.

22. L. Tong, J. Lou, and E. Mazur, “Single-mode guiding properties of subwavelength-diameter silica and silicon wire waveguides”, Opt. Express, vol. 12, no. 6, pp. 1025–1035, 2004.

23. G. Y. Chen, M. Ding, T. P. Newson, and G. Brambilla, “A review of microfiber and nanofiber based optical sensors”, Open Opt. J., vol. 7, pp. 32–57, 2014.

24. M. Wu, W. Huang, and L. Wang, “Propagation characteristics of the silica and silicon subwavelength-diameter hollow wire waveguides”, Chin. Opt. Lett., vol. 6, no. 1, pp. 732–735, 2008.

25. G. Zhai and L. Tong, “Roughness-induced radiation losses in optical micro or nanofibers”, Opt. Express, vol. 15, no. 21, pp. 13805–13816, 2007.

26. M. Sumetsky, Y. Dulashko, P. Domachuk, and B. J. Eggleton, “Thinnest optical waveguide: experimental test”, Opt. Lett., vol. 32, no. 7, pp. 754–756, 2007.

27. M. Sumetsky, “How thin can a microfiber be and still guide light?”, Opt. Lett., vol. 31, no. 7, pp. 870–872, 2006.

28. S. Chuo and L. Wang, “Propagation loss, degradation and protective coating of long drawn microfibers”, Opt. Commun., vol. 284, no. 12, pp. 2825–2828, 2011.

29. F. Xu and G. Brambilla, “Embedding optical microfiber coil resonators in Teflon”, Opt. Lett., vol. 32, no. 15, pp. 2164–2166, 2007.

30. L. Tong, J. Lou, R. R. Gattass, S. He, X. Chen, L. Liu, and E. Mazur, “Assembly of silica nanowires on silica aerogels for microphotonic devices”, Nano Lett., vol. 5, no. 2, pp. 259–262, 2005.

31. J. Teipel, K. Franke, D. Türke, F. Warken, D. Meiser, M. Leuschner, and H. Giessen, “Characteristics of supercontinuum generation in tapered fibers using femtosecond laser pulses”, Appl. Phys. B, vol. 77, no. 2, pp. 245–251, 2003.

32. S. Lacroix, R. J. Black, C. Veilleux, and J. Lapierre, “Tapered single-mode fibers - external refractive-index dependence”, Appl. Opt., vol. 25, no. 15, pp. 2468–2469, 1986.

33. A. Diez, M. V. Andres, and J. L. Cruz, “In-line fiber-optic sensors based on the excitation of surface plasma modes in metal-coated tapered fibers”, Sensor. Actuat. B-Chem., vol. 73, no. 3, pp. 95–99, 2001.

34. W. Liang, Y. Huang, Y. Xu, R. K. Lee, and A. Yariv, “Highly sensitive fiber Bragg grating refractive index sensors”, Appl. Phys. Lett., vol. 86, no. 15, pp. 151122-1–3, 2005.

35. T. Allsop, F. Floreani, K. P. Jedrzejewski, P. V. S. Marques, R. Romero, D. J. Webb, and I. Bennion, “Spectral characteristics of tapered LPG device as a sensing element for refractive index and temperature”, J. Lightwave Technol., vol. 24, no. 2, pp. 870–878, 2006.

36. J. Wo, G. Wang, Y. Cui, Q. Sun, R. Liang, P. P. Shum, and D. Liu, “Refractive index sensor using microfiber-based Mach-Zehnder interferometer”, Opt. Lett., vol. 37, no. 1, pp. 67–69, 2012.

37. Z. Tian, S. S. H. Yam, J. Barnes, W. Bock, P. Greig, J. M. Fraser, H. Loock, and R. D. Oleschuk, “Refractive index sensing with Mach-Zehnder interferometer based on concatenating two single-mode fiber tapers”, IEEE Photonic. Tech. L., vol. 20, no. 8, pp. 626–628, 2008.

38. Z. Tian, S. S. H. Yam, and H. P. Loock, “Refractive index sensor based on an abrupt taper Michelson interferometer in a single-mode fiber”, Opt. Lett., vol. 33, no. 10, pp. 1105–1107, 2008.

39. J. Ding, A. Zhang, L. Shao, J. Yan, and S. He, “Fiber-taper seeded long-period grating pair as a highly sensitive refractive-index sensor”, IEEE Photonic. Tech. L., vol. 17, no. 6, pp. 1247–1249, 2005.

40. J. Li, L. Sun, S. Gao, Z. Quan, Y. Chang, Y. Ran, L. Jin, B. Guan, “Ultrasensitive refractive-index sensors based on rectangular silica microfibers”, Opt. Lett., vol. 36, no. 18, pp. 3593–3595, 2011.

41. W. Tan, Z. Shi, S. Smith, D. Birnbaum, and R. Kopelman, “Submicrometer intracellular chemical optical fiber sensors”, Science, vol. 258, no. 5083, pp. 778–781, 1992.

42. M. Belal, Z. Song, Y. Jung, G. Brambilla, and T. P. Newson, “Optical fiber microwire current sensor”, Opt. Lett., vol. 35, no. 18, pp. 3045–3047, 2010.

43. F. Bueno, O. Esteban, N. Díaz-Herrera, M. Navarrete, and A. González-Cano, “Sensing properties of asymmetric double-layer-covered tapered fibers”, Appl. Opt., vol. 43, no. 8, pp. 1615–1620, 2004.

44. M. Sumetsky, Y. Dulashko, J. M. Fini, and A. Hale, “Optical microfiber loop resonator”, Appl. Phys. Lett., 86(16): pp. 161108-1–3, 2005.

45. M. Sumetsky, Y. Dulashko, J. M. Fini, A. Hale, and D. J. DiGiovanni, “The microfiber loop resonator: theory, experiment, and application”, J. Lightwave Technol., vol. 24, no. 1, pp. 242–250, 2006.

46. G. Vienne, Y. Li, and L. Tong, “Effect of host polymer on microfiber resonator”, IEEE Photonic. Tech. L., vol. 19, no. 17–20, pp. 1386–1388, 2007.

47. P. Pal and W. H. Knox, “Fabrication and characterization of fused microfiber resonators”, IEEE Photonic. Tech. L., vol. 21, no. 12, pp. 766–768, 2009.

48. P. Wang, L. Zhang, Z. Yang, F. Gu, S. Wang, Q. Yang, and L. Tong, “Fusion spliced microfiber closed-loop resonators”, IEEE Photonic. Tech. L., vol. 22, no. 15, pp. 1075–1077, 2010.

49. P. Pal and W. H. Knox, “Low loss fusion splicing of micron scale silica fibers”, Opt. Express, vol. 16, no. 15, pp. 11568–11573, 2008.

50. W. Li, P. Wang, Z. Hu, and L. Tong, “Fusion splicing soft glass microfibers for photonic devices”, IEEE Photonic. Tech. L., vol. 23, no. 12, pp. 831–833, 2011.

51. X. Guo and L. Tong, “Supported microfiber loops for optical sensing”, Opt. Express, vol. 16, no. 19, pp. 14429–14434, 2008.

52. X. Guo, Y. Li, X. Jiang, and L. Tong, “Demonstration of critical coupling in microfiber loops wrapped around a copper rod”, Appl. Phys. Lett., vol. 91, no. 7, pp. 073512-1–3, 2007.

53. X. Jiang, L. Tong, G. Vienne, X. Guo, A. Tsao, Q. Yang, and D. Yang, “Demonstration of optical microfiber knot resonators”, Appl. Phys. Lett., vol. 88, no. 22, pp. 223501-1–3, 2006.

54. Y. Wang, H. Zhu, and B. Li, “Optical characterization of mechanically tunable microwire based resonators by changing ring radius and wire diameter”, Opt. Commun., vol. 284, no. 13, pp. 3276–3279, 2011.

55. K. J. Vahala, “Optical microcavities”, Nature, vol. 424, no. 6950, pp. 839–846, 2003.

56. M. L. Gorodetsky and V. S. Ilchenko, “High-Q optical whispering-gallery microresonators - precession approach for spherical mode analysis and emission patterns with prism couplers”, Opt. Commun., vol. 113, no. 3, pp. 133–143, 1994.

57. M. Sumetsky, Y. Dulashko, and R. S. Windeler, “Super free spectral range tunable optical microbubble resonator”, Opt. Lett., vol. 35, no. 11, pp. 1866–1868, 2010.

58. F. Xu and G. Brambilla, “Manufacture of 3-D microfiber coil resonators”, IEEE Photonic. Tech. L., vol .19, no. 20, pp. 1481–1483, 2007.

59. M. Sumetsky, “Basic elements for microfiber photonics: micro/nanofibers and microfiber coil resonators”, J. Lightwave Technol., vol. 26, no. 4, pp. 21–27, 2008.

60. F. Xu and G. Brambilla, “Demonstration of a refractometric sensor based on optical microfiber coil resonator”, Appl. Phys. Lett., vol. 92, no. 10, pp. 101126-1–3, 2008.

61. F. Xu, P. Horak, and G. Brambilla, “Conical and biconical ultra-high-Q optical-fiber nanowire microcoil resonator”, Appl. Opt., vol. 46, no. 4, pp. 570–573, 2007.

62. F. Xu, Q. Wang, J. Zhou, W. Hu, and Y. Lu, “Dispersion study of optical nanowire microcoil resonators”, IEEE J. of Sel. Top. Quant., vol. 17, no. 4, pp. 1102–1106, 2011.

63. F. Xu, G. Brambilla, J. Feng, and Y. Lu, “Mathematical model for manufacturing microfiber coil resonators”, Opt. Eng., vol. 49, no. 4, pp. 044001-1–4, 2010.

64. J. Scheuer and M. Sumetsky, “Optical-fiber microcoil waveguides and resonators and their applications for interferometry and sensing”, Laser Photonics Rev., vol. 5, no. 4 pp. 465–478, 2011.

65. J. Scheuer, “Fiber microcoil optical gyroscope”, Opt. Lett., vol. 34, no. 11, pp. 1630–1632, 2009.

66. Y. Hsieh, T. Peng, and L. Wang, “Millimeter-sized microfiber coil resonators with enhanced quality factors by increasing coil numbers”, IEEE Photonic. Tech. L., vol. 24, no. 7, pp. 569–571, 2012.

67. A. A. Jasim, K. S. Lim, M. Z. Muhammad, H. Arof, H. Ahmad, S. W. Harun, “Transmission characteristic of multi-turn microfiber coil resonator”, Opt. Laser Technol., vol. 44, no. 6, pp. 1791–1795, 2012.

68. J. Wang and D. Dai, “Highly sensitive Si nanowire-based optical sensor using a Mach-Zehnder interferometer coupled microring”, Opt. Lett., vol. 35, no. 24, pp. 4229–4231, 2010.

69. P. Wang, F. Gu, L. Zhang, and L. Tong, “Polymer microfiber rings for high-sensitivity optical humidity sensing”, Appl. Opt., vol. 50, no. 31, pp. G7–G10, 2011.

70. G. Brambilla, G. S. Murugan, J. S. Wilkinson, and D. J. Richardson, “Optical manipulation of microspheres along a subwavelength optical wire”, Opt. Lett., vol. 32, no. 20, pp. 3041–3043, 2007.

71. M. Noto, F. Vollmer, D. Keng, I. Teraoka, and S. Arnold, “Nanolayer characterization through wavelength multiplexing of a microsphere resonator”, Opt. Lett., vol. 30, no. 5, pp. 510–512, 2005.

72. A. M. Armani and K. J. Vahala, “Heavy water detection using ultra-high-Q microcavities”, Opt. Lett., vol. 31, no. 12, pp. 1896–1898, 2006.

73. J. Zhu, S. K. Ozdemir, Y. Xiao, L. Li, L. He, D. Chen, and L. Yang, “On-chip single nanoparticle detection and sizing by mode splitting in an ultrahigh-Q microresonator”, Nat. Photonics, vol. 4, no. 1, pp. 46–49, 2010.

74. I. M. White, et al., “Versatile waveguide-coupled optofluidic devices based on liquid core optical ring resonators”, Appl. Phys. Lett., vol. 91, no. 24, pp. 241104-1–3, 2007.

75. M. Sumetsky, R. S. Windeler, Y. Dulashko, and X. Fan, “Optical liquid ring resonator sensor”, Opt. Express, vol. 15, no. 22, pp. 14376–14381, 2007.

76. G. S. Murugan, J. S. Wilkinson, and M. N. Zervas, “Selective excitation of whispering gallery modes in a novel bottle microresonator”, Opt. Express, vol. 17, no. 14, pp. 11916–11925, 2009.

77. M. Ding, G. S. Murugan, G. Brambilla, and M. N. Zervas, “Whispering gallery mode selection in optical bottle microresonators”, Appl. Phys. Lett., vol. 100, no. 8, pp. 081108-1–3, 2012.

78. J. C. Knight, G. Cheung, F. Jacques, and T. A. Birks, “Phase-matched excitation of whispering-gallery-mode resonances by a fiber taper”, Opt. Lett., vol. 22, no. 15, pp. 1129–1131, 1997.

79. W. Wong, C. Chan, Y. Zhang, and K. Leong, “Minature single mode fiber refractive index interferometer sensor based on high order cladding mode and core-offset”, IEEE Photonic. Tech. L., vol. 24, no. 5, pp. 359–361, 2012.

80. P. Polynkin, A. Polynkin, N. Peyghambarian, and M. Mansuripur, “Evanescent field-based optical fiber sensing device for measuring the refractive index of liquids in microfluidic channels”, Opt. Lett., vol. 30, no. 11, pp. 1273–1275, 2005.

81. P. Wang, G. Brambilla, M. Ding, Y. Semenova, Q. Wu, and G. Farrell, "High-sensitivity, evanescent field refractometric sensor based on a tapered, multimode fiber interference", Opt. Lett., vol. 36, no. 12, pp. 2233–2235, 2011.

82. S. Qiu, Y. Chen, J. Kou, F. Xu, and Y. Lu, "Miniature tapered photonic crystal fiber interferometer with enhanced sensitivity by acid microdroplets etching", Appl. Opt., vol. 50, no. 22, pp. 4328–4332, 2011.

83. D. Monzon-Hernandez and J. Villatoro, "High-resolution refractive index sensing by means of a multiple-peak surface plasmon resonance optical fiber sensor", Sensor. Actuat. B-Chem., vol. 115, no. 1, pp. 227–231, 2006.

84. F. Xu, G. Brambilla, and Y. Q. Lu, "A microfluidic refractometric sensor based on gratings in optical fibre microwires", Opt. Express, vol. 17, no. 23, pp. 20866–20871, 2009.

85. G. Wang, P. P. Shum, H. Ho, X. Yu, D. Hu, Y. Cui, L. Tong, and C. Lin, "Modeling and analysis of localized biosensing and index sensing by introducing effective phase shift in microfiber Bragg grating (mu FBG)", Opt. Express, vol. 19, no. 9, pp. 8930–8938, 2011.

86. R. Liang, Q. Sun, J. Wo, and D. Liu, "Investigation on micro/nanofiber Bragg grating for refractive index sensing", Opt. Commun., vol. 285, no. 6, pp. 1128–1133, 2012.

87. G. Salceda-Delgado, D. Monzon-Hernandez, A. Martinez-Rios, G. A. Cardenas-Sevilla, and J. Villatoro, "Optical microfiber mode interferometer for temperature-independent refractometric sensing", Opt. Lett., vol. 37, no. 11, pp. 1974–1976, 2012.

88. J. Kou, W. Guo, F. Xu, and Y. Lu, "Highly birefringent optical-fiberized slot waveguide for miniature polarimetric interference sensors: a proposal", IEEE Sens. J., vol. 12, no. 6, pp. 1681–1685, 2012.

89. Y. Tai and P. Wei, "Sensitive liquid refractive index sensors using tapered optical fiber tips", Opt. Lett., vol. 35, no. 7, pp. 944–946, 2010.

90. J. Kou, S. Qiu, F. Xu, Y. Lu, Y. Yuan, and G. Zhao, "Miniaturized metal-dielectric-hybrid fiber tip grating for refractive index sensing", IEEE Photonic. Tech. L., vol. 23, no. 22, pp. 1712–1714, 2011.

91. H. Zhu, Y. Wang, and B. Li, "Tunable refractive index sensor with ultracompact structure twisted by poly(trimethylene terephthalate) nanowires", ACS Nano, vol. 3, no. 10, pp. 3110–3114, 2009.

92. K. Lim, I. Aryanfar, W. Chong, Y. Cheong, S. W. Harun, and H. Ahmad, "Integrated microfibre device for refractive index and temperature sensing", Sensors, vol. 12, no. 9, pp. 11782–11789, 2012.

93. L. Shi, Y. Lu, W. Tan, and X. Chen, "Simulation of optical microfiber loop resonators for ambient refractive index sensing", Sensors, vol. 7, no. 5, pp. 689–696, 2007.

94. F. Xu, V. Pruneri, V. Finazzi, and G. Brambilla, "An embedded optical nanowire loop resonator refractometric sensor", Opt. Express, vol. 16, no. 2, pp. 1062–1067, 2008.

95. L. Sun, J. Li, Y. Tan, X. Shen, X. Xie, S. Gao, and B. Guan, "Miniature highly-birefringent microfiber loop with extremely-high refractive index sensitivity", Opt. Express, vol. 20, no. 9, pp. 10180–10185, 2012.

96. S. S. Pal, S. K. Mondal, U. Tiwari, P. V. G. Swamy, and M. Kumar, "Etched multimode microfiber knot-type loop interferometer refractive index sensor", Rev. Sci. Instrum., vol. 82, no. 9, pp. 095107-1–4, 2011.

97. F. Xu, P. Horak, and G. Brambilla, "Optical microfiber coil resonator refractometric sensor", Opt. Express, vol. 15, no. 12, pp. 7888–7893, 2007.

98. V. Zamora, A. Díez, M. V. Andrés, and B. Gimeno, "Refractometric sensor based on whispering-gallery modes of thin capillaries", Opt. Express, vol. 15, no. 19, pp. 12011–12016, 2007.

99. B. Sun, M. Chen, Y. Zhang, J. Yang, J. Yao, and H. Cui, "Microstructured-core photonic-crystal fiber for ultra-sensitive refractive index sensing", Opt. Express, vol. 19, no. 5, pp. 4091–4100, 2011.

100. J. M. Corres, J. Bravo, I. R. Matías, and F. J. Arregui, "Nonadiabatic tapered single-mode fiber coated with humidity sensitive nanofilms", IEEE Photonic. Tech. L., vol. 18, no. 8, pp. 935–937, 2006.

101. J. M. Corres, F. J. Arregui, and I. R. Matías, "Design of humidity sensors based on tapered optical fibers", J. Lightwave Technol., vol. 24, no, 11, pp. 4329–4336, 2006.

102. J. M. Corres, F. J. Arregui, and I. R. Matías, "Sensitivity optimization of tapered optical fiber humidity sensors by means of tuning the thickness of nanostructured sensitive coatings", Sensor. Actuat. B-Chem., vol. 122, no. 2, pp. 442–449, 2007.

103. C. Bariáin, I. R. Matías, F. J. Arregui, and M. López-Amo, "Optical fiber humidity sensor based on a tapered fiber coated with agarose gel", Sensor. Actuat. B-Chem., vol. 69, no. 2, pp. 127–131, 2000.

104. L. Zhang, F. Gu, J. Lou, X. Yin, and L. Tong, "Fast detection of humidity with a subwavelength-diameter fiber taper coated with gelatin film", Opt. Express, vol. 16, no. 17, pp. 13349–13353, 2008.

105. T. Li, C. Zhao, X. Dong, W. Qian, Y. Jin, and S. Jin, "Relative humidity sensor based on photonic crystal fiber with tapered and filled in polymer", Opt. Sens. Biophoton., vol. 7990, pp. 288–289, 2011.

106. Y. Wu, T. Zhang, Y. Rao, and Y. Gong, "Miniature interferometric humidity sensors based on silica/polymer microfiber knot resonators", Sensor. Actuat. B-Chem., vol. 155, no. 1, pp. 258–263, 2011.

107. M. Hernáez, C. R. Zamarreño, I. R. Matías, and F. J. Arregui, "Optical fiber humidity sensor based on surface plasmon resonance in the infra-red region", J. Phys., vol. 178, pp. 012019-1–5, 2009.

108. A. Stiebeiner, O. Rehband, R. Garcia-Fermandez, and A. Rauschenbeutel, "Ultra-sensitive fluorescence spectroscopy of isolated surface-adsorbed molecules using an optical nanofibers", Opt. Express, vol. 17, no. 24, pp. 21704–21711, 2009.

109. K. P. Nayak, P. N. Melentiev, M. Morinaga, F. Le Kien, V. I. Balykin, and K. Hakuta, "Optical nanofiber as an efficient tool for manipulating and probing atomic fluorescence", Opt. Express, vol. 15, no. 9, pp. 5431–5438, 2007.

110. K. P. Nayak and K. Hakuta, "Single atoms on an optical nanofibre", New J. Phys., vol. 10, pp. 053003-1–9, 2008.

111. T. Vo-Dinh, “Nanobiosensors: probing the sanctuary of individual living cells”, J. Cell. Biochem., vol. 39, pp. 154–161, 2002.

112. R. Lorenzi, Y. M. Jung, and G. Brambilla, “In-line absorption sensor based on coiled optical microfiber”, Appl. Phys. Lett., vol. 98, no. 17, pp. 173504-1–3, 2011.

113. Y. Sun, J. Liu, G. Frye-Mason, S. J. Ja, A. K. Thompson, and X. Fan, “Optofluidic ring resonator sensors for rapid DNT vapor detection”, Analyst, vol. 134, no. 7, pp. 1386–1391, 2009.

114. F. Vollmer, D. Braun, and A. Libchaber, “Protein detection by optical shift of a resonant microcavity”, Appl. Phys. Lett., vol. 80, no. 21, pp. 4057–4059, 2002.

115. Z. Rosenzweig and R. Kopelman, “Development of a submicrometer optical-fiber oxygen sensor”, Anal. Chem., vol. 67, no. 15, pp. 2650–2654, 1995.

116. S. Zhu, F. Pang, and T. Wang, “Single-mode tapered optical fiber for temperature sensor based on multimode interference”, Opt. Sens. Biophoton., vol. 8311, pp. 83112B-1–6 , 2011.

117. P. Lu, L. Men, K. Sooley, and Q. Chen, “Tapered fiber Mach-Zehnder interferometer for simultaneous measurement of refractive index and temperature”, Appl. Phys. Lett., vol. 94, no. 13, pp. 131110-1–3, 2009.

118. C. Ji, C. Zhao, J. Kang, X. Dong, and S. Jin, “Multiplex and simultaneous measurement of displacement and temperature using tapered fiber and fiber Bragg grating”, Rev. Sci. Instrum., vol. 83, no. 5, pp. 053109-1–5, 2012.

119. M. Ding, P. Wang, and G. Brambilla, “A microfiber coupler tip thermometer”, Opt. Express, vol. 20, no. 5, pp. 5402–5408, 2012.

120. G. Rajan, S. Mathews, G. Farrell, and Y. Semenova, “A liquid crystal coated tapered photonic crystal fiber interferometer”, J. Opt., vol. 13, no. 1, pp. 015403-1–10, 2011.

121. Y. Wu, Y. Rao, Y. Chen, and Y. Gong, “Miniature fiber-optic temperature sensors based on silica/polymer microfiber knot resonators”, Opt. Express, vol. 17, no. 20, pp. 18142–18147, 2009.

122. Y. Wu, L. Jia, T. Zhang, Y. Rao, and Y. Gong, “Microscopic multi-point temperature sensing based on microfiber double-knot resonators”, Opt. Commun., vol. 285, no. 8, pp. 2218–2222, 2012.

123. Y. Chen, F. Xu, and Y. Q. Lu, “Teflon-coated microfiber resonator with weak temperature dependence”, Opt. Express, vol. 19, no. 23, pp. 22923–22928, 2011.

124. Y. Chen, Y. Ming, W. Gao, F. Xu, and Y. Lu, “Temperature characteristics of microfiber coil resonators embedded in teflon”, PCFD VIII, pp. 830711-1–6, 2012.

125. Y, Rao, M. Deng, T. Zhu, and H. Li, “In-line Fabry-Perot etalons based on hollow-core photonic bandgap fibers for high-temperature applications”, J. Lightwave Technol, vol. 27, no. 19, pp. 4360–4365, 2009.

126. M. Belal, Z. Song, Y. Jung, G. Brambilla, and T. P. Newson, “An interferometric current sensor based on optical fiber micro wires”, Opt. Express, vol. 18, no. 19, pp. 19951–19956, 2010.

127. K. S. Lim, S. W. Harun, S. S. A. Damanhuri, A. A. Jasim, C. K. Tio, and H. Ahmad, “Current sensor based on microfiber knot resonator”, Sensor. Actuat. A-Phys., vol. 167, no. 1, pp. 60–62, 2011.

128. R. I. Laming and D. N. Payne, “Electric current sensors employing spun highly birefringent optical fibers”, J. Lightwave Technol., vol. 7, no. 12, pp. 2084–2094, 1989.

129. F. J. Arregui, I. R. Matías, C. Bariain, and M. López-Amo, “Experimental design rules for implementing biconically tapered singlemode optical fibre displacement sensors”, EWOFS, vol. 348, pp. 164–168, 1998.

130. H. Luo, X. Li, W. Zou, X. Li, Z. Hong, and J. Chen, “Temperature-insensitive microdisplacement sensor based on locally bent microfiber taper modal interferometer”, IEEE Photonic. J., vol. 4, no. 3, pp. 772–778, 2012.

131. A. Martinez-Rios, D. Monzon-Hernandez, I. Torres-Gomez, and G. Salceda-Delgado, “An intrinsic fiber-optic single loop micro-displacement sensor”, Sensors, vol. 12, no. 1, pp. 415–428, 2012.

132. A. A. Jasim, A. Z. Zulkifli, M. Z. Muhammad, S. W. Harun, H. Ahmad, “A new compact micro-ball lens structure at the cleaved tip of microfiber coupler for displacement sensing”, Sensor. Actuat. A-Phys., vol. 189, pp. 177–181, 2013.

133. H. C. Seat, P. Chawah, M. Cattoen, A. Sourice, G. Plantier, F. Boudin, J. Chéry, C. Brunet, P. Bernard, and M. Suleiman, “Dual-modulation fiber Fabry-Perot interferometer with double reflection for slowly-varying displacements”, Opt. Lett., vol. 37, no. 14, pp. 2886–2888, 2012.

134. D. Monzon-Hernandez, A. Martinez-Rios, I. Torres-Gomez, and G. Salceda-Delgado, “Compact optical fiber curvature sensor based on concatenating two tapers”, Opt. Lett., vol. 36, no. 22, pp. 4380–4382, 2011.

135. S. Zhang, W. Zhang, S. Gao, P. Geng, and X. Xue, “Fiber-optic bending vector sensor based on Mach-Zehnder interferometer exploiting lateral-offset and up-taper”, Opt. Lett., vol. 37, no. 21, pp. 4480–4482, 2012.

136. T. A. Birks, J. C. Knight, and T. E. Dimmick, “High-resolution measurement of the fiber diameter variations using whispering gallery modes and no optical alignment”, IEEE Photonic. Tech. L., vol. 12, no. 2, pp. 182–183, 2000.

137. M. Sumetsky, Y. Dulashko, J. M. Fini, A. Hale, and J. W. Nicholson, “Probing optical microfiber nonuniformities at nanoscale”, Opt. Lett., vol. 31, no. 16, pp. 2393–2395, 2006.

138. M. Sumetsky and Y. Dulashko, “Radius variation of optical fibers with angstrom accuracy”, Opt. Lett., vol. 35, 23, pp. 4006–4008, 2010.

139. L. Wang, P. Liang, Z. Liu, A. Zhou, and L. Yuan, “An optical trapping based microfiber vibration sensor”, OFS-21, pp. 77530F-1–4, 2011.

140. C. Hou, Y. Wu, and X. Zeng, “Novel high sensitivity accelerometer based on a microfiber loop resonator”, Opt. Eng., vol. 49, no. 1, pp. 014402-1–6, 2010.

141. Y. Wu, X. Zeng, Y. Rao, Y. Gong, C. Hou, and G. Yang, “MOEMS accelerometer based on microfiber knot resonator”, IEEE Photonic. Tech. L., vol. 21, no. 20, pp. 1547–1549, 2009.

142. D. L. Gardner, T. Hofler, S. R. Baker, R. K. Yarber, and S. L. Garrett, “A fiber-optic interferometric seismometer”, J. Lightwave Technol., vol. 5, no. 7, pp. 953–960, 1987.

143. T. Wieduwilt, S. Bruckner, and H. Bartelt, “High force measurement sensitivity with fiber Bragg gratings fabricated in uniform-waist fiber tapers”, Meas. Sci. Technol., vol. 22, no. 7, pp. 075201-1–6, 2011.

144. X. Wang, W. Li, L. Chen, and X. Bao, “Thermal and mechanical properties of tapered single mode fiber measured by OFDR and its application for high-sensitivity force measurement”, Opt. Express, vol. 20, no. 14, pp. 14779–14788, 2012.

145. C. R. Dennison and P. M. Wild, “Superstructured fiber-optic contact force sensor with minimal cosensitivity to temperature and axial strain”, Appl. Opt., vol. 51, no. 9, pp. 1188–1197, 2012.

146. M. J. F. Digonnet, “Rotation sensitivity of gyroscopes based on distributed-coupling loop resonators”, J. Lightwave Technol., vol. 29, no. 20, pp. 3048–3053, 2011.

147. B. Xu, Y. Li, M. Sun, Z. Zhang, X. Dong, Z. Zhang, and S. Jin, “Acoustic vibration sensor based on nonadiabatic tapered fibers”, Opt. Lett., vol. 37, no. 22, pp. 4768–4770, 2012.

148. C. Veilleux, J. Lapierre, and J. Bures, “Liquid-crystal-clad tapered fibers”, Opt. Lett., vol. 11, no. 11, pp. 733–735, 1986.

149. X. Li and H. Ding, “All-fiber magnetic field sensor based on microfiber knot resonator and magnetic fluid”, Opt. Lett., vol. 37, no. 24, pp. 5187–5189, 2012.

Chapter 3

3. Temperature sensing with optical microfiber

This chapter describes the various resonant wavelength shift detection schemes that are typically employed for resonator-based temperature sensing, before presenting the theoretical and experimental demonstrations of a sliding MCR-based temperature sensor for the rapid inspection of insulation faults along electrical wires.

3.1 Resonance shift detection schemes

Fiber-optic resonators experience a resonant wavelength shift when the OPL of their cavities are modified by a measurand, as shown in Figure 22. An optical spectrum analyzer (OSA) is typically used in conjunction with a broadband light source. The measurand sensitivity (S) is related to the wavelength resolution ($\Delta\lambda$) of the detection system and the responsivity (R) of the sensor:

$$S = \frac{\Delta\lambda}{R} \tag{3.1}$$

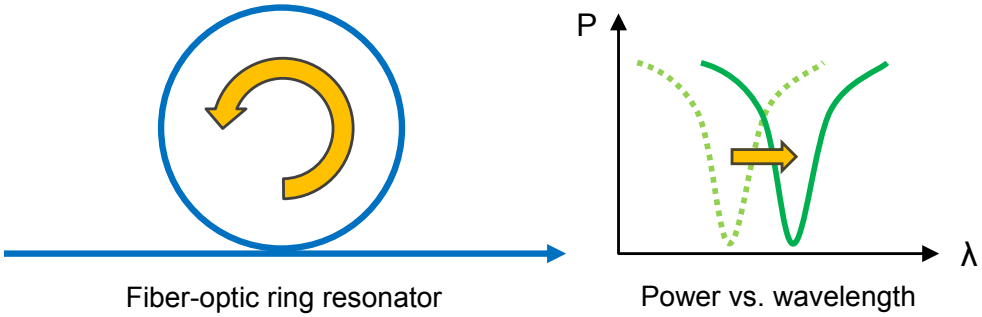

Figure 22. Illustration of how optical resonators respond to changes in the optical path length.

From Equation 3.1, it is evident that the sensitivity depends on the shape of resonance. $\Delta\lambda$ is seldom equal to the minimum wavelength resolution of the OSA, due to the mid-point ambiguity caused by measurement noise in the resonance dips. Narrower resonances facilitate easier wavelength tracking, thereby restoring $\Delta\lambda$ to its intended precision and enhancing the sensitivity. For optical power-based detection schemes operating at a single wavelength, a sharper resonance also constitutes a larger signal change for small perturbations of the resonator.

3.2 Sliding microfiber coil resonator temperature sensor for inspection of electrical wires

A compact and robust thermometer based on a MCR encircling a Teflon tube is presented in this section. The EMI-insensitive probe exhibits a responsivity of 93.4±7.0 pm/ºC and a sensitivity of 2.2±0.2 °C with a wavelength resolution of 200 pm. It can be readily slid along electrical wires to map the local temperature for locating insulation faults and reporting high current surges. The sensor head is simple to fabricate and potentially available at low cost, making it attractive for industrial applications.

3.2.1 Introduction

The main causes of overheating that lead to electrical fires in domestic and industrial environments are excessive current, poor connections and insulation breakdown. A variety of optical thermometers have been reported in recent years [1–7]. However, most devices require high precision in the placement and orientation of the sensor head for accurate results. Optical sensors fabricated from tapered optical fibers offer several potential benefits in comparison to conventional integrated micro-photonic devices, such as low insertion loss, inherent fiber compatibility and flexibility. MLRs and MCRs assembled from self-coupled OMs have shown temperature sensing abilities [5–7] as high as 280 pm/ºC. However, these devices were always immobilized on a slab or support rod that makes them impractical to use.

In this section, a wire-mounted sliding Teflon tube coiled with MCR is presented. Sliding probes can be used to rapidly inspect long electrical wires for fault location. The integrated MCR maps the local temperature to identify positions with insulation faults that can be at risk from electrical arcing. Defects in the insulation integrity are distinguished by an increase in the heat signature. Owing to a helical arrangement of the OM, the ring-shaped detection area facilitates a rotationally symmetric coverage and thus removes the need for radial alignment of the sensor head. Additionally, up-surges in temperature generated by intense currents can also be identified. The minimum bend radii of OMs [8] allow a wide range of wire diameters to be probed, from millimeters to tens of micrometers.

3.2.2 Theory

The schematic of the thermometer is shown in Figure 23, which consists of a MCR wrapped around a hollow Teflon cylinder. The device can slide along electrical wires to measure the local temperature. Owing to the electrical resistance of the current-carrying wire, high current will result in heat dissipation. This heat is then transferred to the Teflon tube and the coiled OM via thermal conduction. The effective index seen by the guided mode in the OM and the physical length of each turn in the MCR will be modified by thermal expansion and the thermal-optic effect, leading to a shift in the resonant wavelength [7]. Details of the MCR model will be given in Chapter 4.

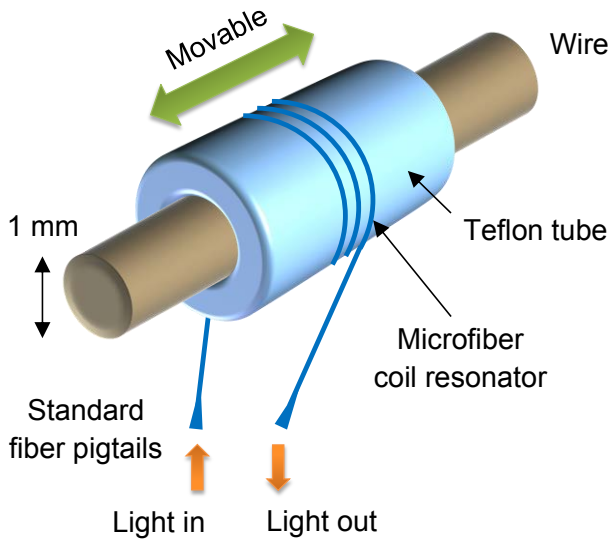

Figure 23. Schematic diagram of the microfiber coil resonator-based thermometer sliding along an electrical wire to measure the local temperature.

Polymer coatings tend to have a negative thermo-optic coefficient, which means their RI decreases with increasing temperature. This strengthens the mode confinement due to the larger RI difference, and with more light propagating in the silica core the effective index increases. However, the fraction of optical power residing in the cladding experiences an RI reduction, and the overall effect is dominated by the latter which results in a decrease in effective index. For the MCR, most of the guided mode is confined to the core. This means the much larger negative thermo-optic coefficient of the polymer is more or less compensated by the smaller positive coefficient of silica. With an additional increase in OM length due to the thermal expansion of the Teflon tube, the OPL increases and thus λ_R experiences

a positive shift. The number of OM turns has no impact on the OPL and thus does not affect the responsivity of the sensor. However, to achieve sufficient self-coupling leading to resonance, the minimum number of OM turns is 2.

To predict the temperature responsivity of the MCR, the behavior of the device under thermal effects was modeled. The Teflon tube shown in Figure 24 is assumed to be unrestricted, since both its physical volume and thermal expansion are larger than that of the silica OM and the polymer coating combined. Hence, the strain imposed on the OM of length L can be approximated by the thermal expansion of the Teflon tube alone:

$$\frac{\Delta L}{L} \approx \alpha_{teflon} \Delta T \tag{3.2}$$

where α is the coefficient of thermal expansion and ΔT is the temperature change.

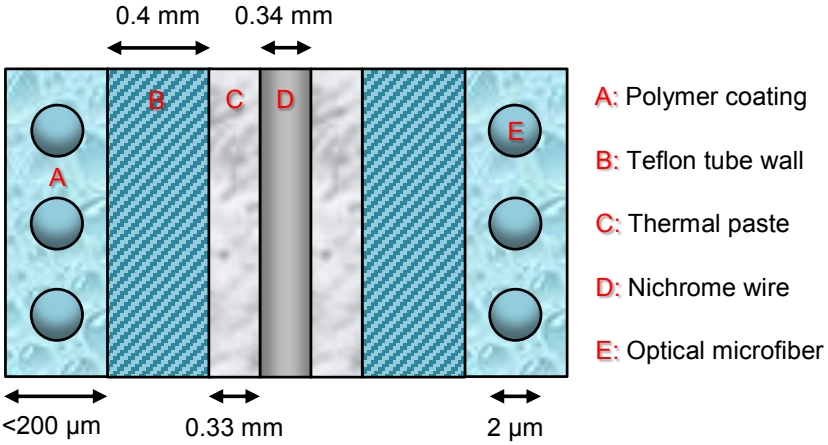

Figure 24. Side cross-sectional view of the microfiber coil resonator sensor with a heating element inside.

In addition to the physical length change of the OM by thermal expansion, the stress-optic effect [9] introduces a change in n_{silica} and similarly in $n_{polymer}$:

$$\Delta n_{silica} = -\frac{n_{silica}^3}{2} \cdot \frac{\Delta L}{L} \cdot [p_{12} - v_{silica} \cdot (p_{11} + p_{12})] \tag{3.3}$$

where n is the RI, v is the Poisson ratio, and p_{ij} is the Pockels coefficient components of the stress-optic tensor of silica (P_{11} = 0.126, P_{12} = 0.270) [10]. The Pockels coefficients are not known for polymer PC-373, but it is assumed to be similar to that of PMMA (P_{11} = 0.3, P_{12} = 0.297) [11].

The thermal-optic coefficients of silica and polymer must also be taken into account. Lastly, the thermal expansion of the OM increases its core diameter and also contributes to the change in the effective index seen by the guided mode. However, the tube-induced strain on the OM decreases its core diameter due to the Poisson Effect. It is reasonable to assume that these two weak effects cancel each other out and thus have a negligible impact on the final OM diameter.

3.2.3 Fabrication

The sensor was built in two stages. The first involved the fabrication of the OM. The modified flame-brushing technique [12] shown in Figure 25 was applied to a section of SMF-28, with the fiber ends fixed to a pair of automated translation platforms and the central section heated using a stationary ceramic micro-heater. To minimize the surface roughness caused by the mechanical stripping of the acrylate layer, the optical fiber was annealed for ~1 min by the micro-heater before being tapered. The surface tension smoothed any surface non-uniformities of the partially melted fiber, preventing the formation of cracks that could break the optical fiber when subject to axial tension. The current applied to the micro-heater was 2.9 A, corresponding to a temperature of ~1300 °C in the hot-zone. By carefully varying the differential motor velocities, the optical fiber can be stretched with sub-micron precision. The tapering process lasted ~10 min with an initial stretching speed of 1 mm/sec that was gradually slowed to ensure an adiabatic taper diameter profile for suppressing the excitation of higher-order modes [13]. A biconical OM was produced, whose diameter varied smoothly from 125 μm to 2 μm, with a uniform waist section of 2 μm diameter and 15 mm length.

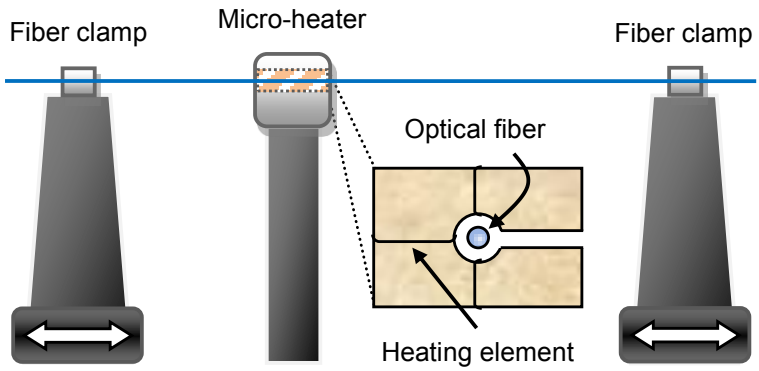

Figure 25. Schematic diagram of the existing tapering rig setup. A computer controls the initial position and differential velocities of the two translation platforms.

The second stage consisted of attaching the fabricated OM to a movable Teflon tube, which also serves as a cylindrical brace. Solid Teflon was chosen for its relatively large thermal expansion, high melting temperature and chemical resistance. In addition, the tube had sufficient stiffness and clearance to ensure geometrical stability. A thin layer of low-RI, ultraviolet (UV)-curable polymer (Efiron PC-373 AP) was deposited on the surface of the Teflon tube before and after coiling the OM for several reasons: (a) to avoid optical leakage into the Teflon layer; (b) to provide a slightly sticky surface for fixing the OM on the tube during coiling process; and (c) to prolong the life-time of the device after UV-curing (e.g. improves repeatability).

Before coiling, the upper un-tapered part of the OM was fixed on a fiber holder, and the lower un-tapered part allowed to hang down. A motorized translation stage shown in Figure 26 was used to adjust the angle between the OM and the tube during the coiling process. The pitch between adjacent OM turns could be controlled within several micrometers. The uniform diameter region of the taper was carefully coiled 2.5 times around a Teflon tube of diameter D = 1.8/1 mm (outer/inner) using a motorized rotation stage. A small winding pitch (Λ < 2 μm) was chosen to enable mode coupling between adjacent OM turns, thus forming a MCR. For the purpose of demonstration, a relatively long segment of Teflon tube was employed for ease of handling during the winding process. The standard optical fiber pigtails of the MCR were also embedded in the same polymer coating and UV-cured for robust packaging.

To monitor the spectral variation of the MCR during the coiling process, one tapered end was connected to the output of an erbium-doped fiber amplifier (EDFA) and the other end to an OSA. Figure 27 shows the transmission spectrum of the packaged sample, which exhibits resonance-splitting due to linear birefringence in the MCR. Light in one axis denoted as the Y-eigenmode had the highest ER of ~3 dB. The optical loss was ~5 dB at a wavelength of λ = 1530 nm. Evidence from non-published work suggests that it was attributed to Rayleigh and Mie scattering due to the presence of micro-bubbles and particles in the polymer. Absorption loss was relatively small due to the low-RI padding around the MCR.

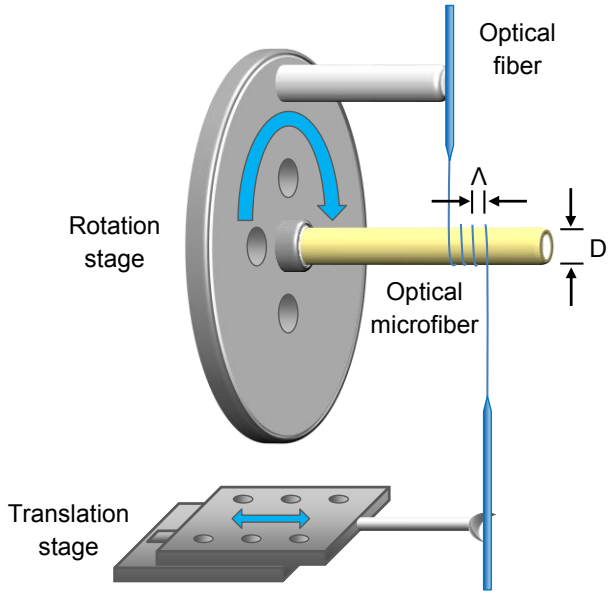

Figure 26. Schematic diagram of the existing coiling rig setup. Both the rotation and translation stages are controlled by a computer.

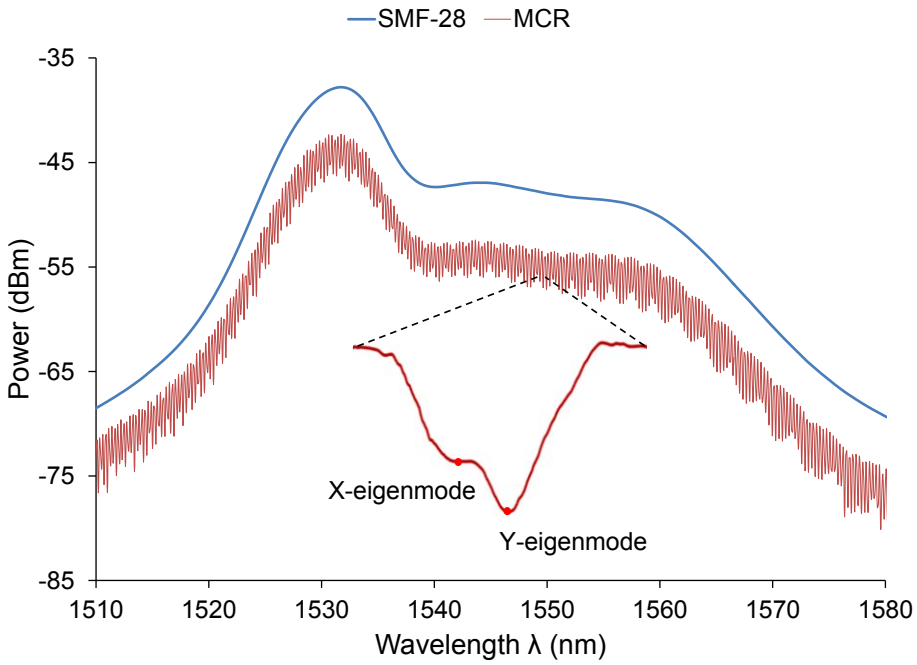

Figure 27. Transmission spectrum of the packaged microfiber coil resonator compared to the original SMF-28. Inset: individual pair of resonances associated with the polarized light in the two orthogonal axes arising from linear birefringence.

3.2.4 Experimental setup

The setup shown in Figure 28 was used to test the thermometer. A Nichrome wire of 0.34 mm diameter and 30 mm length was chosen as the heating element due to its

large electrical resistance (0.2 Ω/cm) and thus a high thermal response to current. The wire was inserted inside the MCR-coiled Teflon tube and filled with thermal paste to improve the heat conduction between the Nichrome wire and the Teflon tube. The output terminals of a 32 V power supply were connected to the two ends of the wire, and the DC was incremented from 0 mA to 800 mA in steps of 50 mA. Broadband light was provided by the amplified spontaneous emission from an EDFA. Although the resulting resonances are less defined due to the low coherence length of light, the EDFA provides a convenient way to monitor changes across a broad wavelength range. As current (I) passed through the Nichrome wire, power dissipated as heat was absorbed by the MCR and its surrounding polymer through thermal conduction. This changed the local temperature and caused a resonant wavelength shift of the MCR. The transmission spectrum was collected by an OSA (Yokogawa AQ6370). A commercial thermocouple (RS 206-3738) was used to provide a reference temperature reading. The sensor head of the thermocouple was very small and thus had a negligible effect on the local temperature. A room temperature of ~23 °C was maintained while the measurement process was repeated 3 times. After each set of measurement, the temperature of the device was allowed to cool down to room temperature before the next set of measurements.

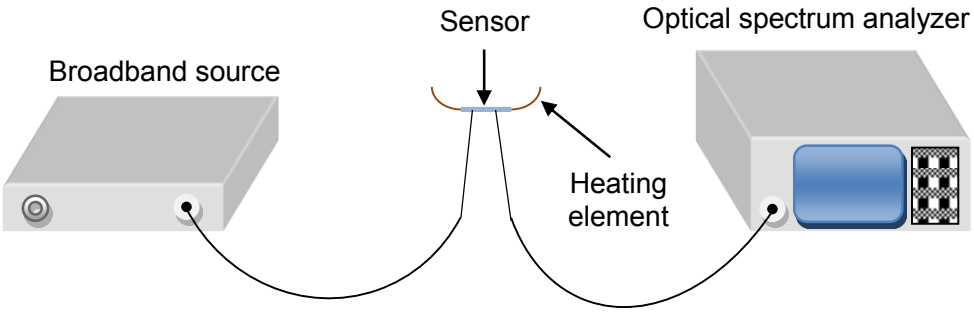

Figure 28. Schematic diagram of the experimental setup.

3.2.5 Simulations

The following parameters are considered for the tube model, starting with Teflon [14–16]: Young's modulus of E_{teflon} = 1.6 GPa, v_{teflon} = 0.42, RI of n_{teflon} = 1.315, and α_{Teflon} = 1×10^{-4} /°C. Likewise, for the silica OM [17]: E_{silica} = 73 GPa, v_{silica} = 0.17, n_{silica} = 1.45, and α_{silica} = 5.5×10^{-7} /°C. Lastly, for the polymer coating [18]: $E_{polymer}$ = 0.1 GPa, $v_{polymer}$ = 0.4, $n_{polymer}$ = 1.373, and $\alpha_{polymer}$ = 1.18×10^{-6} /°C.

The strain experienced by the OM is 1×10^{-4} using Equation 3.2 for a 1 °C rise in temperature. The stress-optic coefficients of silica and polymer are -3.09×10^{-5}/°C and -7.53×10^{-6}/°C respectively using Equation 3.3. The thermal-optic coefficients of silica and polymer are 8.11×10^{-6}/°C [19] and -1×10^{-4}/°C [20] respectively. By consolidating all the thermal effects into the MCR model described in section 4.4.2 (solved using Matlab) and discarding the $\Delta\beta$ terms, a positive wavelength shift of $\Delta\lambda_R$ = 100.0 pm/°C is simulated in Figure 29 for a 1 °C temperature change. The shift direction agrees with the expectation in section 3.2.2.

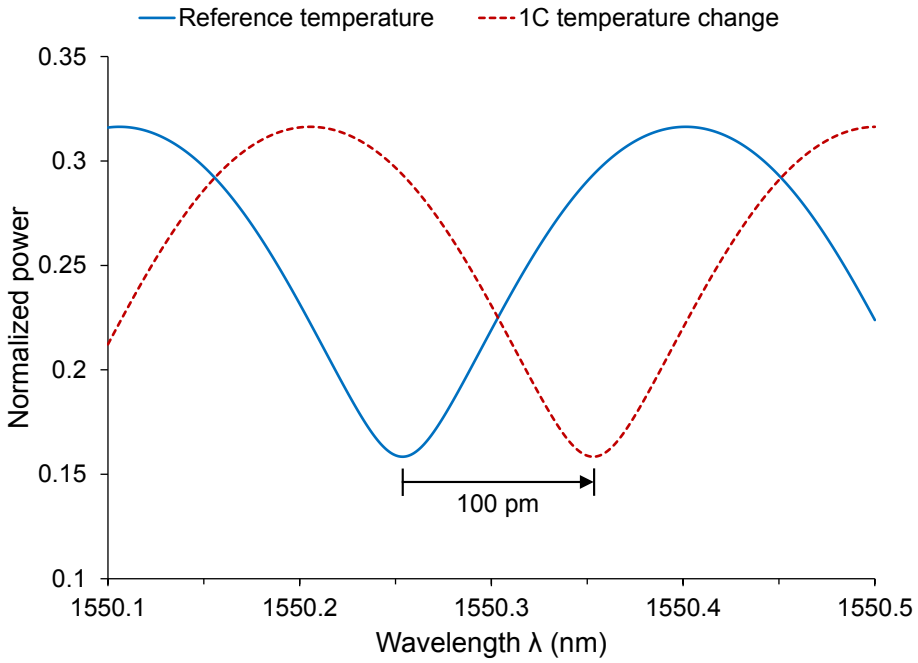

Figure 29. Simulated wavelength shift of the microfiber coil resonator sensor for a 1 °C change in temperature.

3.2.6 Experimental results

First of all, the heating element was characterized. Figure 30 shows that the local temperature change is proportional to the square of the current applied (i.e. electrical power) across the Nichrome wire, at 80.7 °C/A^2. The maximum current error is about ±10 mA due to the instability of the digital power supply. The maximum temperature error is approximately ±1 °C due to a combination of factors, including the resolution of the thermocouple (±0.1 °C) and the slowly varying temperature during the time taken to record each measurement (around ±1 °C within 10 s).

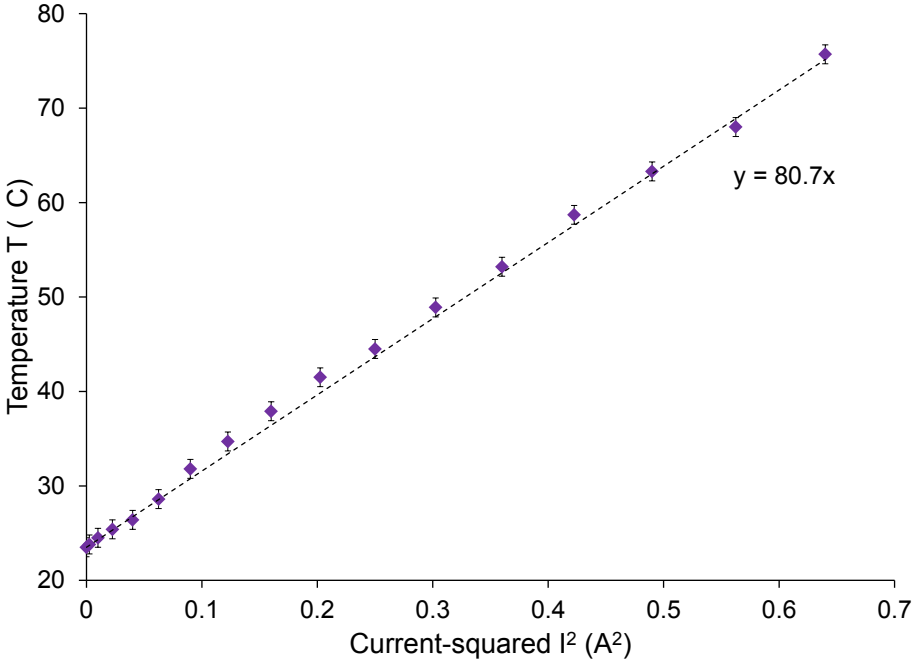

Figure 30. Characterization of the heating element, with a linear fit. Note: error bars are plotted behind the markers.

The resonance around a wavelength of λ = 1550 nm was chosen because it is positioned in the middle of the linear transmission region between 1540–1560 nm. The resonance dip of the Y-eigenmode was easily tracked due to its higher ER (i.e. sharper resonance). Figure 31 shows an average linear responsivity of 93.4±7.0 pm/°C between 26–76 °C for the 4 sets of measurements. Datasets 2–4 are in good agreement, whereas dataset 1 deviates at higher temperatures. This could be attributed to a small but steady rise in the ambient temperature during the time-frame of the first set of measurements. Alternatively, this may be caused by the first-time heating of the device up to a certain temperature. In that case, the repeatability of the device post-warm-up is fairly good. Moreover, the measured responsivity is almost the same as the simulated value of 100.0 pm/°C, and could be equal considering the error. Any minor difference would be the result of the unrestrained modeling of the Teflon tube, which provides an upper limit for the responsivity. Small variations in the ER resulting from changes in the coupling coefficient were observed, which were caused by the thermal expansion of the coil pitch and the RI change of the polymer surroundings.

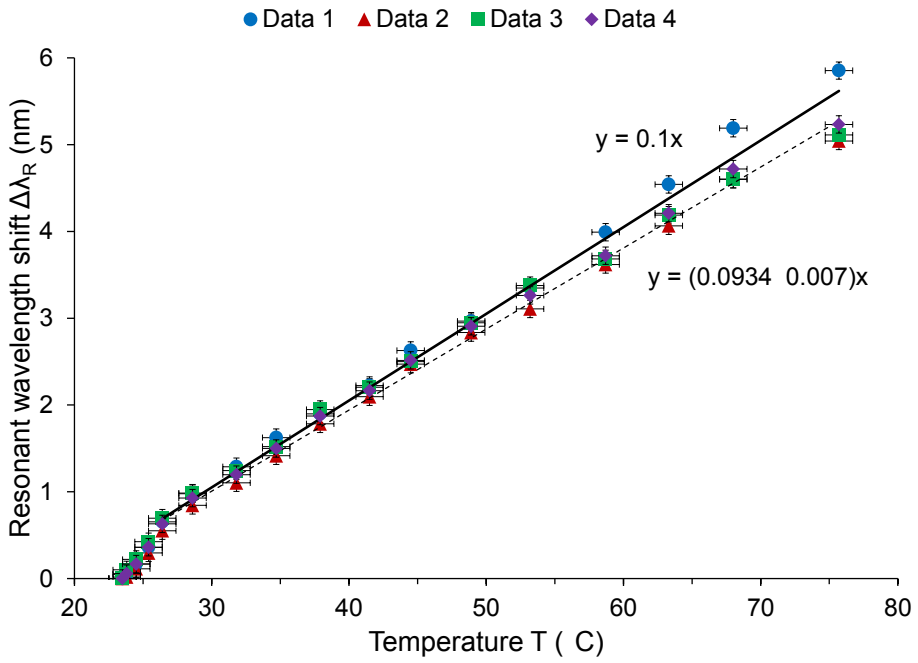

Figure 31. Measured temperature responsivity with an average linear fit (dashed line), compared with the theoretical prediction (solid line).

The detection bandwidth is governed by the transit time of the MCR. Since the effective index change can be positive or negative during the course of propagation by each portion of light, the OPL seen by the guided mode could remain constant despite local changes. As a result, the resonant wavelength shift will drop to zero for the first time beyond a certain modulation frequency (similar to section 4.2.5). The response time of the sensor consists of the time delay for thermal conduction to reach the OM, plus the transit time of light from the output of the MCR to the OSA. The typical response time reported for similar devices [21] are of the order of 10 ms.

The 200 pm resolution of the OSA produced a maximum wavelength error of ±100 pm, but allowed quicker data acquisitions than the lower resolution settings to facilitate faster fault location. A temperature sensitivity of 2.2±0.2 °C was calculated by dividing the wavelength resolution of the OSA by the temperature responsivity of 93.4±7.0 pm/°C, which is sufficient for the purpose of detecting unusual heat signatures along electrical wires. It is arguable that even with the best wavelength resolution setting (e.g. 20 pm), the commercial thermocouple is a better sensor in terms of accuracy. However, the aim and achievement of the MCR thermometer was to avoid manual positioning of the sensor head around the circumference of the wire, and to provide easy navigation along the longitudinal direction of wires.

3.2.7 Conclusion

A compact and robust thermometer based on a 2.5-turn MCR of 2 μm diameter OM and 15 mm uncoiled length encompassing a Teflon tube has experimentally demonstrated a repeatable temperature responsivity of 93.4±7.0 pm/°C (7500±560 pm/A^2) between 26–76 °C, which is competitive amongst existing resonator-based thermometers. Furthermore, the measured responsivity shows close agreement with the simulated value of 100.0 pm/°C. A temperature sensitivity of 2.2±0.2 °C (0.027±0.0025 A^2) is adequate for the designated use. The sensor can be readily slid along electrical wires to examine the insulation integrity by measuring the local temperature. The thermal response of high current surges can also be identified by monitoring shifts in the resonant wavelength.

To increase the responsivity, a material of higher thermal expansion coefficient must be selected for the support tube/rod. The sensitivity can be refined to 0.22 °C by setting the wavelength resolution of the OSA to 20 pm, though each measurement will take longer and ambient perturbations may be greater. To reduce the response time, the fiber length between the MCR and OSA must be kept as short as possible. The upper limit of measurable temperature can be extended by replacing the polymer packaging with Teflon, which has a much higher melting temperature in excess of 300 °C. However, Teflon resin is very expensive and large quantities are needed to fully embed the MCR, due to significant shrinkage in volume after drying in air. To reduce the loss, air bubbles must be removed from the packaging material. The ultimate compactness of the sensor head is restricted by the diameter of the Teflon tube, which has to be larger than the range of wire diameters to be measured. It is then followed by the minimum bend radius of the OM.

3.3 References

1. M. Ding, P. Wang, and G. Brambilla, "A microfiber coupler tip thermometer", Opt. Express, vol. 20, no. 5, pp. 5402–5408, 2012.

2. W. Qian, C. Zhao, C. Chan, L. Hu, T. Li, W. Wong, P. Zu, and X. Dong, "Temperature sensing based on ethanol-filled photonic crystal fiber modal interferometer", IEEE Sens. J., vol. 12, no. 8, pp. 2593–2597, 2012.

3. S. Silva, E. G. P. Pachon, M. A. R. Franco, J. G. Hayashi, F. X. Malcata, Q. Frazão, P. Jorge, and C. M. B. Cordeiro, "Ultrahigh-sensitivity temperature fiber sensor based on multimode interference", Appl. Optics, vol. 51, no. 16, pp. 3236–3242, 2012.

4. J. Ma, J. Ju, L. Jin, W. Jin, and D. Wang, "Fiber-tip micro-cavity for temperature and transverse load sensing", Opt. Express, vol. 19, no. 13, pp. 12418–12426, 2011.

5. X. Zeng, Y. Wu, C. Hou, J. Bai, and G. Yang, "A temperature sensor based on optical microfiber knot resonator", Opt. Commun., vol. 282, no. 18, pp. 3817–3819, 2009.

6. Y. Wu, L. Jia, T. Zhang, Y. Rao, and Y. Gong, "Microscopic multi-point temperature sensing based on microfiber double-knot resonators", Opt. Commun., vol. 285, no. 8, pp. 2218–2222, 2012.

7. G. Y. Chen, T. Lee, Y. Jung, M. Belal, G. Brambilla, N. G. R. Broderick, and T. P. Newson, CLEO/Europe, CH2_2, 2011.

8. H. Yu, S. Wang, J. Fu, M. Qiu, Y. Li, F. Gu, and L. Tong, "Modeling bending losses of optical nanofibers or nanowires', Appl. Optics, vol. 48, no. 22, pp. 4365–4369, 2009.

9. B. Culshaw, "The optical fibre Sagnac interferometer: an overview of its principles and applications", Meas. Sci. Technol., vol. 17, no. 1, pp. R1–R16, 2006.

10. T. G. Giallorenzi, J. A. Bucaro, A. Dandridge, G. H. Sigel Jr., J. H. Cole, S. C. Rashleigh, and R. G. Priest, "Optical fiber sensor technology", IEEE J. Quantum Electronics, vol. 18, no. 4, pp. 626–665, 1982.

11. M. K. Szczurowski, T. Martynkien, G. Statkiewicz-Barabach, W. Urbanczyk, L. Khan, and D. J. Webb, "Measurements of stress-optic coefficient in polymer optical fibers", Opt. Lett., vol. 35, no. 12, pp. 2013–2015, 2010.

12. G. Brambilla, "Optical fibre nanowires and microwires: a review", J. Opt., vol. 12, no. 4, pp. 043001–043020, 2010.

13. Y. Jung, G. Brambilla, and D. J. Richardson, "Efficient higher-order mode filtering in multimode optical fiber based on an optical microwire", AOE, SuB4, 2008.

14. P. J. Raea and D. M. Dattelbaum, "The properties of poly(tetrafluoroethylene) (PTFE) in compression", Polymer vol. 45 , no. 22, pp. 7615–7625, 2004.

15. "Teflon AF Properties", http://www2.dupont.com/Teflon_Industrial/en_US/products /product_by_name/teflon_af/properties.html, accessed on 18/04/2012.

16. "PTFE datasheet", http://www.bearingworks.com/content_files/pdf/retainers /PTFE%20datasheet.pdf, accessed on 18/04/2012.

17. "Fused silica material properties", http://accuratus.com/fused.html, accessed on 10/01/2012.

18. Efiron technical datasheet on PC-373 (AP), version 23/10/2006.

19. P. Childsa, A. C. L. Wong, N. Gowripalan, and G. D. Peng, "Measurement of the coefficient of thermal expansion of ultra-high strength cementitious composites using fibre optic sensors", Cement Concrete Res., vol. 37, no. 5, pp. 789–795, 2007.

20. X. Zeng, Y. Wu, C. Hou, J. Bai, and G. Yang, "A temperature sensor based on optical microfiber knot resonator", Opt. Commun., vol. 282, no. 18, pp. 3817–3819, 2009.

21. Y. Wu, Y. Rao, Y. Chen, and Y. Gong, "Miniature fiber-optic temperature sensors based on silica/polymer microfiber knot resonators", Opt. Express, vol. 17, no. 20, pp. 18142–18147, 2009.

Chapter 4

4. Current sensing with optical microfiber

This chapter focuses on the core subject of this thesis, namely current sensing using OMs. Firstly, a range of polarization rotation detection schemes are compared to identify their merits and demerits. Lessons learnt from this critical analysis are used to select, combine and develop the most promising schemes to be exploited. To begin with, the compactness and gigahertz detection bandwidth capability of OM-based current sensors are introduced. This is followed by a short study on the possible materials for improving the performance of the sensor head. Next, the resonance ability of the sensor head is demonstrated both theoretically and experimentally for responsivity enhancement. To solve the stability issues of the resonator, techniques based on RI chirping (passive) and piezo-electric tuning (active) are discussed. To further refine the sensor head, the problem of birefringence is considered by first critically appreciating the previous contributions relating to eliminating bend- and packaging-induced birefringence, before presenting a solution in the form of SOM. The fabrication details and characterization results are followed by current sensing trials. Moreover, the means to achieve efficient Faraday rotation in both birefringent and non-birefringent MLRs is theoretically analyzed. Lastly, a novel post-fabrication technique is proposed as an alternative to SOM for countering the birefringence-induced reduction in the responsivity of MC-based current sensors.

4.1 Faraday Effect

4.1.1 Introduction

In the previous chapter, thermal effects were analyzed for indirect current sensing. A more established sensing mechanism for fiber-optic current sensors is the Faraday Effect. The Faraday Effect in glass is a well-understood phenomenon that has been intensively studied. It is present in all materials due to the magnetic behavior of the component ions. The magnitude of the Faraday Effect varies with temperature in paramagnetic and ferromagnetic materials, and it is less temperature-dependent in diamagnetic materials [1]. Its magnitude also has an inverse relationship with the wavelength of incident light. As shown in Figure 32, the Faraday Effect is observed

as a circular birefringence, which arises when an external magnetic field is applied through a medium that influences the motion of particles charged by electromagnetic wave propagation and induces a RI difference between left- and right-circularly polarized light. Since a linear polarization can be viewed as a superposition of left- and right-circular polarizations, the ensuing difference in light velocity produces a differential phase change between the circular polarizations that translates to a rotation of the linear polarization by an azimuthal angle linearly proportional to the magnetic field and the distance the light has traveled. Finally, the Faraday rotation is translated to an optical power modulation that provides a measure of magnetic field/current by the detection system. This effect is different from intrinsic circular birefringence, optical chirality or activity due to the direction of its rotation being dependent only on the direction of the magnetic field axial to the path of light propagation and not on the direction of light itself. The reported response time of the Faraday Effect lies between 10^{-9} and 10^{-12} [2]. Faraday active materials are used in high-end applications such as current/magnetic field sensors [3], magneto-optic modulators and switches, and optical isolators.

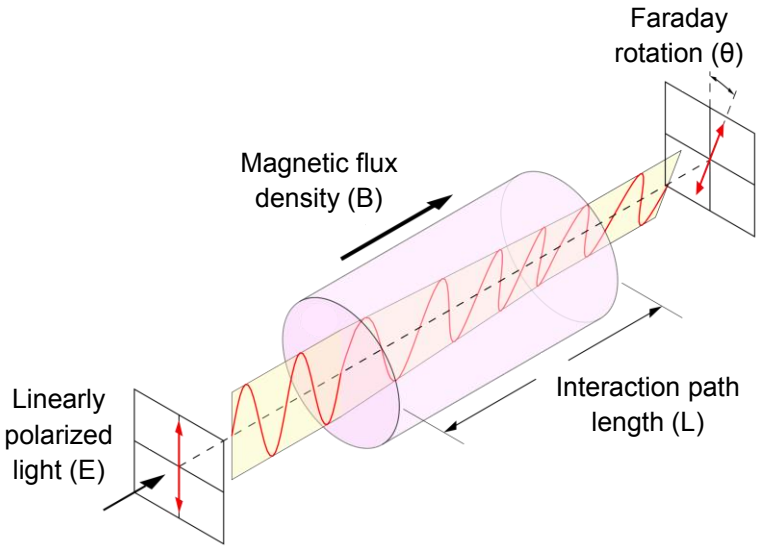

Figure 32. Schematic diagram of the Faraday Effect.

At a more fundamental level, non-reciprocal Faraday rotation can be implicitly inferred from the time-reversal asymmetry of Maxwell's equations:

$$\nabla \times E = -\frac{\partial B}{\partial t} \tag{4.1}$$

$$\nabla \times H = \frac{\partial D}{\partial t} + J \tag{4.2}$$

$$\nabla \cdot D = \rho \tag{4.3}$$

$$\nabla \cdot B = 0 \tag{4.4}$$

Under time reversal, (t) is replaced with ($-t$). This causes the polarity of the current (J) to flip over, while the charge density (ρ) is time-invariant. It is evident that the magnetic field (H) is sign-reversed, whereas the electric field (E) is invariant under time reversal. Since the direction of light is also reversed with a phase change of π from a reflection, Faraday rotation is not susceptible to self-cancellation.

Under the Faraday Effect, the total rotation of the polarization azimuth is defined as:

$$\theta = V \cdot \int_0^L B(l) \cdot \mathrm{d}l \tag{4.5}$$

where V is a temperature- and wavelength-dependent material parameter known as the Verdet constant, B is the axial magnetic flux density, and dl is the infinitesimal distance along the fiber length (L) exposed to the magnetic field.

An empirical expression for the Verdet constant was derived by H. Becquerl in 1897. Although it is widely regarded as too simple, a constant C can be introduced to bury the implications:

$$V = -\frac{\mathrm{d}n}{\mathrm{d}\lambda} \cdot \frac{\lambda}{2c^2} \cdot C \cdot \frac{e}{m_e} \tag{4.6}$$

where n is the RI of the material, λ is the wavelength of light, c is the speed of light in free-space, $-e$ and m_e are the charge and mass of the free electron.

The Faraday rotation experienced by light in an OM could be different from that in a standard optical fiber. For SMF-28, the Verdet constant can be assumed to be approximately uniform from the core to the cladding due to the weak doping profile. In OMs, the solid core and external cladding could have different magnetic flux densities and Verdet constants since they are made of different materials. The effective Faraday rotation can be expressed as a weighted sum of the core and cladding contributions when operating in the linear regime [4]:

$$\theta_{eff} = \theta_{core} \cdot (1 - \eta_{EF}) + \theta_{clad}\eta_{EF} \tag{4.7}$$

where θ_{core} and θ_{clad} are the Faraday rotations in the core and cladding respectively, and η_{EF} represents the fraction of power contained in evanescent field in the cladding.

To lay the foundation for the forthcoming experiments, the following section shows how the magneto-optic properties of a 2 μm diameter silica OM embedded in polymer (Efiron PC-373 AP) can lead to the approximation of the composite structure (~73% power in core from section 2.3.3) as an all-silica material.

Ampere's law can be applied to describe the current-induced magnetic field experienced by an OM enclosed by a solenoid. The guided mode interacts with an axial magnetic field density which can be expressed in terms of the magnetic permeability of free-space ($\mu_0 = 4\pi\times10^{-7}$ H/m), the relative permeability of the OM (μ_r), the number of copper wire turns (N) in the solenoid, the current flow (I), and L:

$$B = \frac{\mu_0 \mu_r NI}{L} \tag{4.8}$$

The Faraday rotation is therefore:

$$\theta \approx VBL = \mu_0 \mu_r NVI \tag{4.9}$$

Rearranging Equation 4.7 in terms of $\mu_r V$ gives:

$$\mu_r V \approx \frac{\theta}{\mu_0 NI} \tag{4.10}$$

To experimentally determine the value of this product, Figure 33 shows a 10 mm length, 2 μm diameter OM polymer-embedded in a straight line to avoid creating birefringence. The sample was placed inside a solenoid of 20 turns (insulated copper wires of 0.5 mm diameter) with 5 A of pulsed current. Outside the solenoid, the OM was bent away from the lines of magnetic flux parallel to the straight OM in order to cut off unwanted Faraday rotation. The Faraday Effect was measured using a detection system described in section 4.3.4, with $\theta = \sin^{-1}(\Delta P/P)/4$. The total received power and signal peak power at the balanced detector (BD) were 2000.5 μW and 541.5 nW respectively, yielding $\mu_r V_{eff} = 0.539$ rad/T.m using Equation 4.10. This value approaches that of silica at a wavelength of $\lambda = 1550$ nm (0.54 rad/T.m [5] at room temperature). Therefore, silica is a reasonably good approximation of a 2 μm diameter OM embedded in polymer when computing its Verdet constant.

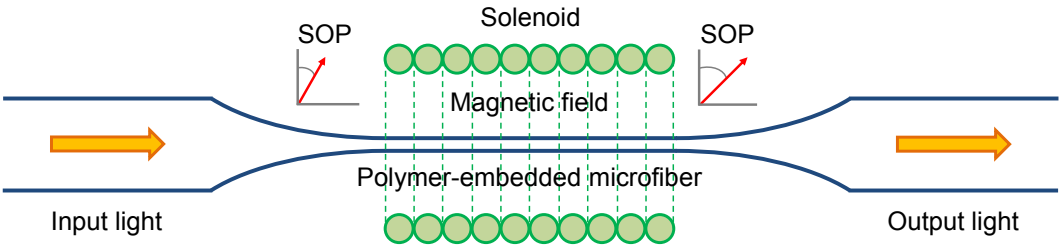

Figure 33. Schematic of the microfiber interrogated by a solenoid to determine the value of $\mu_r V_{eff}$. The curved sections of microfiber outside the solenoid are not drawn.

In the following sections, well-known fiber-optic polarimeters are presented with comments on their unique qualities, followed by an outline of the birefringence problem and noise sources, and ending with a review of novel materials.

4.1.2 Fiber-optic polarization rotation detection schemes

The measurand sensitivity (S_M) is related to the phase/rotation sensitivity (S_P) of the detection system and the responsivity (R) of the sensor. S_P is a function of the noise amplitude voltage (V_n), the signal amplitude voltage (V_s), and the fringe amplitude voltage (V_f). For small signals in a two-path interferometric/polarimetric system operating in the linear regime, it is more intuitive to express S_M as the measurand (M) divided by the signal-to-noise ratio (SNR):

$$S_M = \frac{S_P}{R} \approx \frac{\frac{V_n}{2V_f}}{\left(\frac{V_s}{2V_f}\right)/M} = \frac{M}{\text{SNR}} \tag{4.11}$$

4.1.2.1 Basic polarimeter

The arrangement of the basic detection scheme is illustrated in Figure 34, where the angle offset between the transmission axes of the polarizer and analyzer is aligned at 45° by a polarization controller (PC). Any AC-induced Faraday rotation then translates to a modulation of the output power, given by:

$$P = \frac{P_0}{2} \cdot (1 + \sin 2\theta) \tag{4.12}$$

where P_0 is the input power of light.

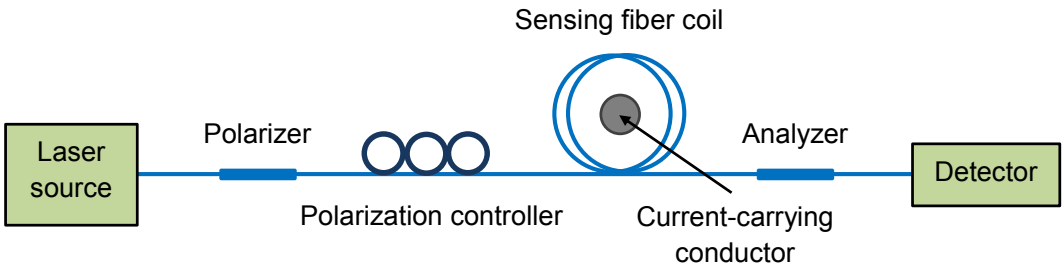

Figure 34. Setup of the basic polarimeter.

In order to eliminate the dependency on the output power of the laser source, the AC component of Equation 4.12 must be normalized by the DC component in real-time to obtain:

$$T = \sin 2\theta \tag{4.13}$$

The basic polarimeter would require calibration when the sensing fiber coil contains non-negligible linear birefringence. The polarized light propagates along both axes of the birefringent fiber due to a possible interface angle-offset and Faraday rotation. Unless the transmission axes of the polarizer is aligned at 45° to that of the birefringent fiber axes such that one of the fiber axes is aligned with that of the analyzer, the two beams with different phase delays may produce unwanted interference effects at the analyzer.

4.1.2.2 Sagnac polarimeter

The advantage of using circularly polarized light rather than linearly polarized light is the higher resistance to bend-induced linear birefringence, though there is a higher susceptibility to twist-induced circular birefringence. Another drawback is the extra optical components required to perform the SOP conversions. Figure 35 shows a Sagnac interferometer configured for the Faraday Effect.

Initially, the linearly polarized light is split into two beams along the polarization-maintaining fibers (PMF) and subsequently converted to left- and right-circularly polarized light using a pair of quarter-wave retarders. The magnetic field of the current induces a Faraday rotation, or equivalently a non-reciprocal differential phase change between the two counter-propagating beams in the optical fiber coil:

$$\Delta\varphi = 2\theta \tag{4.14}$$

This is not to be confused with the references to differential phase from sections 4.2 onwards that are associated with linear polarizations. Upon exiting the optical coil, the circular polarizations are converted back to orthogonal linear polarizations. Finally, the two beams combine in the PMF to produce an optical power modulation at the polarizer:

$$P = \frac{P_0}{2} \cdot (1 + \cos \Delta\varphi) \tag{4.15}$$

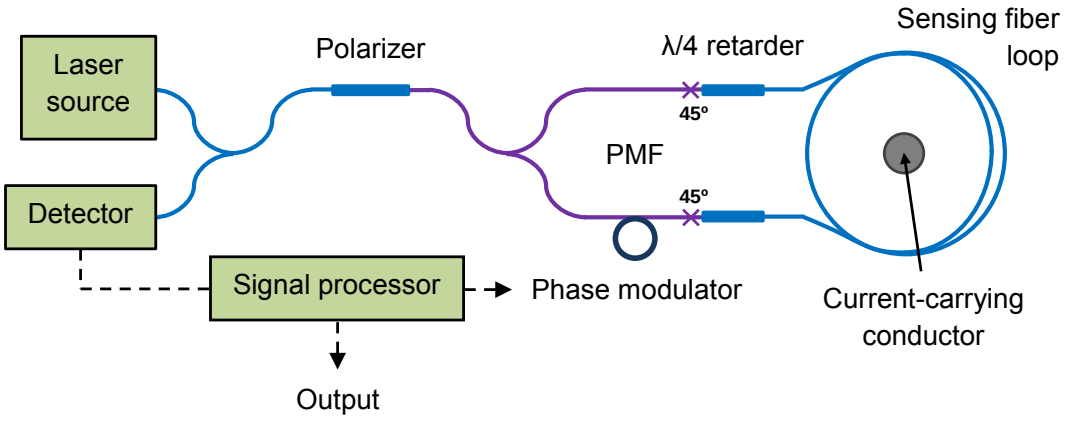

Figure 35. Setup of the Sagnac interferometer.

4.1.2.3 In-line reflection polarimeter

In the in-line configuration shown in Figure 36, a fiber polarizer is set at 45° with respect to the axes of the PMF. As a result, orthogonal linear polarizations along the two axes co-propagate towards the optical fiber coil. Prior to entering the optical fiber coil, the linear polarizations are converted into left- and right-circular polarizations by a quarter-wave retarder. At the end of the optical fiber coil, light is reflected by a Faraday rotator mirror (FRM) and passes through the optical fiber coil a second time. The quarter-wave retarder converts the returning circular polarizations back to orthogonal linear polarizations, which are also interchanged. Finally, the two beams combine in the PMF to produce an optical power modulation at the polarizer. As a result of the polarization swapping, the overall cumulated optical path imbalance of the interfering light is zero. This makes the configuration highly immune to external perturbations, as reciprocal phase noise and polarization-dependent loss (PDL) tend to cancel themselves. Due to the double pass through the optical fiber coil, the current-induced non-reciprocal differential phase change is twice as large as that of the Sagnac configuration:

$$\Delta\varphi = 4\theta \tag{4.16}$$

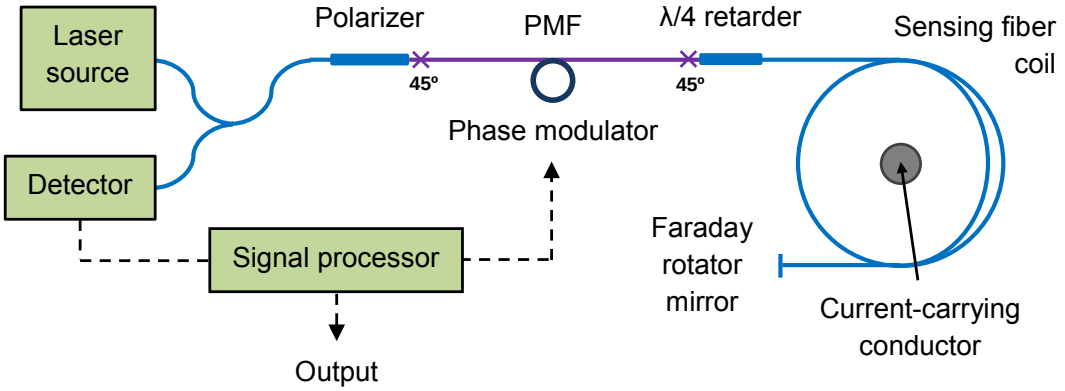

Figure 36. Setup of the in-line reflection polarimeter.

4.1.2.4 Polarization diversity polarimeter

The polarization diversity polarimeter shown in Figure 37 is a commonly used method for measuring current that operates using a balanced detection scheme in which the linearly polarized light from the optical fiber coil output is divided into two orthogonal linear polarizations through a polarization beam splitter (PBS). The power of the two beams are detected separately and subtracted from each other before normalization, to remove common-mode intensity noise from the laser source. To operate at a quadrature point, polarized light can be launched equally into both axes or just into a single axis of the PMF followed by a PMF-PMF splice with 45° offset. The axes of the PMF are aligned with the birefringent fiber axes (if any) of the optical fiber coil and PBS. The output signal can be expressed in terms of the Faraday rotation (section 4.3.4):

$$T = \frac{P_x - P_y}{P_x + P_y} = \sin 2\theta \tag{4.17}$$

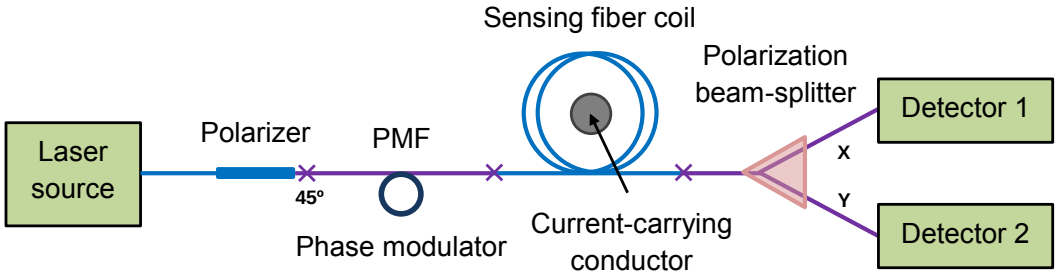

Figure 37. Setup of the polarization diversity polarimeter.

4.1.3 Birefringence

Linear birefringence of the optical fiber caused by bend and packaging is a problem that has plagued current sensors utilizing the Faraday Effect. It causes a reduction in the measured Faraday rotation due to the non-zero differential phase between the eigenmodes of the birefringent fiber. A full description and the numerous solutions to overcome this problem will be described in section 4.5. Unlike linear birefringence, circular birefringence caused by twisting is considered less harmful as it only rotates the SOP by a fixed angle and its reciprocity means it can be undone using a FRM.

4.1.4 Noise sources

The performance of interferometry/polarimetric-based current sensors is limited by noise sources associated with the laser source and the electronics detection system. A breakdown of the noise contributions will be given in section 5.1.5.

4.1.5 High Verdet constant materials

To-date, most fiber-optic current sensors have used silica fiber because of its low loss. However, the Faraday Effect in silica is comparatively weak. This limits the current responsivity, particularly when using a short fiber length so as to reduce the optical transit time and thus obtain a high detection bandwidth. In order to attain a high responsivity, the optical fiber coil requires a large number of fiber turns which will further increase the bend-induced linear birefringence. Compound glasses can have considerably higher Verdet constants but the trade-off is the higher loss which restricts the maximum OPL. Table 8 shows some alternative materials to silica that exhibit high Verdet constants:

Name	Verdet constant	Refractive index	Attenuation	Reference
Fused silica	0.54 rad/T.m @ 1523 nm	1.44 @ 1550 nm	5.0×10^{-6} dB/cm @ 1–1.5 um	[5]
65-wt%-terbium doped silicate	32.1 rad/T.m @ 1053 nm	–	0.024 dB/cm @ 1310 nm	[6]

Yttrium iron garnet ($Y_3Fe_5O_{12}$)	380 rad/T.m @ 780 nm	2.15 @ 1550 nm	6.6 dB/cm @ 780 nm	[7]
Chalcogenide $Ge_{33}As_{12}Se_{55}$	14.1 rad/T.m @ 1550 nm	2.67 @ 1550 nm	0.27 dB/cm @ 1550 nm	[8]
Kigre M18	22.4 rad/T.m @ 1064 nm	1.67 @ 1064 nm	0.022 dB/cm @ 1064 nm	[9]
Schott SF59	3.3×10^{-5} rad/A @ 633 nm	1.94 @ 633 nm	4.665×10^{-2} dB/cm @ 633 nm	[10]
Schott F7	1.1×10^{-5} rad/A @ 633 nm	1.62 @ 633 nm	4.7×10^{-3} dB/cm @ 633 nm	[10]
MolTech MOS10	26.0 rad/T.m @ 1060 nm	1.74 @ 587.5 nm	4.34×10^{-3} dB/cm @ 1060 nm	[11]
XOAT MR4	37.2 rad/T.m @ 1064 nm	1.75 @ 656.3 nm	8.7×10^{-3} dB/cm @ 1064 nm	[12]
Toplent TG-20	21.8 rad/T.m @ 1064 nm	1.69 @ 1064 nm	–	[13]

Table 8. Verdet constants, refractive indices and attenuation for a selection of glasses.

Apart from the higher intrinsic loss, system integration with other fiberized components is another issue that can arise when using non-silica OMs. One method is to splice the pigtails of a non-silica OM to standard optical fibers. However, this usually leads to a strong back-reflection due to the large RI difference. In addition, the splice loss will be much higher than usual due to the different melting temperature of the two materials.

A more effective approach to strengthen the Faraday Effect is to coat silica OMs with high Verdet constant polymers. Smaller diameter OMs produce a larger fraction of power propagating in the evanescent field that that is influenced by the polymer cladding. This approach maintains the standard optical fiber pigtails for easy system integration while providing an enhancement to the Faraday rotation. The only

potential drawback is the loss of such polymers at the wavelength of the input light. Table 9 shows some polymers that feature high Verdet constants:

Name	Verdet constant	Refractive index	Attenuation	Reference
π-conjugated Poly(arylene ethynylene)	4363.3 rad/T.m @ 632.8 nm	–	–	[14]
π-conjugated Poly(3-dodecyl) thiophene	148.4 rad/T.m @ 1550 nm	–	–	[15]
Cobalt nanoparticle doped polymethyl-methacrylate	253 rad/T.m per wt % cobalt @ 532 nm	–	26.5 dB/cm	[16]

Table 9. Verdet constants, refractive indices and attenuation for a selection of polymers.

4.2 High detection bandwidth microfiber coil current sensors

The first demonstrations of MC-based current sensors operating with the Faraday Effect are introduced in this section. These compact sensors have the potential to reach gigahertz detection bandwidth with bend radii of the order of millimeters, though only 40 MHz was demonstrated due to the available current source. Although the reported results are promising, issues such as performance reliability and responsivity scalability need to be addressed. This work serves as the starting point for the forthcoming experiments to advance and optimize OM technology for the application of current sensing. However, the optical behavior that sets an upper limit on the detection bandwidth is often overlooked. The underlying mechanisms are explored in this section to raise awareness about their impact on the measurement results. These findings show that the Faraday Effect cancellation and pulse broadening grow with increasing signal frequency, which result in suppression and distortion of the optical response. A correction factor is proposed for alternating and pulsed signals when using the simplified equation, to maintain an accurate measure of the peak current.

4.2.1 Introduction

Current sensors are widely used to detect transient electrical faults, monitor partial discharges on DC lines, and protect high power equipment and components. Fiber-optic current sensors that exploit the Faraday Effect [17, 18] have attracted a great deal of interest due to their wide dynamic range, robustness and remote sensing capability. However, the optical behavior that limits the detection bandwidth has been largely overlooked. The underlying mechanisms are explored in this section to raise awareness about their impact on the measurement results.

Traditional fiber-optic current sensors are usually quite bulky [19, 20] because of the large bend radius required to maintain sufficiently low loss. Moreover, the relatively low Verdet constant of silica necessitates a large number of fiber turns to produce a measurable Faraday rotation. The first experiment on OM-based current sensing using the Faraday Effect was undertaken by Belal *et al* [21]. The bend insensitivity of OMs had been utilized to down-scale the size of the optical fiber coil. As a result, a 0.5 mm diameter copper wire tightly coiled with 25 turns of OM only required an

OM length of ~4 cm. The short OPL minimized the transit time of light through the MC. Consequently, it allowed for the interrogation of very high frequency currents, potentially of the order of gigahertz. This was something never before possible with standard optical fibers. Although other sensing mechanisms such as thermal effects were recently demonstrated with MKRs and MLRs [22–24], they are generally unstable and lacked the dynamic range, detection bandwidth and response time achievable with the Faraday Effect.

4.2.2 Theory

The sensor head shown in Figure 38 consisted of an OM coiled around a current-carrying wire rather than a conducting wire wound around an OM. Apart from being more viable in real measurement environments, this arrangement also minimizes the load impedance and heating effects in the current-carrying wire. The rotation of the polarization azimuth is linearly proportional to the current-induced magnetic field and the distance the light has traveled. The Faraday rotation is then translated into an optical power modulation, and thus provides a measure of the current.

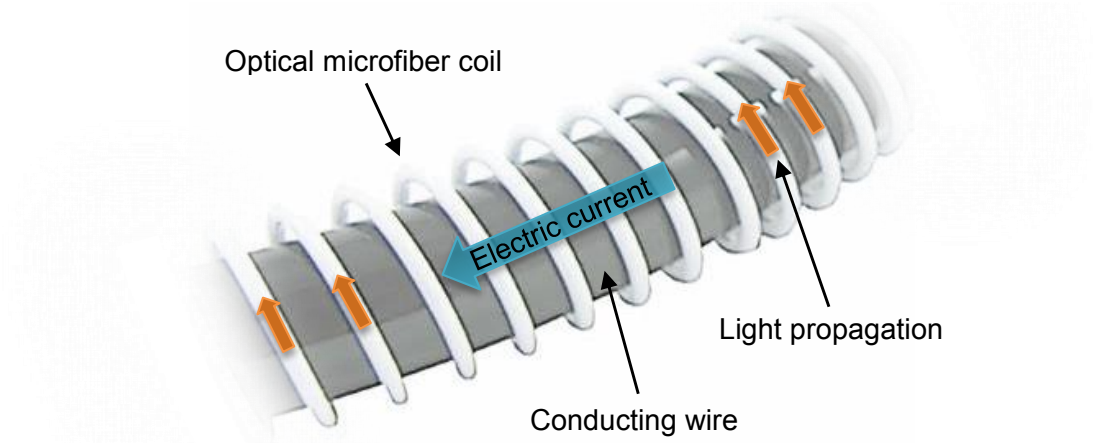

Figure 38. Schematic diagram of the microfiber coil sensor head.

Either Ampere's law or Biot-Savart's law can be applied to describe the current-induced magnetic field experienced by a MC wound around an electrical wire. The guided mode interacts with an axial magnetic field flux density which can be expressed in terms of the magnetic permeability of free-space (μ_0), the relative permeability of the OM (μ_r), the current flow (I), and the MC radius (r):

$$B(l) = \frac{\mu_0 \mu_r I(l)}{2\pi r} \tag{4.18}$$

The total Faraday rotation for N turns of OM is therefore:

$$\theta = V \cdot \int_0^L B(l) \cdot \mathrm{d}l = \frac{\mu_0 \mu_r V}{2\pi r} \cdot \int_0^{2\pi r N} I(l) \cdot \mathrm{d}l \tag{4.19}$$

where V is the effective Verdet constant of the OM, dl is the infinitesimal distance along the fiber length (L) exposed to the magnetic field, and θ can also be expressed in terms of the Faraday rotation per unit length ($\tau = VB$).

For the same peak current, the Faraday rotation of sinusoidal AC signals or pulsed current signals is less or equal to that of the DC equivalent:

$$\theta_{DC} = \mu_0 \mu_r N V I_{DC} \tag{4.20}$$

For the purpose of analyzing the optical behavior that sets an upper limit on the detection bandwidth (B_w), an infinite electrical bandwidth of the current signal is assumed. For OMs, it is reasonable to assume that the MC width is far smaller than its diameter such that the current-induced magnetic field interacts with the entire OPL equally and simultaneously.

For a single-pass configuration measuring sinusoidal AC signals, the total Faraday rotation is proportional to the integrated magnetic field along the length of the electrical wire within the optical fiber coil. By integrating a sinusoidal signal with respect to time for a fixed time interval and dividing by the integral of a DC signal with the same peak current, the normalized frequency response can be shown to resemble a rectified sinc function. At integer multiples of a cycle period, the net rotation is always zero due to the total cancellation of the opposite signs of Faraday rotation. B_w is nominally taken near the –3 dB level of response, where it is equal to a frequency at which its half-cycle period is equal to the integration interval. For standard optical fibers, Figure 39 shows that the integration interval is the difference in transit time (ΔT) between light through the optical fiber coil (ΔT_{coil}) and the magnetic field signal along the electrical wire (ΔT_{wire}). For OMs, ΔT approximates to ΔT_{coil}. The resulting expression for B_w is a function of the effective index seen by the guided mode (n_{eff}), the length of the uncoiled optical fiber (L_{fiber}), the speed of light in free-space (c), the length of the enclosed wire (L_{wire}), and the propagation speed of the electrical signal (c'):

$$B_w = \frac{1}{2\times(\Delta T_{coil} - \Delta T_{wire})} = \frac{1}{2\times\left(\frac{n_{eff}L_{fiber}}{c} - \frac{L_{wire}}{c'}\right)} \tag{4.21}$$

In the extreme case, B_w increases to infinity when the fiber coil pitch becomes infinitely wide and L_{fiber} approximates L_{wire}. As a result, ΔT reduces to zero and each portion of light is able to sample a unique part of the magnetic field signal. Hence, the optical response can keep up no matter how fast the current signal is changing. However, the current responsivity will be reduced to zero due to the negligible magnetic field component axial to the optical fiber.

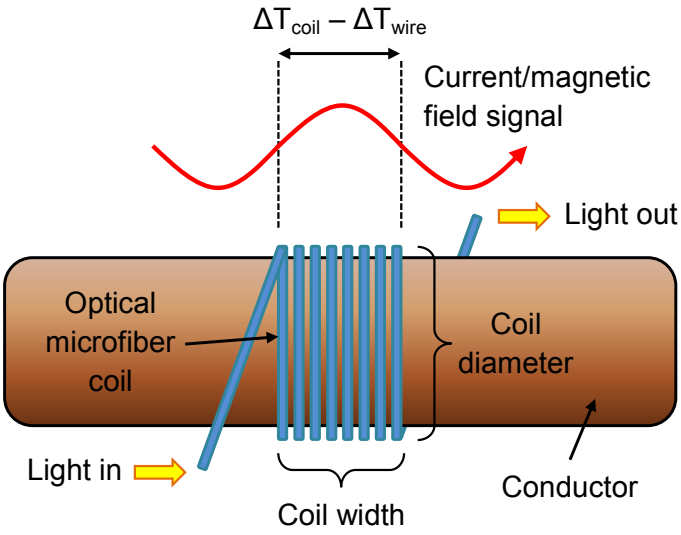

Figure 39. Schematic diagram of the time-varying current-induced magnetic field imposed on light propagating through the microfiber coil.

For a single-pass configuration measuring pulsed current signals, Figure 40 reveals that the integration interval of the magnetic field signal causes a proportional broadening of the pulse shape. B_w is nominally derived in anticipation of a 3 dB factor of broadening, where the current pulse duration is equal to the integration interval. For standard optical fibers, the integration interval is again the difference in transit time between ΔT_{coil} and ΔT_{wire}. For OMs, ΔT approximates to ΔT_{coil}. The resulting expression for B_w is a function of the time-bandwidth product (TBP) associated with the pulse shape [25]. The expression is similar to Equation 4.21:

$$B_w = \frac{\text{TBP}}{\Delta T_{coil} - \Delta T_{wire}} = (\text{TBP}) \cdot \frac{1}{\frac{n_{eff}L_{fiber}}{c} - \frac{L_{wire}}{c'}} \tag{4.22}$$

where TBP ≈ 0.44 for Gaussian-shaped pulses.

For a double-pass configuration, the B_w calculation is more complicated. The fiber length between the sensor head and the mirror must be extremely short or precisely tuned such that each portion of light re-entering the MC is modulated in the exact same way by the magnetic field signal. Otherwise, the optical response to AC signals will distort the waveform or even lead to a total cancellation. Pulsed current signals on the other hand will be distorted or see a manifestation of a second pulse. The response time of the sensor is defined as the transit time of light from the output of the MC to the photoreceiver. Due to the conflicting requirement of the OPL, a trade-off exists between the responsivity and response time or B_w.

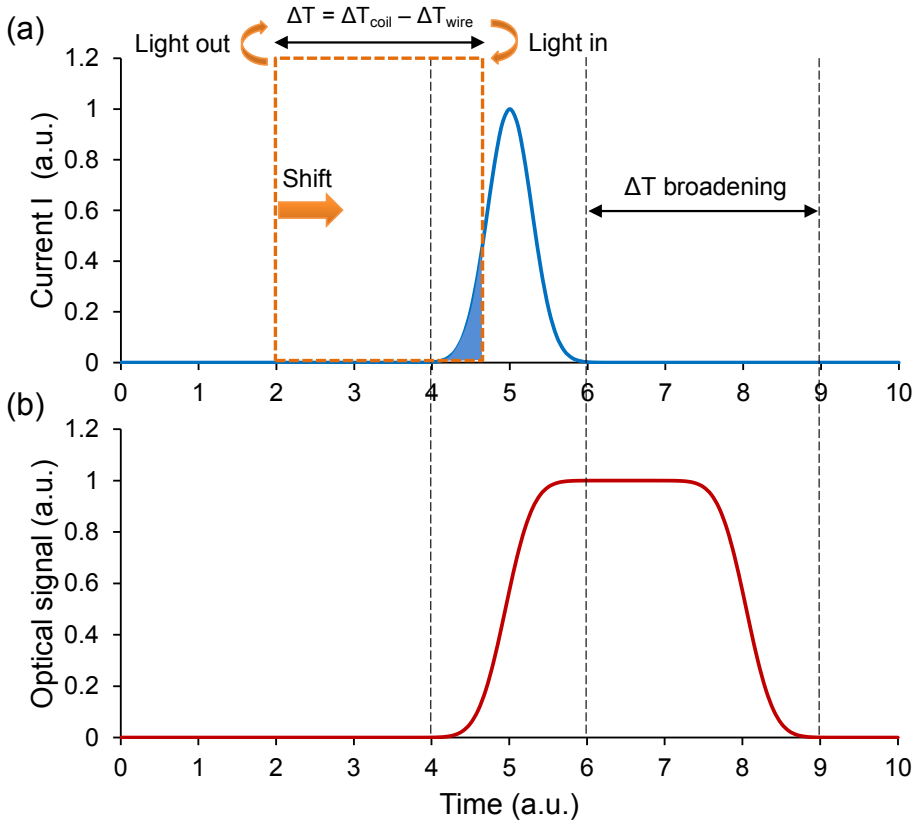

Figure 40. Simulated broadening of the (a) current pulse shape, as seen in the (b) optical response, by an amount equal to the difference in transit time.

Although the inverse transfer function of Equation 4.19 can be used to derive the current for any optical signal, Equation 4.20 is preferred due to its simplicity. However, when the current period or pulse duration decreases relative to ΔT, the moving-averaging effect of the integration introduces an increasingly larger difference in the Faraday rotation between AC/pulsed and DC signals of the same peak current. This leads to errors in the measured current. In the case where the

current signal is known in terms of the shape but not the magnitude, a correction factor can be applied to the peak power of the optical signal to yield a more accurate measure of the peak current. The correction consists of a division by the area under a centered current signal within the integration interval, followed by a multiplication of the interval area of matching height. Although not intentional, this technique can also compensate for the Faraday Effect cancellation in AC signals to artificially increase B_w, as long as the uncorrected optical signal is above the noise floor. Changing r but not N does not change the measured peak current for DC signals or any signal under the correction scheme. This is due to the fact that r changes L_{fiber} (i.e. integration interval) and B (i.e. optical signal magnitude) by reciprocal factors, which cancel out in Equation 4.20.

4.2.3 Fabrication

The fabrication of the OM by Belal *et al* was similar to the procedure described in section 3.2.3. The resulting OM of 5 μm diameter and 10 cm length was wrapped 25 times around a 0.5 mm diameter copper wire for current interrogation. A large pitch (>0.5 mm) between each winding prevented mode coupling between the adjacent turns of the MC. To avoid optical leakage, the copper wire was coated with a thin layer of low-RI, UV-curable polymer (Efiron PC-373 AP) before and after coiling. Lastly, the sample was UV-cured on a glass slide to achieve geometrical stability and robust packaging. The optical loss was ~1.5 dB at a wavelength of λ = 1550 nm.

4.2.4 Experimental setup and results

A basic polarimeter was chosen by Belal *et al* to demonstrate the effectiveness of the MC-based sensor. Both AC (kHz) and pulsed currents (MHz) were applied through the milled copper section. A linear current responsivity of 16.8±0.1 μrad/A was demonstrated up to 2 kHz for AC signals, which shows close agreement with the predicted value of 16.9 μrad/A from Equation 4.20. This provided further evidence that the Verdet constant of the polymer cladding is very similar to that of the silica core (~96% power in core from section 2.3.3). Phase and current sensitivities were 1.56×10^{-6} rad and 4 mA/$\sqrt{\text{Hz}}$ respectively, measured with 10,000 running averages. The performance of the MC-based sensor is expected to increase proportionally with the number of OM turns.

4.2.5 Further demonstration

Following the work of Belal *et al*, further tests confirmed the high detection bandwidth capability of the MC based current sensor. Although an OM of 30 mm length (ΔT = 140 ps, $T_R \approx 10$ ns) is theoretically capable of sensing currents in the gigahertz regime (B_w = 2.9 GHz) using Equation 4.22 with TBP = 0.4 and n_{eff} = 1.4, pulse durations of ~10 ns ($B_w \approx 40$ MHz) have been detected using a very similar polarimeter setup to [21], which was limited by the modulation bandwidth of the available current pulse generator. The OM formed 10.5 turns around a copper wire of 1 mm diameter. Figure 41 shows the optical response tracing a current signal with rise/fall times of the order of nanoseconds with negligible temporal broadening.

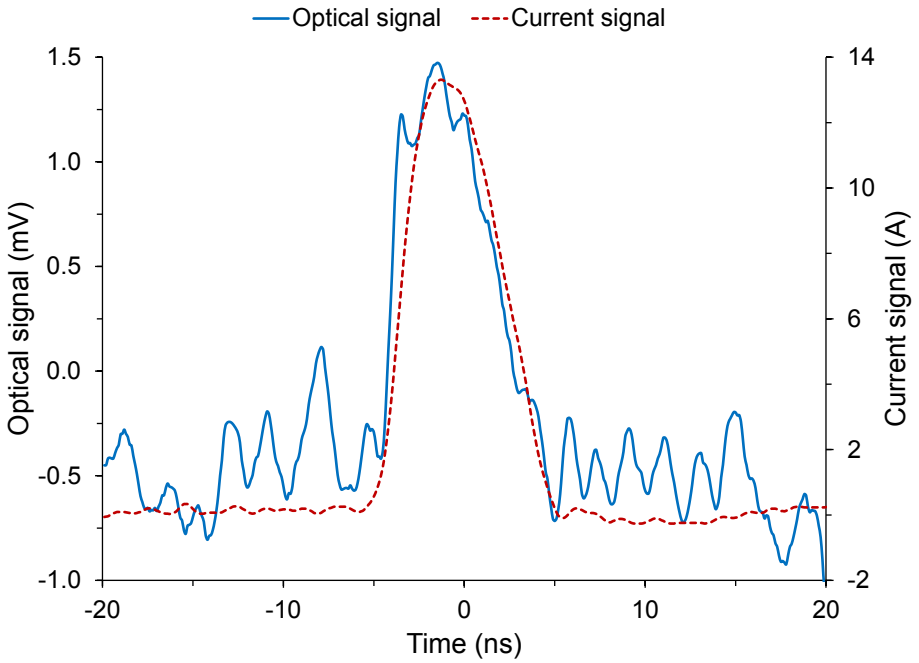

Figure 41. Measured optical signal responding to a fast current pulse (400 data points with 10-point moving-average).

4.2.6 Conclusion

Owing to the non-mechanical nature of the Faraday Effect, it is tempting to assume that fiber-optic current sensors exhibit a constant responsivity with varying signal frequency (i.e. flat frequency response). On the contrary, detrimental effects place an upper bound on the detection bandwidth. It was found that the Faraday Effect cancellation and pulse broadening will grow with increasing signal frequency. As a result, the optical response becomes increasingly suppressed in magnitude and

distorted in shape. A correction factor is proposed for alternating and pulsed signals when using the simplified equation, to maintain an accurate measure of the peak current.

The emergence of MC-based current sensors followed the rise of OM technology. Owing to their short OPL, these compact sensors have the ability to measure fast-changing currents with gigahertz detection bandwidth, which is at least one order of magnitude higher than that of any other fiber-optic current sensor reported to-date. The theoretical detection bandwidth of a 10.5-turn MC of 5 μm diameter OM and 30 mm uncoiled length is 2.9 GHz, but it was only experimentally verified up to 40 MHz due to the limited modulation bandwidth of the available current pulse generator. A current responsivity of 16.8±0.1 μrad/A was demonstrated, showing excellent agreement with the predicted value of 16.9 μrad/A. The resulting current sensitivity was 4 mA/$\sqrt{\text{Hz}}$.

To increase the detection bandwidth, the transit time must be decreased through reducing the length of the uncoiled OM. The response time can be reduced by minimizing the fiber length between the MC and photoreceiver. To increase the responsivity, a larger number of OM turns must be used, with the limiting factor being the maximum length of OM that can be fabricated. Hence, a high detection bandwidth can be achieved at the cost of diminishing the responsivity, and vice versa. The rotation and current sensitivities can be improved by normalizing the AC component of the detected signal by the DC component in real-time to eliminate power fluctuations from the laser source. To reduce the loss, air bubbles must be removed from the polymer packaging. The ultimate compactness of the sensor head is restricted by the diameter of the copper wire to be measured, followed by the minimum bend radius of the OM. It must be pointed out that MCs are not the ideal candidates for measuring large-diameter wires/cables, because the advantages of small dimensions and high detection bandwidth are lost.

4.3 Resonantly enhanced Faraday rotation in microfiber coil resonators

A proof-of-concept experimental demonstration with theoretical modeling is presented in this section for resonantly enhanced Faraday rotation in a MCR-based current sensor. The recirculation of light within the MCR gives rise to cumulative Faraday rotation and thus higher current responsivity. A gain factor of 3.1 was experimentally achieved and supported by simulations. MCRs with higher ERs are predicted to yield larger enhancements. The maximum current responsivity and current sensitivity associated with OM of 2 μm diameter and 10 mm length were 4.4±0.6 μrad/A and 932.7±147.3 mA respectively, with a detection bandwidth capability of 3.5 GHz. This type of current sensor is potentially capable of matching the responsivity of MC-based designs with unrivalled compactness. Furthermore, the balance between responsivity and detection bandwidth can be tailored.

4.3.1 Introduction

MC-based current sensors demonstrated exceptional compactness and high detection bandwidth, but limited current responsivity. To increase the current responsivity, one approach is to employ significantly longer lengths of OM. However, this is not feasible with existing tapering rigs. To solve this problem, the self-coupling ability of MCs to form MCRs is explored in this section. The advantage of MCRs is that they potentially only require a few turns as their responsivity depends more on the proximity from critical coupling and the detuning from resonance than the physical OM length. Resonantly enhanced Faraday rotation can arise due to the larger power transfer of the resonant eigenmode. Furthermore, the balance between responsivity and detection bandwidth can be tuned via the input wavelength. Despite the issue of stability, MCR sensor heads offer unrivalled compactness and higher detection bandwidth compared to the regular-sized fiber coil sensor heads of traditional fiber-optic current sensors.

4.3.2 Theory

Similar to the MC, the MCR consists of an OM in a helical arrangement shown in Figure 42. The difference is the inter-turn coupling due to a smaller coil pitch. At resonant wavelengths, the backward-coupled forward-propagating light interferes

constructively with the forward-propagating light in the previous turn, while the forward-coupled forward-propagating light interferes destructively with the forward-propagating light in the next turn.

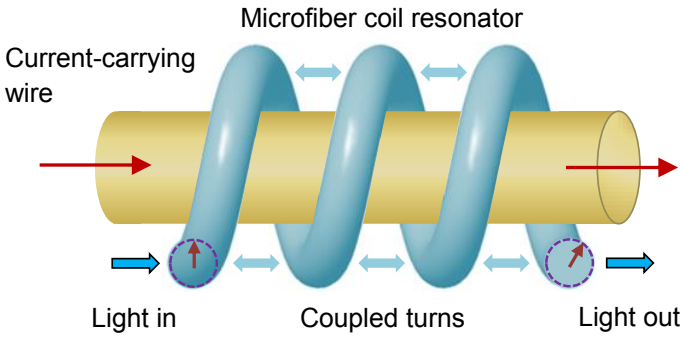

Figure 42. Schematic diagram of the microfiber coil resonator sensor head being interrogated by current. The directions of light propagation and coupling are shown as arrows. The arrows in dashed-circles represent the Faraday rotation.

Before modeling the Faraday Effect in a MCR, the concept of Faraday rotation per unit length (τ) is visualized in Figure 43. The rotation of the polarization azimuth for a small change in the propagation distance (Δz) can be expressed as:

$$\theta = \tau \Delta z \tag{4.23}$$

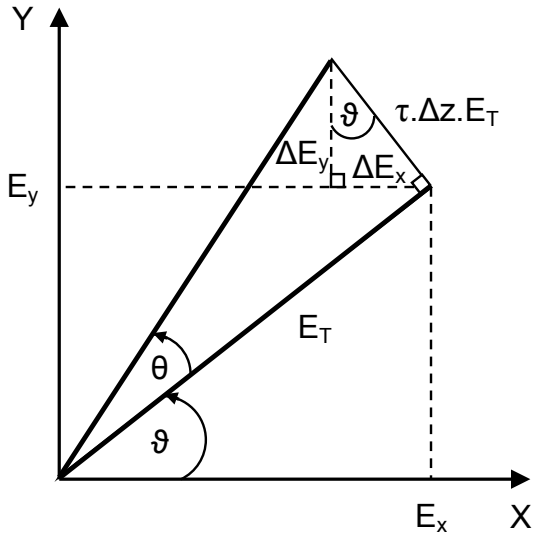

Figure 43. Analysis of E_x and E_y for a small Faraday rotation.

The orthogonal electric field amplitudes E_x and E_y can be written in terms of the combined electric field amplitude E_T in relation to the initial angle ϑ that is determined by the power-splitting ratio between the two axes:

$$E_x = E_T \cos\vartheta \tag{4.24}$$

$$E_y = E_T \sin\vartheta \tag{4.25}$$

The small change in E_x with Δz can be expressed by:

$$\Delta E_x = -\tau \Delta z E_T \sin\vartheta = -\tau \Delta z E_y \tag{4.26}$$

$$\frac{\mathrm{d}E_x}{\mathrm{d}z} = -\tau E_y \tag{4.27}$$

Similarly, the small change in E_y with Δz can be expressed by:

$$\Delta E_y = \tau \Delta z E_T \cos\vartheta = \tau \Delta z E_x \tag{4.28}$$

$$\frac{\mathrm{d}E_y}{\mathrm{d}z} = \tau E_x \tag{4.29}$$

Hence, small changes in the orthogonal electric field amplitudes during Faraday rotation can be governed by the simple differential equations:

$$\frac{\mathrm{d}}{\mathrm{d}z}\begin{pmatrix} E_x \\ E_y \end{pmatrix} = \begin{pmatrix} 0 & -\tau \\ \tau & 0 \end{pmatrix} \cdot \begin{pmatrix} E_x \\ E_y \end{pmatrix} \tag{4.30}$$

The direction of Faraday rotation is clockwise from the launch perspective if the magnetic field is of the same direction as that of the optical propagation.

4.3.3 Fabrication

The sensor was built in two stages. Firstly, the fabrication of the OM was developed based on the procedure described in section 3.2.3. The resulting OM of 2 μm diameter and 10 mm length at the uniform waist had a near-adiabatic taper diameter profile of $\psi = 0.1$ [26] to suppress the excitation of higher-order modes [27].

For the second stage, the MCR shown in Figure 44 was fabricated by coiling the OM 3 times around a copper wire with a pitch of a few micrometers between each winding to permit mode coupling between the adjacent turns. The wire was coated with a thin layer of low-RI, UV-curable polymer (Efiron PC-373 AP) before and after coiling to provide good confinement of light. Geometrical stability and robust packaging was ensured after UV-curing the sample on a glass slide. The optical loss was ~3 dB at a wavelength of λ = 1550 nm, and it was attributed to Rayleigh and Mie scattering due to the presence of micro-bubbles and particles in the polymer.

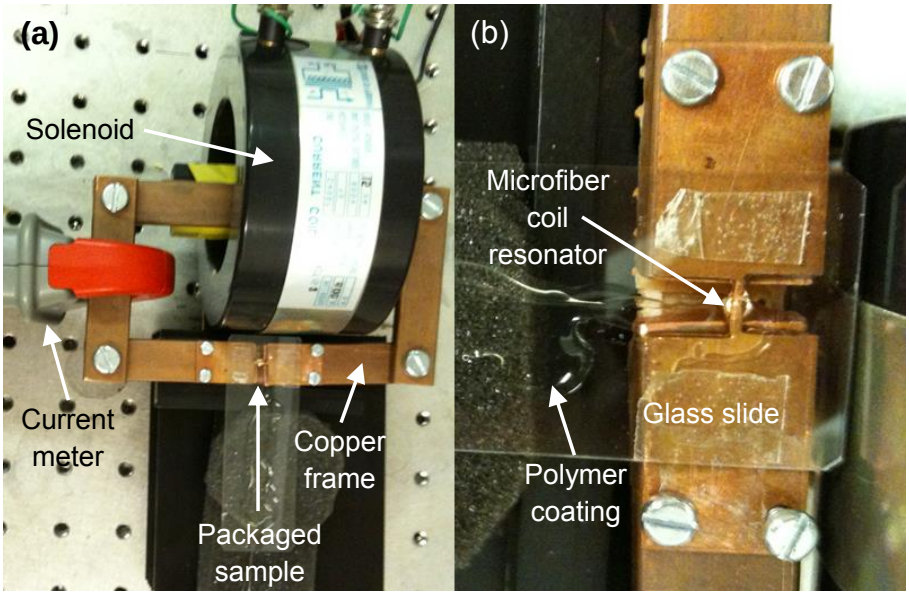

Figure 44. Sensor interrogation using (a) a transformer to generate AC, and (b) a packaged microfiber coil resonator to sense the current via the Faraday Effect.

4.3.4 Experimental setup

The setup shown in Figure 45 was used to test the current sensor. Linearly polarized light from a tunable laser source (TLS) (Agilent 81940A) was launched into PMF. The 45° splice produced two orthogonal beams of equal power, which propagated through a polarization-maintaining circulator (PMC) to the MCR. A PC was used to align the transmission axes of the PMF-SMF interface to that of the birefringent MCR to minimize unwanted interference effects. A signal generator (SG) driving a current transformer (CT) with the copper wire of the sensor forming the secondary circuit induced AC along the wire that translated into a varying magnetic field. A commercial current clamp-meter was used to measure the current as a reference. When no current was applied, the polarized light propagating along each fiber axis was reflected back via the other axis by the FRM. This also provided a means to increase the total Faraday rotation from a second pass through the MCR. Light re-entering the PMF can be seen as an optical power modulation varying with the SOP. With a PBS, the eigenmodes were separated into the two PD ports of a BD (New Focus 2117). The BD amplified the difference between the AC components of the two optical signals. An AC-coupled oscilloscope (Agilent DSO6034) on 25 MHz bandwidth-limited mode captured 1000 data points per measurement with 65536 running averages followed by a 32-point moving median filter.

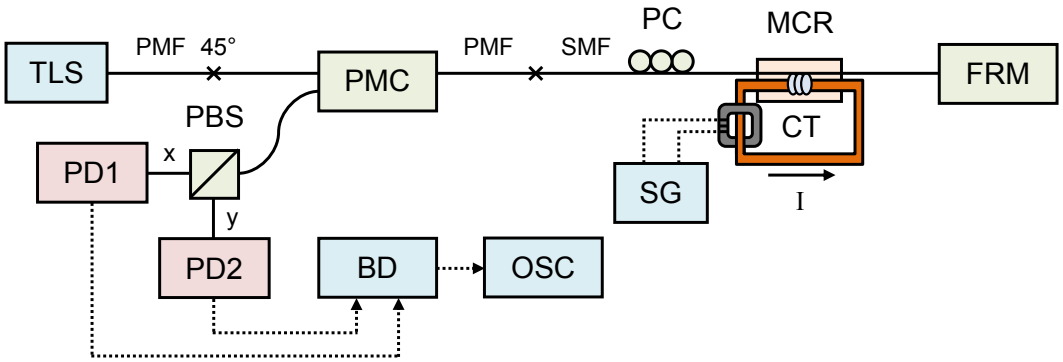

Figure 45. Schematic diagram of the experimental setup. TLS: tunable laser source, PMF: polarization-maintaining fiber, PMC: polarization-maintaining circulator, SMF: single-mode fiber, PC: polarization controller, MCR: microfiber coil resonator, CT: current transformer, SG: signal generator, FRM: Faraday rotator mirror, PBS: polarization beam splitter, PD: photodetector/photoreceiver, BD: balanced detector, OSC: digital oscilloscope.

A dummy optical fiber coil with a sufficiently large bend radius (i.e. negligible birefringence) was used to calibrate the system. The length of PMF between the TLS and the PMF-SMF interface was controlled via the cut-back method such that the sensor head was initialized with a zero differential phase ($\Delta\varphi$) between the two orthogonal axes. This calibration was accomplished by finding the maximum constructive interference when the PMF end was butt-coupled to an in-line polarizer aligned at 45° to its axes. The length of SMF between the MCR and the FRM was also controlled in the same manner such that the double-pass configuration did not distort the optical response due to a timing mismatch of the magnetic field exposure.

For PD_1 and PD_2, the output eigenmode electric field amplitudes (E_{out}) can be derived from the Jones matrices of Faraday rotations and a FRM. Although rotations in a 2-dimensional geometry graph can produce negative signs, these will be rectified after the power conversion. Phase information is implicit so as to avoid sign ambiguity. The FRM is composed of a 45° Faraday rotator ($\vec{F}_0$) and a mirror (M_r), with a second pass through the rotator ($\overleftarrow{F}_0$) to provide a total rotation of 90°:

$$R = \overleftarrow{F}_0 M_r \vec{F}_0$$

$$R = \begin{pmatrix} \cos 45° & -\sin 45° \\ \sin 45° & \cos 45° \end{pmatrix} \cdot \begin{pmatrix} 1 & 0 \\ 0 & 1 \end{pmatrix} \cdot \begin{pmatrix} \cos 45° & -\sin 45° \\ \sin 45° & \cos 45° \end{pmatrix} = \begin{pmatrix} 0 & -1 \\ 1 & 0 \end{pmatrix} \quad (4.31)$$

The current-induced magnetic field signal modulates the Faraday rotation with amplitude θ_0, radial frequency ω and initial phase ϕ:

$$\theta = \theta_0 \sin(\omega t + \phi) \tag{4.32}$$

Now considering a double-pass Faraday rotation ($\vec{F}_1$ and $\overleftarrow{F}_1$) with a FRM:

$$S = \overleftarrow{F}_1 R \vec{F}_1$$

$$S = \begin{pmatrix} \cos\theta & -\sin\theta \\ \sin\theta & \cos\theta \end{pmatrix} \cdot \begin{pmatrix} 0 & -1 \\ 1 & 0 \end{pmatrix} \cdot \begin{pmatrix} \cos\theta & -\sin\theta \\ \sin\theta & \cos\theta \end{pmatrix} = \begin{pmatrix} -\sin 2\theta & -\cos 2\theta \\ \cos 2\theta & -\sin 2\theta \end{pmatrix} \tag{4.33}$$

The Faraday rotation (θ) represents the MCR behavior that will be modeled in the next section. Propagation loss is ignored since it does not influence the output signal. Lastly, E^{out} is presented as a function of the input electric field amplitudes (E^{in}):

$$E^{out} = S \cdot E^{in}$$

$$\begin{pmatrix} E_x^{out} \\ E_y^{out} \end{pmatrix} = \begin{pmatrix} \sin 2\theta & \cos 2\theta \\ \cos 2\theta & -\sin 2\theta \end{pmatrix} \cdot \begin{pmatrix} E_x^{in} \\ E_y^{in} \end{pmatrix} \tag{4.34}$$

The corresponding optical powers (P^{out}) are:

$$\begin{pmatrix} P_x^{out} \\ P_y^{out} \end{pmatrix} = \begin{bmatrix} \sin^2 2\theta \cdot \left(E_x^{in}\right)^2 + \cos^2 2\theta \cdot \left(E_y^{in}\right)^2 + 2\sin 2\theta \cos 2\theta \cdot E_x^{in} E_y^{in} \\ \cos^2 2\theta \cdot \left(E_x^{in}\right)^2 + \sin^2 2\theta \cdot \left(E_y^{in}\right)^2 - 2\sin 2\theta \cos 2\theta \cdot E_x^{in} E_y^{in} \end{bmatrix} \tag{4.35}$$

The signal processing with the BD output is given by:

$$T = \frac{P_x^{out} - P_y^{out}}{P_x^{out} + P_y^{out}} \tag{4.36}$$

The output signal for a 45° splice angle (e.g. $E_x^{in} = E_y^{in} = 1$) is expressed as:

$$T_{45^\circ} = \sin 4\theta = \sin[4\theta_0 \sin(\omega t + \phi)] \tag{4.37}$$

Substituting for θ from Equation 4.32 and expanding in terms of Bessel functions of the first kind:

$$T_{45^\circ} = 2\sum_{n=1,3,..} J_n(4\theta_0) \sin[n(\omega t + \phi)] \tag{4.38}$$

As only the modulation amplitude is of interest, Equation 4.37 can be rewritten in terms of the signal amplitude (ΔP_{pk}) and the measured fringe amplitude (P_{total}):

$$2\theta_0 = \frac{1}{2}\sin^{-1}\left(\frac{\Delta P_{pk}}{P_{total}}\right) \tag{4.39}$$

Similarly, for a 0° splice angle (e.g. $E_x^{in} = 0$, $E_y^{in} = 1$):

$$T_{0^\circ} = \cos 4\theta = \cos[4\theta_0 \sin(\omega t + \phi)] \tag{4.40}$$

Likewise, in terms of Bessel functions of the first kind:

$$T_{0^\circ} = J_0(4\theta_0) + 2\sum_{n=2,4,..} J_n(4\theta_0)\cos[n(\omega t + \phi)] \tag{4.41}$$

Since only the modulation amplitude is of interest, Equation 4.40 can be rewritten in terms of the signal peak-to-peak (ΔP_{pp}) and the measured fringe amplitude:

$$2\theta_0 = \frac{1}{2}\cos^{-1}\left(1 - \frac{\Delta P_{pp}}{P_{total}}\right) \tag{4.42}$$

The double-pass Faraday rotation is given by $2\theta_0$. The output voltage polarity of the detection system depends not only on the direction of current flow, but also on the coiling arrangement of the OM, the electric field orientation of the input light with respect to the PMF axes, the initial $\Delta\varphi$, and the signal processing. Equation 4.38 indicates that a 45° splice produces a signal predominately of the fundamental frequency, and Equation 4.41 shows that a 0° splice results in even harmonics. Equations 4.39 and 4.42 are only valid for rotations under a quarter of a fringe ($2\theta_0 < \pi/2$) and half of a fringe respectively ($2\theta_0 < \pi$), before tracking fringes become necessary. Fringe-tracking techniques were not used as the rotations were sub-fringe.

4.3.5 Simulations

The double-pass MCR was simplified to a single-pass MCR of matching ER. This gives roughly the same number of roundtrips by light since propagation loss is multiplicative, and thus the ER of on-resonance indicates the number of additional roundtrips over that of off-resonance. The single-pass approximation can be justified by the same underlying principles of the FRM to increase the total Faraday rotation: (a) due to the end-reflection, a differential phase change of π reverses the direction of Faraday rotation; (b) at the same time, the direction of the magnetic field relative to the direction of light propagation is also reversed, which cancels the preceding effect; and (c) the FRM rotates the SOP of the returning light by 90°. Although light from the forward and backward propagation occupy the same physical volume in the

MCR, power transfers arising from the Faraday Effect are either between the two orthogonal axes of the backward-propagating light, or between the corresponding axes of the forward- and backward-propagating light. The latter is a closed-loop behavior that has effectively no impact on the eventual power residing in the two orthogonal axes of backward-propagating light. Hence, the combination of these factors enables a continuation of the Faraday rotation when passing through the MCR a second time.

Firstly, the underlying coupled mode equations [28, 29] are modified by incorporating a τ term to account for the Faraday rotation. It is assumed that the propagation constant ($\beta = (2\pi/\lambda).n_{eff}$) remains constant throughout the MCR. The $\Delta\beta$ term models the linear birefringence, n_{eff} is the effective index seen by the guided mode, κ is the coupling coefficient between adjacent turns, α is the loss coefficient, and N is the number of OM turns. It is assumed that the MCR has a shape close to a helix with all turns of equal length, which is reasonable since the copper wire also acted as a cylindrical brace. It is further assumed that the coil pitch is comparable to the OM diameter and the wavelength of light (λ). Finally, the polarization dependency of the coupling factors is neglected, and the geometrical/Berry's phase is ignored due to its reciprocity and static behavior.

For the j^{th} turn between $j = 2$ and N–1, the changes in the electric field amplitude components E_x^j and E_y^j aligned with the orthogonal axes are expressed by:

$$\frac{\mathrm{d}E_x^j(s)}{\mathrm{d}s} = i\kappa \cdot \left(E_x^{j-1}(s) + E_x^{j+1}(s)\right) - \alpha E_x^j(s) - \tau E_y^j(s) \tag{4.43}$$

$$\frac{\mathrm{d}E_y^j(s)}{\mathrm{d}s} = i\kappa \cdot \left(E_y^{j-1}(s) + E_y^{j+1}(s)\right) + i\Delta\beta E_y^j(s) - \alpha E_y^j(s) + \tau E_x^j(s) \tag{4.44}$$

where ds is the infinitesimal curvilinear distance along each turn length (S).

Since the phase velocity differs for the eigenmodes, the SOP will vary between linear and elliptical within the MCR. For the first and last turn, Equations 4.43 and 4.44 are modified such that light only couples to the second and penultimate turn respectively. The boundary conditions imposed by field continuity are defined as:

$$\text{For } j = 1,\ E^1(0) = E_{in} \tag{4.45}$$

$$\text{For } j > 1,\ E^j(s_0) = E^{j-1}(s_0 + S)exp(i\beta S) \tag{4.46}$$

where s_0 is an arbitrary common point of two adjacent turns.

β can be obtained by solving the eigenvalue equation of a circular cross-section waveguide [30]. The ordinary differential equations are then solved numerically by the Runge-Kutta method in Matlab, with the boundary conditions applied at the end of each iteration to compute the output/input of each turn. The algorithm is repeated with the Newton-Raphson method to optimize the starting vector until the difference between successive iterations (k) falls below an error threshold, by which the system is deemed to be in a steady-state and the transmission of the MCR can be obtained from $E_x^N(S)$ or $E_y^N(S)$. The total error is calculated as follows:

$$E_{total} = \sum_{j=0}^{N}\left(\sum_{s=s_0,s+\Delta s}^{s_0+S}\left[{}^{k}E_x^j(s) - {}^{k-1}E_x^j(s)\right]\right) \tag{4.47}$$

The summation of the iteration-based errors from small-step increments (Δs) along each and every turn ensures that any change within the MCR can be detected and taken into account. The error tolerance and wavelength step size must be minimized to achieve high accuracy in the simulated values of Faraday rotation, allowing the detection of sharp transitions in the wavelength-dependent output.

To begin with, the output spectra of a birefringent MCR are studied in Figure 46 with $\Delta\varphi$ = 0 and an ER of 10.9 dB. For initially near-equal power in the two axes, the double-pass Faraday rotation can be derived from the rotation matrix:

$$2\theta_0 \approx \frac{\Delta P_{x,y}}{2P_{x,y}} \tag{4.48}$$

For initially unequal power in the two axes, small angles of Faraday rotation can be approximated as:

$$2\theta_0 = \sqrt{\frac{P_y^{in}}{P_x^{in}} - 2 \times \left(\sqrt{\frac{P_x^{out}}{P_x^{in}}} - 1\right)} - \sqrt{\frac{P_y^{in}}{P_x^{in}}} \tag{4.49}$$

Due to the single-pass modeling of the MCR, the off-resonance Faraday rotation must be doubled before comparing with that of the on-resonance, as the latter is already configured to approximate the double-pass MCR in the experiment. As a result, the simulated resonance enhancement factor of M = 0.5 between the Faraday

rotation of on- and off-resonance is less than unity. It can also be observed that the transitions between the two resonance states involve a sharp reversal in polarity (Figure 46 only shows magnitude). This trend could be initiated by an interplay of birefringence- and coupling-induced shifts in $\Delta\varphi$ that affects the direction of Faraday rotation. Details of this phenomenon will be explained in section 4.5.

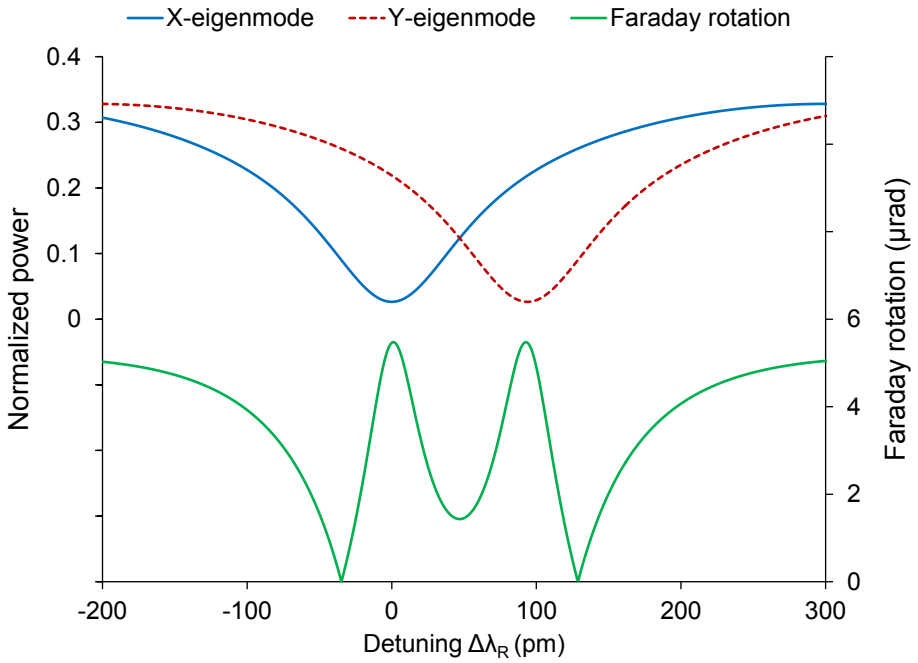

Figure 46. Simulated transmission and Faraday rotation spectra of the microfiber coil resonator (N = 3, r = 0.5 mm, n_{core} = 1.45, n_{clad} = 1.373, $\mu_0 = 4\pi\times10^{-7}$, μ_r = 1, V = 0.54 rad/T.m, I = 7.9 A, κ = 5523 m^{-1}, α = 69 m^{-1}, $\Delta n = 7.7\times10^{-5}$).

4.3.6 Experimental results

Figure 47 shows the double-pass transmission spectra of the fabricated MCR with an ER of 10.9 dB, loss of 3 dB and birefringence-induced resonance separation of 100 pm. The wavelengths at which the Faraday Effect was investigated were λ_0 = 1550.015 nm, λ_M = 1550.222 nm and λ_R = 1550.270 nm, which correspond to off-resonance, midway-to-resonance, and on-resonance respectively. The non-identical received power at the two resonant wavelengths associated with the two eigenmodes indicates the possible occurrence of direction-dependent coupling and loss. Consequently, the measured optical signals in the time-domain were dominated by a second harmonic of the current signal, due to one path having undergone a significantly higher loss than the other path through a double-pass of the MCR.

Although the FRM would normally compensate for reciprocal phase noise and PDL, this is no longer the case with directional behavior. In addition, the returning X and Y-polarized light do not propagate at 90° to the original path through the MCR in the presence of non-reciprocal Faraday rotation. Hence, under such circumstances the device behaved as if the system was initialized with a 0° PMF-PMF splice.

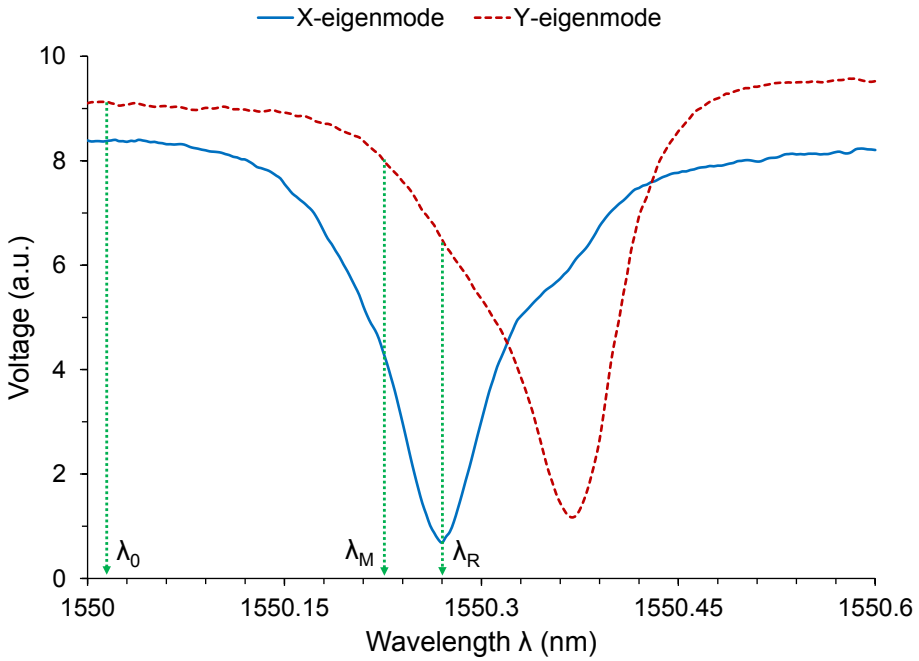

Figure 47. Measured double-pass transmission spectra of the microfiber coil resonator for X and Y-polarized light, with no current signal.

By comparing the resonant wavelength separation in Figure 47 with that of the simulated spectrum in Figure 46 and finding the value of the corresponding Δn, the polarization beat length was deduced to be ~20 mm. The fact that the current responsivity at λ_0 was non-zero in both the simulation and the experimental results despite the OM length being half the beat length confirms the theory that the adjacent turns in a MCR were not completely uncoupled at off-resonance.

The BD had an overall response of 210 V/mW, a bandwidth of 10–100 Hz, and a noise-equivalent power of 0.4 pW/$\sqrt{\text{Hz}}$ for a gain setting of 300. Since the optical signals of small currents were too weak to be picked up by the digital oscilloscope (300 μV_{rms} noise, 300 MHz bandwidth) due to the high PDL of the MCR, an additional low-noise voltage amplifier was employed with an overall gain of 111.6 dB, a bandwidth of DC–1 MHz, and a noise-equivalent power of 1 nV/$\sqrt{\text{Hz}}$. Using

Equation 4.40, a total received power of 50.0 µW (for all measurements) corresponds to a maximum fringe amplitude of 3978.0 KV. This relates to the maximum power transfer and it is not necessary to measure it, unlike interferometric detection schemes where the visibility needs to be determined. The Faraday rotation was calculated using the signal peak-to-peak of the BD output and the maximum fringe amplitude (Equation 4.42). The current responsivity was calculated from dividing the Faraday rotation by the current measured with the commercial current clamp-meter. Figure 48 shows a linear responsivity of 4.4±0.6 µrad/A at λ_R that is higher than the initial prediction of 0.7 µrad/A from Figure 46.

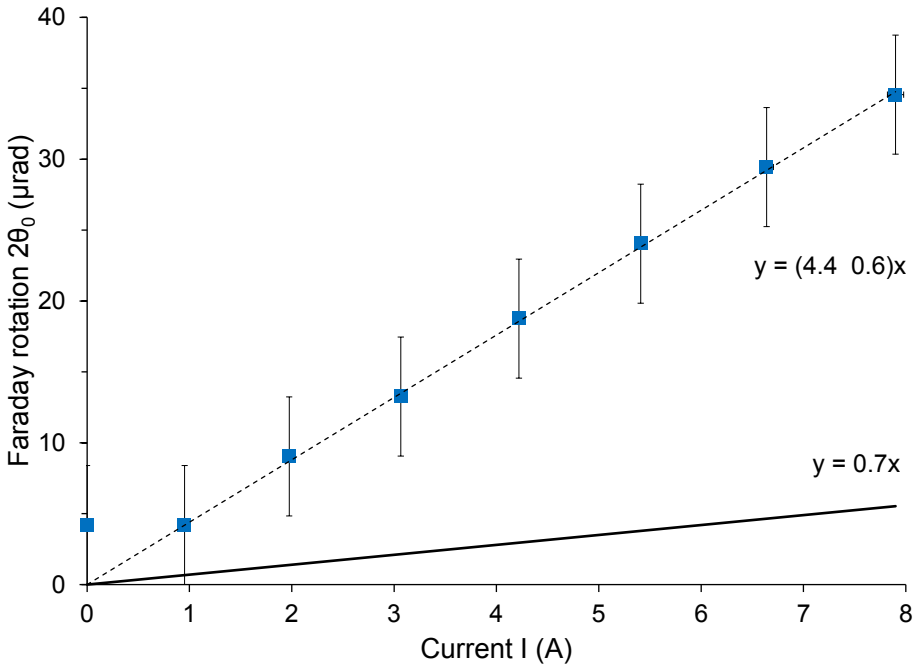

Figure 48. Measured current responsivity (λ_R) at a signal frequency of 30 Hz with a linear fit (dashed line), compared with the theoretical prediction (solid line). For no current or small current-induced signals with SNR < 1, the noise-equivalent rotation based on the measured noise amplitude was plotted instead.

Figure 49 compares the optical signals at the selected wavelengths. The signal peak-to-peak at λ_0 corresponds to a Faraday rotation of 11.2 µrad, which is in good agreement with the simulated value of 10.2 µrad from Figure 46. The large discrepancy between experimental and simulated values at λ_M (13.3 µrad, 1.4 µrad) and λ_R (34.6 µrad, 5.5 µrad) was most likely caused by non-uniform regions of birefringence and coupling in the fabricated MCR, which can manipulate the evolution of $\Delta\varphi$ and thus the measured Faraday rotation. Finally, an enhancement

factor of M = 3.1 between the Faraday rotation of on-resonance and off-resonance was deduced from the experimental results. Surprisingly, this is far greater than the predicted enhancement factor of M = 0.5.

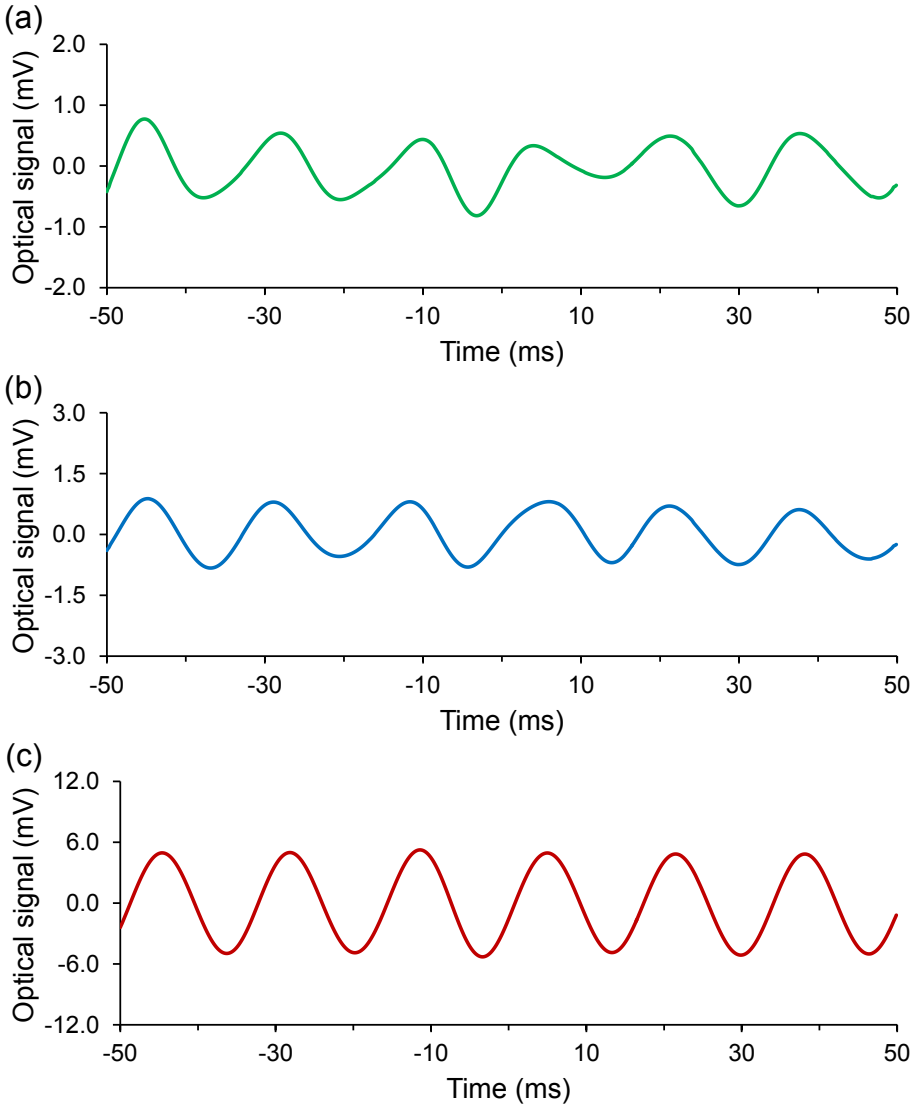

Figure 49. Optical signal at (a) λ_0 (b) λ_M and (c) λ_R in response to current signal modulated at I = 7.9 A, f = 30 Hz.

Assuming an initial $\Delta\varphi$ calibration error of $\pm\pi/4$, Figure 50 reveals that the simulated value of M could actually be in the range of $0.05 < M < 4.7$. It can be seen that the off-resonance Faraday rotation is larger for a greater negative bias of $\Delta\varphi$ (Y-eigenmode). This is due to the accumulation of Faraday rotation with increasing $\Delta\varphi$ under a positive Faraday efficiency regime between $-\pi/2 < \Delta\varphi < \pi/2$ (sections 4.5 and 4.6). The on- and off-resonance Faraday rotations generally maintain a difference of ~14 μrad, and become progressively negative for an increasingly

positive bias. Hence, in terms of magnitude, the Faraday rotation of on-resonance is superior to that of off-resonance when the bias of $\Delta\varphi$ is positive and large.

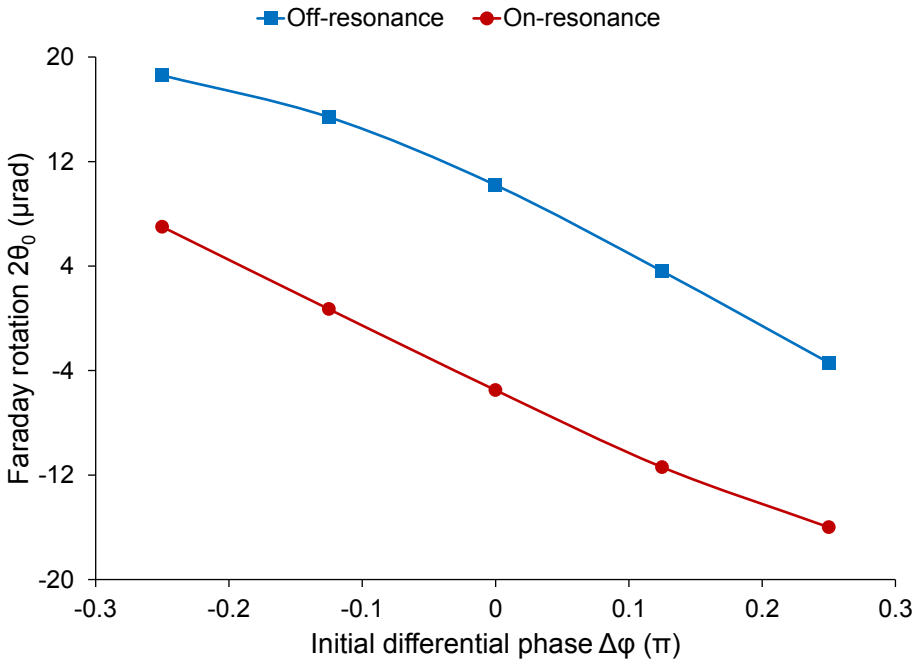

Figure 50. Simulated relationship between the initial differential phase and the double-pass Faraday rotation.

To predict the performance of the existing setup with MCRs of higher ER, Figure 51 shows a simulation of the potential enhancement when the system is initialized with $\Delta\varphi = \pi/8$ that best fits the experimental results with $M = 3.2$. Beyond a pivotal point, MCRs operating at λ_R can provide larger enhancements to the Faraday rotation and thus the current responsivity.

The detection bandwidth of MCs (section 4.2.5) can be accurately predicted unlike the fundamental frequency associated with mechanical transducers. Hence, experimental verification is not always necessary. For the MCR, this calculation is more complicated as the effective transit time of light must be known. As a rule of thumb, the effective transit time is roughly equal to the uncoupled transit time multiplied by the enhancement factor M. In this case, the detection bandwidth of the MCR sensor head is around ~3.5 GHz. The response time ($T_R \approx 10$ ns) of the sensor is defined as the transit time of light from the output of the MCR to the BD. Due to the recirculation of light within the MCR, the eigenmode at λ_R experience an effective OPL much longer than the physical length of the MCR. Hence, any

enhancement in responsivity would be accompanied by a delay in the response time and a reduction in the detection bandwidth. An integrated PZT can be used for easier tuning between high responsivity and high detection bandwidth.

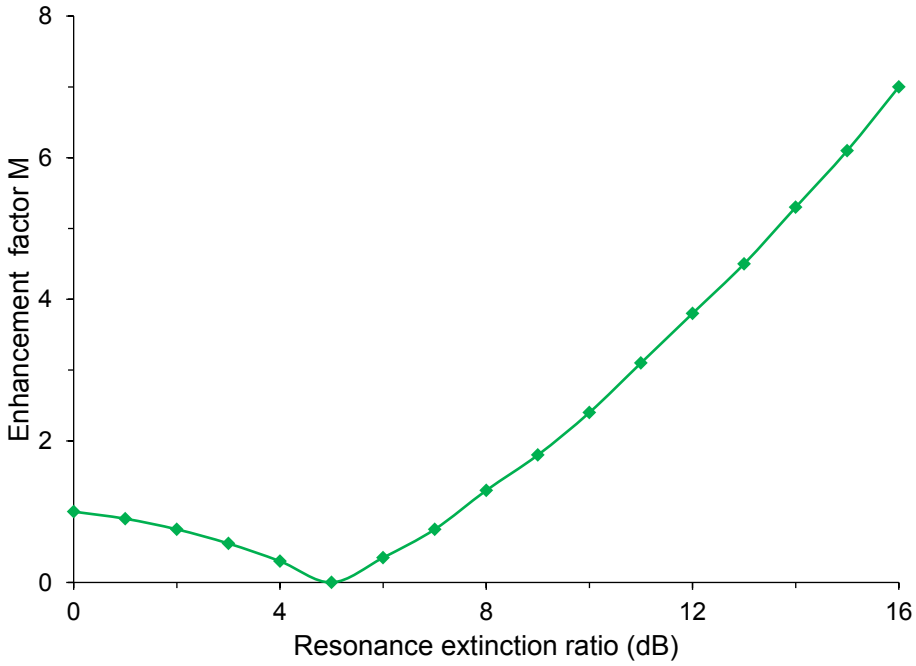

Figure 51. Simulated relationship between the extinction ratio and the enhancement factor.

The maximum current error is approximately ±1% according to the specifications of the commercial current clamp-meter. Unlike in the laboratory, where the passively damped optical bench minimized the effect of vibrations, in real measurement environments unsuppressed mechanical vibrations of the order of 1–100 Hz may influence the geometrical stability of the MCR. Meanwhile, dynamic ambient temperature fluctuations up to a few hertz are outside the frequency range of the measured current signal. However, static temperature deviations can detune the MCR and thus influence the responsivity, as evident from the temperature sensing ability of MCRs in section 3.2. A simple solution is to perform a one-point calibration of the sensing system by wavelength-tuning before each measurement.

The system noise (i.e. shot noise dominated) measured over a time-frame of 100 ms with 65536 running averages and a 32-point moving median filter was 67.0 μV, by means of computing the Fast Fourier Transform (FFT) of the optical signal with no measurand and selecting the highest power spectral density (PSD) component. This corresponds to a rotation sensitivity of 4.1 μrad using Equation 4.42. The average

noise of ~70 μV in the measurement data corresponds to a rotation error of ±4.2 μrad. From dividing the rotation sensitivity by the responsivity of 4.4±0.6 μrad/A at λ_R, the current sensitivity is 932.7±147.3 mA. The noise-equivalent signal generally corresponds to a worst-case scenario of the sensitivity, because for a shot noise dominated system, the noise floor is not constant but falls if the signal power decreases. Lastly, it must be pointed out that this performance was only a preliminary achievement. The non-ideal fabricated MCR sensor head featured high linear birefringence which caused Faraday rotation to undo itself, and high PDL that disabled the ability of the BD to reject common-mode laser intensity noise.

4.3.7 Conclusion

Current-induced Faraday rotation can be enhanced by the resonant cavity of the MCR to overcome the OM length limit imposed by fabrication. An experimental demonstration using a 3-turn MCR of 2 μm diameter OM and 10 mm uncoiled length with an ER of 10.9 dB and a loss of ~3 dB achieved an enhancement factor of 3.1 in Faraday rotation between off- and on-resonance. This factor of gain sits comfortably within the theoretical bounds of higher than 0.05 but lower than 4.7, with phase calibration errors taken into account. The maximum current responsivity and current sensitivity were 4.4±0.6 μrad/A and 932.7±147.3 mA respectively, with a detection bandwidth capability of 3.5 GHz.

To increase the enhancement factor and thus the responsivity, it is imperative to fabricate MCRs of higher ER, lower birefringence and lower PDL. A low-loss MCR allows the sensing system to operate at a quadrature point, which benefits from improved rotation and current sensitivities. To increase the detection bandwidth, the transit time must be decreased through reducing the OM turn length and ER. The response time can be reduced by minimizing the fiber length between the MCR and BD. To reduce the loss, air bubbles must be removed from the polymer packaging. The MCR sensor head can be made more practical by utilizing the sliding tube mechanism in section 3.2, instead of permanently binding the MCR to a single electrical wire. The non-contact approach allows the same MCR sample to probe a multitude of wires instead of being one-use. The problem with connecting an existing wire in series with a circuit under test is that the additional impedance will load the system and consequently deteriorate the accuracy of the measurement.

4.4 Passive and active stabilization techniques for microfiber coil resonators

Environmental effects have a major impact on the stability of optical resonators. The temperature sensing ability of MCRs is well-known, and it is a weakness in their use as current sensors. A geometrical design is proposed in this section to reduce such effects by chirping the RI of successive paired turns in the MCR. The resistance to external effects such as temperature drifts can be considerably improved by optimizing the coupling coefficients and chirping profile, such that the wavelength span of the resonance region is maximized without compensating its responsivity to the desired measurand. Another technique demonstrated is based on resonant wavelength tuning using a compact piezo-electric ceramic (PZC) disk of only 3 mm diameter and 1 mm thickness, attaining a tuning slope of 67.5±8.0 fm/V and estimated modulation bandwidth of ~2 MHz.

4.4.1 Introduction

Since the MCR transmission spectrum is governed by its geometry [31], even a minor change in the relative position of the OMs can radically alter its resonance shape and cause a significant resonance detuning. Temperature drifts are known to produce a spectral shift of ~100 pm/°C with silica MCRs embedded in polymer PC-373 [32], and ~10 pm/°C when embedded in Teflon resin [33].

In this section, the chirped MCR is presented and its enabling properties to keep the MCR on resonance despite temperature drifts are discussed. Secondly, a PZC-wound MCR is demonstrated, which makes it possible to minimize the detuning of the MCR in real-time by actively correcting its geometrical structure. This approach offers the benefit of continuous operation, but comes with the requirement of integrating an electrically active element into the MCR package.

4.4.2 Theory of chirped microfiber coil resonators

For resonantly enhanced sensors and devices exploiting the maximum recirculation of light at the resonant wavelength, a wider margin at zero detuning will significantly improve the stability of the resonator output under thermal fluctuations (<10 Hz) as well as mechanical vibrations and acoustic waves (<1 kHz).

As depicted in the transmission spectra of Figure 52(a), a small temperature-induced resonant wavelength shift ($\Delta\lambda_R$) results in a large optical power modulation (ΔP) for a standard MCR. However, by chirping the MCR, the resonant condition can be extended such that the output power of the resonator is constant across a broader wavelength range. Figure 52(b) shows a chirped MCR where the reduction in throughput is negligible, so the initial resonant wavelength remains on-resonance.

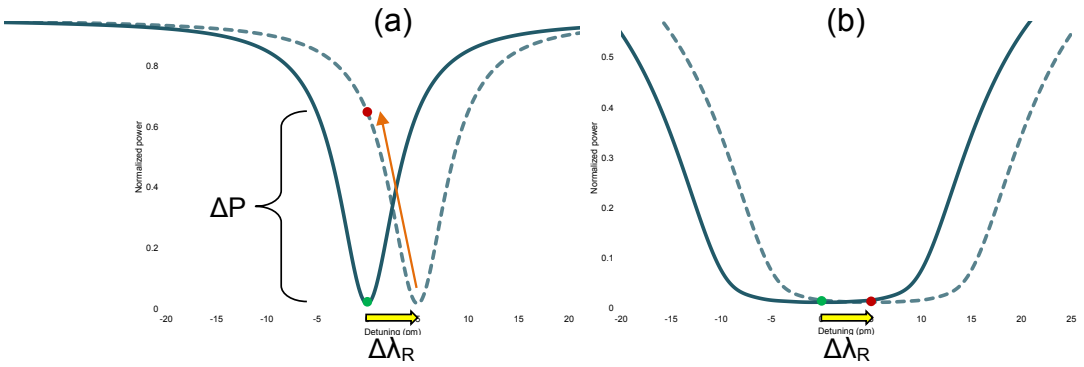

Figure 52. Effect of thermally induced resonance shift on the transmission spectrum of a (a) 3-turn microfiber coil resonator, and a (b) 12-turn chirped microfiber coil resonator. The two dots compare the output power before and after the shift, when initially operating at the resonant wavelength.

As mentioned previously, the MCR is a helical arrangement of OM with self-coupling between adjacent turns. For the standard coil, it is assumed that all turns are of equal length, with the coil pitch being comparable to the OM diameter and the wavelength of light (λ). Modifications of the resonator geometry have been previously investigated by Xu *et al* [34]. However, tailored optical structures such as those presented in Figure 53 have not yet been reported in literature.

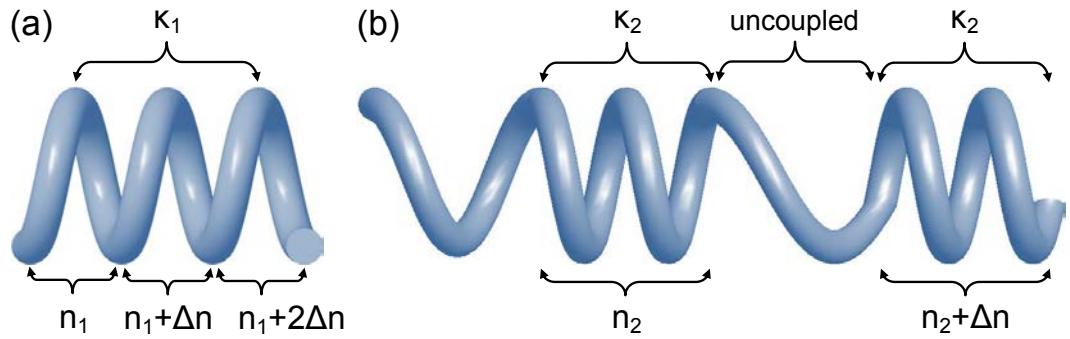

Figure 53. Configurations of the chirped microfiber coil resonator with (a) individual turns, and (b) paired turns.

The MCR is modeled for the two distinct configurations using a set of coupled mode equations. Linear birefringence, the polarization dependency of the coupling factors and the geometrical/Berry's phase are neglected in the ideal case. Firstly, for the MC in Figure 53(a) with N turns, the changes in the field amplitude E^j for the j^{th} turn between $j = 2$ and $N–1$ are expressed by Equation 4.50. For the first and last turn, light only couples to the second and penultimate turn, given by Equations 4.51 and 4.52 respectively:

$$\frac{\mathrm{d}E^j(s)}{\mathrm{d}s} = i\kappa \cdot \left(E^{j-1}(s) + E^{j+1}(s)\right) + i\Delta\beta_j E^j(s) - \alpha E^j(s) \tag{4.50}$$

$$\frac{\mathrm{d}E^1(s)}{\mathrm{d}s} = i\kappa E^2(s) + i\Delta\beta_1 E^1(s) - \alpha E^1(s) \tag{4.51}$$

$$\frac{\mathrm{d}E^N(s)}{\mathrm{d}s} = i\kappa E^{N-1}(s) + i\Delta\beta_N E^N(s) - \alpha E^N(s) \tag{4.52}$$

where $\beta_j = (2\pi/\lambda).n_j$ is the propagation constant, $\Delta\beta$ describes the relative change in the propagation constant between successive turns due to RI chirping, n_j is the effective index seen by the guided mode, κ is the coupling coefficient between the adjacent turns, α is the loss coefficient, and ds is the infinitesimal curvilinear distance along each turn length.

β_j can be obtained by solving the eigenvalue equation of a circular cross-section waveguide [30]. The ordinary differential equations are then solved numerically under the boundary conditions imposed by field continuity described in section 4.3.5. For the MCR devised in Figure 53(b) consisting of $N/2$ paired turns, Equation 4.50 must be modified such that coupling only occurs within each pair and none between pairs.

The chirping of the MCR can be realized using femtosecond irradiation to modify the RI of local areas of polymer surrounding each pair of turns, such that n_j is changed accordingly. The geometrical arrangement in Figure 53(b) can be achieved by coiling the paired turns with a smaller winding angle and a larger winding angle for the uncoupled regions. The paired turn configuration also provides higher feasibility for the femtosecond beam, since high spatial resolution is not required when operating on a larger surface area. The reproducibility of such structures can be made very high with high-precision translation stages.

A notable application is resonantly enhanced current sensing. It must be stressed that chirping does not necessarily affect the current responsivity, which depends on the OPL, coupling conditions, ER and linear birefringence. After chirping the MCR, each of the M paired turns will have a frequency-shifted resonance of lower individual ER. Since the ER is dependent on the proximity to critical coupling, it can be engineered to maintain the original responsivity by controlling the coil pitch with high-precision translation stages [35]. An alternative way of achieving high ERs via critical coupling has been recently demonstrated by nano-scale modifications of the fiber surface and RI using CO_2 laser and UV excimer laser beam exposures [36]. Furthermore, the responsivity is a function of the Verdet constant, which is mainly associated with the core of large OM diameters and it should be relatively unaffected by the laser irradiation on the polymer coating.

4.4.3 Simulations

Firstly, the effects of changing κ and Δn of a 3-turn MCR are compared, with an OM diameter of 1 μm, coil diameter of 1 mm and α = 4.6 m^{-1}. The base RI of the air-cladded silica OM is n = 1.45. These parameters are the same for all latter simulations. It is evident from Figure 54(a) that varying κ mostly changes the ER, whereas Figure 54(b) shows that increasing the chirping broadens the resonance and simultaneously decreases the ER.

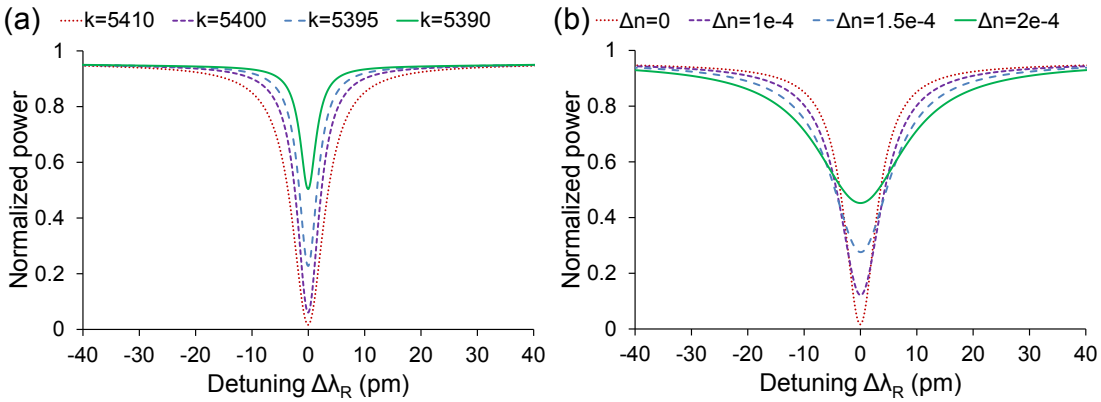

Figure 54. For a 3-turn microfiber coil resonator: simulated effect on the resonance shape when (a) the coupling coefficient is varied with no chirping (Δn = 0), and (b) the chirp is varied with a fixed coupling coefficient (κ = 5410 m^{-1}).

Instead, it is desirable to cascade several resonances in the wavelength domain, in order to achieve resonance broadening without trading-off the ER. However, a chirped MCR with any number of turns is still unable to produce a relatively flat region around zero detuning due to cross-coupling between turns. The solution is to arrange the MCR in pairs of turns, such that coupling only occurs within each pair and no coupling occurs between pairs. This way, the resonance condition of each pair is isolated and can be cascaded in series to produce a superimposed resonance shape matching the criteria. To begin with, a MCR with 12 turns configured in 6 pairs is analyzed. Figure 55 shows that by varying the pitch between adjacent turns in each pair, the proximity from critical coupling can be adjusted, which in turn causes the ER to change without affecting the relative shape of the resonance.

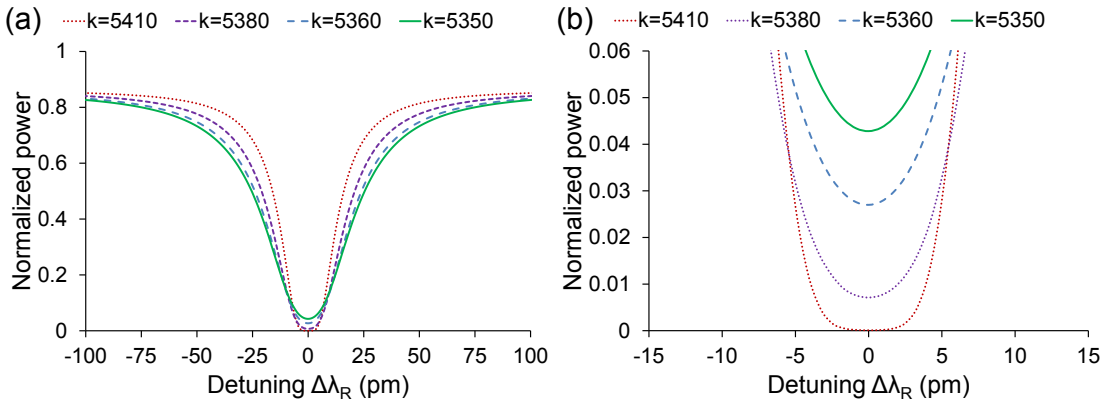

Figure 55. For a 12-turn regular microfiber coil resonator: simulated effect on the resonance shape when the coupling coefficient is varied with no chirping ($\Delta n = 0$), at (a) full scale, and (b) enlarged selection around resonance.

By introducing chirping between successive pairs in the same MCR, the individual resonances separate and cause a noticeable flattening of the lower region of the resonance shape, as seen in Figure 56. Although the ER is reduced, it can be compensated by bringing κ closer to critical coupling. However, increasing Δn beyond a certain limit will create ripples in the resonance shape.

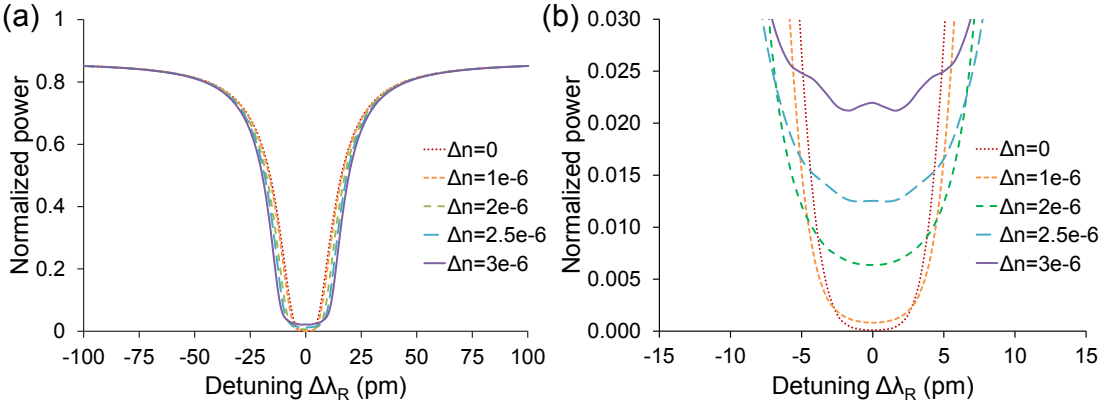

Figure 56. For a 12-turn chirped microfiber coil resonator: simulated effect on the resonance shape when the chirp is varied with a fixed coupling coefficient (κ = 5410 m^{-1}), at (a) full scale, and (b) enlarged section around resonance.

Figure 57 (a) compares the spectral width (1% tolerance at minimum transmittance) of varying ERs between a 12-turn regular MCR and a 12-turn chirped MCR. It is clear from Figure 57(b) that the spectral width changes at different rates for the two configurations. An increase of the spectral width broadening factor (i.e. ratio between modified/original widths) can be seen with increasing ER. The upper limit of spectral broadening for any ER is proportional to the number of paired turns and it is determined by the total OM length. Most conventional tapering rigs are capable of manufacturing OM lengths up to tens of millimeters [37] and some can even produce tens of meters [38]. To summarize, the chirped MCR can reduce the susceptibility of the device to thermal drifts by flattening its resonance region. From simulations, it is predicted that greater enhancements to the stability can be attained at higher ERs.

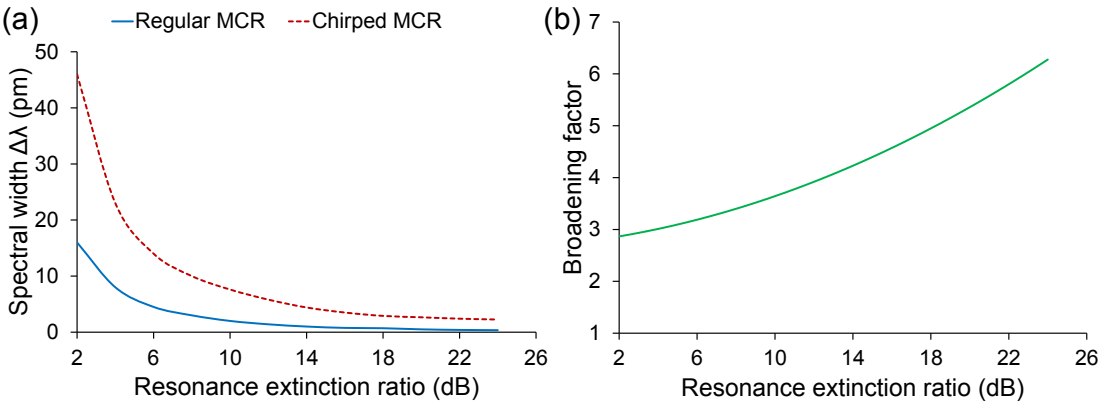

Figure 57. (a) Simulated spectral width as a function of resonance extinction ratio for 12-turn regular and chirped microfiber coil resonators, and (b) the broadening factor in spectral width for a range of extinction ratios.

4.4.4 Theory of PZC-wound microfiber coil resonators

Unlike the previous technique which relies on passive stabilization by flattening the lower region of the resonance shape, the following technique is based on the active stabilization of the resonant wavelength by shifting the transmission spectrum to compensate for any temperature drifts. The subsequent sections present details of the fabrication process to make the PZC-wound MCR, and the results from the experimental demonstration are compared with those of simulations.

The schematic of the PZC-wound MCR is shown in Figure 58(a). Due to the electro-mechanical effect of the piezo-electric material illustrated by Figure 58(b), strain-induced changes in the OPL of the bound OM changes the phase condition of the MCR for resonance, and thus instigates a shift in the resonant wavelength (λ_R). For negative voltages, the disc waist expands such that each turn of the MCR increases in OPL despite a small offset by the stress-optic effect, and thus λ_R experiences a positive shift.

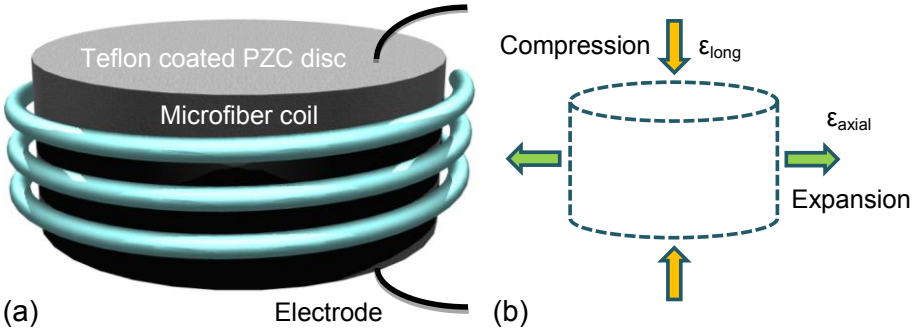

Figure 58. (a) Schematic diagram of the microfiber coil resonator attached to the Teflon-coated piezo-electric ceramic disc, and (b) an illustration of the physical deformation under piezo-electric and Poisson effects.

To predict the responsivity of the MCR, the behavior of the device under an applied voltage was modeled. The PZC shown in Figure 59 is assumed to be unrestricted for the following reasons: (a) Teflon has a very low Young's modulus compared to that of the PZC; (b) the layer of Teflon coating (<100 μm) is very thin compared to the radius of the PZC disc; (c) the MCR has only 2.5 turns; and (d) the OM diameter is relatively tiny. Hence, for a voltage of V applied across a PZC disc of thickness t, the relative change in the physical length of the OM (L) is approximately the relative

change in the circumference of the disc (ε_{axial}) due to the elastic deformation caused by electro-mechanical strain in the longitudinal direction (ε_{long}):

$$\frac{\Delta L}{L} \approx \varepsilon_{axial} = -\nu_{PZC}\varepsilon_{long} = -\nu_{PZC} \cdot \frac{d_{33}V}{t} \tag{4.53}$$

where d_{33} is the piezo-electric strain coefficient, ν is the Poisson ratio and t is the thickness.

The stress-optic effect [39] arises from the physical length change of the OM:

$$\Delta n_{silica} = -\frac{n_{silica}^3}{2} \cdot \frac{\Delta L}{L} \cdot [p_{12} - \nu_{silica} \cdot (p_{11} + p_{12})] \tag{4.54}$$

where n is the RI, p_{ij} is the Pockels coefficient components of the stress-optic tensor of silica ($p_{11} = 0.126$, $p_{12} = 0.270$) [40].

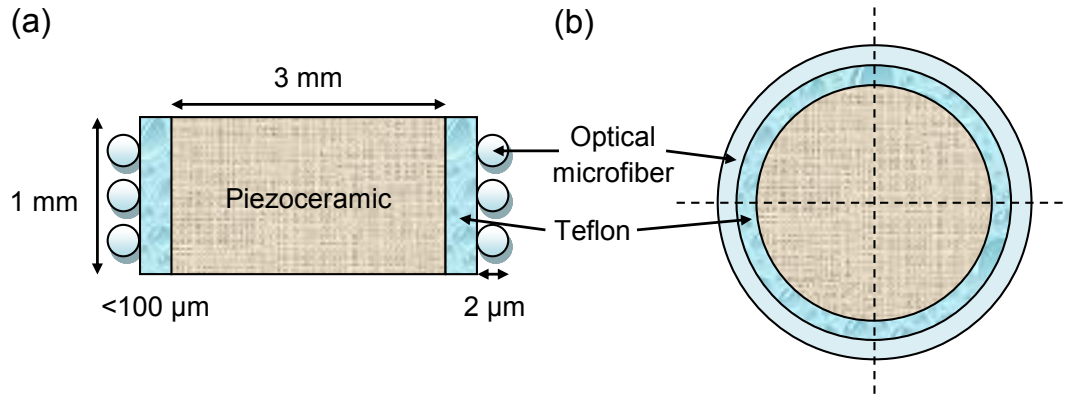

Figure 59. Schematic diagram showing the cross-sectional view of the Teflon-coated piezo-electric ceramic disc coiled with optical microfiber, from (a) the side, and (b) the top.

Lastly, the OM diameter decreases when its physical length is elongated via the Poisson coefficient, which influences the effective index seen by the guided mode. By using the material's Poisson ratio ($\nu_{silica} = -\varepsilon_{trans}/\varepsilon_{axial}$), the reduction in OM diameter is 3.06 pm. Since the surface area of OM exposed to the Teflon layer was negligible, the cladding is modeled with air.

4.4.5 Fabrication

The device was built in three stages. Firstly, a micro-cylindrical PZC measuring 3 mm in diameter was micro-machined from a bulk sheet of 1 mm thickness using

high-precision diamond cutting and milling tools. There are silver electrodes on the top and bottom sides, which are connected to copper wires for electrical connection. Smaller PZCs are feasible but are more difficult to handle during the coiling process.

For the second stage, the fabrication of the OM was developed based on the procedure described in section 3.2.3. The resulting OM of 2 μm diameter and 25 mm length at the uniform waist had a near-adiabatic taper diameter profile of $\psi = 0.1$ [26] to suppress the excitation of higher-order modes [27].

In the final stage, the disc was coated with a thin layer of Teflon and left to dry in room temperature. This process was repeated 3 times to build up a uniform layer of Teflon on the disc to reduce optical scattering and surface roughness-induced losses. At the same time, the Teflon exhibited a low RI to help confine light within the OM. The responsiveness of the device is proportional to the number of OM turns or the length of the uncoiled OM. However, only 2.5 turns around the disc was managed due to fabrication limitations. Coincidentally, coupling only occurred between two adjacent turns in the MCR, where the pitch was of the order of micrometers. To achieve sufficient self-coupling leading to resonance, the minimum number of OM turns is 2. The average ER was measured to be ~1.5 dB. The optical loss was ~0.3 dB at $\lambda = 1530$ nm, and it was attributed to Rayleigh and Mie scattering due to the presence of micro-bubbles and particles in the polymer.

4.4.6 Experimental setup

The setup shown in Figure 60 was used to test the PZC. A 32 V power supply was used to provide the input to a high-voltage amplifier, which has a maximum output voltage of 1 kV (DC). The output terminals of the amplifier were connected to the electrodes of the PZC, and the voltage applied to was incremented from 0 V to 600 V in steps of 50 V. It was assumed that the electro-mechanical modulation of the PZC did not generate heat, as there was negligible current flow. As the voltage across the electrodes was increased, the PZC material contracted in thickness and expanded orthogonally to the poling direction. The OM bound to the disc was stretched, which increased the OPL and thus λ_R. An OSA was used to track the shifts in resonant wavelength when the MCR was excited with broadband light provided by the amplified spontaneous emission from an EDFA. The average interval between each measurement was ~15 s.

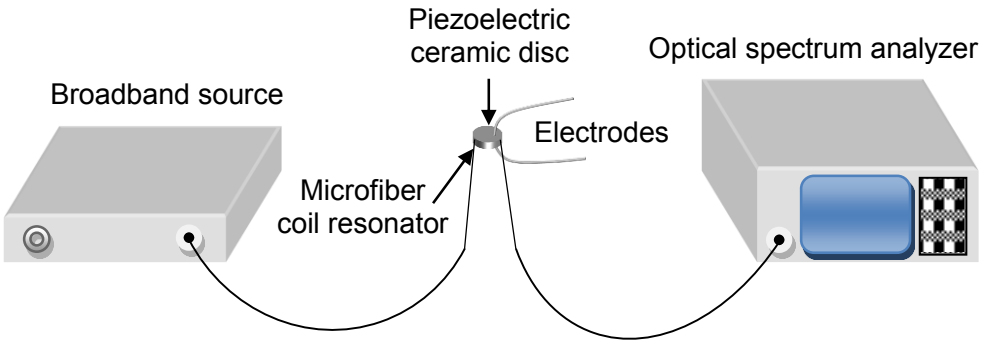

Figure 60. Schematic diagram of the experimental setup.

4.4.7 Simulations

The following parameters are considered for the disc model, starting with the PZC material [41, 42]: Young's modulus of E_{PZC} = 111 GPa, d_{33} = 300×10^{-12} m/V, and ν_{PZC} = 0.3. Similarly for Teflon [43, 44]: E_{teflon} = 1.2 GPa, ν_{teflon} = 0.42, and RI of n_{teflon} = 1.315. Finally for silica [45]: E_{silica} = 73 GPa, ν_{silica} = 0.17, and n_{silica} = 1.45.

The strain experienced by the OM is 9×10^{-6} using Equation 4.53 with V = 100 volts. The stress-optic coefficient of silica is –2.78×10^{-6}/100V using Equation 4.54. After consolidating all the effects into the MCR model described in section 4.4.2 (solved using Matlab) and discarding the $\Delta\beta$ terms, the normalized power spectrum before and after the PZC was driven with high voltage is simulated in Figure 61, showing a positive wavelength shift of $\Delta\lambda_R$ = 90.0 fm/V. The shift direction agrees with the expectation detailed in section 4.4.4.

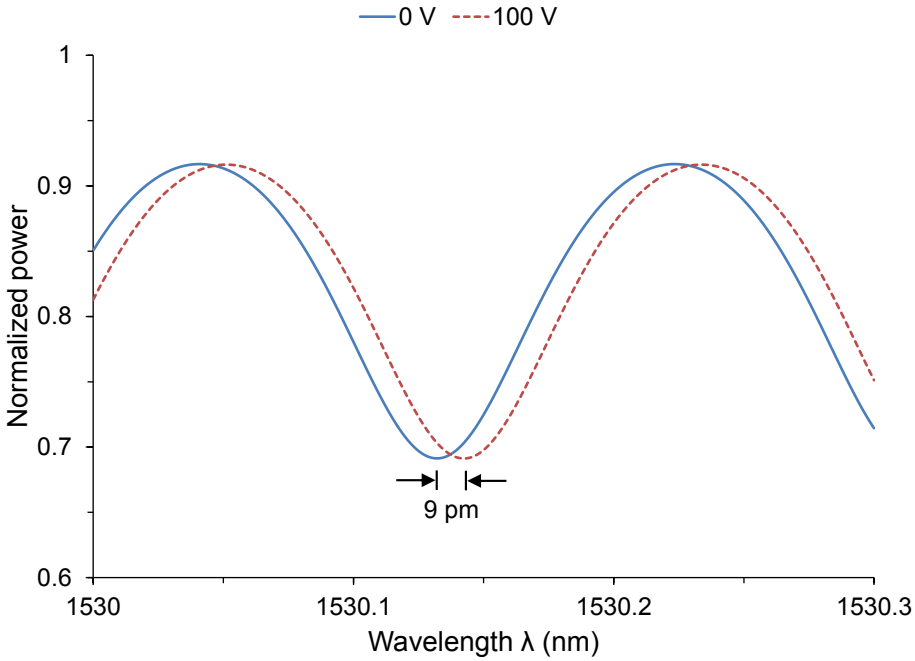

Figure 61. Simulated wavelength shift of the microfiber coil resonator when 100 V is applied across the electrodes of the piezo-electric ceramic disc.

4.4.8 Experimental results

The normalized power spectra are plotted in Figure 62(a), which was obtained by initially subtracting the reference spectrum of the original SMF-28 from the transmission spectra of the MCR (dB scale). The loss and extinction ratio were ~0.3 dB and ~1.5 dB respectively. The relationship between the applied voltage and the measured resonant wavelength shift was approximately linear. Variations in the ER resulting from changes in the coupling coefficient based on the coil pitch were negligible, due to the inefficient strain transfer along the longitudinal direction of an open-ended structure with a single-sided fixture. Figure 62(b) shows a responsivity of 67.5±8.0 fm/V, which is of the same order of magnitude as the simulated value of 90.0 fm/V. This difference arises from the unrestrained modeling of the PZC disc, which provides an upper limit for the responsivity. Additionally, the cut of the PZC disc from its bulk form was observed under a microscope and found to be rugged and not perfectly circular, which could have been another factor.

The maximum voltage error is about ±5 V due to the instability of the digital power supply. The maximum spectral shift error is ±5 pm since the resolution of the OSA is 10 pm. The additional deviations from the fitted line are most likely due to air flows,

causing a change in ambient temperature. The thermal responses of the materials change the OPL of the MCR, and thus induce a noticeable wavelength drift. This further highlights the need to employ a PZC disc with feedback control, such that any thermal effects in the MCR can be minimized.

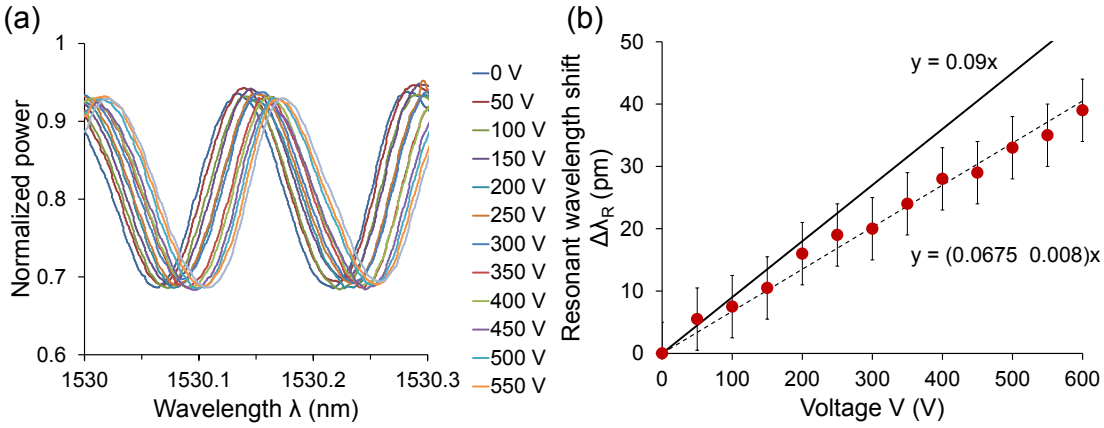

Figure 62. (a) Normalized power spectra showing spectral shift with different voltages, and (b) the measured voltage responsivity with a linear fit (dashed line) compared with the theoretical prediction (solid line).

The fundamental frequency of the PZC disc was predicted to be ~2 MHz using the thickness mode vibration model [42]:

$$F_R = \frac{N_t}{t} \tag{4.55}$$

where F_R is the resonant frequency and N_t = 1920 Hz.m is thickness frequency constant [41]. It is clear that a response frequency of ~2 MHz can adequately cope with temperature drifts, which typically occur at frequencies lower than 10 Hz. Regrettably, due to the lack of a high modulation bandwidth, high-voltage source, the anticipated modulation bandwidth could not be verified.

4.4.9 Conclusion

Two different ways of improving the optical stability of MCRs were proposed and discussed. The first technique involves reconfiguring the MCR into paired turns and chirping the RI of successive pairs to attain a maximum region of flat resonance. This facilitates a stable detuning range for resonantly enhanced sensors and devices to improve immunity not only against thermal drifts, but also mechanical vibrations and acoustic waves. By further optimizing the coupling coefficients, the reduced

sensitivity to environmental effects can be achieved without compromising the sensitivity to the desired measurand. The limit of resonance flattening is governed by the number of turns and ultimately by the total OM length.

The second technique replaces the passive support rod of the MCR with a compact PZC disc, which can be modulated to maintain zero detuning of the resonant wavelength. An experimental demonstration using a 2.5-turn MCR of 2 μm diameter OM and 25 mm uncoiled length obtained a responsivity of 67.5±8.0 fm/V, which is comparable in magnitude with the simulated value of 90.0 fm/V. The estimated modulation bandwidth is ~2 MHz. This device is easier to fabricate than the chirped MCR because of the lower design complexity. On the other hand, it requires an electrically active element to be integrated into the MCR package, which may not be suitable for applications that operate in sensitive environments.

To increase the tuning range of the PZC, a disc material of higher piezo-electric strain coefficient is needed. The stability of the sensor head can be improved further by combining the passive and active stabilization techniques, such that a PZC is integrated inside a chirped MCR. The foreseeable challenge would be to modulate all OM turns in such a way that the collection of resonances shift by the same magnitude in the wavelength domain, so as to prevent distortions in the combined spectral shape.

4.5 Spun optical microfiber for high performance current sensing

Linear birefringence is highly detrimental to the Faraday Effect of any fiber-optic current sensor. The first report of SOM is presented in this section, with details of the fabrication method and a demonstration of its important role in making practical MC- and MCR-based current sensors. SOM exhibits superior resistance to bend- and packaging-induced linear birefringence than their unspun counterparts, which can improve the responsivity, reliability and reproducibility of the sensor head.

4.5.1 Introduction

Although the minimum permissible bend radii of OMs is significantly smaller than those based on regular-sized optical fibers, the same problem of linear birefringence arises after packaging the MC/MCR in UV-curable polymer for geometrical stability and optical confinement. In the presence of linear birefringence (i.e. non-zero differential phase), the net power transfer between the fast- and slow-axes due to Faraday rotation is maximum after a quarter of the beat length, and reduces to zero over half of the beat length. Hence, for OMs longer than a quarter of the beat length, the only section in which interaction with the magnetic field will be measurable is the length remaining after subtracting an integer number of half beat lengths. Although the differential phase is more relevant to the underlying problem, the corresponding linear birefringence is more fundamental to fiber design and fabrication. Owing to the focus of this section, the latter is often quoted instead.

Numerous solutions have been reported over the years. One technique uses a 45° Faraday rotator and a mirror to undo reciprocal linear and circular birefringence in the optical fiber. At the same time, the non-reciprocal Faraday rotation is doubled [46]. However, a total cancellation of perturbation-induced effects is only possible for small Faraday rotations. Another technique is to utilize highly birefringent (hi-bi) fiber with periodically spaced regions of current-induced magnetic field such that sections are skipped where the Faraday contribution is in the wrong sense. Alternatively, reversing the magnetic field direction at half beat length intervals ensures that the Faraday contributions continue to add [47]. Unfortunately, this technique raises design complexities as a current sensor and it is not feasible for MC/MCRs where the final packaged birefringence is only known post-fabrication.

A different technique to achieve efficient Faraday rotation utilizes an optical fiber coil wound accurately such that its circumference is exactly equal to the beat length of its linear birefringence [48]. Again, this technique is impractical for MC/MCRs as their final birefringence cannot be determined before packaging. An alternative approach is to anneal the sensor head post-fabrication to relieve the internal stresses in the coiled optical fiber [49]. Although this technique works well with standard optical fibers such as SMF-28, it cannot be applied to an embedded MC/MCR due to the low melting temperature of polymers. If annealed in the pre-packaged state, linear birefringence will be introduced during the packaging stage. Yet another interesting technique involves canceling the bending-induced linear birefringence by inducing a controlled anisotropy in a direction orthogonal to the bending plane [50]. This is typically performed by coiling hi-bi fiber with the slow-axis parallel to the direction of the wire. The drawback is the difficulty of drawing an OM with a specific linear birefringence equal to the post-fabrication birefringence of the MC/MCR.

One of the earliest and simplest techniques to suppress linear birefringence was the use of twisted fiber [51]. Twisting adds circular birefringence to the optical fiber, which is effective for large coils with a few turns. For the MC/MCR, the amount of twist required to achieve a noticeable effect is likely to exceed the breaking strength of the OM. Additionally, such twists are temperature-dependent and therefore unstable. The use of spun fibers is another solution to overcome the birefringence problem. This involves producing a low-birefringence fiber [52] by spinning the preform during fiber drawing to average the fast and slow birefringence axes. Again, when packaged in a coil the optical fiber suffers from bend-induced birefringence. As a result, spun hi-bi optical fibers [46] were introduced, which featured better resistance to external perturbations. Spun hi-bi optical fibers have sufficient circular birefringence to overcome the bend- and packaging-induced linear birefringence.

Due to the effectiveness of the spun fiber technique and the feasibility for the OM to be spun in a similar fashion, it is of interest to study the SOM and its application for current sensing. In this section, the fabrication procedure of SOM is detailed and the anticipated improvements to current responsivity are experimentally confirmed.

4.5.2 Theory

When an optical fiber is pulled from a preform while simultaneously being rotated, a large uniform spin rate is written into the optical fiber. The photo-elastic effect can be neglected as the spinning occurs in the furnace hot-zone, where the glass viscosity is sufficiently low to prevent the build-up of shear stress. With a large spin, the optical fiber behaves as an isotropic waveguide that is almost center-symmetric due to the rapid rotation of the fiber axis. This optical fiber is capable of transmitting and preserving any SOP. Owing to their intrinsic geometrical symmetry, spun fibers have insignificant birefringence. The advantage is that they are insensitive to temperature and wavelength effects. The disadvantage is that the spun fiber is just as sensitive to external effects (e.g. twist, stress and bend) as a normal low-birefringence fiber.

A more successful variant of the spun fiber is made by spinning highly (linear) birefringent preforms during the drawing process to impart a rapid built-in rotation of the birefringent fiber axes. The result shown in Figure 63 is that the optical fiber becomes elliptically birefringent. By carefully choosing the spin rate relative to the intrinsic linear birefringence, the resulting elliptically-polarized light can have an optical response to magnetic fields approaching that of an isotropic fiber. The benefit of this technique is that the optical fibers still retain a sufficiently large elliptical birefringence that establishes a high resistance to external perturbations. This type of spun fiber, now conventional, can be considered as a compromise between the high linearly birefringent fiber that is polarization-maintaining (PM), and the isotropic fiber with a high responsivity to current.

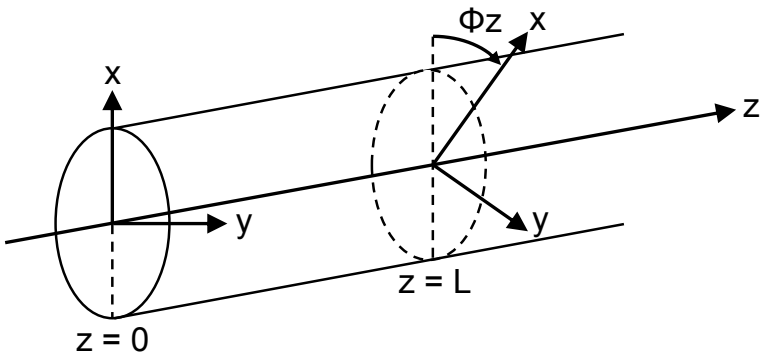

Figure 63. Schematic diagram of the spun microfiber with a constant spin rate Φ along fiber axis *z*.

For the polarization diversity polarimeter, the total Faraday rotation for an unspun fiber coil (non-resonator) with constant Faraday rotation per unit length (τ) and non-zero linear birefringence as a function of fiber length (L) was reported to be [52]:

$$\theta = \frac{1}{2}\sin^{-1}\left[\frac{2\tau}{\gamma}\cdot\sin(\gamma L)\right] \tag{4.56}$$

where $0 < \theta < \pi/2$, $\gamma = \sqrt{\Delta\beta^2 + 4\tau^2}$, $\beta = (2\pi/\lambda).n$ is the propagation constant, $\Delta\beta$ models the linear birefringence, n is the effective index seen by the guided mode, and λ is the wavelength of light.

The maximum Faraday rotation limited by birefringence can be expressed by:

$$\theta_{max} = \frac{1}{2}\sin^{-1}\left(\frac{2\tau}{\gamma}\right) \tag{4.57}$$

Assuming that the polarized light encounters the current-induced magnetic field and the linear birefringence at the same time, a simpler expression can be derived from Equation 4.57 or inferred from first principles [47]:

$$\theta = \int_0^L \tau\cos(\Delta\beta\cdot l)\cdot dl = \frac{\tau}{\Delta\beta}\cdot\sin(\Delta\beta\cdot L) \tag{4.58}$$

The upper limit of Faraday rotation also occurs at $\Delta\beta.L = \pi/2$ (quarter beat length):

$$\theta_{max} = \frac{\tau}{\Delta\beta} \tag{4.59}$$

The differential phase of a conventional spun fiber can be written as a function of spin rate (Φ rad/m), L and $\Delta\beta$ [53]:

$$\Delta\varphi = \frac{2\pi}{\lambda}\cdot\Delta n_{eff}\cdot L = \frac{\sin(\Phi L)}{\Phi}\cdot\Delta\beta \tag{4.60}$$

Rearranging Equation 4.60 produces a relationship between the effective linear birefringence and the intrinsic linear birefringence (Δn_{int}):

$$\Delta n_{eff} = \frac{\sin(\Phi L)}{\Phi L}\cdot\Delta n_{int} \tag{4.61}$$

The maximum current responsivity of a spun fiber coil normalized to the sensitivity of an isotropic fiber can be expressed in terms of the polarization beat length (L_B) of the unspun fiber and spin pitch (L_P) [46]:

$$R = \frac{4\times\left(\frac{L_B}{L_P}\right)^2}{1+4\times\left(\frac{L_B}{L_P}\right)^2} \tag{4.62}$$

where $L_B = \frac{\lambda}{\Delta n_{int}}$ and $L_P = \frac{2\pi}{\Phi}$

4.5.3 Fabrication

To fabricate hi-bi OM that is the pre-requisite of SOM, the starting fiber is SMF-28. The middle section of the optical fiber was processed while the two ends were kept as pigtails for easy integration with other fiberized components. To begin with, the acrylate coating of the middle section was removed with a fiber stripper and the exposed bare fiber was placed in the groove of a fiber holder. Next, the folded edge of an ultra-fine, micro-gritted sand paper was used to carefully side-polish a small area of the middle section to produce a D-shaped section, as shown in Figure 64. The polishing depth determines Δn_{int} of the tapered fiber. The lower limit of polishing length on a section of SMF-28 (r_{SMF}) for a given polishing depth (d), OM average uniform radius (r_{OM}) and OM length (L_{OM}) can be determined by calculating the cross-sectional area ($A_{P\text{-}SMF}$) of the polished fiber:

$$L_{SMF} = \frac{\pi r_{OM}^2}{A_{P-SMF}} \cdot L_{OM} \tag{4.63}$$

where $A_{P-SMF} = r_{SMF}^2 \cdot \left[\pi - \frac{1}{2}\cos^{-1}\left(1 - \frac{d}{r_{SMF}}\right)\right] + (r_{SMF} - d) \cdot \sqrt{d \cdot (2r_{SMF} - d)}$

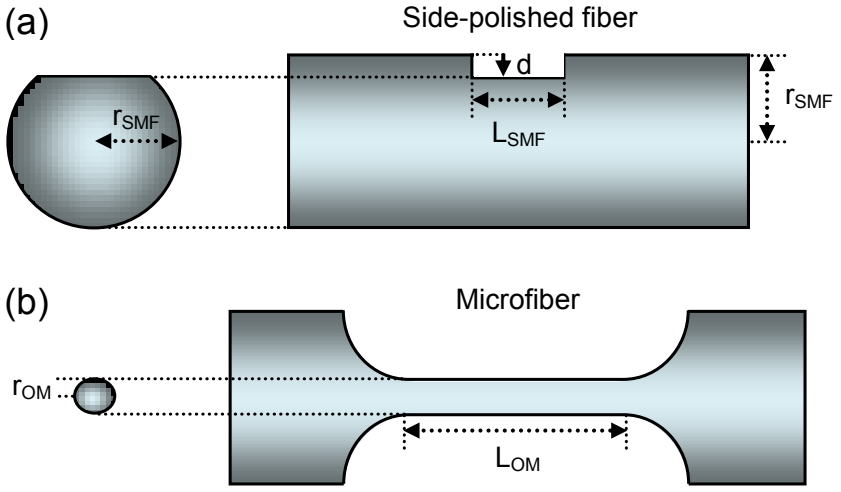

Figure 64. Side view of (a) a side-polished fiber, and (b) the waist of a tapered fiber.

The sand paper has micron-sized abrading particles that can remove a few micrometers from the fiber surface in order to eliminate the circular symmetry typical of optical fibers. It is not essential to ensure that all linear birefringence is created precisely within the region to be tapered and spun. The tolerance to over-polishing can be drastically improved by tapering and spinning simultaneously. This minimizes linear birefringence outside the target region, where fiber polishing is already becoming increasingly less important as the mode is confined more and more into the core. The reproducibility of side-polishing can be primed with practice.

After polishing, the D-fiber section was rinsed with isopropanol to wash away any debris. The fabrication of the hi-bi OM was developed based on the procedure described in section 3.2.3. The resulting hi-bi OM of ~2 μm diameter and 10 mm length at the uniform waist had a taper diameter profile of ψ = 0.3 [26]. The fiber cross-section was slightly elliptical due to the surface tension of the partially melted silica. The setup shown in Figure 65 was used to produce both SOMs and unspun OMs, with the rotator module (Thorlabs CR1-Z7) removed for the latter.

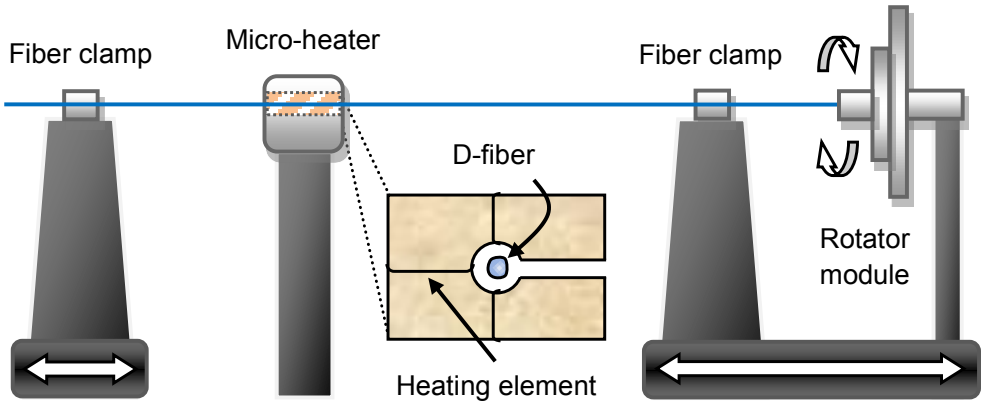

Figure 65. Schematic diagram of the newly developed tapering and spinning rig setup. A computer controls the initial position and differential velocities of the two translation platforms and the rotator module.

Next, the spin process of the SOM was initiated in the micro-heater hot-zone, where the glass viscosity was sufficiently low to ensure a fully plastic deformation. The resulting fiber shape appeared circular due to the averaging effect of the spin process, as shown in Figure 65. Φ is ideally small and comparable to $\Delta\beta$, so that $\Delta\beta$ is only partially canceled by the spin process. The spin ratio ($\Phi/\Delta\beta$ or L_B/L_P) is typically in the range of 0.5–1 for most reported spun fibers [54]. A SOM with a high spin ratio

is sensitive to bending and applied stress. For this reason, high spin ratios were avoided to ensure isolation from external effects. The final stage involved packaging the samples in low-RI, UV-curable polymer (Efiron PC-373 AP) on a glass slide for geometrical stability and protection against environmental effects.

4.5.4 Simulations

SOMs with a diameter smaller than 10 µm allow a significant portion of the guided modes to propagate in the polymer cladding outside the silica OM. Therefore, the averaging effect of spinning the OM will be less than that of a conventional spun fiber with the same Φ. Figure 66 shows the simulated relationship between Δn_{eff} and the final linear birefringence (Δn) after packaging the sample. The effective indices were obtained by solving the eigenvalue equation of a circular cross-section waveguide [30]. The effect of polymer packaging on SOM is visibly diminished when the OM diameter is larger than 10 µm. Although the polymer packaging can reduce Δn_{eff} to some extent, the material itself also contributes to Δn when cured and it tends to increase with time. Hence, by spinning the OM, both micro-bending and packaging-related effects can be minimized.

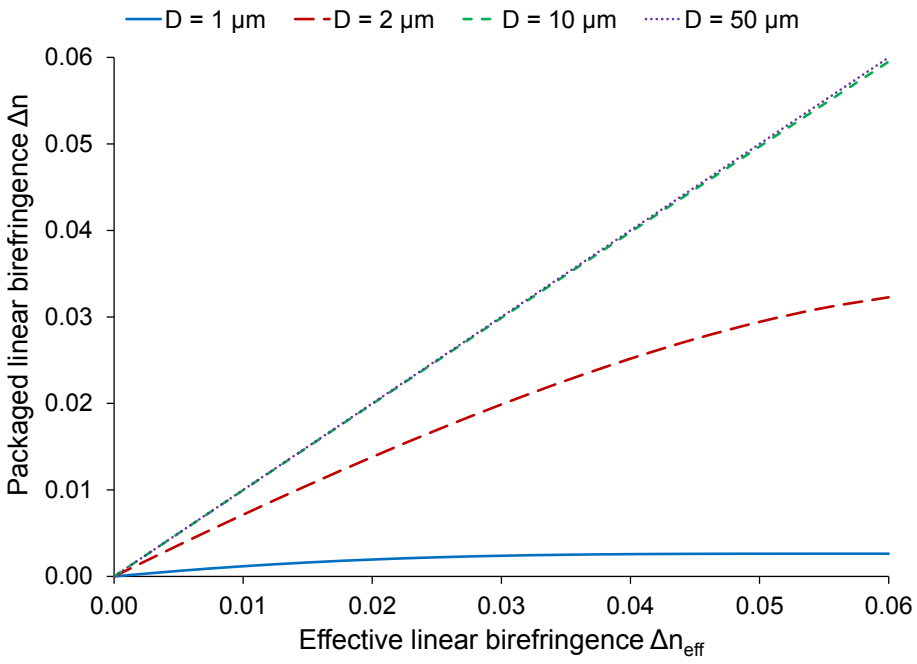

Figure 66. Simulated relationship between the effective linear birefringence and the packaged linear birefringence with $\Delta n_{eff} = n_x - n_y$ (where $n_x = 1.45$).

Based on Equation 4.61, Figure 67 shows that Δn_{eff} oscillates, falling to zero with increasing Φ even for high values of Δn_{int}. This can be explained by Equation 4.60, which reflects the averaging effect of spinning the birefringent OM axes that result in a periodic cancellation in $\Delta\varphi$. Consequently, increasing Φ for a fixed L leads to a smaller cumulated $\Delta\varphi$ and thus a lower Δn_{eff}. On the contrary, increasing L for a fixed Φ does not alter the maximum $\Delta\varphi$ during each revolution, and so Δn_{eff} becomes smaller instead. Hence, by increasing both Φ and L in Figure 68, the reduction in Δn_{eff} (i.e. gain in L_B) can be accelerated. Unlike L, Φ solves the underlying problem.

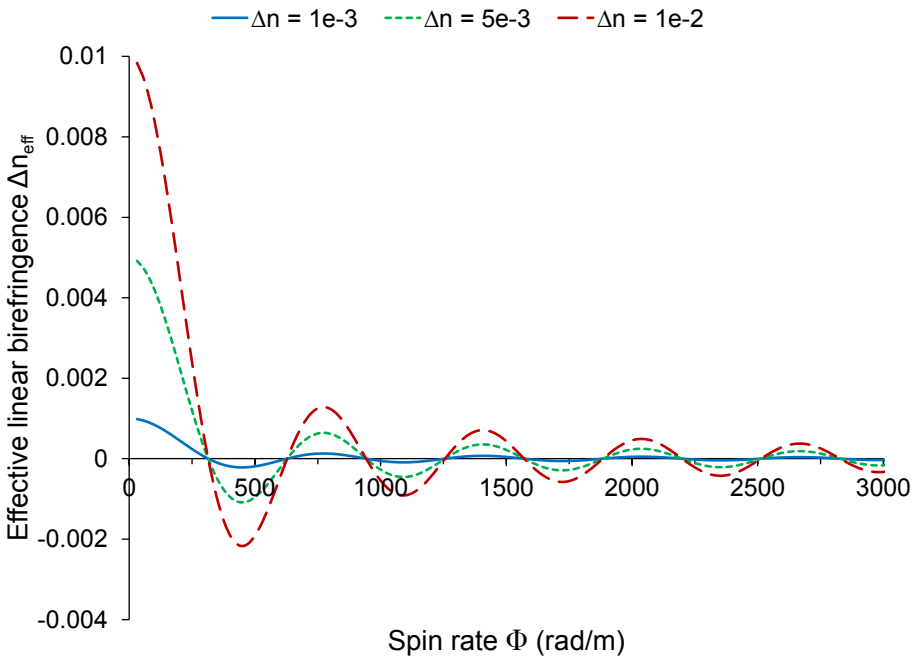

Figure 67. Simulated effective linear birefringence as a function of spin rate, for different intrinsic linear birefringence with L = 1 cm.

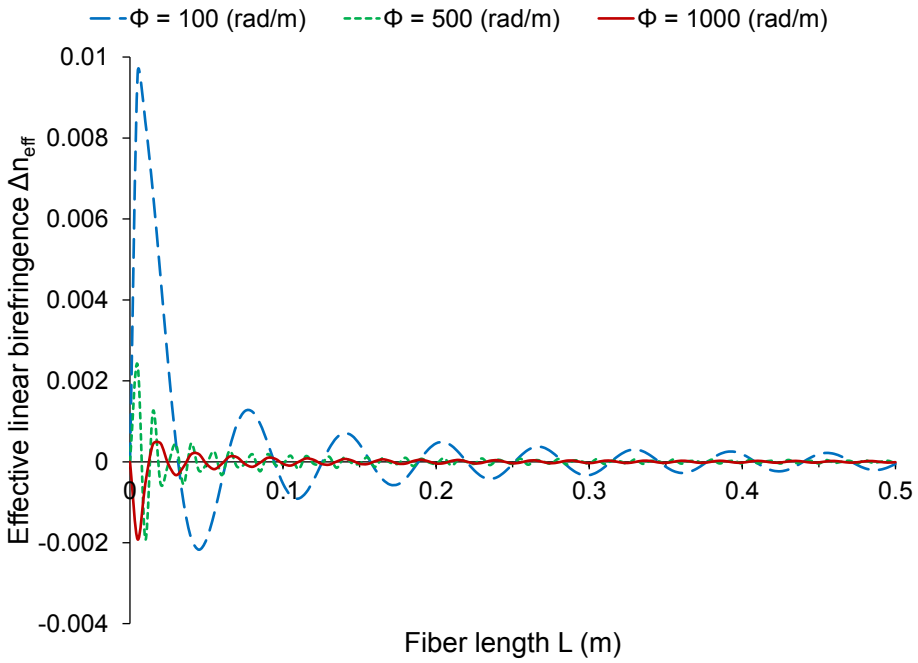

Figure 68. Simulated effective linear birefringence as a function of fiber length, for different spin rates with $\Delta n_{int} = 1\times10^{-2}$.

To better understand how spinning the birefringent OM axes in a MC sensor head affects the measured Faraday Effect, Figure 69(a) illustrates the evolution of $\Delta\varphi$ with increasing distance along the optical fiber (l). L_{P1} and L_{P2} denote a quarter of the spin pitch for high and low spin rates respectively. Figure 69(b) shows the corresponding efficiency ($\eta = \theta/\theta_{ideal}$) of the Faraday Effect, in which the area under the curve is linearly proportional to the total Faraday rotation. For higher Δn_{int}, the swing of $\Delta\varphi$ becomes larger and consequently the ripples in η deepen. For lower Φ, the slower changing $\Delta\varphi$ not only results in a longer period but also a larger amplitude. Consequently, the enlarged ripples in η have a stronger degrading effect on the total Faraday rotation. Beyond a certain extent, η becomes bipolar and the total Faraday rotation may approach zero at specific positions along the optical fiber. This explains how a lower Φ can lead to a higher Δn_{eff} that is closer to Δn_{int}, and vice versa.

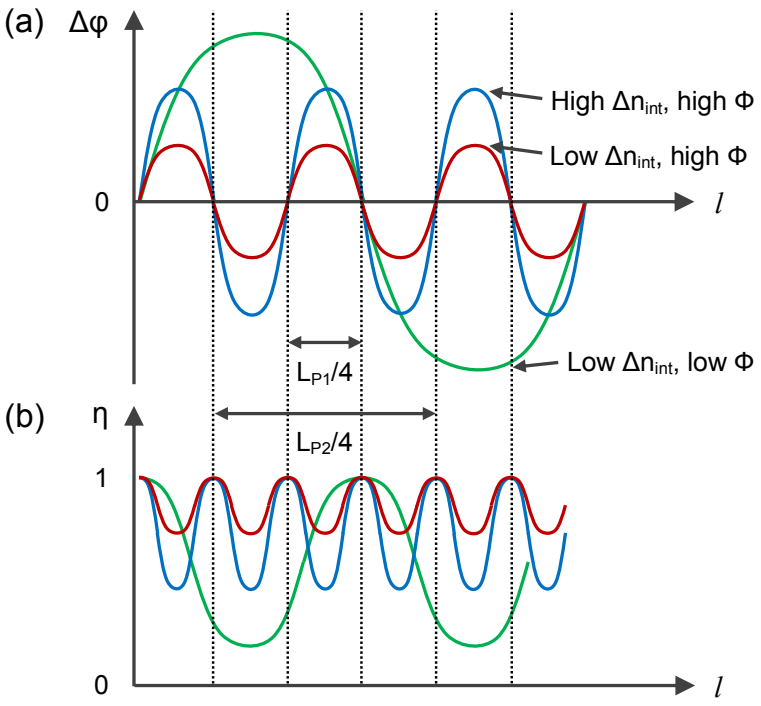

Figure 69. Simulated relationships between (a) differential phase, and (b) Faraday efficiency, with increasing distance along the optical fiber.

The relationship between L_B and L_P defined by Equation 4.62 implies that any magnitude of Δn_{eff} can be neutralized by an appropriate value of Φ to produce the maximum level of current responsivity (R = 1). As might be expected, Figure 70 shows that the current responsivity is lowest with short L_B (i.e. high-birefringence) and long L_P (i.e. small spin). Conversely, it is highest with long L_B (i.e. low-birefringence) and short L_P (i.e. large spin). However, a high spin ratio should be avoided for the SOM to remain insensitive to external effects.

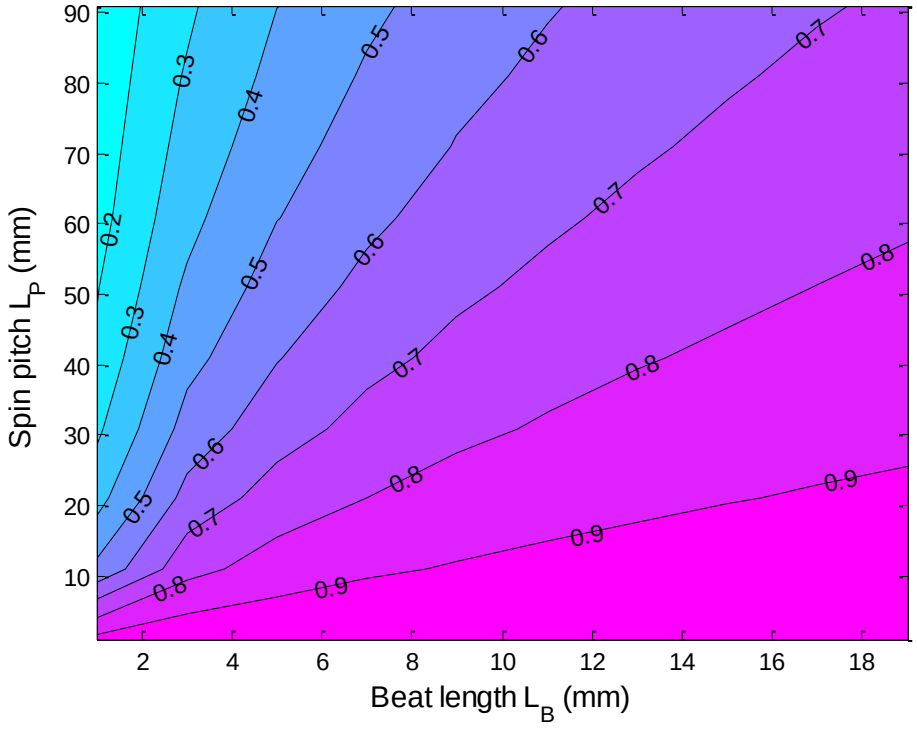

Figure 70. Simulated normalized current responsivity with varying values of beat length and spin pitch.

4.5.5 Fiber characterization

To confirm the effect of spinning the OM, Δn_{int} of the hi-bi OM was compared with Δn of the corresponding SOM. Finding the beat length increase ratio is equivalent to deducing the birefringence reduction factor. The following experiment was performed for each fabricated sample. Light was coupled from a TLS with a PMF pigtail into an in-line polarizer aligned at 45° to the axis of the FUT of length L, such that equal powers of light was transmitted along the fast- and slow-axes. Light emerging from the two orthogonal axes interfered at an analyzer set at 45° to the axis of the FUT. The transmission spectrum was captured by a PD and sampled by a digital oscilloscope. L_B is revealed as oscillations in the spectrum with a period of $\Delta\lambda$:

$$L_B = \frac{\lambda}{\Delta n} = \frac{\Delta\lambda}{\lambda} \cdot L \tag{4.64}$$

The optical losses of the packaged samples were typically 0.5–1 dB at a wavelength of λ = 1510 nm, and were attributed to Rayleigh and Mie scattering due to the presence of micro-bubbles and particles in the polymer.

It can be seen from Figure 71 that spinning at a rate of $\Phi = 8\pi$/cm has increased L_B of the hi-bi OM by a factor of 3. By doubling the rate to $\Phi = 16\pi$/cm, L_B was increased by factor of 6. Higher L_B is anticipated for larger values of Φ. However, the actual Φ experienced by the hi-bi OM may be slightly smaller than expected, due to the build-up of shear stress along the section of fiber between the micro-heater and the rotator module (~30 cm).

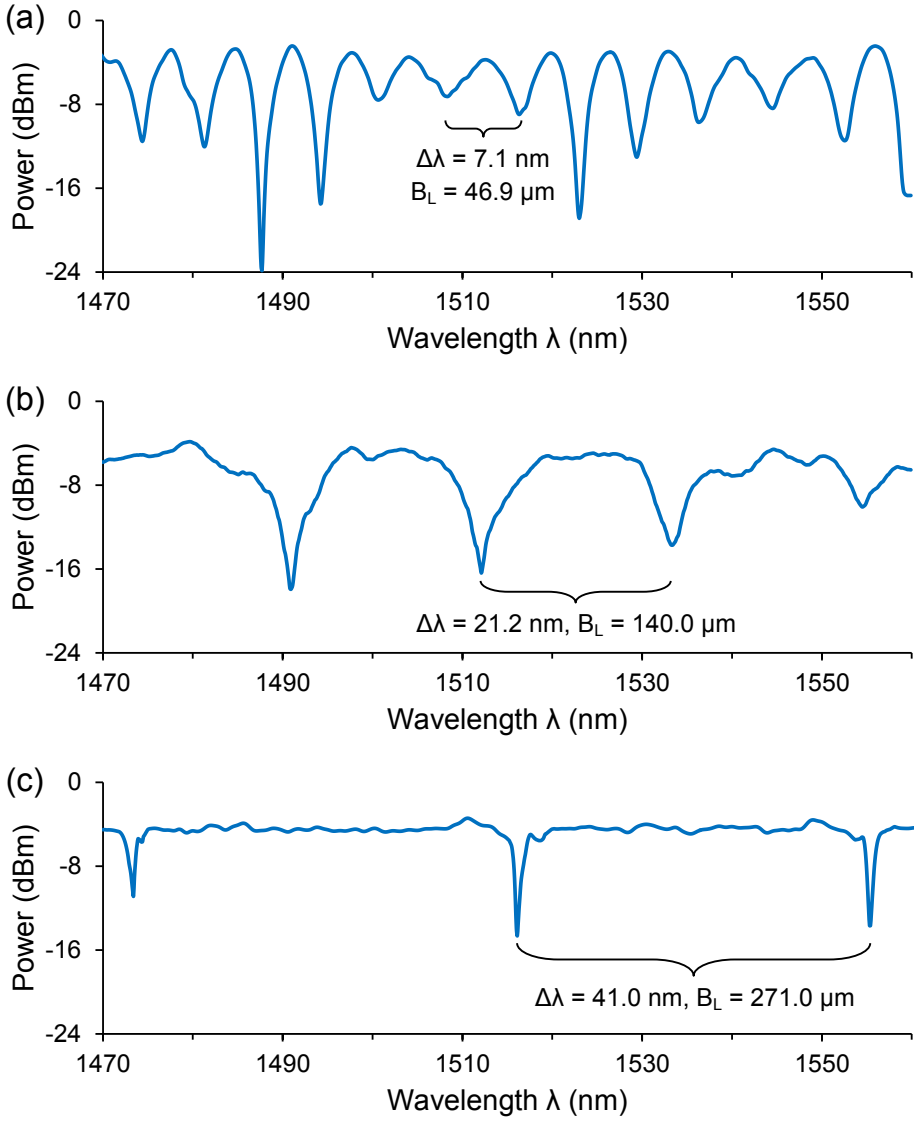

Figure 71. Transmission spectra of spun microfibers with (a) $\Phi = 0$ rad/cm, (b) $\Phi = 8\pi$/cm, and (c) $\Phi = 16\pi$/cm, each fabricated from a 2 μm diameter hi-bi microfiber with $L_{OM} = 10$ mm and $\Delta n_{int} = 3.23\times10^{-3}$.

The varying ER was attributed to the output light of the TLS not being completely confined to one axis of the PMF pigtail. Consequently, the degree of polarization (DOP) of light prior to the polarizer was wavelength-dependent and this affected the

ratio of power in the two orthogonal axes that beat together at the analyzer. Nonetheless, it is evident that the beat length ratio between the SOM and unspun OM can be changed by varying Φ. This allows SOMs to be made with a high Δn_{int} to resist external perturbations, and a low Δn_{eff} to permit the full Faraday rotation to be measured.

4.5.6 Experimental setup

To demonstrate that MC current sensors based on SOM are more resilient to bend- and packaging-induced Δn than those made using unspun OM, three MC samples were fabricated for each type of OM. All six samples were of 2 μm diameter and 30 mm length at the uniform waist with $\psi = 0.3$ [26]. A spin rate of $\Phi = 24\pi$/cm was chosen for the SOM samples, with $\Delta n_{int} \approx 1\times10^{-3}$ achieve a spin ratio of ~1. A thin layer of polymer was deposited on a 1 mm diameter copper wire before and after coiling the optical fiber to ensure good confinement of light. Each MC had 7.5 turns with a large winding pitch (>0.5 mm) to prevent mode coupling between adjacent turns. UV-curing of the polymer ensured geometrical stability and robustness packaging. A photograph of a packaged sample on a glass slide can be seen in Figure 72.

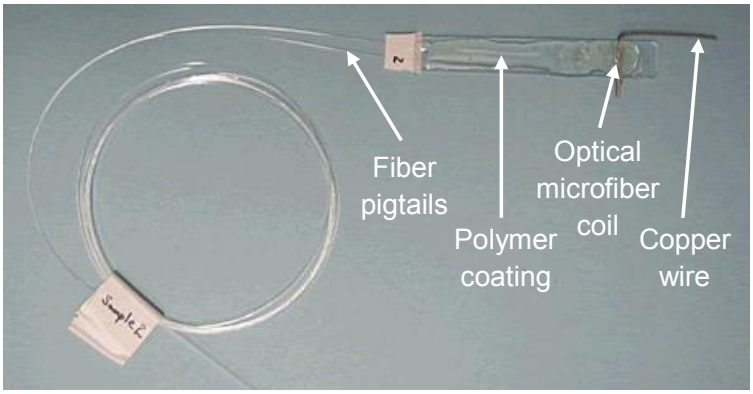

Figure 72. Photograph of a packaged sample. The microfiber coil sensor head was embedded in polymer on a glass slide.

To test the MC sensor heads made using SOM and unspun OM, the same experimental setup and procedure described in section 4.3.4 were used. The only difference is the replacement of the MCR with the MC, as shown in Figure 73.

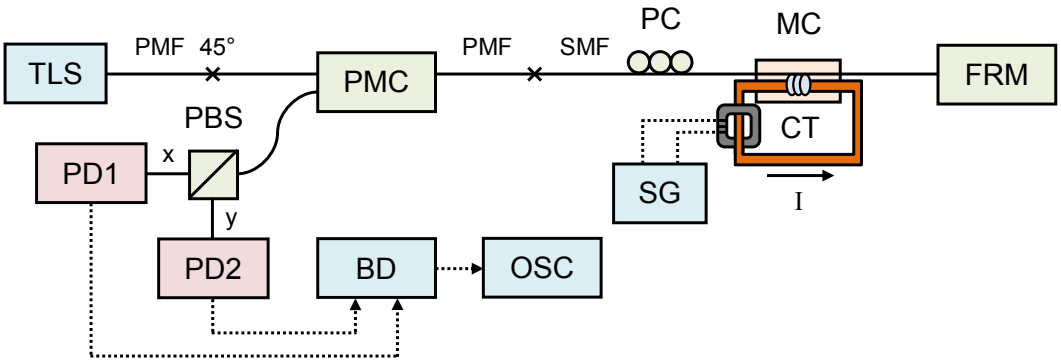

Figure 73. Schematic diagram of the experimental setup. TLS: tunable laser source, PMF: polarization-maintaining fiber, PMC: polarization-maintaining circulator, SMF: single-mode fiber, PC: polarization controller, MC: optical microfiber coil, CT: current transformer, SG: signal generator, FRM: Faraday rotator mirror, PBS: polarization beam splitter, PD: photodetector/photoreceiver, BD: balanced detector, OSC: digital oscilloscope.

4.5.7 Experimental results

The experimental results from Figure 74 show that the SOM-based MC samples were able to reach an average current responsivity of ~8.6 μrad/A that is 84% of the theoretical maximum of 10.2 μrad/A from Equation 4.20. This normalized value shows excellent agreement with $R = 0.841$ obtained from Equation 4.62, using a spin ratio of unity. In comparison, the unspun OM-based MC samples showed less consistency with an average linear responsivity of ~5.7 μrad/A. This indicates that spinning the OM offers a better suppression of Δn. Moreover, the reproducibility of unspun OMs is worse due to the unpredictable build-up of Δn during the coiling and packaging process. For the initial demonstration to prove the feasibility of fabricating SOMs and the advantages of the corresponding current sensors, noise analysis was not of critical importance.

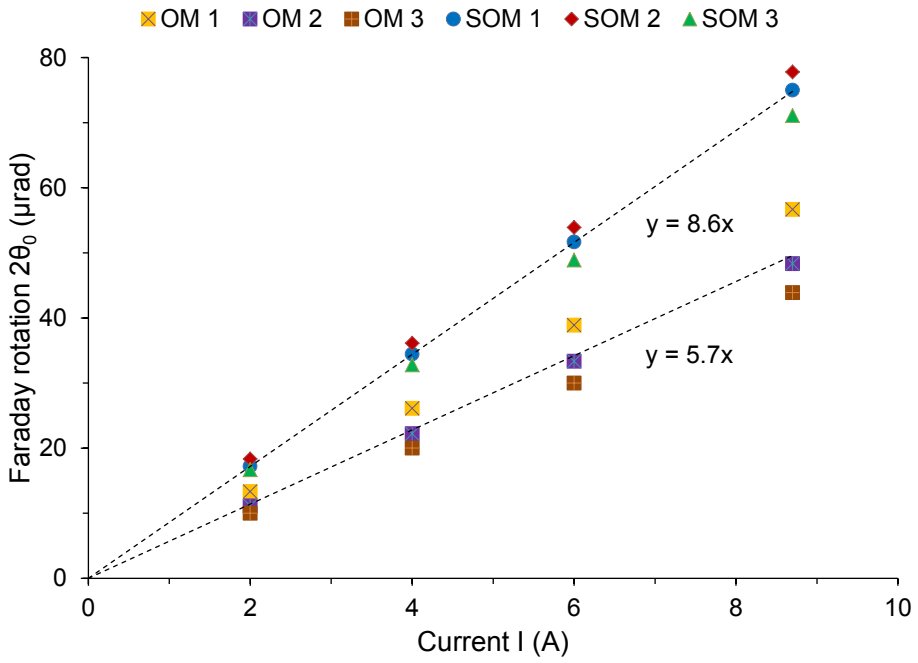

Figure 74. Measured current responsivity for spun and unspun microfibers at a signal frequency of 30 Hz, with average linear fits.

On the other hand, sensor heads comprising of SOM-based MCRs will always contain intrinsic linear birefringence. This is because the modal overlap in the coupling regions creates dielectric perturbations that lead to a self-modification of the propagation constant. While this effect sets the fundamental limit of linear birefringence in SOM-based MCRs, it is theoretically possible for this effect to be canceled out with the right magnitude of externally induced uniform linear birefringence. Nevertheless, SOM-based MCR samples were not fabricated and tested because there are further issues that will be addressed in the next section.

4.5.8 Conclusion

A simple yet cost-effective method to manufacture SOM from SMF-28 was proposed and demonstrated. Such fibers are very important for making practical MC- and MCR-based current sensors. The fiber polishing depth governs the linear birefringence of the hi-bi OM, the intrinsic birefringence of the SOM, and ultimately the resilience to bend- and packaging-induced linear birefringence. The fiber spin rate determines the circular birefringence of the SOM, the effective linear birefringence, and ultimately the efficiency of Faraday rotation. These two parameters can be optimized in conjunction with each other to yield a good balance between resilience to external effects and responsivity. From the preliminary results,

MC sensor heads made using SOM (2 μm diameter and 30 mm length, 7.5 turns, $\sim 1\times10^{-3}$ linear birefringence, 24π/cm spin rate) possessed higher responsivity and reproducibility than those made using unspun OM. These findings agree with expectations based on well-established results from conventional spun fibers.

To further increase the current responsivity, the spin rate can be increased for the same intrinsic linear birefringence. However, there is a trade-off with the higher susceptibility to external effects.

4.6 Efficient Faraday rotation in birefringent microfiber loop resonators

The optimization of resonantly enhanced Faraday rotation in MLRs exhibiting linear birefringence is presented in this section. For a sufficiently large birefringence-induced resonance separation, the evolution of differential phase between the polarized light in the two orthogonal axes can lead to efficient Faraday rotation when certain phase-matching conditions are met. This study provides the groundwork for designing MLR-based current sensors that can operate with near-maximum responsivity despite the presence of birefringence.

4.6.1 Introduction

Resonantly enhanced Faraday rotation was previously demonstrated in MCR-based current sensors (section 4.3). Yet, the observed enhancement factor was low due to the effect of linear birefringence (Δn_{eff}) and the arbitrary choice of geometry. Even small values of Δn_{eff} can drastically reduce the measured Faraday rotation due to the reversal in polarity every π interval in differential phase ($\Delta\varphi$), as shown by the sinusoidal dependence in Figure 75. For non-resonant sensors, this is a quarter of the polarization beat length (L_B) if the initial $\Delta\varphi$ of the sensor head was equal to zero or integer multiples of 2π. To extend the maximum usable fiber length to $L_B/2$, the initial $\Delta\varphi$ bias must equal $\pi/2$ or $3\pi/2$, plus integer multiples of 2π. This can be implemented in practice using a birefringent modulator or by selecting the appropriate fiber length, provided the birefringence is known. Even if the birefringence was eliminated using SOM, changes in $\Delta\varphi$ due to non-optimized inter-turn coupling can have an unpredictable effect on the current responsivity. In this section, geometrical optimizations are studied for the simpler MLR to overcome the OPL limitation. It can be shown that efficient Faraday rotation is feasible for birefringent sensor heads incorporating unspun OM, and maximum Faraday rotation can be obtained for non-birefringent sensor heads employing SOM.

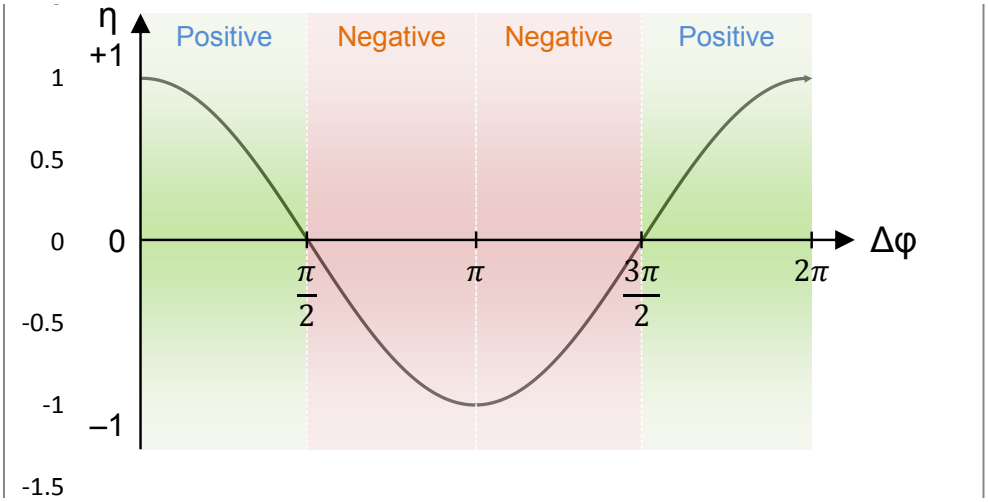

Figure 75. Dependence of Faraday efficiency ($\eta = \theta/\theta_{ideal}$) on differential phase.

4.6.2 Simulations

A MLR [55] can be fabricated from the uniform waist of a biconical fiber taper by forming a self-coupled loop in the region of close contact shown in Figure 76. As a current sensor, it is desirable for the Faraday Effect to occur at the resonant wavelength (λ_R), where light confinement is at its maximum and the OPL is considerably longer than the physical length of the loop (L_C). The MLRs discussed in this section are assumed to support only a single mode, which can be achieved in practice by limiting the OM diameter or ensuring an adiabatic taper transition from SMF-28. The initial $\Delta\varphi$ of the MLRs is also assumed to be zero.

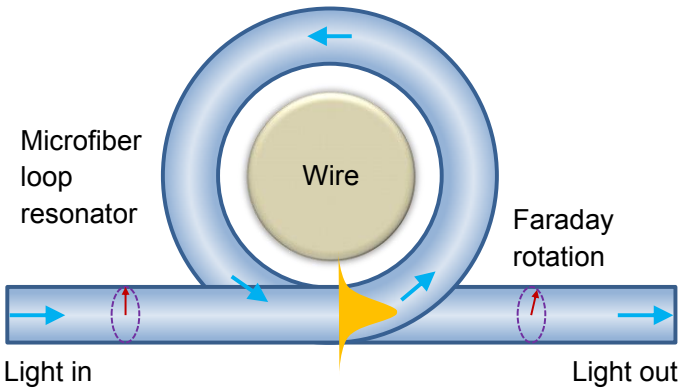

Figure 76. Schematic diagram of a microfiber loop resonator-based current sensor. The directions of light propagation and coupling are shown as arrows. The arrows in dashed-circles represent the Faraday rotation.

Figure 77(a) shows the ideal case in which Δn_{eff} is zero, which applies to perfect samples or those made using SOM. The eigenmodes of the two orthogonal axes

(denoted by X and Y) propagate with equal phase velocities and thus the Faraday rotation is at its maximum efficiency between eigenmodes with the same propagation distance. However, the light content at any point in the MLR is actually comprised of eigenmodes that have entered the resonator at different times. Only when operating at the precise wavelength of λ_R, can the maximum efficiency of Faraday rotation be maintained between the eigenmodes of different roundtrips. This is due to the mutual condition for on-resonance, in which the cumulated phase (φ) per roundtrip including the π/2 contribution from coupling is equal to an integer multiple of 2π, as illustrated in Figure 78(a). This value of φ can be translated into a set of values for L_C in terms of λ_R, the effective index (n_{eff}) of the eigenmode in the fast-axis, and an integer C:

$$\varphi = 2\pi C = \frac{2\pi}{\lambda_R} \cdot n_{eff} L_C + \frac{\pi}{2} \tag{4.65}$$

$$L_C = \frac{\lambda_R \cdot (C - 1/4)}{n_{eff}} \tag{4.66}$$

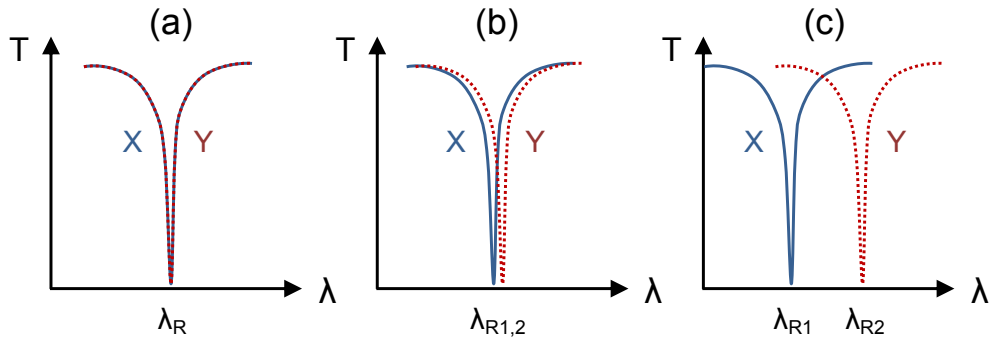

Figure 77. Transmission spectra of microfiber loop resonators, with (a) zero birefringence, (b) a small/moderate birefringence-induced resonance separation, and (c) a large birefringence-induced resonance separation.

In practice, Δn_{eff} is non-zero as a result of bend- and packaging-induced stresses in the MLR. Optical leakage into the support rod is another possible cause for birefringence and PDL. In those cases, λ_R of the eigenmodes are no longer identical due to different n_{eff}. Figures 77(b) and 77(c) illustrate the spectral-splitting phenomenon. For MLRs with a small to moderate birefringence-induced resonance separation ($\Delta\lambda_R$) shown in Figure 77(b), there is no mutual agreement in the requirement of φ between the eigenmodes of arbitrary roundtrips. Hence, no condition exists for efficient Faraday rotation.

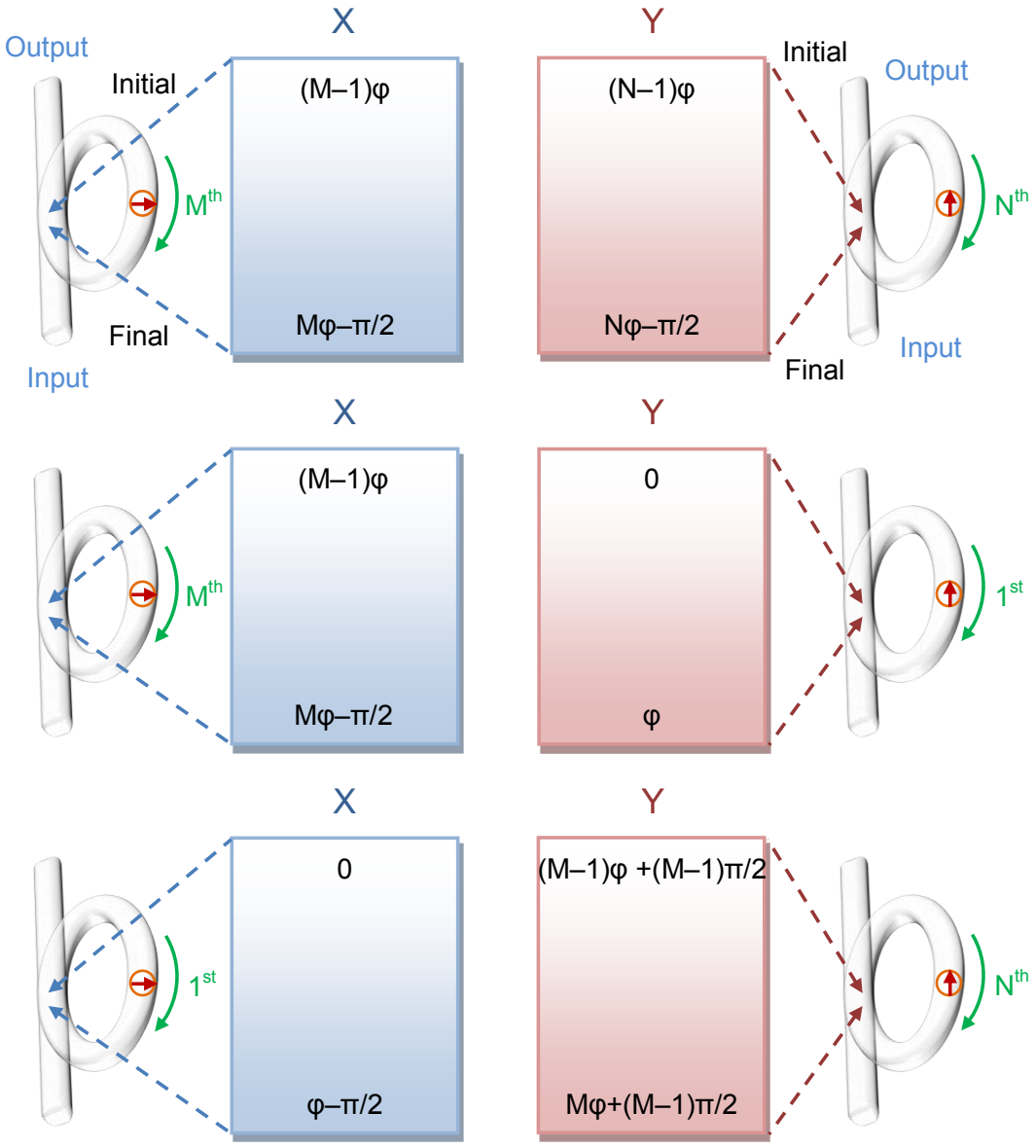

Figure 78. Roundtrip phase analysis for microfiber loop resonators operating at the resonant wavelength, with (a) zero birefringence, (b) X-eigenmode on-resonance with large birefringence-induced resonance separation (L_B = 4L_C), and (c) Y-eigenmode on-resonance with large birefringence-induced resonance separation (L_B = 4L_C). The initial phase (coupled in light) and final phase (prior to coupling back in) are labeled inside rectangles that represent the M^{th} and N^{th} roundtrip of the eigenmode in the fast- and slow-axes respectively.

For MLRs with a large birefringence-induced resonance separation (Figure 77(c)) such that, at a particular wavelength one eigenmode (e.g. X of fast-axis) experiences maximum recirculation while the other eigenmode (e.g. Y of slow-axis) is assumed to be uncoupled. The removal of the cumulative birefringence-induced phase

component in one axis simplifies the phase-matching conditions and efficient Faraday rotation between the eigenmodes of arbitrary roundtrips can be obtained with $L_B = 4L_C$ and φ (i.e. including $\pi/2$ from coupling and excluding $\pi/2$ from birefringence) equal to an integer multiple of 2π. Once again, this coincides with the on-resonance condition of the fast-axis. As shown in Figure 78(b), $\Delta\varphi$ only grows from 0 to $\pi/2$ during each roundtrip. Hence, Faraday rotation is uni-directional and accumulates with increasing OPL. Similarly, this value of φ can be converted into a set of values for L_C:

$$\varphi = 2\pi C = \frac{2\pi}{\lambda_R} \cdot n_{eff} L_C + \frac{\pi}{2} \tag{4.67}$$

$$L_C = \frac{\lambda_R \cdot (C - 1/4)}{n_{eff}} \tag{4.68}$$

The resonance separation $\Delta\lambda_R$ is related to Δn_{eff} by the following expression:

$$\frac{\Delta\lambda_R}{\lambda_R} = \frac{\Delta n_{eff}}{n_{eff}} \tag{4.69}$$

L_B can be expressed in terms of λ_R and Δn_{eff}:

$$L_B = \frac{\lambda_R}{\Delta n_{eff}} \tag{4.70}$$

By combining Equations 4.69 and 4.70 with $L_B = 4L_C$, another expression for the loop length is obtained:

$$L_C = \frac{\lambda_R^2}{4\Delta\lambda_R n_{eff}} \tag{4.71}$$

Equating Equations 4.68 and 4.71 produces a rule between integer C and $\Delta\lambda_R$:

$$C = \frac{\lambda_R}{4\Delta\lambda_R} + \frac{1}{4} \tag{4.72}$$

These geometrical design rules are very flexible. To start with, the user provides a desired resonant wavelength/turn length and the effective index of the fast-axis. From this information, Equation 4.71 produces a rough turn length/resonant wavelength that roughly satisfies the conditions for efficient Faraday rotation. This is then substituted into Equation 4.68 to find the integer C. The turn length/resonant wavelength is then updated to fully comply with the conditions for efficient Faraday

rotation. Lastly, the new/existing turn length can be used to deduce the linear birefringence and other parameters of interest, such as the free spectral range (FSR).

For MLRs of 0.5–1.5 mm loop diameter, $\Delta\lambda_R \approx 250$ pm would be sufficient to ensure that one eigenmode is maximally recirculated while the other is more or less uncoupled. For example, when $\lambda_R = 1550$ nm and $n_{eff} = 1.45$ (fast-axis), the result is $C = 1550$. From Equation 4.68, the loop circumference is $L_C = 1657$ μm and the loop diameter is 527 μm. From Equation 4.70, the beat length of $L_B = 6627$ μm corresponds to a linear birefringence of $\Delta n_{eff} = 2.339\times10^{-4}$. In practice, the magnitude of Δn_{eff} typically ranges from ~10^{-7} to ~10^{-4}.

In the conjugate case where the eigenmode (Y) in the slow-axis experiences maximum recirculation while the eigenmode (X) in the fast-axis is assumed to be uncoupled, efficient Faraday rotation between the eigenmodes of arbitrary roundtrips can be obtained with $L_B = 4L_C$ (i.e. lower bound) and φ (i.e. including π/2 from coupling and excluding π/2 from birefringence) equal to 3π/2 plus an integer multiple of 2π. Likewise, this condition naturally occurs at the on-resonance of the slow-axis. As shown in Figure 78(c), $\Delta\varphi$ only grows from 0 to π/2 during each roundtrip. Again, this value of φ can be converted into a set of values for L_C:

$$\varphi = \frac{3\pi}{2} + 2\pi C = \frac{2\pi}{\lambda_R} \cdot n_{eff} L_C + \frac{\pi}{2} \tag{4.73}$$

$$L_C = \frac{\lambda_R \cdot (C+1/2)}{n_{eff}} \tag{4.74}$$

Equating Equations 4.71 and 4.74 produces a rule between integer C and $\Delta\lambda_R$:

$$C = \frac{\lambda_R}{4\Delta\lambda_R} - \frac{1}{2} \tag{4.75}$$

For example, using $\Delta\lambda_R \approx 250$ pm with $\lambda_R = 1550$ nm and $n_{eff} = 1.45$ (fast-axis) again yields $C = 1550$. From Equation 4.74, the loop circumference is $L_C = 1657$ μm and the loop diameter is 528 μm. From Equation 4.70, the beat length of $L_B = 6630$ μm corresponds to a linear birefringence of $\Delta n_{eff} = 2.338\times10^{-4}$.

For simplicity, it was previously assumed that the eigenmode at off-resonance passes through the loop only once (i.e. uncoupled). Unaccounted for, a large portion of the guided light at λ_R actually couples out in the first instance, and thus avoids passing

through the loop. The phase delay associated with this portion of light is π/2. For the eigenmodes at on-resonance, a small portion of the guided light emerges from the loop with a phase delay of π/2, by coupling out straight-away. Although these eigenmodes do not follow the 2π roundtrip rule, their absence in the loop means the recirculating light undergoing efficient Faraday rotation is undisturbed. Hence, it is reasonable to neglect them in the designs rules as their phase has no impact on the Faraday Effect.

4.6.3 Conclusion

MLR-based current sensors which exhibit linear birefringence can greatly suppress Faraday rotation and thus reduces the current responsivity. Although efficient Faraday rotation naturally coincides with on-resonance, in the presence of linear birefringence a special relationship is required between the turn length and linear birefringence. It was shown that for MLRs with a sufficiently large birefringence-induced resonance separation, efficient resonantly enhanced Faraday rotation can arise when the loop circumference is a quarter of the beat length and the total roundtrip phase (i.e. including contributions from coupling and birefringence) of the eigenmodes in the fast- and slow-axis are equal to 2π and π/2 respectively for the fast-axis on resonance, or 3π/2 and 2π respectively for the slow-axis on resonance, all plus an integer multiple of 2π. These phase conditions can be translated into geometrical design rules that are important for fabricating MLR sensor heads which can facilitate an efficient build-up of Faraday rotation for multi-roundtrips despite the presence of linear birefringence. It would be of interest to demonstrate this experimentally, once the challenge of controlling the post-curing effective index can be overcome.

To further improve the Faraday efficiency and thus increase the current responsivity, it is possible to apply the same technique of initial differential phase biasing that doubles the maximum usable fiber length of non-resonator sensor heads. This has the effect of shifting the π/2 differential phase evolution window backwards (e.g. π/4) to incorporate a higher average Faraday efficiency. The width of the windows itself can be tailored depending on the magnitude of the achievable linear birefringence. Without phase biasing the maximum window width is π/2 (i.e. quarter beat length), and with phase biasing it becomes π (i.e. half beat length).

4.7 Birefringence treatment of non-ideal optical microfiber coils for continuous Faraday rotation

A flexible technique to periodically perturb the evolution of differential phase in birefringent OMs is proposed. This conceptual demonstration offers a simpler approach than the SOM to rectify non-ideal MC sensor heads with linear birefringence for high-performance current sensing. Furthermore, it can minimize resource- and time-consumption that will be beneficial for large-scale manufacturing.

4.7.1 Introduction

Previously in section 4.6, optimized MLRs rely on precise geometry in accordance to the magnitude of linear birefringence to ensure that any roundtrip of light initializes with a differential phase equal to an integer multiple of 2π, and exits with a differential phase of $\pi/2$ plus an integer multiple of 2π. For uncoupled MCs, an similar method of manipulating differential phase is explored with considerably lower design complexity than SOMs.

4.7.2 Simulations

By modifying the local birefringence at selective regions along the OM shown in Figure 79, a gain of $\pm\pi$ in differential phase between the polarized light in the two orthogonal axes of the birefringent OM can lift the device from a state that is on the brink of a reversal in Faraday rotation, to a state that is just emerging back into the same direction of Faraday rotation. Since the Faraday Effect is linearly proportional to the interaction length, each region must be kept as short as possible to minimize the negative contribution to the total Faraday rotation. The required birefringence modulation to achieve polarity-skipping for a given region length (L) is expressed by:

$$\Delta n_{eff} = \frac{\lambda}{2L} \tag{4.76}$$

As shown in Figure 80(b), the steady increase of differential phase with increasing distance along the OM is accompanied by the gradual reversal in Faraday efficiency in Figure 80(c). At the zero Faraday efficiency, Figure 80(a) shows a sharp rise in local birefringence that is sustained just long enough for the differential phase to grow by π, facilitating positive Faraday rotation once again in Figure 80(d).

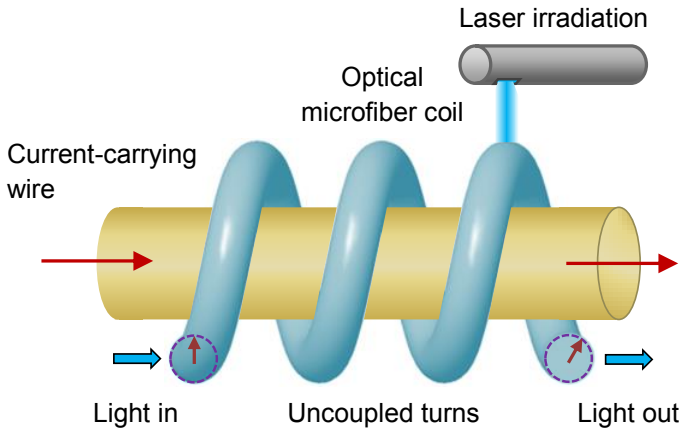

Figure 79. Schematic diagram of the birefringence modulation technique operating at selective regions along the microfiber coil. The directions of light propagation and coupling are shown as arrows. The arrows in dashed-circles represent the Faraday rotation.

This approach offers enormous flexibility and superior tolerance to both initial fabrication imperfections and post-fabrication treatment inaccuracies over existing techniques reported in literature for improving the total Faraday rotation (section 4.5). It is assumed that light only makes a single pass along the MC. By further assuming a uniform linear birefringence distribution along the OM, the procedure simply involves measuring the polarization beat length of a fabricated MC sample, before altering the local birefringence at initially a quarter of the beat length, and subsequently every half beat length interval. The birefringence modification can be performed by femtosecond laser irradiation, or by any other means that has control over the magnitude and spatial length of RI modulation along the MC without damaging the polymer packaging. The preciseness of the localized modification in terms of the position and width is not critical, as long as the change in differential phase can result in a rising Faraday efficiency to prolong the positive trend of the total Faraday rotation. Furthermore, improvements to the current responsivity from this post-fabrication treatment can be monitored in real-time.

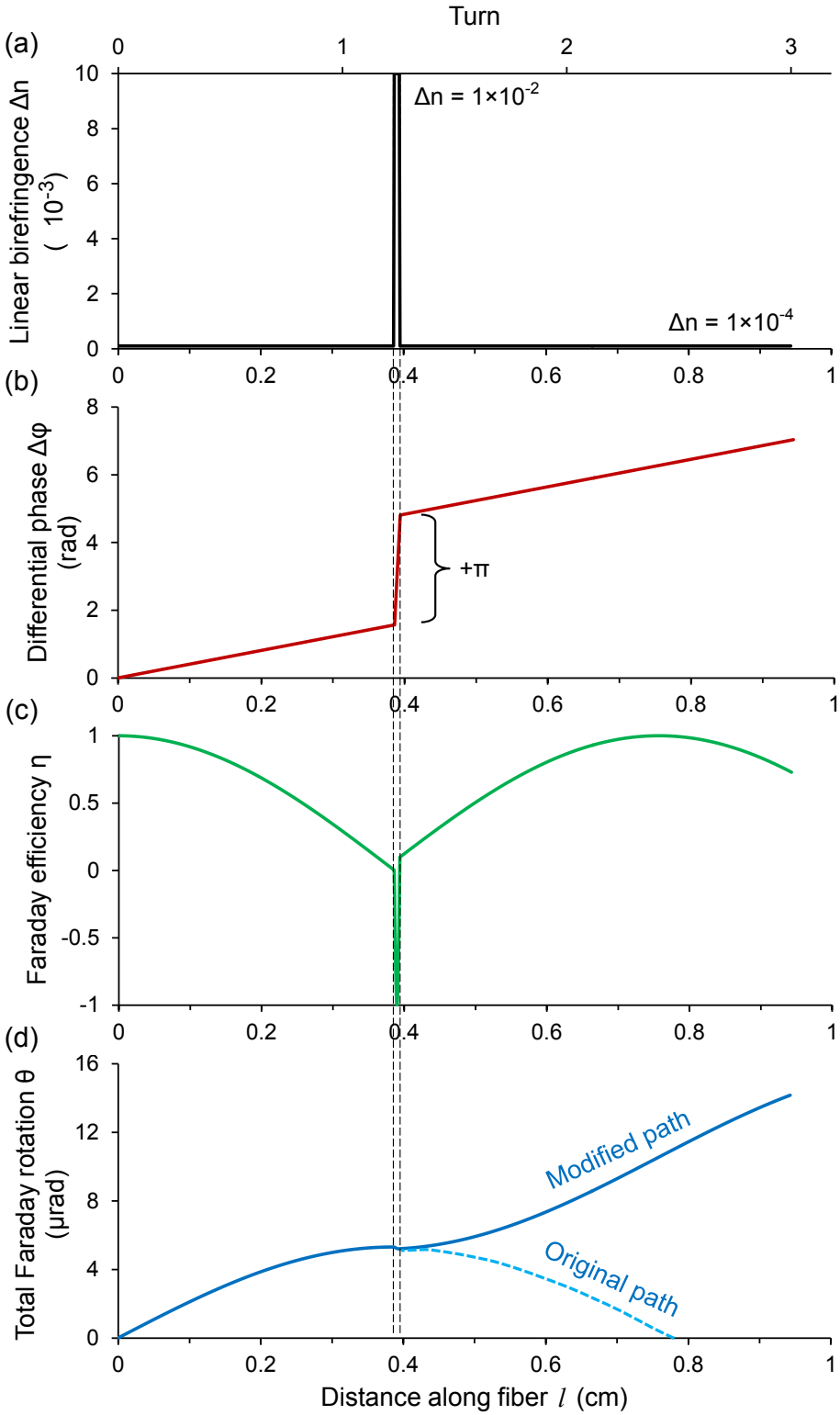

Figure 80. Simulations of birefringence modulation in a microfiber coil (λ = 1550 nm, $\mu_0 = 4\pi\times10^{-7}$, μ_r = 1, I_{DC} = 10 A, V = 0.54 rad/T.m, r = 0.5 mm) to rectify the direction of Faraday rotation for an efficient build-up of current responsivity over fiber length. The impact of changing (a) the local birefringence, is reflected in (b) the differential phase, (c) the Faraday efficiency, and (d) the total Faraday rotation.

4.7.3 Conclusion

Non-ideal MC sensor heads can be revived for high-performance current sensing via the proposed birefringence modulation technique. The birefringence at selective regions along the OM is modified to manipulate the evolution of differential phase that results in continuous Faraday rotation. This post-fabrication technique is highly flexible and exhibits great tolerance to both initial fabrication imperfections and post-fabrication treatment inaccuracies. From a practical point of view, it can minimize resource- and time-consumption that will be valuable for large-scale fabrications. Hence, it would be of interest to experimentally verify the predicted feasibility in future research.

To further increase the current responsivity, the modified sensor heads must be used in conjunction with a FRM to double the OPL and thus the total Faraday rotation. Since the returning eigenmodes occupy the orthogonal axis, the differential phase evolution is reversed and the Faraday efficiency trend for the backward propagation is a mirror image of that of the forward propagation. As a result, the total Faraday rotation is doubled. If an ordinary mirror is employed, then the fiber length is critical in the sense that the remaining fiber length after the final birefringence modulation must be less or equal to a quarter of the beat length. This will ensure that the differential phase does not exceed $\pm\pi$, and therefore prevent a reversal in the direction of Faraday rotation before returning to the nearest phase-correction point.

The topics covered in this chapter looked at ways of increasing the detection bandwidth; overcoming the OM length limitations with resonator designs; suppressing stability issues with passive and active compensation techniques; improving the OM fabrication process to increase tolerance to externally induced linear birefringence; optimizing resonator designs for efficient Faraday rotation; and rectifying non-ideal OM samples by manipulating the local birefringence. If one were to combine the detrimental effects of high-frequency current signals and linear birefringence-induced differential phase, the detection bandwidth of the sensor head can be abnormally extended at the cost of possible signal distortion and current ambiguity. Overall, most concepts were demonstrated experimentally, with a few exceptions in which the existing fabrication techniques need to be advanced, in order to deliver the level of precision required by the experiment.

4.8 References

1. P. A. Williams, A. H. Rose, G. W. Day, T. E. Milner, and M. N. Deeter, "Temperature dependence of the Verdet constant in several diamagnetic glasses", Appl. Opt., vol. 30, no. 10, pp. 1176-1178, 1991.

2. D. Wang, X. Zheng, A. Verevkin, R. Sobolewski, M. Mikulics, R. Adam, P. Kordos, and A. Mycielski, "Subpicosecond Faraday effect in Cd1-xMnxTe and its application in magneto-optical sampling", Appl. Phys. Lett., vol. 85, no. 17, pp. 3806–3808, 2004.

3. K. B. Rochford, A. H. Rose, M. N. Deeter, and G. W. Day, "Faraday effect current sensor with improved sensitivity-bandwidth product", Opt. Lett., vol. 19, no. 22, pp. 1903–1905, 1994.

4. L. Sun, S. Jiang, J. D. Zuegel, and J. R. Marciante, "Effective Verdet constant in a Terbium-doped-core phosphate fiber", Opt. Lett., vol. 34, no. 11, pp. 1699–1701, 2009.

5. J. L. Cruz, M. V. Andres, and M. A. Hernandez, "Faraday effect in standard optical fibers: dispersion of the effective Verdet constant", Appl. Opt., vol. 35, no. 6, pp. 922–927, 1996.

6. L. Sun, S. Jiang, and J. R. Marciante, "Compact all-fiber optical Faraday components using 65-wt%-terbium–doped fiber with a record Verdet constant of –32 rad/(Tm)", Opt. Express, vol. 18, no. 12, pp. 12191–12196, 2010.

7. L. Weller, K. S. Kleinbach, M. A. Zentile, S. Knappe, I. G. Hughes, and C. S. Adams, "An optical isolator using an atomic vapor in the hyperfine Paschen-Back regime", Opt. Lett., vol. 37, no. 16, pp. 3405–3407, 2012.

8. Y. Ruan, R. A. Jarvis, A. V. Rode, S. Madden, and B. Luther-Davies, "Wavelength dispersion of Verdet constants in chalcogenide glasses for magneto-optical waveguide devices", Opt. Commun., vol. 252, no. 1, pp. 39–45, 2005.

9. "Kigre M18 Faraday rotator glass datasheet", http://www.kigre.com/files /faradayglass.pdf, accessed on 04/01/2013.

10. H. O. Edwards, K. P. Jedrzejewski, R. I. Laming, and D. N. Payne, "Optimal design of optical fibers for electric current measurement", Appl. Optics, vol. 28, no. 11, pp. 1977–1979, 1989.

11. "MolTech MOS10 datasheet", http://www.mt-berlin.com/frames_cryst/descriptions /faraday.htm, accessed on 04/01/2013.

12. "XOAT MR4 datasheet", http://www.xaot.com/sdp/173803/4/cp-4304059/0 /Magneto-Optical_Glass.html, accessed on 04/01/2013.

13. "Toplent TG20 datasheet", http://www.toplent.com/Faraday%20rotatar%20 glasses.htm, accessed on 04/01/2013.

14. F. Araoka, M. Abe1, T. Yamamoto1, and H. Takezoe, "Large Faraday rotation in a π-conjugated Poly(arylene ethynylene) thin film", Appl. Phys. Express, vol. 2, no. 1, pp. 011501-1–3, 2009.

15. P. Gangopadhyay, G. Koeckelberghs, and A. Persoons, "Magneto-optic properties of Regioregular Polyalkylthiophenes", Chem. Mater., vol. 23, no. 3, pp. 516–521, 2011.

16. H. Yu, A. Argyros, G. Barton, S. G. Leon-Saval, and M. A. van Eijkelenborg, "Magneto-optical effect in cobalt nanoparticle doped polymer optical material", OECC/ACOFT, pp. 1–2, 2008.

17. G. W. Day, D. N. Payne, A. J. Barlow, and J. J. Ramskov-Hansent, "Faraday rotation in coiled, monomode optical fibers: isolators, filters, and magnetic sensors", Opt. Lett., vol. 7, no. 5, pp. 238–240, 1982.

18. J. Blake, P. Tantaswadi, and R. T. de Carvalho, "In-line Sagnac interferometer current sensor", IEEE Trans. Power Del., vol. 11, no. 1, pp. 116–121, 1996.

19. D. Kersey and D. A. Jackson, "Current sensing utilizing heterodyne detection of the Faraday effect in single-mode optical fiber", J. Lightwave Technol., vol. 4, no. 6, pp. 640–644, 1986.

20. A. H. Rose, S. M. Etzel, and K. B. Rochford, "Optical fiber current sensors in high electric field environments", J. Lightwave Technol., vol. 17, no. 6, pp. 1042–1048, 1999.

21. M. Belal, Z. Song, Y. Jung, G. Brambilla, and T. P. Newson, "Optical fiber microwire current sensor", Opt. Lett., vol. 35, no. 11, pp. 3045–3047, 2010.

22. X. Guo, Y. Li, X. Jiang, and L. Tong, "Demonstration of critical coupling in microfiber loops wrapped around a copper rod", Appl. Phys. Lett., vol. 91, no. 7, pp. 073512-1–3, 2007.

23. X. Zeng, Y. Wu, C. Hou, J. Bai, and G. Yang, "A temperature sensor based on optical microfiber knot resonator", Opt. Commun., vol. 282, no. 18, pp. 3817–3819, 2009.

24. M. Belal, Z. Song, Y. Jung, G. Brambilla, and T. P. Newson, "An interferometric current sensor based on optical fiber micro wires", Opt. Express, vol. 18, no. 19, pp. 19951–19956, 2010.

25. "Time-bandwidth product", http://www.rp-photonics.com/time_bandwidth _product.html, accessed on 02/12/2011.

26. T. A. Birks and Y. Li, "The shape of fiber tapers", J. Lightwave Technol., vol. 10, no. 4, pp. 432–438, 1992.

27. Y. Jung, G. Brambilla, and D. J. Richardson, "Efficient higher-order mode filtering in multimode optical fiber based on an optical microwire", AOE, SuB4, 2008.

28. M. Sumetsky, "Optical fiber microcoil resonator", Opt. Express, vol. 12, no. 10, pp. 2303–2316, 2004.

29. T. Lee, N. G. R. Broderick, and G. Brambilla, "Berry phase magnification in optical microcoil resonators", Opt. Lett., vol. 36, no. 15, pp. 2839–2841, 2011.

30. G. Brambilla, "Optical fibre nanotaper sensors", Opt. Fiber Technol., vol. 16, no. 6, pp. 331–342, 2010.

31. G. Brambilla, "Optical fibre nanowires and microwires: a review", J. Opt., vol. 12, no. 4, pp. 043001-1–19, 2010.

32. G. Y. Chen, T. Lee, Y. Jung, M. Belal, G. Brambilla, N. G. R. Broderick, and T. P. Newson, "Investigation of thermal effects on embedded microcoil resonators", CLEO/Europe, CH2_2, 2011.

33. Y. Chen, F. Xu, and Y. Lu, “Teflon-coated microfiber resonator with weak temperature dependence”, Opt. Express, vol. 19, no. 23, pp. 22923–22928, 2011.

34. F. Xu, P. Horak, and G. Brambilla, “Optimized design of microcoil resonators”, J. Lightwave Technol., vol. 25, no. 6, pp. 1561–1567, 2007.

35. Y. Jung, G. S. Murugan, G. Brambilla, and D. J. Richardson, “Embedded optical microfiber coil resonator with enhanced high-Q”, IEEE Photonic. Tech. L., vol. 22, no. 22, pp. 1638–1640, 2010.

36. M. Sumetsky, D. J. DiGiovanni, Y. Dulashko, J. M. Fini, X. Liu, E. M. Monberg, and T. F. Taunay, “Surface nanoscale axial photonics: robust fabrication of high-quality-factor microresonators”, Opt. Lett., vol. 36, no. 24, pp. 4824–4826, 2011.

37. G. Brambilla, F. Xu, and X. Feng, “Fabrication of optical fibre nanowires and their optical and mechanical characterisation”, Electron. Lett., vol. 42, no. 9, pp. 517–519, 2006.

38. N. Vukovic, N. G. R. Broderick, M. Petrovich, and G. Brambilla, “Novel method for the Fabrication of long optical fiber tapers”, IEEE Photonic. Tech. L., vol. 20, no. 14, pp. 1264–1266, 2008.

39. B. Culshaw, “The optical fibre Sagnac interferometer: an overview of its principles and applications”, Meas. Sci. Technol., vol. 17, no. 1, pp. R1–R16, 2006.

40. T. G. Giallorenzi, J. A. Bucaro, A. Dandridge, G. H. Sigel Jr., J. H. Cole, S. C. Rashleigh, and R. G. Priest, “Optical fiber sensor technology”, IEEE J. Quantum Electronics, vol. 18, no. 4, pp. 626–665, 1982.

41. “Piezoceramic materials”, http://www.piceramic.com/pdf/piezo_material.pdf, accessed on 28/02/2012.

42. “Piezoelectric ceramics”, http://lib.chipdip.ru/250/DOC000250624.pdf, accessed on 28/02/2012.

43. P. J. Raea and D. M. Dattelbaum, “The properties of poly(tetrafluoroethylene) (PTFE) in compression”, Polymer vol. 45 , no. 22, pp. 7615–7625, 2004.

44. “Teflon AF Properties”, http://www2.dupont.com/Teflon_Industrial/en_US/products /product_by_name/teflon_af/properties.html, accessed on 18/04/2012.

45. “Fused silica material properties”, http://accuratus.com/fused.html, accessed on 28/02/2012.

46. R. I. Laming and D. N. Payne, “Electric current sensors employing spun highly birefringent optical fibers”, J. Lightwave Technol., vol. 7, no. 12, pp. 2084–2094, 1989.

47. R. H. Stolen and E. H. Turner, “Faraday rotation in highly birefringent optical fibers”, Appl. Optics, vol. 19, no. 6, pp. 842–845, 1980.

48. G. W. Day, D. N. Payne, A. J. Barlow, and J. J. Ramskov-Hansen, “Faraday rotation in coiled, monomode optical fibers: isolators, filters, and magnetic sensors”, Opt. Lett., vol. 7, no. 5, pp. 238–240, 1982.

49. D. Tang, A. H. Rose, G. W. Day, and S. M. Etzel, “Annealing of linear birefringence in single-mode fiber coils: application to optical fiber current sensors”, J. Lightwave Technol., vol. 9, no. 8, pp. 1031–1037, 1991.

50. C. D. Perciante and J. A. Ferrari, “Cancellation of bending-induced birefringence in single-mode fibers: application to Faraday sensors”, Appl. Optics, vol. 45, no. 9, pp 1951–1956, 1991.

51. S. C. Rashleigh and R. Ulrich, “Magneto-optic current sensing with birefringent fibers”, Appl. Phys. Lett., vol. 34, no. 11, pp. 768–770, 1979.

52. J. Barlow, J. J. Ramskov-Hansen, and D. N. Payne, “Birefringence and polarization mode-dispersion in spun single-mode fibers”, Appl. Optics, vol. 20, no. 17, pp. 2962–2968, 1981.

53. D. N. Payne, A. J. Barlow, and J. J. R. Hansen, “Development of low- and high-birefringence optical fibers”, J. Quantum Elect., vol. 18, no. 4, pp. 323–334, 1982.

54. J. Qian, Q. Guo, and L. Li, “Spun linear birefringence fibres and their sensing mechanism in current sensors with temperature compensation”, IEE Proc.-Optoelectron., vol. 141, no.6, pp. 373–380, 1994.

55. C. Caspar and E. J. Bachus, “Fibre-optics micro-ring-resonator with 2mm diameter,” Electron. Lett., vol. 25, no. 11, pp. 1506–1508, 1989.

Chapter 5

5. Acceleration sensing with optical microfiber

This chapter initially explores the existing range of interferometers and phase demodulation schemes to identify their pros and cons, before discussing issues such as drifting, ambiguity, signal fading and noise. The benefits of combining OM with interferometry for acceleration sensing are then presented, with the experimental demonstrations of a FD accelerometer supported by simulations.

5.1 Interferometry

5.1.1 Introduction

Optical interferometry allows the measurement of extremely small (e.g. micro-radians) relative phase shifts in the optical fiber generated by the measurand. The phase delay of light passing through an optical fiber is given by:

$$\varphi = kn_{eff}L \tag{5.1}$$

where n_{eff} is the effective index seen by the guided mode, $k = 2\pi/\lambda$ is the propagation constant of light in free-space, λ is the wavelength of light, and L is the physical length of the optical fiber. $n_{eff}k$ is known as the propagation constant, $n_{eff}L$ is referred to as the OPL, and the difference between two OPLs is known as the optical path difference (OPD).

Small variations in the phase delay are found by differentiation of Equation 5.1:

$$\frac{\mathrm{d}\varphi}{\varphi} = \frac{\mathrm{d}L}{L} + \frac{\mathrm{d}n_{eff}}{n_{eff}} + \frac{\mathrm{d}k}{k} \tag{5.2}$$

The first two terms are related to physical changes in the optical fiber caused by the perturbation to be measured. The product of Δn and ΔL is ignored in the presence of other terms that are larger by a few orders of magnitude. The last term accounts for any wavelength variation associated with the laser source. The multi-parameter equation is an approximation that is adequate for interferometric systems but not for polarimetric-interferometric systems, because even the smallest components matter when calculating the change in differential phase.

Fiber-optic interferometers operate on the principle of interference between two or more beams of light within the optical fiber. Typically, external measurands cause the OPL of one beam to change (i.e. relative phase shift). The proceeding change in the OPD between the two interfering beams (i.e. differential phase change) then translates to an optical power modulation. The total power of the constructive/destructive wave-fronts is conserved. The output signal can be demodulated to obtain absolute or relative information about the measurand. It is important that the coherence length of the source must exceed the OPD, and the two beams should emerge with the same power and SOP in order to maximize the visibility of the interference pattern.

In the following sections, well-known fiber-optic interferometers are presented with comments on their unique qualities, followed by an outline of phase demodulation techniques to tackle the issues of drifting and ambiguity, and ending with a discussion on signal fading and noise sources.

5.1.2 Fiber-optic interferometer types

The measurand sensitivity (S_M) is related to the phase sensitivity (S_P) of the detection system and the responsivity (R) of the sensor. S_P is a function of the noise amplitude voltage (V_n), the signal amplitude voltage (V_s), and the fringe amplitude voltage (V_f). For small signals in a two-path interferometric system using the balanced detection scheme operating in the linear regime, it is more intuitive to express S_M as the measurand (M) divided by the SNR:

$$S_M = \frac{S_P}{R} \approx \frac{\frac{V_n}{V_f}}{\left(\frac{V_s}{V_f}\right)/M} = \frac{M}{\mathrm{SNR}} \tag{5.3}$$

5.1.2.1 Mach–Zehnder interferometer

There are several interferometric configurations that are commonly used in fiber-optic sensing, with the MZI (Figure 81) widely regarded as the simplest type. MZIs are classified depending on whether they are intrinsic, extrinsic or in-line. The intrinsic MZI can be implemented using a multi-core fiber, whereas the extrinsic MZI is the standard two-fiber configuration. The in-line MZI is based on a pair of abrupt down-taper and up-taper, where the modes initially escape the core due to the

non-adiabatic taper diameter profile and propagate a short distance in the cladding layer before recombining at the second stage.

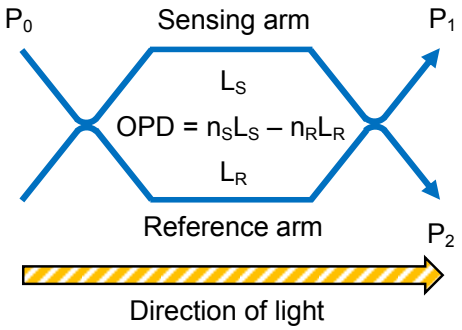

Figure 81. Schematic diagram of the fiber-optic Mach–Zehnder interferometer.

The two paths of the interferometer are typically named the sensing arm and the reference arm. Often, the reference arm is shielded from the environment and only the sensing arm is exposed to the measurand. This is not a requirement, and in some sensors both arms are used for sensing in either differential or push-pull configurations to increase the responsivity of the transducer.

For equal input powers, the output powers are related to the relative phase shift ($\Delta\varphi$) by the following expression [1]:

$$P_{1,2} = \frac{P_0}{2} \cdot (1 \pm V \cos \Delta\varphi) \tag{5.4}$$

where $\Delta\varphi = (2\pi/\lambda).(\text{OPD})$, P_0 is the input power of light, λ is the wavelength of light, and V is the interference visibility.

The Mach–Zehnder arrangement has a significant advantage in that it has better immunity to common-mode effects when a balanced detection scheme is employed, ideally with equal powers in the two ports. The complimentary outputs of the MZI are subtracted and normalized by the total received power (i.e. real-time processing is more effective than using an average value during post-processing) to give an output in the form of:

$$T = \frac{P_1 - P_2}{P_1 + P_2} = \cos \Delta\varphi \tag{5.5}$$

The FSR of a MZI is the wavelength or frequency separation between successive transmitted maxima or minima:

$$\Delta\lambda_{FSR} = \frac{\lambda^2}{\mathrm{OPD}} \tag{5.6}$$

$$\Delta f_{FSR} = \frac{c}{\mathrm{OPD}} \tag{5.7}$$

where c is the speed of light in free-space, OPD = $n.\Delta L$ for two-path interferometry, and OPD = $\Delta n.L$ for polarimetric interferometry.

5.1.2.2 Michelson interferometer

The MI (Figure 82) has extremely flexible geometry in addition to the high responsivity that it shares with the MZI. MIs are either extrinsic or in-line. Extrinsic MIs use the standard two-fiber configuration that is terminated by a pair of mirrors or FRMs. In-line MIs are based on an abrupt down-taper followed by an end-reflection, similar to the working principles of the in-line MZI.

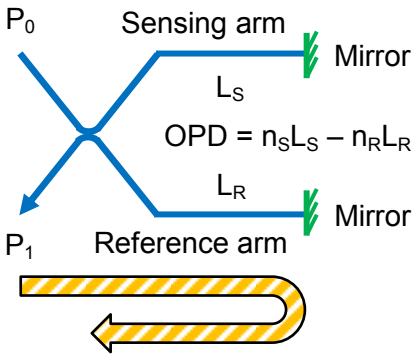

Figure 82. Schematic diagram of the fiber-optic Michelson interferometer.

Light in the two-path interferometer propagates to the end of the arms before being reflected back by mirrors. The two beams recombine at the coupler similar to the MZI (i.e. single-output) and any phase difference is translated into an optical power modulation. For non-reciprocal modulations in the sensing arm (e.g. Faraday Effect), FRMs can be used instead of mirrors to rotate light by 90° such that it travels back in the orthogonal axis. The result is beneficial reversal of changes in SOP (e.g. thermally or strain-induced phase noise) that minimize the impact of external perturbations.

The FSR of a MI can similarly be expressed as:

$$\Delta\lambda_{FSR} = \frac{\lambda^2}{2\times\mathrm{OPD}} \tag{5.8}$$

5.1.2.3 Fabry–Perot interferometer

FPIs (Figure 83) can be made into compact probes for high spatial resolution measurements, and they are often used as high-resolution optical spectrometers. There are three distinct types of FPIs, namely intrinsic, extrinsic and in-line. The intrinsic FPI uses mirror coatings in an optical fiber by fusion-splicing end-coated fibers to form the interferometer. The extrinsic type uses an optical cavity formed by the air gap between two uncoated fiber end-faces, held together by epoxy resin. Lastly, the in-line FPI comprises of two fibers fusion-spliced to a section of hollow-core fiber.

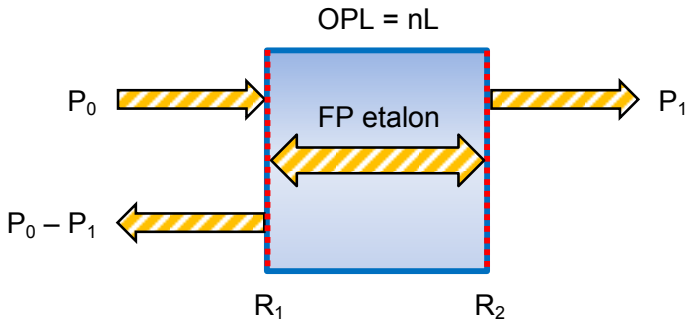

Figure 83. Schematic diagram of the fiber-optic Fabry–Perot interferometer.

In a Fabry–Perot etalon, a beam of light undergoes multiple reflections between two reflecting surfaces, and the resulting optical transmission or reflection is periodic in wavelength. The expression for FPI transmission is given below [2]:

$$P_T = P_0 \cdot \left(\frac{(1-R_1)^2 \cdot (1-R_2)^2}{(1-R_1R_2)^2 + 4\sqrt{R_1R_2}\sin^2\left(\frac{2\pi \cdot \mathrm{OPL}}{\lambda}\right)} \right) \tag{5.9}$$

where R_1 and R_2 denote the end-face reflectivities, n is the RI of the cavity medium, and L is the cavity length.

The FSR of a FPI is the wavelength separation between successive transmitted or reflected maxima or minima:

$$\Delta\lambda_{FSR} = \frac{\lambda^2}{2 \times \mathrm{OPL}} \tag{5.10}$$

5.1.2.4 White-light interferometer

White light interferometry (WLI) (Figure 84) possesses a considerable advantage with regard to the ability to provide absolute and unambiguous measurements compared with homodyne and heterodyne interferometry. An unbalanced MI is used to interrogate a Fabry–Perot etalon by creating two optical paths of interest. One path is formed between the first boundary of the FPI and the longer arm of the MI. The other path consists of the second boundary of the FPI and the shorter arm of the MI. When the OPD between these two paths falls within the coherence length of the white light source, interference fringes are produced. It must be pointed out that the beating between different wavelengths of light produce difference and sum of frequency components that are too fast to be detected. Instead, the average effect of the constructive and destructive interferences is observed over time. Compared to two-path interferometry, the interference visibility is lower and falls with increasing differential path length because the superposition of different optical frequencies is inefficient, and the predictability of the phase relationship is gradually lost.

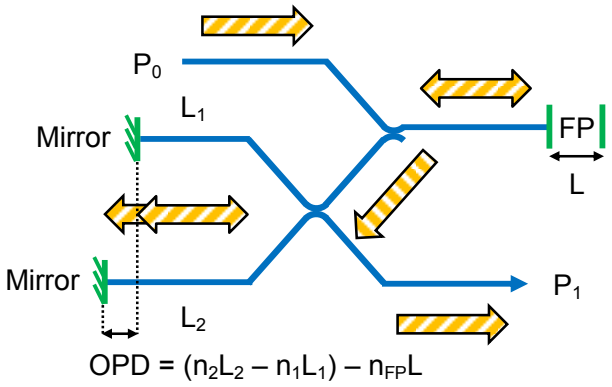

Figure 84. Schematic diagram of the fiber-optic white light interferometer.

The separation between the central fringe envelope (zero-order fringe) and the adjacent fringe (first-order fringe) corresponds to the exact OPL, and the spectral width is inversely proportional to the source bandwidth. Unwanted Fabry–Perot cavities formed by connection interfaces do not contribute to the interferometric output due to the small coherence length.

5.1.2.5 Sagnac interferometer

The Sagnac interferometer (Figure 85) has been principally used to measure rotation and has established itself over the years to replace mechanical and ring-laser gyros in traditional applications as well as opening new navigation and guidance opportunities. Two types of fiber-optic gyros are being developed. The first is an open-loop configuration and these fiber-optic gyros are generally used for low-cost applications where dynamic range and linearity are not crucial. The second is the closed-loop fiber-optic gyro that are primarily targeted at medium to high accuracy navigation systems that have high turning rates and require high linearity and large DR. The basic idea consists in using feedback control that cancels the Sagnac phase shift by adding a controlled phase delay.

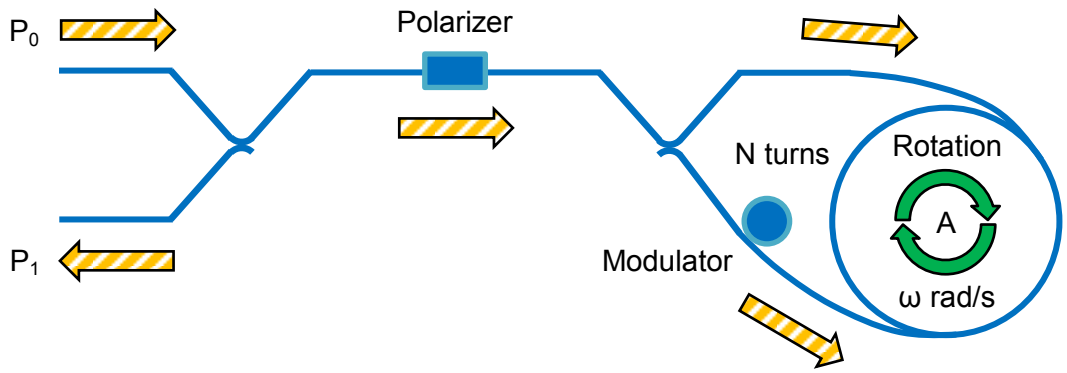

Figure 85. Schematic diagram of the fiber-optic Sagnac interferometer.

For a rotating optical fiber coil, two beams of light traveling in opposite directions experience different OPLs, which results in different transit times and a phase difference between the two paths. This relative phase shift is generally written as [3]:

$$\Delta\varphi = \frac{8\pi N n_{eff}}{\lambda c} \cdot A \cdot \omega \tag{5.11}$$

where N is the number of coil turns, n_{eff} is the effective index seen by the guided mode, c is the speed of light in free-space, A is the area enclosed by the optical fiber coil, and ω is the angular frequency.

5.1.2.6 Passive ring resonator

Fiber-optic ring resonators (Figure 86) do not require facets or gratings to create an optical cavity and are thus particularly suited for monolithic integration with other

fiberized components. Ring resonators consist of a closed-loop optical waveguide, coupled to one or more input/output waveguides. Similar waveguides exist in the form of open loops, knots and 3-dimensional coils.

When light of the appropriate wavelength (i.e. resonant wavelength) is coupled to the loop, it builds up in intensity over multiple round-trips due to constructive interference, while the output port emerges with destructive interference. Since only certain wavelengths are enhanced within the loop, it can also function as an add-drop filter with the addition of a second coupling region. For resonance to take place, the roundtrip phase must be an integer multiple (m) of 2π. Equivalently, the OPL of the loop must be a positive integer multiple of λ:

$$\mathrm{OPL} = m\lambda \tag{5.12}$$

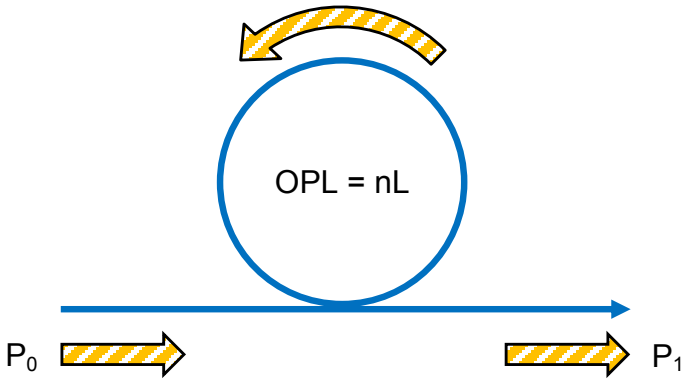

Figure 86. Schematic diagram of the fiber-optic passive ring resonator.

The Q-factor of an optical resonator is defined as 2π times the ratio of the stored energy to the energy dissipated per oscillation cycle. Or equivalently, the ratio of the resonant wavelength (λ_R) to the FWHM linewidth ($\Delta\lambda_{FWHM}$) of the resonance shape:

$$Q = \frac{\lambda_R}{\Delta\lambda_{FWHM}} \tag{5.13}$$

The finesse of an optical resonator is related to the resonator losses and it is independent of the resonator length. A high finesse enables a high spectral resolution in a wide spectral range:

$$F = \frac{\Delta\lambda_{FSR}}{\Delta\lambda_{FSR}} \tag{5.14}$$

The FSR of a ring resonator is the wavelength separation between successive resonances:

$$\Delta\lambda_{FSR} = \frac{\lambda^2}{\mathrm{OPL}} \tag{5.15}$$

5.1.3 Phase demodulation

It is evident from the sinusoidal output of an interferometer shown in Figure 87 that a detection system generally experiences the highest SNR when operating at a quadrature point. From another perspective, the phase sensitivity is at its maximum because the noise-equivalent phase is at its lowest value, despite producing a higher shot noise than operating at a minima. Consequently, the measurand sensitivity is optimal when operating at a quadrature point. On the contrary, this is not true for an ideal detection system that is shot noise-limited with a perfect interference visibility, because the phase and measurand sensitivities are optimal when operating at a minima.

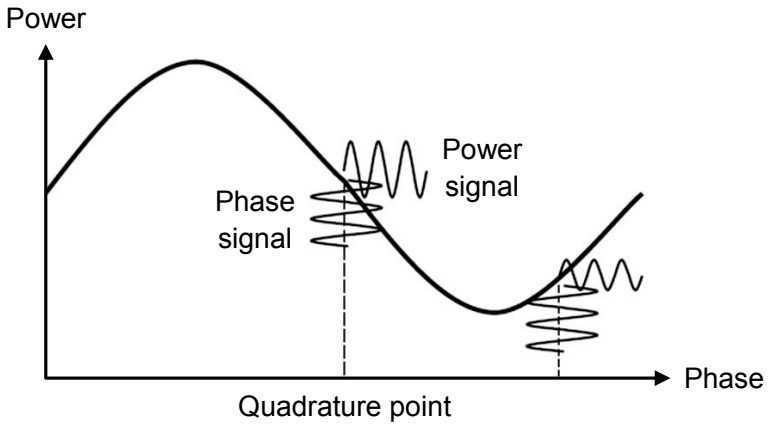

Figure 87. Different magnitudes of phase-induced optical power modulation along an interference fringe.

In practice, interferometers are nearly always biased at a quadrature point due to a non-ideal detection system. However, all-fiber interferometers are very sensitive by nature. Their performances are highly susceptible to degradation by drifting and ambiguity. Any change in ambient conditions can cause $\Delta\varphi$ to drift away from a quadrature point. When excited by a single monochromatic source, there is a further issue with the unambiguous range of a simple interferometric sensor, where it is limited to a single interference fringe.

5.1.3.1 Active homodyne

A common solution is the active-phase-tracking homodyne [4], where the signal and reference beams of the interferometer are coherently mixed without any frequency shift in either of the beams. In this case, the signal of the measurand is taken from the error correction signal in the feedback control that keeps the output signal at a quadrature point. Figure 88 shows a simple way of regulating the OPD for a two-path interferometer, by wrapping the optical fiber around a cylindrical piezo-electric transducer (PZT). The feedback signal derived from the detector output is fed back into the PZT element. By introducing a relative phase shift ($\Delta\varphi_m$) to the existing phase difference ($\Delta\varphi_0$), the quadrature point can be held so that: $\Delta\varphi_0 + \Delta\varphi_m = (2i + 1) \times \pi/2$, where i is an integer number.

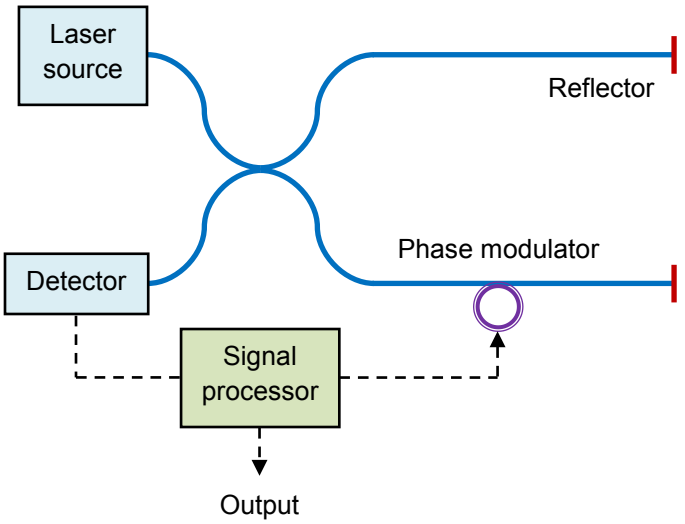

Figure 88. Schematic diagram of a fiber-optic interferometer with feedback control.

Although this scheme is easy to implement and relatively linear in its operation, there are a number of drawbacks. For example, the scheme uses an electrically active element, which may not be suitable in hazardous environments. Additionally, the method is incapable of absolute fringe referencing and can only track multiple fringe shifts correctly if the tracking process remains uninterrupted. Furthermore, although the theoretical limit of relative phase shift exceeds 2π, in practice it is ultimately limited by the maximum phase change obtainable with the PZT. Larger phase excursion may require resetting the system, with consequent loss of information.

Rather than using dL or dn_{eff} to vary φ, a more elegant method [5] uses the dk term of Equation 5.2, where the value of λ corresponding to a quadrature point is maintained using feedback control. The advantage is that no electrically active elements are required in the interferometer. The disadvantage is that to convert the wavelength shift to a relative phase shift, a non-zero OPD is required, which may allow ambient phase noise to be the limiting factor of the measurand sensitivity.

5.1.3.2 Passive techniques

A number of approaches have been developed to allow passive interrogation (no feedback control) of fiber-optic interferometric sensors. Techniques providing the sensing information encoded on carrier signals include phase-generated carrier homodyne [6], synthetic heterodyne [7], and differential delay heterodyne [8]. In these approaches, an electro-optic device produces the modulation. Optical approaches to passive demodulation include schemes based on optical biasing using 3×3 couplers [9], polarization selection [10] and path-matched differential interferometry [11]. For large relative phase shifts, the Fast Fourier Transform of the interferometric signal allows sinusoidally modulated measurands to be tracked with a reasonable degree of accuracy in the frequency domain [12].

5.1.4 Signal fading

It is evident with true monochromatic light that the interference visibility is unity if the power of the two interfering beams is equal, and the SOP in the two arms of an interferometer is identical. Conversely, the visibility is zero if all power is in one beam or the SOP of the two beams are orthogonal. The phenomenon of polarization-induced signal fading can arise in interferometric systems when the SOP of the interfering beams drift randomly due to polarization mode conversion. This could occur as a result of transversely-oriented changes in the measurand, asymmetric variations in the ambient temperature, or shifts in the position of the fiber. Well-known solutions to this problem are PM components and active polarization control.

5.1.5 Noise sources

The key components of any interferometric system are the laser that provides the optical signal, the optical fiber which guides light through the system, the fiber-optic couplers that split light to and from the arms of the interferometer, and the detectors

which detect the incident optical power. All of these components are commercially available. The performance of each component impacts the overall system performance. The noise of an electro-optic system comprises of four main sources: (a) noise associated with the laser source; (b) fundamental photon noise limit; (c) noise associated with the detector and amplifier electronics; and (d) noise associated with the digital oscilloscope.

Noise originating from the laser source powering the interferometer can be separated into intensity and frequency noise. Relative intensity noise caused by gain medium fluctuations has an incoherent component that can be suppressed by time-domain averaging, and a coherent component that can only be eliminated by subtracting the two complementary outputs of the interferometer using a balanced detection scheme. Frequency noise is mostly caused by cavity/grating perturbations. Any variation in λ is converted to phase noise by the interferometer, and it is linearly proportional to the path imbalance. This can be minimized by using feedback control to lock λ to that of a stable reference. Lastly, $1/f$ noise contributes to both intensity and frequency noise. Although it widely occurs in nature, not much is known about its exact theory and it remains a current research interest.

The detector noise generated by a planar diffused photodiode operating in the reverse-bias mode is a combination of shot noise and thermal noise. Shot noise is the fundamental photon noise limit generated by random fluctuations of current flowing through the photoreceiver, which may be dark current (I_d) or photocurrent (I_p). The combined shot noise produced by the dark current (i.e. leakage current generated by bias voltage) and the photocurrent (i.e. from optical input signal) is a function of the total current, the electron charge (q), and the noise bandwidth (Δf) [13]:

$$I_{n(shot)} = \sqrt{2q \cdot \left(I_d + I_p\right) \cdot \Delta f} \tag{5.16}$$

The thermal noise of the detector is a function of Boltzmann's constant (k), temperature (T), shunt resistance (R_s) and Δf [13]:

$$I_{n(thermal)} = \sqrt{\frac{4kT\Delta f}{R_s}} \tag{5.17}$$

Another contribution is amplifier noise, which is a function of the amplifier input leakage current (I_a), amplifier input noise voltage (V_a), radial frequency (ω), and total input capacitance seen by the amplifier (C_T) [13]:

$$I_{n(amplifier)} = \sqrt{I_a^2 + (V_a \omega C_T)^2} \tag{5.18}$$

Lastly, digital oscilloscopes add noise due to the analog front-end and digitizing process. This must be taken into account as it degrades the signal measurement accuracy, especially for low-level signals and high detection bandwidth operation.

The system noise is the quadratic sum of laser intensity and frequency noise, shot noise, thermal noise and amplifier noise. Apart from the laser frequency noise that is non-white, they all have a flat power spectral density. Applying N running averages will reduce the white noise by a factor of $\sqrt{N}$, but at the cost of increasing the measurement time by a factor of N. Furthermore, low-frequency noise is not observable in short time-frames, and high-frequency noise is not detectable with an insufficient number of data points. Despite these noise sources, the typical single-mode fiber-optic interferometer is an intrinsically quiet device. Generally, the main noise source associated with uncompensated systems is ambient thermal fluctuations acting on the transduction element in the sensing arm, causing unwanted phase noise.

5.2 Compact flexural disc-based acceleration sensor

The proof-of-principle demonstrations of an OM-based, centrally supported FD accelerometer are presented in this section. An acceleration responsivity of 4.0 rad/g and an acceleration sensitivity of 2.0 mg were achieved using an OM measuring only 10 μm in diameter and 60 mm in length. A detection bandwidth in excess of 1 kHz was observed with a disc of 25 mm diameter. The small minimum bend radii and reduced fiber size can facilitate high device compactness and high responsivity at the same time. FDs attached with different OM lengths, diameters and spatial configurations are theoretically modeled, and experimentally confirmed with two FD sensor heads of different OM lengths and diameters. An automated technique is also proposed to achieve higher packing density of spirally wound OM.

5.2.1 Introduction

Accelerometers play an important part as existing and next-generation tools for inertial navigation, guidance systems, earthquake monitoring, platform stabilization for space applications, vibration monitoring in machinery, vehicles, vessels, and portable electronics such as free-fall sensors. Fiber-optic accelerometers have several inherent advantages over micro-electromechanical-systems-based accelerometers, such as higher responsivity and better immunity to EMI. To-date, optical accelerometers have been reported in many different forms, with the most extensively researched being compliant cylinders/mandrels [14, 15] and central/edge-supported FDs [12, 16–18], which are interferometry-based. Other types include hollow/multi-core fibers [19, 20], micro-loop resonators [21], weighted reflective diaphragms [22], and FBGs [23]. In-fiber designs are highly compact but are limited by low responsivity. Although designs based on compliant cylinders/mandrels and weighted reflective diaphragms showed some positive attributes, notably very high responsivity around ~10^4 rad/g [14], they also exhibit low detection bandwidth that is typically below 1 kHz. FD designs exhibit poor responsivity in small packages. Previously, as much as 75 m of SMF-28 has been used in bulky FD designs to reach high responsivity [18]. Still, FD designs have detection bandwidths up to several kilohertz that is higher than most configurations. For portable applications where weight and size requirements are stringent, FDs face a serious design problem.

In this section, a solution is presented in the form of an OM-based, centrally-supported FD accelerometer. This design has the potential to achieve higher compactness and higher responsivity than conventional FDs that use standard optical fibers or even bend-insensitive fiber (BIF). The OMs used have diameters in the region of 2–10 μm, meaning that small bend radii of the order of millimeters can be achieved [24] without inducing significant PDL and depolarization of light. Therefore, high compactness is feasible without deterioration in expected performance. A smaller disc size also constitutes a higher fundamental frequency and thus a higher detection bandwidth. Since OMs have remarkably small diameter and low stiffness, massive lengths can be packed onto the surface of a regular-sized disc (i.e. diameter in excess of several centimeters), leading to a larger response to strain and thus a higher responsivity to acceleration.

5.2.2 Theory

Figure 89 illustrates the working principle of the accelerometer sensor head consisting of a centrally supported FD with spirally wound OM bound to both sides of the disc using a thin layer of adhesive polymer coating. Axial acceleration causes extensive strain in one fiber spiral and compressive strain in another, providing a push-pull enhancement and effectively doubling the accelerometer's response while providing common-mode rejection of environmental effects. This subsequently translates to a phase modulation that can be measured with a MI.

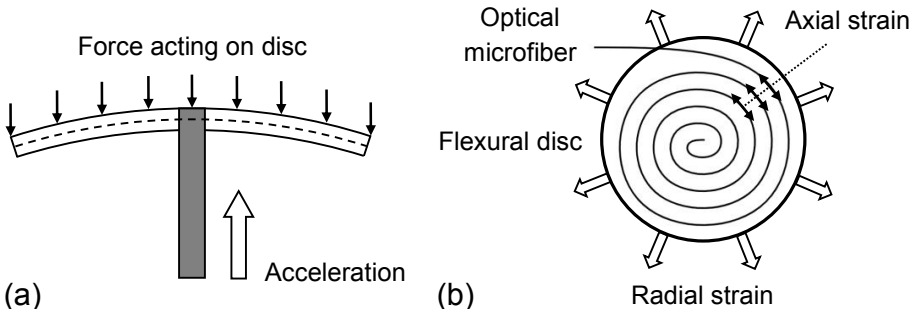

Figure 89. (a) Schematic diagram of the equivalent force/pressure imposed on the flexural disc resulting from acceleration, and (b) the top view of the disc showing radial strain translating into axial strain on the optical microfiber.

To predict the responsivity of the OM-based FD accelerometer, the behavior of the device under acceleration was modeled. The equation for the angular displacement

of centrally supported disc under a uniform force or pressure (Δp) on its top surface is shown by [25]:

$$\theta(r) = \frac{M_{rb}}{F_L} \cdot rF_5(r) + \frac{Q_b}{F_L} \cdot r^2 F_6(r) - \frac{\Delta p}{F_L} \cdot r^3 G_{14}(r) \tag{5.19}$$

where $M_{rb} = -\frac{\Delta p \cdot a^2}{C_8} \cdot \left[\frac{C_9}{2ab} \cdot (a^2 - b^2 - L_{17})\right]$ is the unit radial bending moment,

$C_8 = \frac{1}{2} \times \left[1 + v + (1 - v) \cdot \left(\frac{b}{a}\right)^2\right]$ is a plate constant,

$C_9 = \frac{b}{a} \cdot \left[\frac{1+v}{2} \cdot \ln\left(\frac{a}{b}\right) + \frac{1-v}{4} \cdot \left[1 - \left(\frac{b}{a}\right)^2\right]\right]$ is a plate constant,

$L_{17} = \frac{1}{4} \times \left[1 - \frac{1-v}{4} \cdot \left[1 - \left(\frac{b}{a}\right)^4\right] - \left(\frac{b}{a}\right)^2 \cdot \left[1 + (1 + v) \cdot \ln\left(\frac{a}{b}\right)\right]\right]$ is a loading constant,

$F_5(r) = \frac{1}{2} \times \left[1 - \left(\frac{b}{r}\right)^2\right]$ is a plate function,

$F_6(r) = \frac{b}{4r} \cdot \left[\left(\frac{b}{r}\right)^2 - 1 + 2\ln\left(\frac{r}{b}\right)\right]$ is a plate function,

$Q_b = \frac{\Delta p \cdot (a^2 - b^2)^2}{2b}$ is the unit shear force,

$G_{14}(r) = \frac{1}{16} \times \left[1 - \left(\frac{b}{r}\right)^4 - 4 \times \left(\frac{b}{r}\right)^2 \cdot \ln\left(\frac{r}{b}\right)\right]$ is a plate function,

$F_L = \frac{E \cdot (2h)^3}{12 \times (1 - v^2)}$ is the flexural modulus,

a is the disc radius, b is the central support radius, $2h$ is the disc thickness, E is the effective Young's modulus, and v is the effective Poisson ratio.

As depicted in Figure 90, if $\theta(r)$ is the angle subtended by the tangent at a radial distance r from the disc center to the horizontal, then the horizontal displacement of a point at a distance z from the original neutral surface is approximately χ. If the solid line is taken as the neutral surface then a point on the disc, at a distance z along the normal to the neutral surface, will undergo a displacement in the x direction. The local strain in the disc at radius r and distance z from the neutral surface is then calculated by:

$$\frac{\chi}{r} = \frac{z \sin[\theta(r)]}{r} \tag{5.20}$$

The acceleration-induced strain of the disc material (χ/r) is taken as the strain transferred to the OM ($\Delta L/L$) of length L, since the disc model use effective parameters that accounts for loading effects of the OM. For small angular displacements of an OM loop wound on the surface of the disc, z is replaced by h:

$$\Delta L \approx 2\pi h\theta(r) \tag{5.21}$$

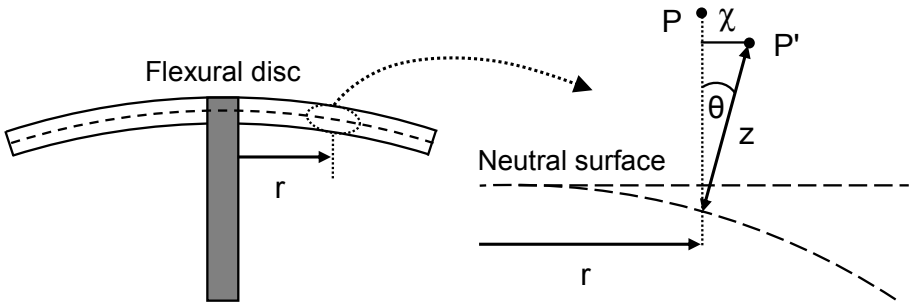

Figure 90. Schematic diagram of the displacements in a flexing disc.

In the FD model, there are two approximation errors that cancel out during a flexing motion: (a) the new fiber circumference is measured from the horizontal distance rather than from the hypotenuse (i.e. negative error); and (b) the transverse reference line is fixed instead of being shifted closer towards the center (i.e. positive error). Therefore, only the bend angle determines the change in fiber length. As one might expect, the maximum change occurs at 90° when the flexing motion is at its maximum.

When the FD is incorporated into the sensing arm of a MI and subjected to vertical acceleration, the reference arm and the standard optical fiber sections of the sensing arm outside the FD can be disregarded due to their constant phase delay. The relative phase shift ($\Delta\varphi$) consists of two key contributions, one from the physical length change (ΔL) of the OM and the other from the change in effective index (Δn_{eff}) due to the stress-optic effect. The stress-optic effect of silica OMs is assumed to be the same as bulk silica and approximately equal to doped silica fibers [26]. A third term that describes the physical change in OM diameter can be neglected:

$$\frac{\Delta\varphi}{\varphi} = \frac{\Delta L}{L} + \frac{\Delta n_{eff}}{n_{eff}} \tag{5.22}$$

where $\varphi = (2\pi/\lambda).n_{eff}.\Delta L$, n_{eff} is the effective index seen by the guided mode, and λ is the wavelength of light.

The second term can be shown to be –21.3% and –5.5% of the first term (section 5.2.5), for silica and polymer respectively. The fraction of power that resides in the core of 2 μm and 10 μm diameter embedded OMs is ~73% and ~99% respectively (section 2.3.3). Hence, the second term is roughly –17% and –21% of the first term, for a 2 μm and 10 μm diameter OM respectively. A factor of η is used to account for the responsivity reduction due to the stress-optic effect:

$$\frac{\Delta\varphi}{\varphi} = \eta \cdot \frac{\Delta L}{L} \tag{5.23}$$

The relative phase shift for a double-pass configuration using only one side of the disc is expressed by:

$$2\Delta\varphi = 4\pi \times \frac{n_{eff}\eta\Delta L}{\lambda} \tag{5.24}$$

The pressure responsivity is given by the following:

$$\frac{2\Delta\varphi}{\Delta p} = 4\pi \times \frac{n_{eff}\eta\Delta L}{\lambda\Delta p} \tag{5.25}$$

Assuming that mass is uniformly distributed throughout the disc, the responsivity to pressure is then converted into a responsivity to acceleration (A) knowing that pressure is force per unit area, force is the product of mass and acceleration, and mass is the product of volume and density (ρ):

$$\Delta p = 2h\rho A \tag{5.26}$$

Finally, the acceleration responsivity in terms of rad/g can be deduced by approximating the total OM length (L_{total}) as the sum of nested OM rings:

$$\frac{2\Delta\varphi}{A} = 9.81 \times 8\pi \times \frac{h\rho n_{eff}\eta\Delta L_{total}}{\lambda\Delta p} \tag{5.27}$$

It is desirable for the accelerometer to exhibit a constant responsivity with varying signal frequency (i.e. flat frequency response) such that acceleration can be detected without significant distortion. However, the fundamental frequency of the FD sets an upper limit on the detection bandwidth (B_w). An approximate expression for B_w is

shown below [16, 18], where Λ^2 is the resonance frequency parameter [27] from plate vibrations theory:

$$B_w = \frac{\Lambda^2 h}{\pi a^2} \cdot \sqrt{\frac{E}{12\rho \cdot (1-v^2)}} \tag{5.28}$$

5.2.3 Fabrication

The following section describes the design and fabrication process for the FD using OM diameters of 2 and 10 μm. The sensors were built in three stages. Firstly, it was necessary to consider the layout of the OM on the surface of the disc. The arrangement style is very important, since it determines the maximum length of OM that can be efficiently utilized. Two kinds of spatial arrangement for the OM are illustrated in Figure 91. To achieve high responsivity, it is necessary to pack as much OM as physically possible onto the disc surface. For the purpose of demonstration, the design in Figure 91(a) was chosen as it was the easiest to produce without the aid of automated machinery. It must be stressed that OMs are particularly difficult to handle as the uniform waist cannot be touched, in order to evade contamination. The design shown in Figure 91(b) avoids the problem of passing the returning OM over the overlaid OM on the disc surface, but is more difficult to fabricate by hand.

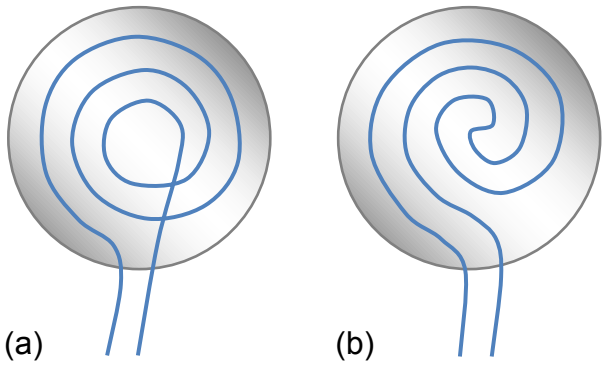

Figure 91. Schematic diagram of two possible optical microfiber arrangements on the surface of a flexural disc.

Thermal expansion has a strong influence on the phase drift of the accelerometer when incorporated into an interferometer. Therefore, a pyrolytic graphite material with a low coefficient of thermal expansion was selected for the construction of the disc. The composite structure is reasonably stiff to ensure efficient transfer of strain from the disc to the OM. The dimensions of the disc were chosen for a good balance

between responsivity and B_w. It measures 25 mm in diameter and 0.5 mm in thickness. The central support was made using a metal screw of 3 mm diameter, and was securely attached to the underside of the disc for mounting onto the PZT shaker. The total weight of the disc plus screw was ~4 g.

OMs have a strong evanescent field since they confine light through a large RI difference between the solid core and its surrounding medium. Therefore, adjacent loops within the spiral must be sufficiently separated to prevent unwanted coupling. In practice, because of the error in positioning the OM on the FD, OMs with diameters in excess of 2 μm should have a separation distance of at least 20 μm. At λ = 1550 nm, an OM of 2 μm diameter embedded in a polymer with RI of n = 1.373 guides light in a single mode, whereas an OM diameter of 10 μm enables multi-mode transmission. However, the larger diameter OM may experience lower absorption and scattering effects, due to less light propagating in the polymer cladding outside the OM. Moreover, the bend radius is still small enough to avoid significant PDL. The key advantage of using larger diameters is the ease of handling when winding long lengths of OM on the disc surface.

For the second stage, the fabrication of the OM was developed based on the procedure described in section 3.2.3. The resulting OM of 2 μm diameter and 10 mm length at the uniform waist had reasonable lengths of SMF-28 fiber pigtails kept for convenient integration with other fiberized components. In the final stage, the OM was bound to the top side of the disc with low-RI, UV-curable polymer (Efiron PC-373 AP) in a U-shape arrangement at 8 mm from the disc center, which will be denoted as Sample 1. The optical loss of Sample 1 was ~0.5 dB at λ = 1550 nm, and it was attributed to Rayleigh and Mie scattering due to the presence of micro-bubbles and particles in the polymer.

Likewise, Sample 2 with an OM of 10 μm diameter, 60 mm length was manufactured in the same way. The OM length of Sample 2 was sufficient to demonstrate the feasibility of the spiral arrangement shown in Figure 91(a). The 10 μm diameter OM has the capacity to support multiple modes. For that reason, the taper diameter profile of both samples was designed to be near-adiabatic with ψ = 0.1 [28], such that excitation of higher-order modes was significantly suppressed [29]. The OM was wound 1.5 turns at 6 mm from the disc center, on the top side of

the disc. The loss of Sample 2 was ~2.5 dB at λ = 1550 nm. The higher loss was attributed to the longer uniform waist length and possible bend loss [30] induced by the overlaying point in the spiral arrangement, as the curvature radius of the underlying polymer-cladded OM could be relatively small.

For both samples, a thin layer of polymer was initially deposited on the surface of the disc. In the case of Sample 2, a localized deposition of polymer resin was made at the point of contact between the first and second windings for two purposes: (a) to prevent mode coupling; and (b) to reduce bending loss when the top OM curves over the bottom OM. A final layer of polymer was added after the OM spiral was wound on the disc to provide good confinement of light. Lastly, the polymer was UV-cured to bind the OM and disc together for efficient strain transfer, as well as to provide geometrical stability and robust packaging. Nonetheless, the amount of polymer deposited was kept to a minimum to preserve the flexibility of the disc. Moreover, drifts in the ambient temperature can otherwise cause undesirable thermal expansion and contraction of the polymer that will be transferred to the OM, inducing unpredictable shifts in the phase of the interferometer.

In order to achieve the full potential of the sensor head, the entire disc surface would need to be packed with a dense spiral of OM. Controlling the separation distance in such circumstances will be exceedingly difficult by hand. A new setup with an automated method of winding the OM in a spiral pattern is envisaged in Figure 92. The first step is to hang the OM loosely above the center of the FD such that it can be inserted inside the fiber groove etched on the disc. A small quantity of polymer is to be deposited along the groove before and after the OM is placed inside, to avoid mode coupling between the OM and subsequent windings of OM on the surface. The strip of polymer can be cured with UV light from the lamp to secure it in place. The ejected polymer from the micropipette bonds the suspended OM to the rotating disc. The UV lamp cures the freshly embedded OM for geometrical stability. The translation stage slowly scans from the center to the edge of the disc to control the spacing between each winding of the OM. The micropipette can be fitted with an actuator that is controlled by a computer to regulate its throughput rate. The same computer can simultaneously control the rotator module and the translation stage.

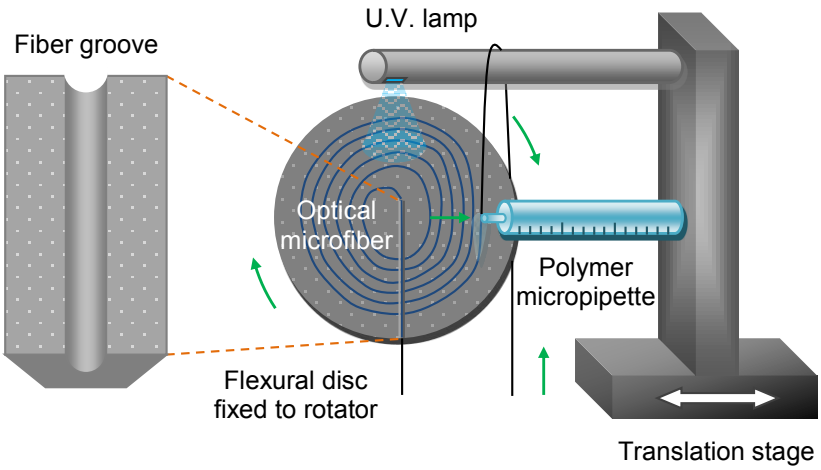

Figure 92. Proposed automated winding technique for long microfibers. The arrows indicate the direction of motion.

5.2.4 Experimental setup

The setup shown in Figure 93 was used to test the accelerometer. Linearly polarized light at a wavelength of λ = 1550 nm from a TLS (Agilent 81940A) was launched into the MI consisting of a coupler (50:50 for sensing/reference arms). The FD sensor head was connected to a FRM forming the sensing arm, and another FRM was attached to the reference arm of near-equal length (±1 cm) and near-equal loss (bending method). The coherence length of light was minimized to ~4 m by suppressing the laser linewidth of the TLS. The use of FRMs ensured that random changes in the SOP along the two arms canceled out. The double pass also provided a means to increase the total phase change. The FD was mounted on a PZT shaker, which was controlled by a SG. The returning light was collected by a photoreceiver (New Focus 1811) and sampled by an AC-coupled oscilloscope (Agilent DSO6034) on 25 MHz bandwidth-limited mode, with 1000 data points per measurement and 64 running averages.

The relative phase shift between the modes in the sensing and reference arms is governed by the initial OPL-induced phase difference ($\Delta\phi$) plus any time-dependent phase noise caused by the ambient environment, and the acceleration-induced phase modulation with amplitude $2\Delta\varphi_0$, radial frequency $\omega = 2\pi f$ and initial phase Φ:

$$\Delta\varphi = \Delta\phi + 2\Delta\varphi_0 \cos(\omega t + \Phi) \tag{5.29}$$

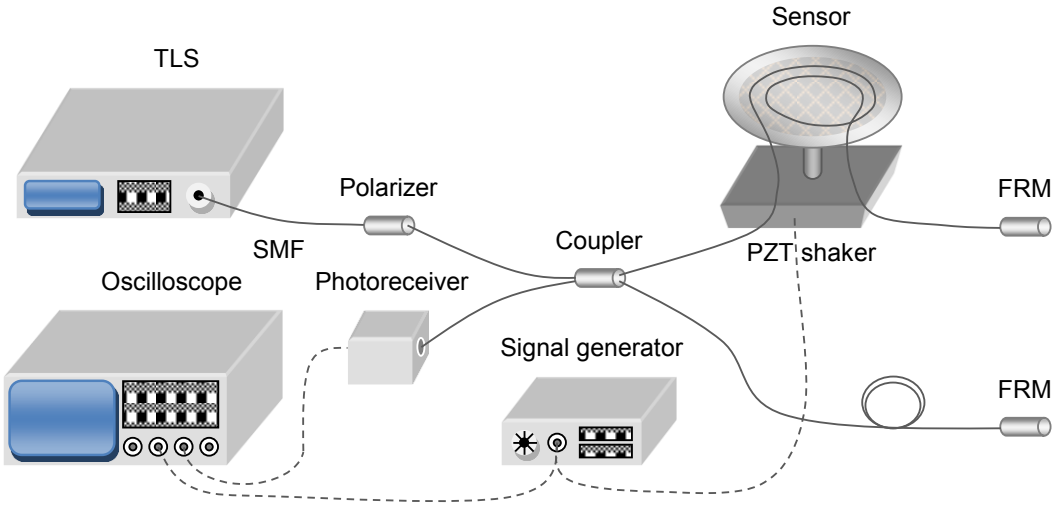

Figure 93. Schematic diagram of the experimental setup. TLS: tunable laser source, SMF: single-mode fiber, PZT: piezo-electric transducer, FRM: Faraday rotator mirror.

The output power of the MI can be generally written as:

$$P = A + B\cos\Delta\varphi \tag{5.30}$$

The constants A and B are linearly proportional to the input power, with B also dependent on the visibility of the interferometer. It is assumed that the PZT shaker generates negligible heating effects. Equation 5.30 can be written purely in terms of the acceleration-induced contribution to the total $\Delta\varphi$ at a quadrature point where $\Delta\phi$ is equal to $\pi/2$ (plus integer multiples of π). Due to the AC-coupled operation, the DC term is discarded:

$$P = -B\sin[2\Delta\varphi_0\cos(\omega_0 t + \Phi)] \tag{5.31}$$

Since only the modulation amplitude is of interest, Equation 5.31 can be further simplified to:

$$P_{amp} = B\sin(2\Delta\varphi_0) \tag{5.32}$$

The maximum relative phase shift is therefore related to the signal amplitude and the measured fringe amplitude:

$$2\Delta\varphi_0 = \sin^{-1}\left(\frac{P_{amp}}{B}\right) \tag{5.33}$$

The double-pass relative phase shift is given by $2\Delta\varphi_0$. The output voltage polarity of the detection system depends not only on the direction of vertical acceleration but also on the initial $\Delta\phi$ and the signal processing. Equation 5.33 is only valid for relative phase shifts under a quarter of a fringe ($2\Delta\varphi_0 < \pi/2$), before tracking fringes become necessary. Fringe-tracking techniques were not used as the phase modulation was sub-fringe.

During the characterization of the fabricated sensors, the TLS wavelength was swept and an average interference fringe period of $\Delta\lambda \approx 100$ pm was observed for the MI. Hence, the quadrature condition in Equation 5.33 can easily be achieved by tuning the input wavelength.

A Fabry–Perot etalon was used to measure the acceleration of the PZT shaker. It was constructed by aligning the end of a suspended flat-cleaved fiber to a small, light-weight mirror fixed at the disc center, mounted on the PZT shaker. The maximum displacement of the PZT shaker from its neutral position was calculated by counting the number of fringes (N) between the center and peak of an oscillation:

$$= \frac{N\lambda}{2} \tag{5.34}$$

N can be obtained accurately by including any fractional fringes using arc-sine and arc-cosine functions. Figure 94 shows an example set of interference fringes. It is possible to resolve sub-fringes once the fringe amplitude has been determined. The acceleration was then calculated from the second derivative of displacement:

$$|A| = \omega_0^2 \ = 2\pi^2 N\lambda f^2 \tag{5.35}$$

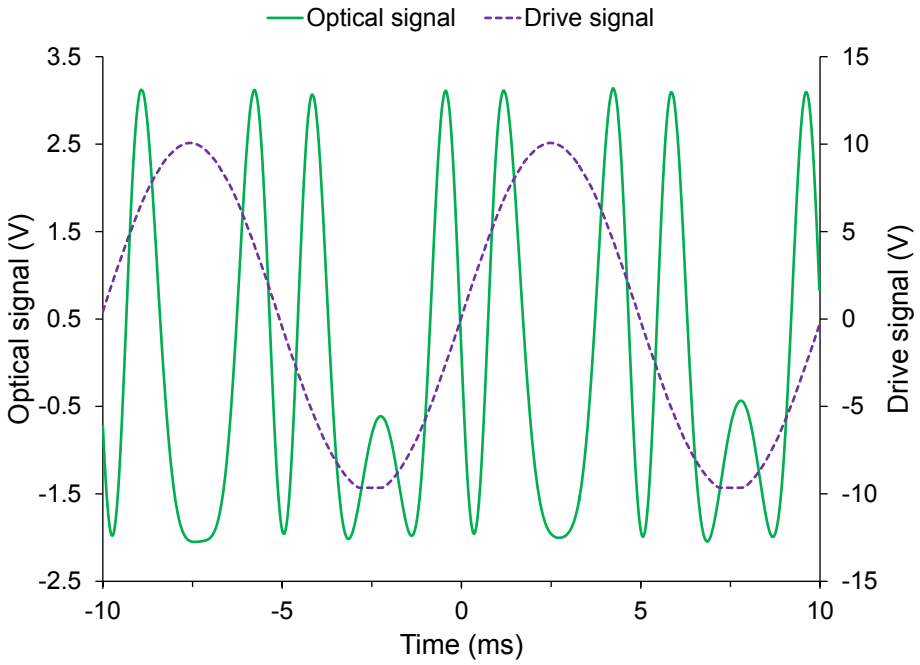

Figure 94. Example fringe analysis for the Fabry–Perot reference interferometer.

5.2.5 Simulations

To compare the responsivity and B_w of different FD accelerometers (double-pass, single-sided), Equations 5.27 and 5.28 were explored with disc parameters that are altered accordingly with the fiber length (L) and diameter (D). The disc geometry was chosen to be much smaller than the traditional FD designs, and it consists of: a = 12.5 mm, b = 1.5 mm, and h = 0.25 mm.

The following parameters are considered for the FD model, using pyrolytic graphite [31, 32] as the disc material: Λ^2 = 4.235, ν_{disc} = –0.15, E_{disc} = 4.8 GPa, and ρ_{disc} = 2250 kg/m^3. Likewise, for the silica OM [33]: ν_{silica} = 0.17, E_{silica} = 73 GPa, ρ_{silica} = 2200 kg/m^3, n_{silica} = 1.45, and λ = 1550 nm. Lastly, for the polymer coating [34]: $\nu_{polymer}$ = 0.4, $E_{polymer}$ = 0.1 GPa, $\rho_{polymer}$ = 1550 kg/m^3, and $n_{polymer}$ = 1.373.

The impact on the responsivity by increasing L at a fixed distance from the disc center (r) is shown in Figure 95 for D = 2 µm and 10 µm, with comparison to that of the SMF-28 model. It is clear that L has a positive influence on the phase response to acceleration. The difference widens between D = 2 µm, 10 µm and 125 µm, as L increases. The responsivity of the SMF-28 model is noticeably outperformed by the OM models at longer lengths due to the greater stiffness of larger fiber diameters and the larger negative stress-optic contribution of silica compared with polymer, despite

increasing the effective disc density. This shows that OM models can achieve higher responsivity per unit length than the SMF-28 model.

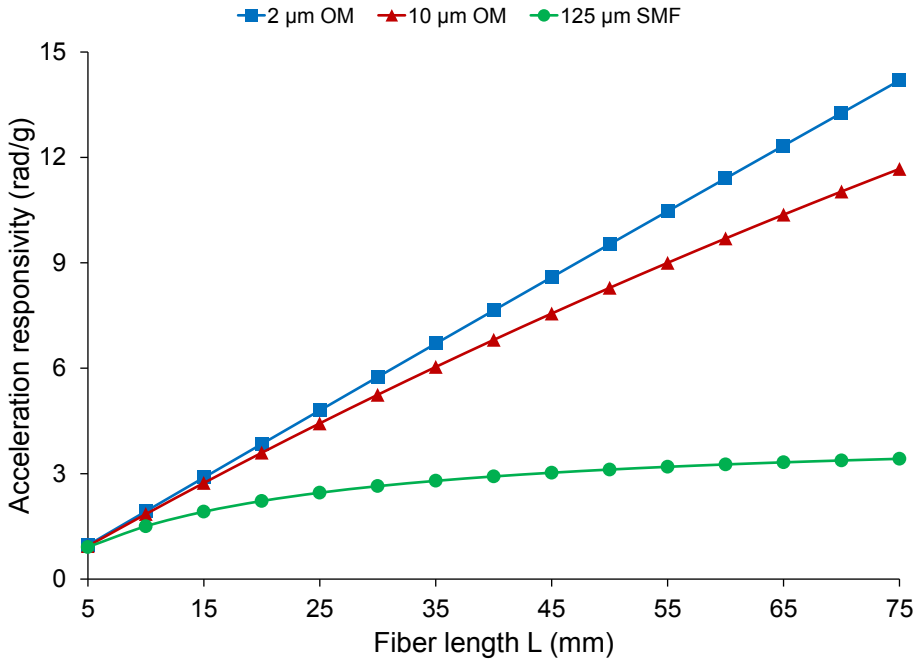

Figure 95. Simulated relationship between the fiber length and the acceleration responsivity, for different fiber diameters at $r = 12$ mm.

Figure 96 shows the effect of increasing r with a fixed value of L. It can be seen that the responsivities are generally very low close to the base of the central support due to the inability of the disc to flex. However, as r increases the responsivities gradually ascend to an asymptotic value due to the convergence of axial strain away from the fixed boundary.

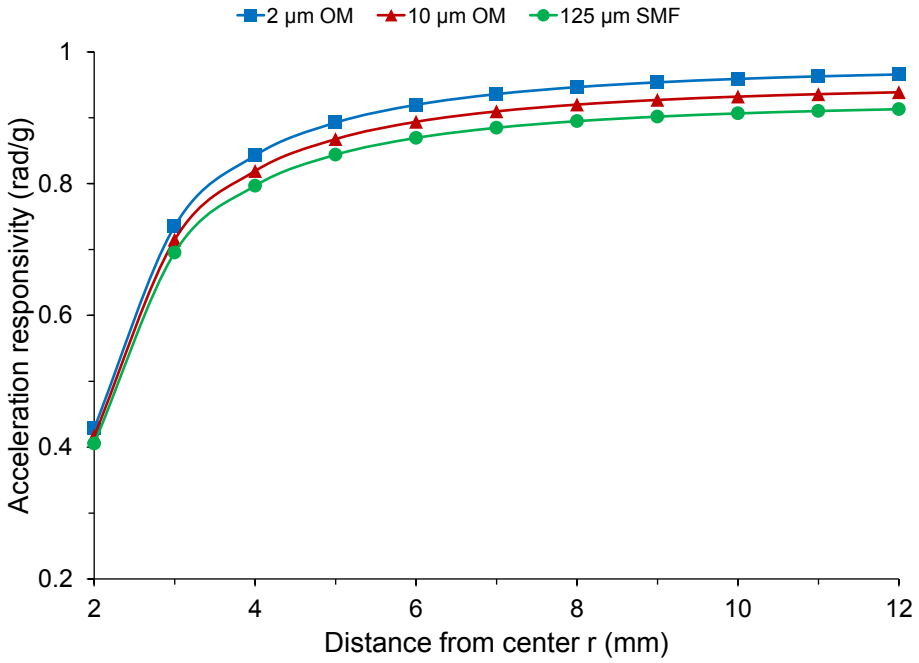

Figure 96. Simulated relationship between the distance from the disc center and the acceleration responsivity, for different fiber diameters at L = 5 mm.

Figure 97 predicts the change in the fundamental frequency of the FD as a function of a, with a single layer of fiber on one side of the disc. It is evident that B_w falls rapidly with growing disc radius, leading to a trade-off between the acceleration responsivity and B_w when optimizing the disc size. Equation 5.28 shows that increasing the disc thickness will also increase B_w, but at the expense of lowering the responsivity according to Equation 5.27. For any disc size, the values of B_w associated with OMs of D = 2 μm and 10 μm are similar, with the larger diameter accommodating a slightly higher B_w. On the other hand, FDs based on SMF-28 exhibit a greater B_w due to the substantially higher effective Young's modulus. However, the average density of the disc plus fiber is also higher, which decreases B_w slightly. Nevertheless, the magnitude of B_w for FDs based on OMs are comparable with those using SMF-28. For disc radii below 5 mm, the bend loss becomes too high for SMF-28, thus only OMs can be incorporated in such small packages.

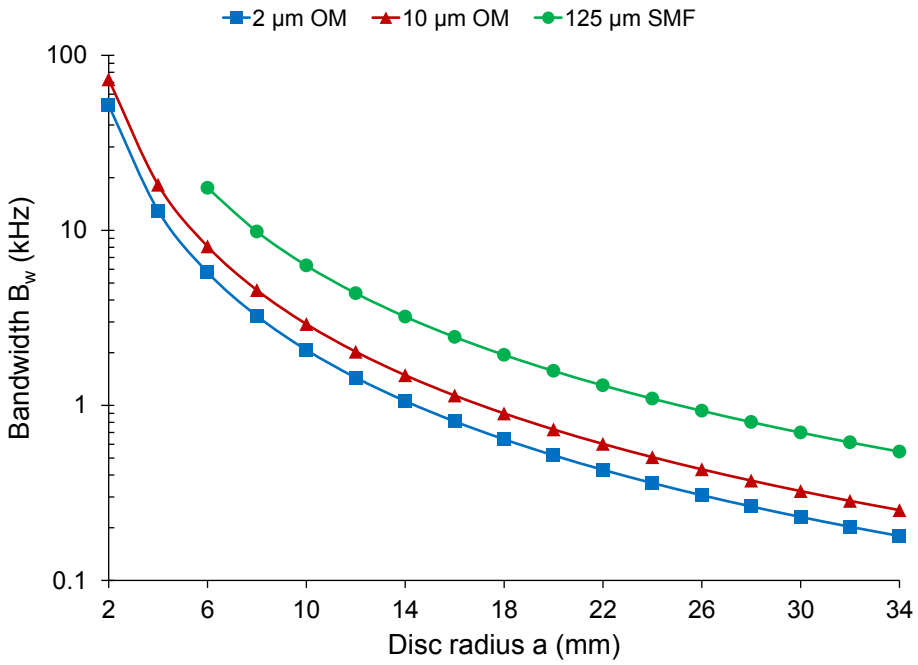

Figure 97. Simulated relationship between the disc radius and the detection bandwidth for different fiber diameters.

To compare the responsivity and B_w achievable with OM against those of BIF (e.g. Corning HI 1060 FLEX), Figure 98 shows the simulated results for single-sided carbon-polymer discs fully packed with a single-layer of fiber. The OM-based disc was wound from r = 1.5 mm to the edge, whereas the BIF-based disc was wound from r = 5 mm to the edge. The minimum spacing requirement of 20 μm was taken into account for the OM model. From the plots, it is evident that using OM leads to considerably higher responsivity, despite lowering B_w. For a disc radius of a = 12.5 mm, the responsivity of the FD using 2 μm diameter OM (~1940 rad/g) is at least one order of magnitude higher than that of the BIF-based FD (~40 rad/g). More importantly, the nominal macro-bend radius limit of BIF is 5 mm, which sets a lower bound on the disc size.

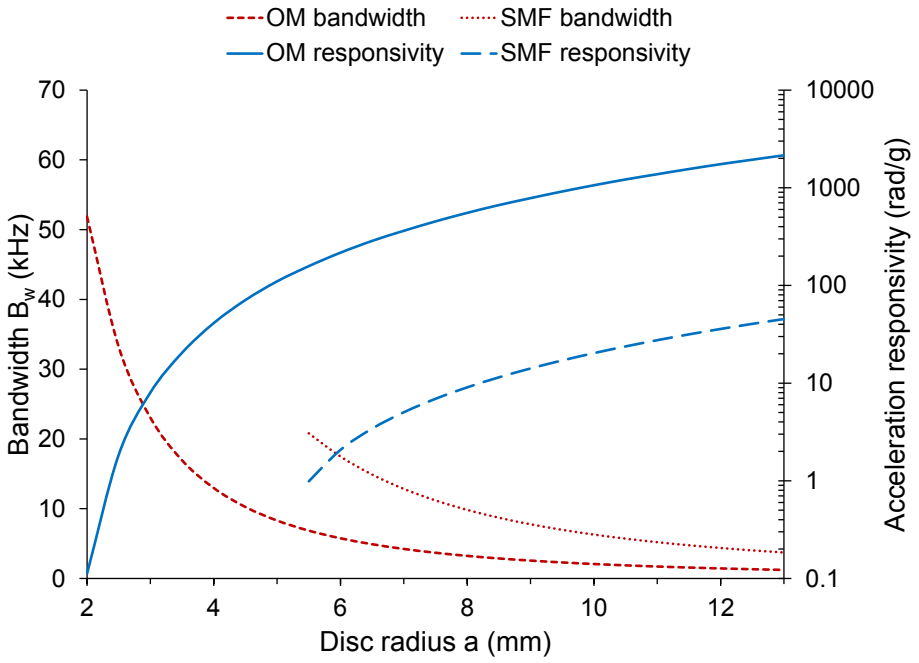

Figure 98. Simulated acceleration responsivities and detection bandwidths of microfiber and bend-insensitive fiber-based flexural discs of varying sizes.

Finally, the impact of the ambient environment on the FD accelerometer is investigated by predicting the phase modulation imposed on the optical fiber when subjected to thermal effects shown in Figure 99. The coefficient of thermal expansion for pyrolytic graphite, silica and polymer are: $\alpha_{disc} = 1\times10^{-6}$/°C [32], $\alpha_{silica} = 5.5\times10^{-7}$/°C [33] and $\alpha_{polymer} = 1.18\times10^{-6}$/°C [34] respectively.

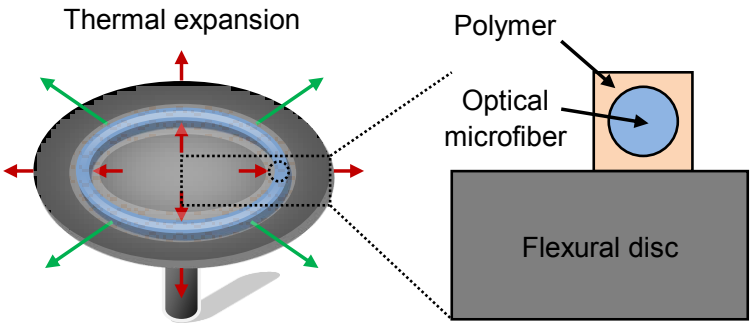

Figure 99. Schematic diagram showing the side cross-sectional structure of the optical microfiber loop embedded in polymer and attached to the disc.

The pyrolytic graphite disc is assumed to be unrestricted, since its physical volume is greater than that of the silica OM and the polymer coating combined. Hence, the resulting strain ($\Delta L/L$) on the OM can be approximated by the thermal expansion of the pyrolytic graphite disc alone:

$$\frac{\Delta L}{L} \approx \alpha_{disc} \Delta T \tag{5.36}$$

In addition to the physical length change of the OM by thermal expansion, the stress-optic effect [3] introduces a change in n_{silica} and similarly in $n_{polymer}$:

$$\Delta n_{silica} = -\frac{n_{silica}^3}{2} \cdot \frac{\Delta L}{L} \cdot [p_{12} - v_{silica} \cdot (p_{11} + p_{12})] \tag{5.37}$$

where p_{ij} is the Pockels coefficient components of the stress-optic tensor of silica (P_{11} = 0.126, P_{12} = 0.270) [35]. The Pockels coefficients are not known for this particular type of polymer, but it is assumed to be similar to that of PMMA (P_{11} = 0.3, P_{12} = 0.297) [36]. The strain experienced by the optical fiber is 1×10^{-6} for a 1 °C rise in temperature. The stress-optic coefficients of silica and polymer are -3.09×10^{-7}/°C and -7.53×10^{-8}/°C respectively. For a 1 °C rise in temperature, this produces an effective index change (Δn_s) of -2.41×10^{-7}, -3.09×10^{-7} and -3.09×10^{-7} for the fiber diameters of 2, 10 and 125 μm respectively.

The thermal-optic coefficients of silica and polymer are 8.11×10^{-6}/°C [37] and -1×10^{-4}/°C [38] respectively. For a 1 °C rise in temperature, this produces an effective index change (Δn_t) of -2.57×10^{-5}, 7.56×10^{-6} and 8.11×10^{-6} for the fiber diameters of 2, 10 and 125 μm respectively.

Lastly, the thermal expansion of the OM increases its core diameter and also contributes to the change in n_{eff}. However, the disc-induced strain on the OM decreases its core diameter due to the Poisson Effect. It is reasonable to assume that these two weak effects cancel each other out and thus have a negligible impact on the final OM diameter.

By consolidating all the thermal effects, the normalized phase change can be written as:

$$\frac{\Delta\varphi}{\varphi} = \alpha_{disc} \Delta T + \frac{\Delta n_s + \Delta n_t}{n_{eff}} \tag{5.38}$$

where n_{eff} = 1.402, 1.446 and 1.450, for fiber diameters of 2, 10 and 125 μm respectively.

Finally, the double-pass phase change for a given length of fiber is expressed by:

$$2\Delta\varphi = \frac{4\pi L}{\lambda} \cdot \left(n_{eff}\alpha_{disc}\Delta T + \Delta n_s + \Delta n_t\right) \quad (5.39)$$

The influence of the ambient environment is shown in Figure 100, where the thermally induced phase change for a localized 1 °C temperature variation is evaluated for different OM diameters compared with that of SMF-28. It can be concluded that ambient phase noise is higher with smaller fiber diameters due to the larger contribution of the thermo-optic coefficient of the polymer cladding. The thermally induced phase change of any fiber with length in excess of 25 mm is enough to drive an interferometer from maximum responsivity at a quadrature point to minimum responsivity at a maxima/minima. By considering a 1 °C change for a 60 mm length of fiber wound at 12 mm from the center, the responsivities from Figure 95 combined with the phase change from Figure 100 give thermally induced acceleration errors of 1.045 g, 0.437 g and 1.379 g for D = 2 µm, 10 µm and 125 µm respectively. Overall, thermal effects have the greatest impact on the minimum detectable acceleration of very large and very small diameter fibers due to their low responsivity and large phase change respectively.

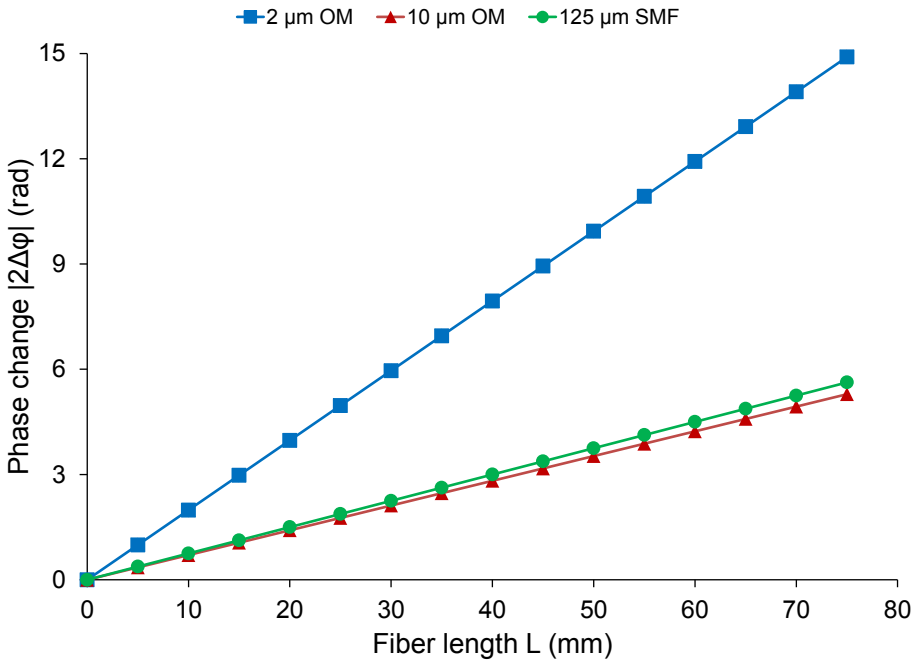

Figure 100. Simulated relationship between the fiber length and the double-pass phase change for different fiber diameters.

5.2.6 Experimental results

The photoreceiver has a gain of 42 V/mW, a bandwidth of DC–125 MHz, and a noise-equivalent power of 2.5 pW/$\sqrt{\text{Hz}}$. Using Equation 5.32, a received power of 27.3 μW (at a quadrature point) corresponds to a maximum fringe amplitude of 1146.6 mV. The measured fringe amplitude was 979.0 mV, indicating an interference visibility of 0.85. The relative phase shift was calculated using the signal amplitude from the photoreceiver output and the measured fringe amplitude (Equation 5.33). The acceleration responsivity was calculated from dividing the relative phase shift by the acceleration measured with the reference FPI. Figure 101 shows a linear responsivity of 2.0 rad/g for Sample 1 and 4.0 rad/g for Sample 2, for an acceleration signal of 500 Hz. These values are comparable in magnitude with the simulated values of 1.9 rad/g and 7.6 rad/g respectively. The differences could be caused by the imperfect center-symmetric construction of the FDs. As expected, the longer length of OM produced higher responsivity, due to the longer interaction length with the transducer. However, this effect was slightly offset by the larger OM diameter that increased the effective Young's modulus of the composite disc.

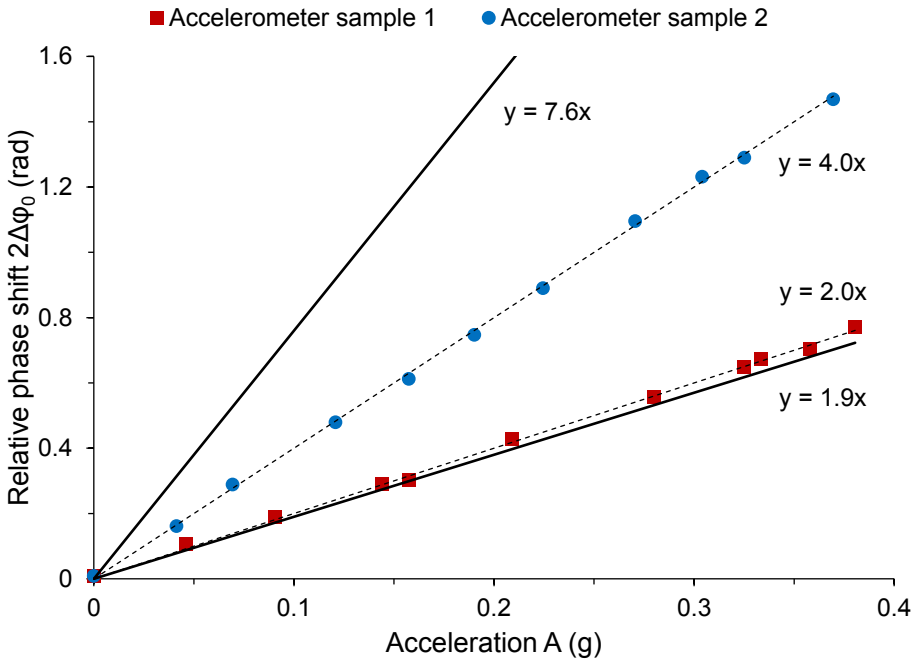

Figure 101. Measured acceleration responsivity of Samples 1 and 2 at a signal frequency of 500 Hz with linear fits (dashed lines), compared with the theoretical prediction (solid lines). For no acceleration or small acceleration-induced signals

with SNR < 1, the noise-equivalent phase based on the measured noise amplitude was plotted instead. Note: error bars may be obscured by the markers.

Figure 102 shows the frequency response of the two FD samples, which was obtained by measuring the responsivity at varying signal frequencies of fixed amplitude. The responsivity of Sample 2 was less frequency-dependent due to a closed loop arrangement of the OM. The responsivity of Sample 1 fluctuated more due a U-shaped arrangement of the OM, where the non-center-symmetric polymer deposition on the surface of the FD caused some parts to flex more than others at certain frequencies. The fundamental frequency of the two samples was modeled to be 1.5 kHz and 2.9 kHz respectively (Equation 5.28). However, it was not possible to confirm the detection bandwidths experimentally because the modulation bandwidth of the available PZT shaker does not exceed 1 kHz. The average responsivities of Samples 1 and 2 are 2.0 rad/g and 4.0 rad/g respectively, which are similar to the simulated values of 1.9 rad/g and 7.6 rad/g respectively The response time of the sensors depends on the wave propagation delay from the disc center to the loop of OM, plus the transit time of light from the output of the OM to the photoreceiver.

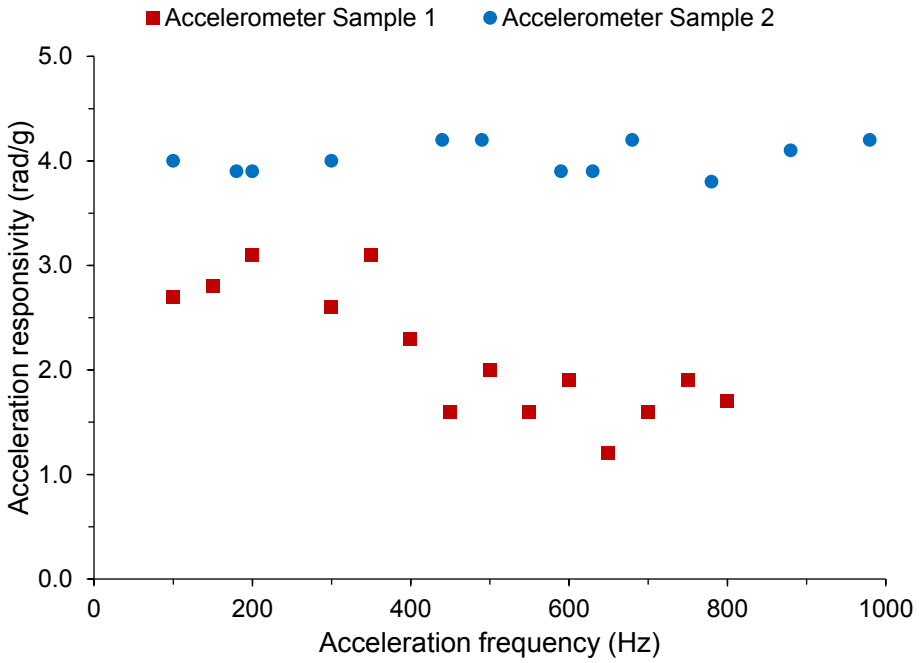

Figure 102. Measured frequency response for acceleration responsivities.

Acoustic waves generated by the PZT shaker can form standing waves along the OM. The effective index perturbation due to dynamic strain is periodic with the periodicity of the acoustic wavelength. However, the OM would not facilitate efficient modal coupling unless the acoustic wavelength matches the beat length between the fundamental and higher-order modes [39]. It can be argued that the modal conversion was negligible, since wavelength-dependent behavior was not observed when the FD was detached from the MI and tested with the PZT shaker.

Unlike in the laboratory, where the passively damped optical bench minimized the effect of vibrations, in real measurement environments unsuppressed vibrations of the order of 1–100 Hz may affect the acceleration measured by the reference FPI. Meanwhile, dynamic ambient temperature fluctuations up to a few hertz are outside the frequency range of the measured acceleration signal. However, static temperature deviations can affect the quadrature condition and thus influence the responsivity, as evident from the thermal analysis. A simple solution is to perform a one-point calibration of the sensing system by wavelength-tuning before each measurement.

Typically over 24 hrs, the TLS exhibits relative intensity noise of –145 dB/Hz, and frequency noise resulting from wavelength instability of ±2.5 pm. The oscilloscope noise is in the region of 300 μV_{rms} for a bandwidth of 300 MHz. The system noise (i.e. laser frequency noise dominated) measured over a time-frame of 10 ms was 7.7 mV with 64 running averages, by means of computing the FFT of the optical signal with no measurand and selecting the highest PSD component. This corresponds to a phase sensitivity of 7.9 mrad using Equation 5.33. The average noise of ~8 mV in the measurement data corresponds to a phase error of ±8.2 mrad. From dividing the phase sensitivity by the responsivity of 4.0 rad/g (Sample 2) at a signal frequency of 500 Hz, the acceleration sensitivity is 2.0 mg. The acceleration sensitivities of Samples 1 and 2 are plotted as a function of frequency in Figure 103, with average values of 3.9 mg and 2.0 mg respectively.

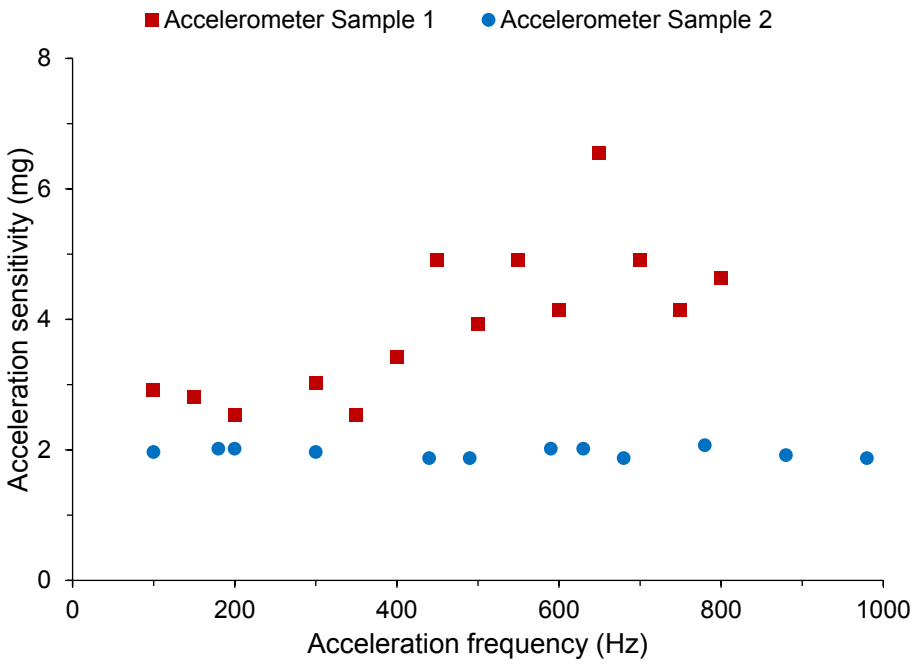

Figure 103. Measured frequency response for acceleration sensitivities.

5.2.7 Conclusion

OM-based FD accelerometers have been proposed and demonstrated. The advantages of OM over SMF-28 and BIF include smaller permissible disc size, higher packing density and lower stiffness that are anticipated to raise the acceleration responsivity by at least one order of magnitude (Figure 98). The responsivity and detection bandwidth of FDs employing different OM lengths and diameters have been simulated, at varying distances from the disc center and with different disc sizes.

To verify the outcome of simulations, two different samples were compared. Sample 1 was an OM with short length (10 mm) and small diameter (2 μm). Sample 2 had a longer length (60 mm) but a larger diameter (10 μm) to improve handling during the winding process due to the fragility of OMs. The two samples were embedded in low-RI polymer on a 0.5 mm thick pyrolytic graphite disc of 12.5 mm radius. The average responsivity of Sample 2 was 4.0 rad/g, which is greater than Sample 1 with 2.0 rad/g. The experimental results are comparable in magnitude with those of simulations, at 7.6 rad/g and 1.9 rad/g respectively. The average acceleration sensitivities were 2.0 mg and 3.9 mg respectively. The detection bandwidth of the two samples was predicted to be 1.5 kHz and 2.9 kHz respectively, but it was only

experimentally verified up to 1 kHz due to the limited modulation bandwidth of the available PZT shaker.

To increase the responsivity, a longer length of OM must be used. The limiting factor is the maximum length of OM that can be fabricated, which can be vastly extended using a modified tapering rig described in section 6.3. A disc of larger radius and lower thickness with a material of lower Young's modulus and higher density would also be beneficial. The phase and acceleration sensitivities can be optimized with a balanced detection scheme to eliminate common-mode intensity noise from the TLS. In addition, the MI can be temperature-compensated by attaching the reference arm to the underside of the FD, so that any thermal expansion would equally affect both OPLs. To increase the fundamental frequency and thus the detection bandwidth, a disc of smaller radius and greater thickness, with a material of higher Young's modulus, lower density and higher Poisson ratio is required. Hence, there is an optimization issue with the disc radius, thickness, Young's modulus and density to deliver a good balance between responsivity and detection bandwidth. The response time can be reduced by keeping the fiber length between the OM and photoreceiver as short as possible. To reduce the loss, air bubbles must be removed from the polymer packaging. The ultimate compactness of the sensor head is restricted by the minimum bend radius of the OM.

5.3 References

1. E. Udd and W. B. Spillman Jr., “Fiber optic sensors: an introduction for engineers and scientists”, Wiley-Blackwell, 2nd dd., 2011.

2. “Etalon introduction”, http://www.precisionphotonics.com, accessed on 23/04/2013.

3. B. Culshaw, “The optical fibre Sagnac interferometer: an overview of its principles and applications”, Meas. Sci. Technol., vol. 17, no. 1, pp. R1–R16, 2006.

4. D. A. Jackson, R. G. Priest, A. Dandridge, and A. B. Tveten, “Elimination of drift in a single-mode optical-fiber interferometer using a piezoelectrically stretched coiled fiber”, Appl. Opt., vol. 19, no. 17, pp. 2926–2929, 1980.

5. A. Dandridge and L. Goldberg, “Current-induced frequency modulation in diode lasers”, Electron. Lett., vol. 18, no. 7, pp. 302–304, 1982.

6. A. Dandridge, A. B. Tveten, and T. G. Giallorenzi, “Homodyne demodulation scheme for fiber optic sensors using phase generated carrier”, IEEE J. Quantum Electron., vol. 18, no. 10, pp. 1647–1653, 1982.

7. J. H. Cole, B. A. Danver, and J. A. Bucaro, “Synthetic heterodyne interferometric demodulation”, IEEE J. Quantum Electron., vol. 18, no. 4, pp. 694–697, 1982.

8. M. L. Henning, S. W. Thornton, R. Carpenter, W. J. Stewart, J. P. Dakin, and C. A. Wade, “Optical fibre hydrophones with down lead insensitivity”, Proceedings of the First International Conference on Optical Fibre Sensors, 1983.

9. K. Koo, A. B. Tveten, and A. Dandridge, “Passive stabilization scheme for fiber interferometry using (3×3) fiber directional couplers”, Appl. Phys. Lett., vol. 41, no. 7, pp. 616–618, 1982.

10. A. D. Kersey, D. A. Jackson, and M. Corke, “Passive compensation scheme suitable for use in the single-mode fiber interferometer”, Electron. Lett., vol. 18, no. 9, pp. 392–393, 1982.

11. S. A. Al-Chalabi, B. Culshaw, and D. E. N. Davies, “Partially coherent sources in interferometric sensors”, Proceedings of the First International Conference on Optical Fibre Sensors, 1983.

12. Y. Wang, H. Xiao, S. Zhang, F. Li, and Y. Liu, “Design of a fibre-optic disc accelerometer: theory and experiment”, Meas. Sci. Technol., vol. 18, no. 6, pp. 1763–1767, 2007.

13. N. Bertone and P. Webb, “Noise and stability in PIN detectors”, EG&G Optoelectronics Canada, 1996.

14. D. L. Gardner, T. Hofler, S. R. Baker, R. K. Yarber, and S. L. Garrett, “A fiber-optic interferometric seismometer”, J. Lightwave Technol., vol. 5, no. 7, pp. 953–960, 1987.

15. R. D. Pechstedt and D. A. Jackson, “Design of a compliant-cylinder-type fiber-optic accelerometer: theory and experiment”, Appl. Optics, vol. 34, no. 16, pp. 3009–3017, 1995.

16. D. A. Brown and S. L. Garrett, “An interferometric fiber optic accelerometer”, FOLS VIII, vol. 1367, pp. 282–288, 1990.

17. Y. Shindo, N. Tsuchida, K. Dobashi, and H. Kamata, “Fiber-optic accelerometer”, OFS-12, pp. 202–205, 1997.

18. G. A. Cranch and P. J. Nash, “High-responsivity fiber-optic flexural disk accelerometers”, J. Lightwave Technol., vol. 18, no. 9, pp. 1233–1243, 2000.

19. T. Ke, T. Zhu, Y. Rao, and M. Deng, “Accelerometer based on all-fiber Fabry-Perot interferometer formed by hollow-core photonic crystal fiber”, Microw. Opt. Techn. Let., vol. 52, no. 11, 2531–2535, 2010.

20. A. Fender, W. N. MacPherson, R. R. J. Maier, J. S. Barton, D. S. George, R. I. Howden, G. W. Smith, B. J. S. Jones, S. McCulloch, X. F. Chen, R. Suo, L. Zhang, and I. Bennion, “Two-axis temperature-insensitive accelerometer based on multicore fiber Bragg gratings”, IEEE Sens. J., vol. 8, no. 7, pp. 1292–1298, 2008.

21. C. Hou, Y. Wu, and X. Zeng, “Novel high sensitivity accelerometer based on a microfiber loop resonator”, Opt. Eng., vol. 49, no. 1, pp. 014402-1–6, 2010.

22. G. A. Gerges, T. P. Newson, and D. A. Jackson, “Practical fiber-optic-based submicro-g accelerometer free from source and environmental perturbations”, Opt. Lett., vol. 14, no. 20, pp. 1155–1157, 1989.

23. M. D. Todd, G. A. Johnson, B. A. Althouse, and S. T. Vohra, “Flexural beam-based fiber Bragg grating accelerometers”, IEEE Photonic Tech. L., vol. 10, no. 11, pp. 1605–1607, 1998.

24. H. Yu, S. Wang, J. Fu, M. Qiu, Y. Li, F. Gu, and L. Tong, “Modeling bending losses of optical nanofibers or nanowires”, Appl. Optics, vol. 48, no. 22, pp. 4365–4369, 2009.

25. W. C. Young, “Roark’s formulas for stress and strain”, McGraw-Hill, 7th Ed., case 2l, 1989.

26. J. Barlow and D. N. Payne, “The stress-optic effect in optical fibers”, IEEE J. Quantum Elect., vol. 19, no. 5, pp. 834–839, 1983.

27. W. Leissa, “Vibration of plates”, NASA Tech. Doc. Sp-160-N70-18461, 1969.

28. T. A. Birks and Y. Li, “The shape of fiber tapers”, J. Lightwave Technol., vol. 10, no. 4, pp. 432–438, 1992.

29. Y. Jung, G. Brambilla, and D. J. Richardson, “Efficient higher-order mode filtering in multimode optical fiber based on an optical microwire”, AOE, SuB4, 2008.

30. X. Zhang, M. Belal, G. Y. Chen, Z. Song, G. Brambilla, and T. P. Newson, “Compact optical microfiber phase modulator”, Opt. Lett., vol. 37, no. 3, pp. 320–322, 2012.

31. “Pyrolytic graphite supplier data”, http://www.goodfellow.com, accessed on 10/01/2012.

32. “Pyrolytic graphite properties”, http://www.cidraprecisionservices.com/pm/materials/pyrolytic-graphite.html, accessed on 10/01/2012.

33. “Fused silica material properties”, http://accuratus.com/fused.html, accessed on 10/01/2012.

34. “Efiron technical datasheet on PC-373 (AP)”, version 23/10/2006.

35. T. G. Giallorenzi, J. A. Bucaro, A. Dandridge, G. H. Sigel Jr., J. H. Cole, S. C. Rashleigh, and R. G. Priest, "Optical fiber sensor technology", IEEE J. Quantum Electronics, vol. 18, no. 4, pp. 626–665, 1982.

36. M. K. Szczurowski, T. Martynkien, G. Statkiewicz-Barabach, W. Urbanczyk, L. Khan, and D. J. Webb, "Measurements of stress-optic coefficient in polymer optical fibers", Opt. Lett., vol. 35, no. 12, pp. 2013–2015, 2010.

37. P. Childsa, A. C. L. Wong, N. Gowripalan, and G. D. Peng, "Measurement of the coefficient of thermal expansion of ultra-high strength cementitious composites using fibre optic sensors", Cement Concrete Res., vol. 37, no. 5, pp. 789–795, 2007.

38. X. Zeng, Y. Wu, C. Hou, J. Bai, and G. Yang, "A temperature sensor based on optical microfiber knot resonator", Opt. Commun., vol. 282, no. 18, pp. 3817–3819, 2009.

39. T. A. Birks, P. St. J. Russell, and C. N. Pannell, "Low power acousto-optic device based on a tapered single-mode fiber", IEEE Photonic Tech. L., vol. 6, no. 6, pp. 725–727,1994.

Chapter 6

6. Acoustic sensing with optical microfiber

This chapter briefly describes the polarimetric variant of interferometry, before exploring the benefits of using OM for acoustic sensing. A compact ABM microphone is presented to further demonstrate the potential of OM-based sensors. This sensor design can be modified for operating underwater as a hydrophone.

6.1 Polarimetric interferometry

Closely related to two-path interferometric sensors (two-fiber) are those based on polarimetry. A polarimetric-interferometric sensor (one-fiber) can be thought of as one in which the two beams occupy essentially the same volume of space but are distinguished by the orthogonality of their SOP. The transduction mechanism in this case is the modulation of the differential phase ($\Delta\varphi$) between the eigenmodes. In order to make the two orthogonal beams interfere, they must each be resolved to give components in a common direction. Figure 104 shows that by placing a polarizer at the output of a highly birefringent fiber, the eigenmodes can beat together. The advantage of polarimetric interferometry can also be considered as its disadvantage, which is the insensitivity to external effects. It is inherently stable from ambient disturbances, though the measured phase shifts are typically several orders of magnitude lower than those obtained from two-fiber interferometry. Hence, there is little overall impact on the sensitivity to the measurand compared to the latter.

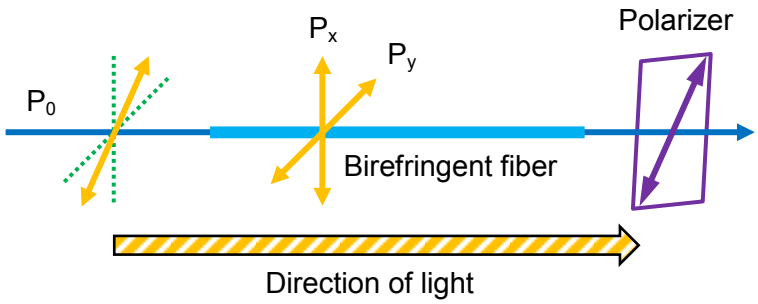

Figure 104. Schematic diagram of the simple polarimeter. The arrows indicate: the polarization azimuth of the input light (yellow), the axes of the birefringent fiber (dotted green), and the polarization azimuth of the analyzer (purple).

6.2 Compact air-backed mandrel-based acoustic sensor

A compact microphone comprising of a MC wrapped around an ABM of only 3 mm diameter is demonstrated as a proof-of-theory in this section. The low stiffness and bend insensitivity of OMs give rise to extremely small package sizes without compromising the responsivity. An average acoustic responsivity of –136.7 dB re. rad/μPa.m and an average acoustic sensitivity of 31.7 dB_{SPL} within a detection bandwidth of ~1 kHz was achieved using an OM measuring only 2 μm in diameter and 35 mm in length.

6.2.1 Introduction

Acoustic sensing, with its commercial use spanning several decades, is one of the most successful applications in the field of fiber-optic sensors. Rapid advances in this area have been driven by increasing demands from industries such as defense, most notably for hydrophones. The acoustic signatures of tanks, aircrafts, helicopters and submarines can be monitored for high-precision battlefield awareness and surveillance. Optical microphones in the form of an ABM have proven to be a simple yet effective design, with the potential for very high acoustic responsivity [1–3]. Scaling down the size of acoustic sensors gives a battlefield advantage due to easier deployment and disguise in all types of terrain. However, due to the large minimum bend radii of standard optical fibers, very compact designs are not feasible. Even though state-of-the-art BIFs can achieve a bend radius down to several millimeters [4], the fiber diameters are still large relative to the dimensions of the down-scaled transducer, leading to severe limitations on the responsivity.

In this section the first experimental demonstration of a compact ABM exploiting the excellent mechanical properties of OM is presented. Due to the bend insensitivity of OMs, bend radii of a few micrometers can be readily achieved with relatively low bending-loss [5]. Furthermore, such small diameters can substantially reduce the effective stiffness of the mandrel for higher responsivity.

6.2.2 Theory

The working principle of the ABM is illustrated in Figure 105(a). Acoustic waves produce local pressure variations that uniformly deform the hollow mandrel and

exert axial strain on the coiled birefringent OM. The change in the OPD of the eigenmodes propagating along the OM is detected using a single-fiber polarimetric interferometer, which reduces design complexity and facilitates better immunity against external perturbations. The upper measurable limit of acoustic pressure is governed by the clearance between the mandrel shell and the support rod.

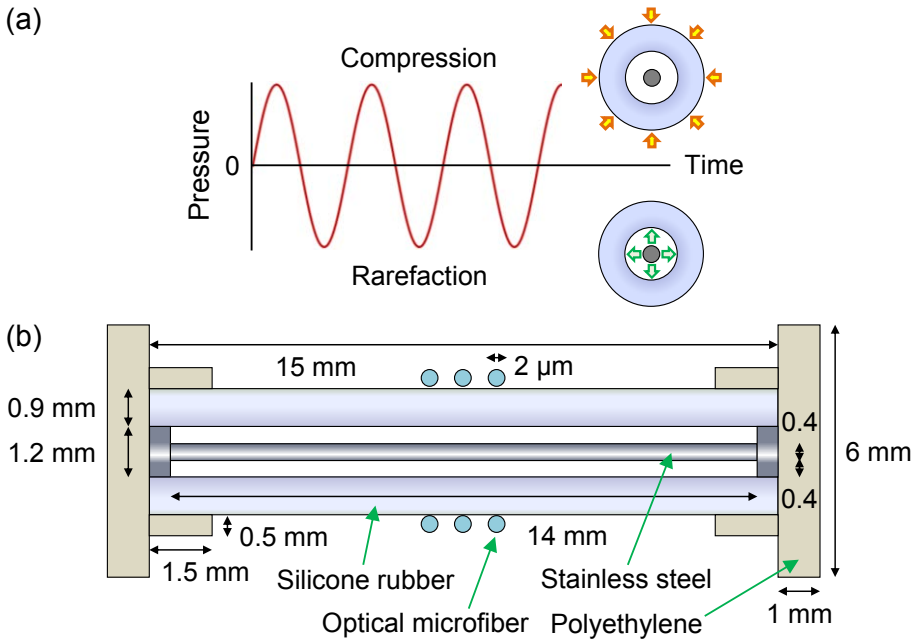

Figure 105. (a) Working principle of the air-backed mandrel bound with a microfiber coil, and (b) a schematic diagram of the construction.

To predict the acoustic responsivity of the OM-based ABM, the behavior of the device under acoustic pressure was modeled based on the Lame's equations of thick-walled cylinders, where the mandrel wall thickness is more than a tenth of its radius. It is assumed that any deformations are symmetric about the axis parallel to the support rod, such that the tangential deformation and the shear stress are zero. Therefore, displacements due to internal or external pressure will be in the radial direction only. It is also assumed that the mandrel waist is long enough for the middle section to remain flat, and the axial strain is constant throughout. The distribution of stress far away from the fixed ends of the mandrel can be expressed by the stress components in the radial (r), tangential (θ) and axial (z) directions [6]:

$$\sigma_r = \frac{p_1 a^2 - p_2 b^2}{b^2 - a^2} - \frac{a^2 b^2 \cdot (p_1 - p_2)}{r^2 \cdot (b^2 - a^2)} \tag{6.1}$$

$$\sigma_\theta = \frac{p_1 a^2 - p_2 b^2}{b^2 - a^2} + \frac{a^2 b^2 \cdot (p_1 - p_2)}{r^2 \cdot (b^2 - a^2)} \tag{6.2}$$

$$\sigma_z = \frac{p_1 a^2 - p_2 b^2}{b^2 - a^2} \tag{6.3}$$

When analyzing the stresses at the surface of the mandrel, Equations 6.1 and 6.2 can be simplified with the boundary condition of $r = b$:

$$\sigma_r = -p_2 \tag{6.4}$$

$$\sigma_\theta = \frac{2p_1 a^2 - p_2 \cdot (a^2 + b^2)}{b^2 - a^2} \tag{6.5}$$

By applying Hooke's Law in the tangential direction, an expression for the axial strain is obtained:

$$\varepsilon_\theta = \frac{1}{E} \cdot [\sigma_\theta - v \cdot (\sigma_r + \sigma_z)] \tag{6.6}$$

where v is the effective Poisson ratio of the mandrel, E is the effective Young's modulus of the mandrel, a is the inner mandrel radius, b is the outer mandrel radius, p_1 is the internal pressure, p_2 is the external pressure, and the acoustic pressure is stated relative to the atmospheric air pressure, which in this case is $\Delta p = p_2 - p_1$.

The strain ($\Delta L/L$) transferred to the OM of length L attached to the middle section of the mandrel can be approximated by the acoustic pressure-induced strain (ε_θ) of the silicone rubber mandrel alone. This is a reasonable assumption because its physical volume is greater than that of the silica OM and the polymer coating combined.

When the ABM is subject to acoustic pressure, the standard optical fiber sections outside the ABM and the initial length of OM can be disregarded due to their constant $\Delta\varphi$. The $\Delta\varphi$ contribution from the elongated section (ΔL) is deduced by simplifying Equation 5.2 and replacing L with ΔL. Furthermore, the stress-optic effect does not contribute to the change in $\Delta\varphi$ as the two paths share the same fiber and are equally affected. The relatively small change in OM diameter can also be neglected:

$$\frac{\Delta\varphi}{\varphi} = \frac{\Delta n_{eff}}{n_{eff}} \tag{6.7}$$

where $\varphi = (2\pi/\lambda).n_{eff}.\Delta L$, n_{eff} is the effective index of the fast-axis (arbitrary), Δn_{eff} is the linear birefringence, and λ is the wavelength of light.

The differential phase change for a double-pass configuration is therefore:

$$2\Delta\varphi = \frac{4\pi}{\lambda} \cdot \Delta n_{eff} \cdot \Delta L \tag{6.8}$$

The pressure responsivity is given by the following:

$$\frac{2\Delta\varphi}{\Delta p} = \frac{4\pi}{\lambda \Delta p} \cdot \Delta n_{eff} \Delta L \tag{6.9}$$

The detection bandwidth of the ABM is limited by its fundamental (radial) frequency in air, given by [7]:

$$B_w = \frac{C}{2\pi} \cdot \sqrt{\frac{gEI}{\mu h^4}} \tag{6.10}$$

where C is a configuration-specific constant that includes all the correction factors for a straight pipe, g is a gravitational constant, I is the area moment of inertia ($I = \pi (b^4 – a^4)/4$), μ is the mass per unit length ($\mu = \rho A$), ρ is the mandrel density, and h is the length of the mandrel length.

6.2.3 Fabrication

The sensor was built in three stages. Firstly, the hollow mandrel was fabricated from silicone rubber chosen for its low Young's modulus. A relatively thick wall was chosen to ensure a high fundamental frequency, which yields a high detection bandwidth. A double-headed stainless steel pin was inserted in the mandrel as a rigid support to enable efficient transfer of strain. The two ends of the mandrel were epoxy-sealed with high-density polyethylene caps. Figure 105(b) shows the dimensions of the ABM, which weighs only ~0.5 grams.

For the second stage, the initial SMF-28 was slightly side-polished before the fabrication of the OM proceeded based on the procedure described in section 3.2.3. The resulting birefringent OM of ~2 μm diameter and 35 mm length at the uniform waist had an adiabatic taper diameter profile to suppress the excitation of higher-order modes [8]. The fiber cross-section was slightly elliptical due to the surface tension of the partially melted silica.

In the final stage, the OM was wound 3.5 turns around the middle of the mandrel waist with a large pitch (>0.5 mm) to prevent mode coupling between the adjacent turns of the MC. A thin layer of low-RI, UV-curable polymer (Efiron PC-373 AP) was deposited on the mandrel before and after coiling the OM to ensure good confinement of light. Lastly, the sample was mounted upright on a glass slide shown in Figure 106(a) and UV-cured to ensure geometrical stability and robust packaging. The optical loss of the fabricated sample shown in Figure 106(b) was ~6 dB at a wavelength of λ = 1556 nm, and it was attributed to Rayleigh and Mie scattering due to the presence of micro-bubbles and particles in the polymer.

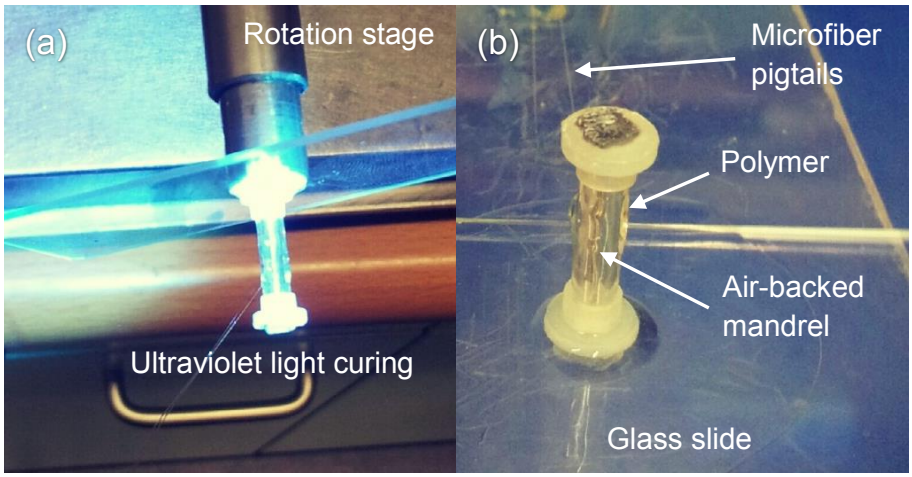

Figure 106. (a) Photograph of the UV-curing process of the polymer coating, and (b) the resulting sensor fixed on a glass slide for testing.

6.2.4 Experimental setup

The setup shown in Figure 107 was used to test the microphone. Linearly polarized light at a wavelength of λ = 1556 nm from a TLS (Agilent 81940A) was split into two orthogonal beams due to the axes of the birefringent OM not being aligned with those of the incident beam. $\Delta\varphi$ of the eigenmodes varied as a function of the acoustic pressure generated by a loudspeaker (LS), which was positioned to face the sensitive waist of the ABM. A commercial microphone was used to accurately measure the acoustic pressure. A mirror was employed to double $\Delta\varphi$ and thus the responsivity of the sensor. The returning eigenmodes combined interferometrically at the PMC-SMF interface, before a PBS separated the eigenmodes into the two PD ports of a BD (New Focus 2117). The BD eliminated common-mode intensity noise from the TLS and amplified the difference between the two optical signals. An AC-coupled

oscilloscope (Agilent DSO6034) on 25 MHz bandwidth-limited mode captured 1000 data points per measurement with only 2 running averages for fast data acquisitions.

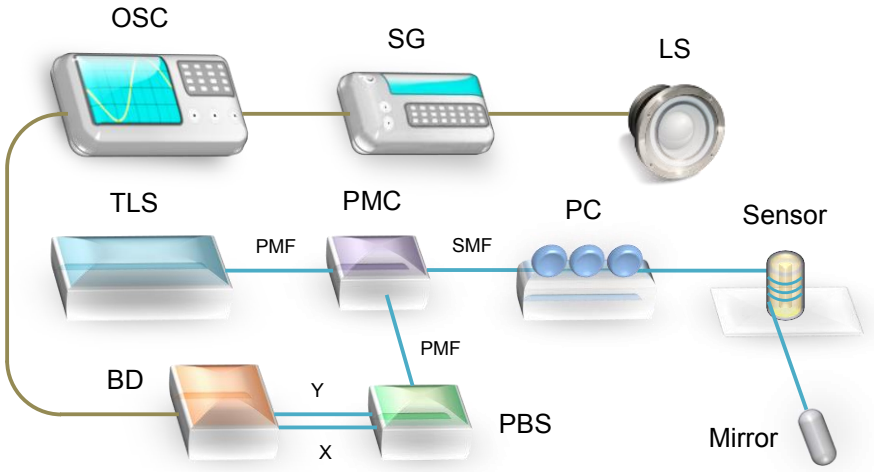

Figure 107. Schematic diagram of the experimental setup. TLS: tunable laser source, PMF: polarization-maintaining fiber, PMC: polarization-maintaining circulator, SMF: single-mode fiber, PC: polarization controller, ABM: air-backed mandrel, PBS: polarization beam splitter, BD: balanced detector, OSC: digital oscilloscope, SG: signal generator, LS: loudspeaker with power amplifier.

Assuming there is no mode coupling between the two orthogonal axes, the output electric field amplitudes after returning through the PMC can be expressed as a Jones matrix product of the input electric field amplitudes (E_{in}), the angle offset between the axes of the PMC and the birefringent OM ($R_{1,2}$), the differential phase due to the initial birefringence plus the acoustic pressure modulation (Q), and the in-line mirror (M):

$$E^{out} = R_2 \cdot Q \cdot M \cdot Q \cdot R_1 \cdot E^{in} \tag{6.11}$$

The common time- and distance-dependent phase components are neglected along with the propagation loss as they have no impact on the final output. The linearly polarized output light from the TLS is confined to one axis of the PMF:

$$E^{in} = \begin{pmatrix} E_x^{in} \\ 0 \end{pmatrix} \tag{6.12}$$

The angle-offset (α) between the axes of the PMC and birefringent OM can be represented by the following rotation matrices:

$$R_1 = \begin{pmatrix} \cos\alpha & -\sin\alpha \\ \sin\alpha & \cos\alpha \end{pmatrix} \quad \text{and} \quad R_2 = \begin{pmatrix} \cos\alpha & \sin\alpha \\ -\sin\alpha & \cos\alpha \end{pmatrix} \tag{6.13}$$

The differential phase between the eigenmodes is governed by the initial birefringence-induced phase difference ($\Delta\phi$) and the acoustic pressure-induced phase modulation with amplitude $\Delta\varphi_0$, radial frequency ω and initial phase Φ:

$$Q = \begin{pmatrix} e^{i\frac{\Delta\varphi}{2}} & 0 \\ 0 & e^{-i\frac{\Delta\varphi}{2}} \end{pmatrix} \tag{6.14}$$

where $\Delta\varphi = \Delta\phi + \Delta\varphi_0 \cos(\omega t + \Phi)$

The in-line mirror can be modeled by:

$$M = \begin{pmatrix} -1 & 0 \\ 0 & 1 \end{pmatrix} \tag{6.15}$$

For phase modulation beginning at a quadrature point, the mirror shifting $\Delta\varphi$ by π simply transfers it to an adjacent quadrature point. The electric field amplitudes at the PMC combine and the resulting optical powers (P_{out}) are a function of α and $\Delta\varphi$:

$$E_{out} = \begin{pmatrix} E_x^{out} \\ E_y^{out} \end{pmatrix} = E_x^{in} \cdot \begin{pmatrix} -e^{i\Delta\varphi}\cos^2\alpha + e^{-i\Delta\varphi}\sin^2\alpha \\ e^{i\Delta\varphi}\sin\alpha\cos\alpha + e^{-i\Delta\varphi}\sin\alpha\cos\alpha \end{pmatrix} \tag{6.16}$$

$$P_{out} = \begin{pmatrix} P_x^{out} \\ P_y^{out} \end{pmatrix} = P_x^{in} \cdot \begin{pmatrix} 1 - \sin^2(2\alpha)\cos^2(\Delta\varphi) \\ \sin^2(2\alpha)\cos^2(\Delta\varphi) \end{pmatrix} \tag{6.17}$$

The PC can be used to adjust the angle-offset such that $\alpha = \pi/4$, simplifying the signal processing with the BD output:

$$T = \frac{P_x^{out} - P_y^{out}}{P_x^{out} + P_y^{out}} = -\cos(2\Delta\varphi) \tag{6.18}$$

The output signal can be written purely in terms of the acoustic pressure-induced contribution to the total $\Delta\varphi$ at a quadrature point where $2\Delta\phi$ is equal to $\pi/2$ (plus integer multiples of π):

$$T = \sin[2\Delta\varphi_0 \cos(\omega_0 t + \Phi)] \tag{6.19}$$

Since only the modulation amplitude is of interest, the maximum differential phase change is related to the signal amplitude (ΔP_{pk}) and the measured fringe amplitude (P_{total}):

$$2\Delta\varphi_0 = \sin^{-1}\left(\frac{\Delta P_{pk}}{P_{total}}\right) \quad (6.20)$$

The double-pass differential phase change is given by $2\Delta\varphi_0$. The output voltage polarity of the detection system depends not only on the acoustic pressure polarity but also on the electric field orientation of the input light with respect to the birefringent OM axes, the initial $\Delta\phi$ and the signal processing. Equation 6.20 is only valid for differential phase changes under a quarter of a fringe ($2\Delta\varphi_0 < \pi/2$), before tracking fringes become necessary. Fringe-tracking techniques were not used as the phase modulation was sub-fringe.

During the characterization of the fabricated sensor, the TLS wavelength was swept and an interference fringe period of $\Delta\lambda$ = 30.965 nm was observed for the in-line MZI. Hence, the quadrature condition in Equation 6.20 can easily be achieved by tuning the input wavelength.

6.2.5 Simulations

The following parameters are considered for the ABM model, starting with the silicone rubber mandrel [9]: $v_{mandrel}$ = 0.49, $E_{mandrel}$ = 30 MPa, a = 0.6 mm, b = 1.5 mm, h = 12 mm, C = 2000, g = 9.81 m/s^2, $I = 3.874\times10^{-12}$, $\rho_{mandrel}$ = 1110 kg/m^3, μ = 6590.75 kg/m, p_1 = 101.325 kPa (i.e. atmospheric air pressure), and p_2 = 101.326 kPa. Likewise, for the silica OM [10]: v_{silica} = 0.17, E_{silica} = 73 GPa, ρ_{silica} = 2200 kg/m^3, L = 35 mm, and $\Delta n = 1.117\times10^{-3}$. Lastly, for the polymer coating [11]: $v_{polymer}$ = 0.4, $E_{polymer}$ = 0.1 GPa, and $\rho_{polymer}$ = 1550 kg/m^3.

From Equation 6.9, the upper limit of acoustic responsivity for an ABM using a 35 mm length of OM is 427.6 mrad/Pa. In practice, the fixed ends of the relatively short mandrel will impose a restriction on the displacement of the air-backed wall, leading to a reduction in the acoustic responsivity. It is reasonable to assume that the accurate value lies in the region of two orders of magnitude lower around ~4 mrad/Pa or –168.0 dB re. rad/μPa. The responsivity can be increased by lowering the Young's modulus and Poisson ratio of the mandrel material. The detection bandwidth calculated using Equation 6.10 is 0.9 kHz, and it can be increased by choosing a mandrel material of higher Young's modulus, lower density and shorter length. Since the responsivity and bandwidth have conflicting requirements in the Young's modulus, a careful choice can deliver a good balance of both attributes.

6.2.6 Experimental results

The BD had an overall response of 210 V/mW, a bandwidth of DC–10 kHz, and a noise-equivalent power of 0.4 pW/$\sqrt{\text{Hz}}$ for a gain setting of 300. Using Equation 6.19, a total received power of 157.8 μW corresponds to a maximum fringe amplitude of 33138.0 mV. The measured fringe amplitude was 30170.0 mV, indicating an interference visibility of 0.91. The differential phase change was calculated using the signal amplitude of the BD output and the measured fringe amplitude (Equation 6.20). The acoustic responsivity was calculated from dividing the differential phase change by the acoustic pressure measured with the commercial microphone. The linear responsivity of 4.9±0.5 mrad/Pa shown in Figure 108 for an acoustic signal of 70 Hz is near the theoretical value of ~4 mrad/Pa. Differences can be explained by the non-symmetrical mandrel cross-section due to bending effects.

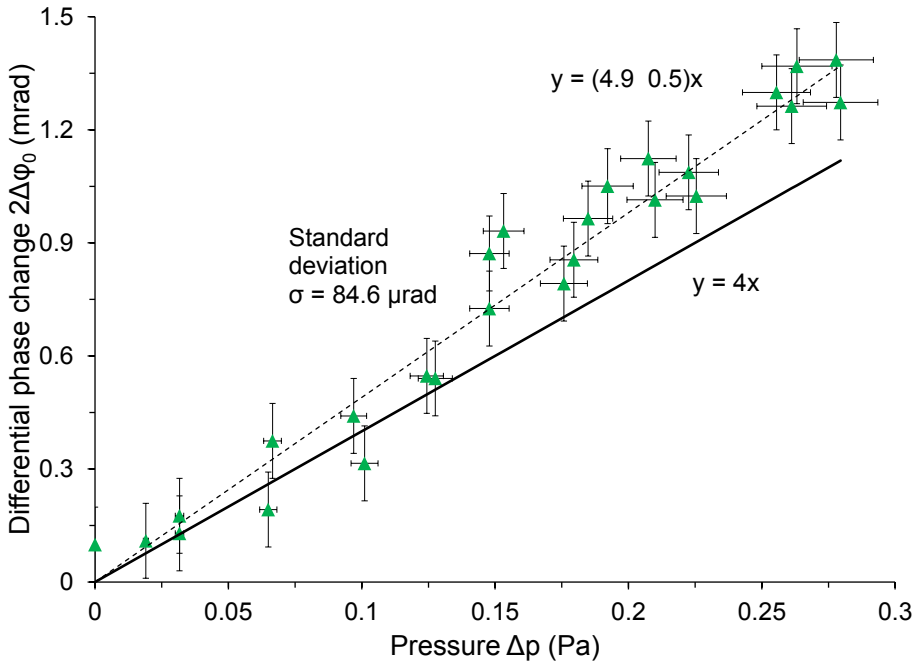

Figure 108. Measured acoustic responsivity at a signal frequency of 70 Hz with a linear fit (dashed line), compared with the theoretical prediction (solid line). For no acoustic or small acoustic-induced signals with SNR < 1, the noise-equivalent phase based on the measured noise amplitude was plotted instead.

The acoustic frequency response in Figure 109 was obtained by measuring the responsivity at varying signal frequencies of fixed amplitude. The fundamental frequency of the ABM can be observed at ~1 kHz, which is in good agreement with

the predicted value of 0.92 kHz. The average responsivities are –165.9 dB re. rad/µPa (–136.7 dB re. rad/µPa.m) and –171.2 dB re. rad/µPa (–142.1 dB re. rad/µPa.m) from 40 Hz to 500 Hz and 1.5 kHz to 4 kHz respectively. These are comparable in magnitude with –168.0 re. rad/µPa from simulations. The responsivity per unit length is at least one order of magnitude higher than most conventional polarimetric ABM-based microphones [12] despite the miniaturization. The response time of the sensor depends on the deformation delay of the elastic mandrel wall, plus the transit time of light from the output of the MC to the BD.

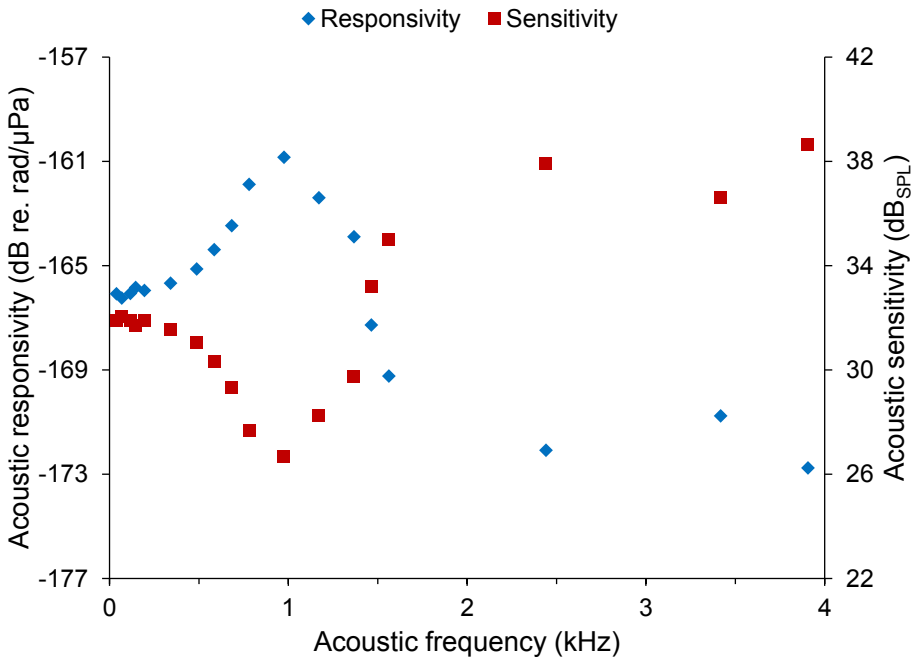

Figure 109. Measured frequency response for acoustic responsivities and sensitivities.

The maximum pressure error is ±5% based on the specifications of the commercial microphone. Although dynamic ambient temperature fluctuations up to a few hertz are outside the frequency range of the measured acoustic signal, static temperature deviations can affect the quadrature condition (section 5.2.5) and thus influence the responsivity. A simple solution is to perform a one-point calibration of the sensing system by wavelength-tuning before each measurement.

Ambient acoustic noise was the dominant source of noise in the measurement data, ranging from a few hertz to a few kilohertz. Figure 110 shows an example measurement at a signal frequency of 1562.5 Hz that was analyzed to check the noise levels. The FFT of the optical signal was computed and a SNR of 11 was

calculated. The highest noise PSD component of ~3 mV corresponds to a phase error of ±99.4 µrad using Equation 6.20. From dividing the phase error by the responsivity of 3.5±0.5 mrad/Pa at a signal frequency of 1562.5 Hz, the ambient acoustic noise was 63.0±1.3 dB_{SPL} (re. 20 µPa). This was comparable with 50–65 dB_{SPL} obtained from a commercial sound-meter over a period of 1 hr.

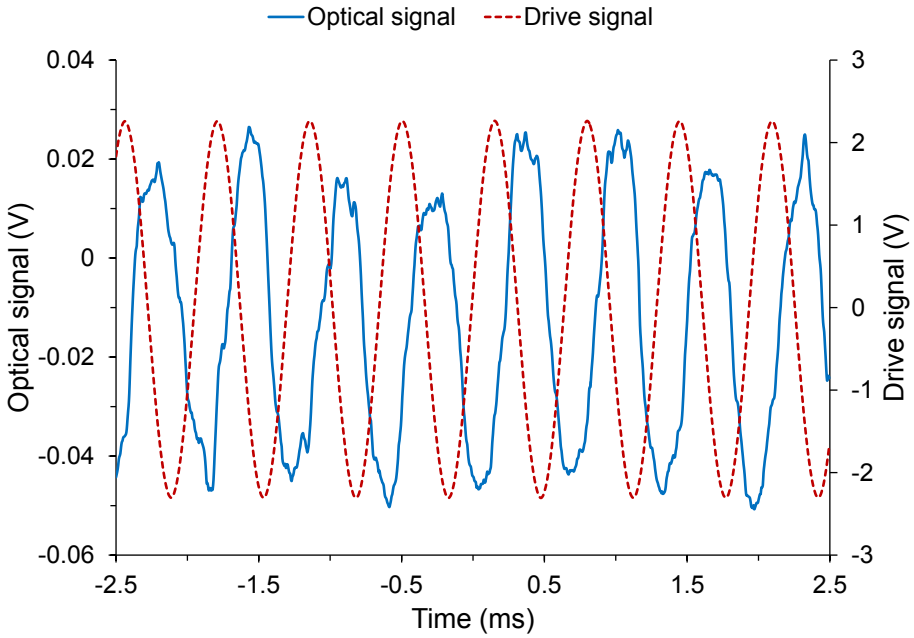

Figure 110. Optical and loudspeaker drive signals at the frequency of 1562.5 Hz. The temporal offset is due to the time delay for the acoustic signal to reach the sensor.

Typically over 24 hrs, the TLS exhibits relative intensity noise of –145 dB/Hz, and frequency noise resulting from wavelength instability of ±2.5 pm. The oscilloscope noise is in the region of 300 μV_{rms} for a bandwidth of 300 MHz. The system noise (i.e. laser frequency noise dominated) measured over a time-frame of 1 ms with 2 running averages was 118.5 µV, by means of computing the FFT of the optical signal with no measurand and selecting the highest PSD component. Since ambient acoustic noise is an unwanted component of the measurand and not a part of the system noise, it was filtered out by shielding the previously exposed ABM to ensure a complete absence of the measurand during the noise measurement. This yields a phase sensitivity of 3.9 µrad and an acoustic sensitivity of 35.0±1.3 dB_{SPL} at a signal frequency of 1562.5 Hz. The acoustic sensitivity is plotted as a function of frequency in Figure 109, with average values of 31.7 dB_{SPL} and 37.0 dB_{SPL} from 40 Hz to 500 Hz and 1.5 kHz to 4 kHz respectively.

6.2.7 Conclusion

The use of OM technology for ABM-based microphones has been demonstrated. High compactness and high acoustic responsivity are anticipated, which are attractive qualities in applications with stringent space requirements, such as in defense and biomedical uses. An experimental demonstration using a MC of 2 μm diameter OM and 35 mm uncoiled length exhibited average responsivities of –165.9 dB re. rad/μPa and –171.2 dB re. rad/μPa, and average acoustic sensitivities of 31.7 dB_{SPL} and 37.0 dB_{SPL}, from 40 Hz to 500 Hz and 1.5 kHz to 4 kHz respectively. The measured responsivities show some agreement with the simulated value of –168.0 re. rad/μPa. The detection bandwidth of the ABM is ~1 kHz, which is close to the simulated value of 0.92 kHz.

To increase the responsivity, a longer length of OM must be used. The limiting factor is the maximum length of OM that can be fabricated, which can be vastly extended using a modified tapering rig presented in the next section. A mandrel material of lower Young's modulus and lower Poisson ratio would also be preferable. Moreover, the wall thickness of the mandrel and the polymer packaging can be reduced to lower the stiffness while still maintaining clearance of the central support. The phase and acoustic sensitivities can be enhanced by applying a larger number of averages for each measurement, though at the expense of prolonging the measurement time. To increase the fundamental frequency and thus the detection bandwidth, a mandrel material of higher Young's modulus, lower density and shorter length would be ideal for the assembly of the ABM. Hence, there is an optimization issue with increasing the Young's modulus to extend the detection bandwidth and decreasing it to improve the responsivity. The response time can be reduced by minimizing the fiber length between the MC and BD. To reduce the loss, air bubbles must be removed from the polymer packaging. The ultimate compactness of the sensor head is restricted by the diameter of the mandrel, which has to be wider than the diameter of the support pin. It is then followed by the minimum bend radius of the OM.

6.3 Development of tapering rig for fabricating long optical microfibers

The development and testing of a new tapering rig specialized for making long fiber tapers is reported in this section. The aim is to deliver sufficient lengths (e.g. tens of meters) of OM to realize the full potential of OM-based sensors.

6.3.1 Introduction

As highlighted in the previous chapters, the responsivity of non-resonator OM-based sensors can be scaled up by making use of longer OMs so as to increase the interaction length with the measurand. The existing tapering rig employed for the experiments described in this thesis is only capable of producing OMs up to ~10 cm in total length. To-date, most conventional tapering rigs reported in literature can only produce OM lengths up to tens of millimeters with diameters of the order of microns. A recent attempt [13] using a similar tapering configuration to the one described in this section was unable to achieve micron-order diameters. Although the taper length was ~10 m, the reduction of the fiber diameter was less than 1%. The true capabilities of this type of tapering rig is presented in this section by addressing the previous short-comings, with the demonstration of a fiber taper featuring 10 μm diameter and 0.4 m length at the uniform waist. Critical improvements over the original design include extensive fiber cleaning, setup enclosure, and smooth differential velocity transitions.

6.3.2 Tapering setup

The tapering rig shown in Figure 111 consists of five main stages: the feed and exit motors, the fiber-cleaner module, the ceramic micro-heater, and the laser measuring head. The entire setup was encased in a robust, transparent enclosure to minimize air flows that could perturb the tapering process. The differential velocity between the feed and exit motors controls the pull rate and thus the taper diameter profile. Typically, the feed motor velocity is kept constant while the exit motor velocity is increased to stretch the optical fiber. The fiber-cleaner module comprises of two glass slides sandwiching a folded, medical-grade tissue paper soaked with isopropanol. The cavity of the micro-heater was vertically aligned to be level with the optical fiber. The micro-heater itself was mounted on a rail so that it can quickly

engage or withdraw from the optical fiber. Lastly, the measuring head monitors the fiber diameter with a resolution of 0.1 μm in real-time using red laser beams.

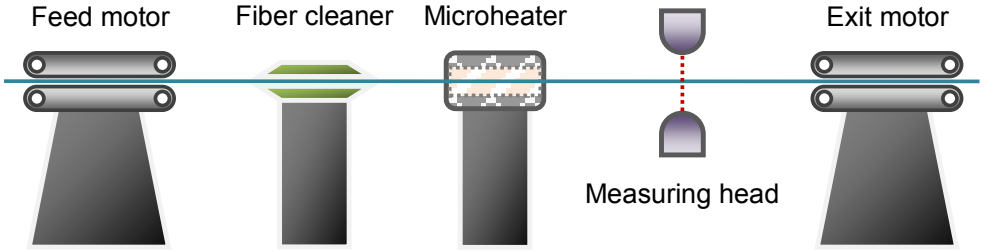

Figure 111. Schematic diagram of the newly developed tapering rig setup.

6.3.3 Tapering procedure

Two meters of SMF-28 was soaked in acetone for ~10 min to soften the acrylate layer before it was mechanically stripped in a smooth motion. The bare fiber was then thoroughly cleaned with isopropanol to remove any acrylate residue. Even small quantities can ignite in the micro-heater and disturb the temperature uniformity, potentially weakening the OM. After the preparation, the bare fiber was tapered with a single pass through the micro-heater over the duration of ~20 min, as shown in Figure 112. The temperature inside the hot-zone was ~1350 °C, measured using a commercial thermometer.

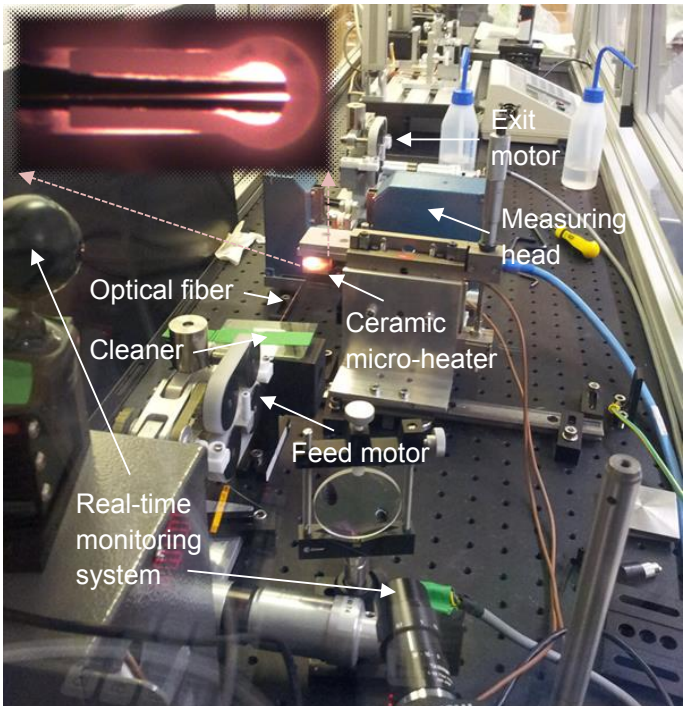

Figure 112. Photograph showing the tapering rig inside the enclosure. Inset: side-view of the micro-heater with the optical fiber positioned in the center of the cavity.

6.3.4 Experimental results

The preliminary results obtained from the testing of the tapering rig indicated the successful fabrication of a 10 µm diameter, 0.4 m length OM. The fiber diameter profile in Figure 113 shows the down-taper from 125 µm to 10 µm, followed by a near-uniform waist length of ~0.4 m, then followed by the up-taper back to 125 µm. The maximum error at the waist region is 8.5%. Due to the distance between the measuring head and the exit motor, the measured diameter profile lagged behind the ideal trace. However, the two plots have been shifted together in Figure 113 for better comparison. Figure 114 shows the transmission spectrum of the uncoated OM. The average loss of the air-cladded OM is ~6 dB from 1450 nm to 1650 nm. At a wavelength of λ = 1550 nm, the normalized loss is α = ~7 dB/m.

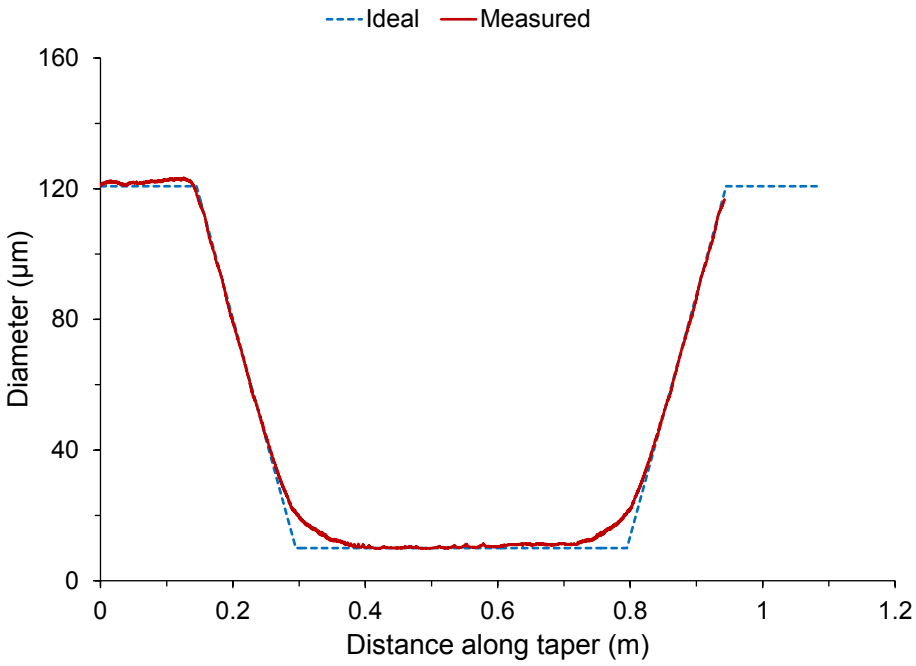

Figure 113. Measured and ideal fiber taper diameter profiles.

It is worth mentioning that there is no theoretical limit to the length of OM that can be fabricated using this tapering rig, as it is based on motors rather than translation stages. However, the minimum achievable OM diameter depends on several factors. The first factor is the cleanliness of the motor treads, as specks of dust and acrylate lumps can crush the fragile OM in the touching zone of the motor treads. More importantly, unwanted materials could stick to the surface of the OM and cause high loss due to the absorption and scattering of the evanescent field. The second factor is

the vertical alignment of the successive stages, as an OM under tension will experience extra friction at the edges of each stage and thus it will be more prone to breaking. Furthermore, vertical misalignment on either side of the micro-heater must be avoided, because the high roughness of the heated ceramic surface will terminate the OM upon contact.

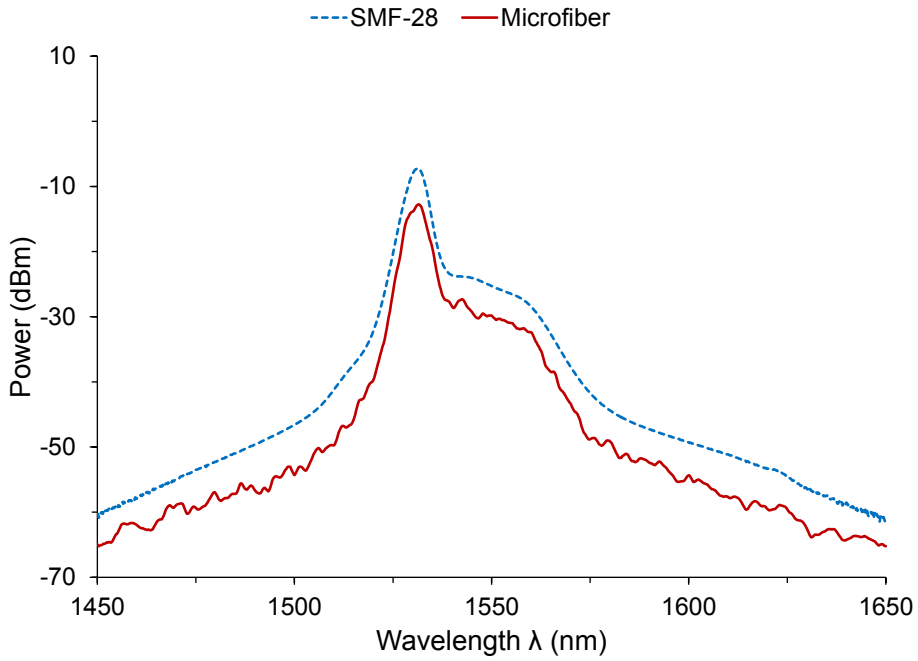

Figure 114. Transmission spectra of the optical microfiber compared to the original SMF-28.

6.3.5 Conclusion

A significant increase in the maximum OM length is anticipated with the new tapering rig. A preliminary demonstration yielded a near-adiabatic taper with 0.4 m of uniform waist diameter and a normalized loss of ~7 dB/m. Further work is required to reduce the waist diameter from 10 µm to 2 µm for single-mode applications, such as the various sensors described in this thesis.

6.4 References

1. S. Niu, Y. Hu, Z. Hu, and H. Luo, "Fiber Fabry-Perot hydrophone based on push-pull structure and differential detection", IEEE Photonic. Tech. L., vol. 23, no. 20, pp. 1499–1501, 2011.

2. H. Wagaard, G. B. Havsgård, and G. Wang, "An investigation of the pressure-to-acceleration responsivity ratio of fiber-optic mandrel hydrophones", J. Lightwave Technol., vol. 19, no. 7, pp. 994–1003, 2001.

3. G. H. Ames and J. M. Maguire, "Miniaturized mandrel-based fiber optic hydrophone", J. Acoust. Soc. Am., vol. 121, no. 3, 1392–1395, 2007.

4. "Corning ClearCurve optical fiber datasheet", http://www.corning.com, accessed on 10/08/2012.

5. L. Tong, J. Lou, R. R. Gattass, S. He, X. Chen, L. Liu, and E. Mazur, "Assembly of silica nanowires on silica aerogels for microphotonic devices", Nano Lett., vol. 5, no. 2, pp. 259–262, 2005.

6. L. S. Negi, "Strength of materials", McGraw-Hill, 2011.

7. "Natural frequencies for common systems", IES seminar, http://faculty.uml.edu /pavitabile/22.403/web_downloads/Frequencies_of_Common_Systems.pdf, accessed on 04/01/2013.

8. Y. Jung, G. Brambilla, and D. J. Richardson, "Efficient higher-order mode filtering in multimode optical fiber based on an optical microwire", AOE, SuB4, 2008.

9. ASM International, "Materials and Coatings for Medical Devices: Cardiovascular", 2009.

10. "Fused silica material properties", http://accuratus.com/fused.html, access on 10/01/2012.

11. "Efiron technical datasheet on PC-373 (AP)", version 23/10/2006.

12. S. C. Rashleigh, Acoustic sensing with a single coiled monomode fiber", Opt. Lett., vol. 5, no. 9, pp. 392–394, 1980.

13. N. Vukovic, N. G. R. Broderick, M. Petrovich, and G. Brambilla, "Novel method for the fabrication of long optical fiber tapers", IEEE Photonic Tech. L., vol. 20, no. 14, pp. 1264–1266, 2008.

Chapter 7

7. Summary, Discussion and Conclusion

This chapter concludes the thesis with a summary of results and a discussion on future work aimed at overcoming challenges and scaling the performance of existing OM-based sensors.

7.1 Summary

This thesis has presented both theoretical and experimental research work on demonstrating the temperature, current, acceleration and acoustic sensing ability of OMs. Both interferometric and polarimetric detection schemes were employed, in addition to resonance shift detection. It was the principal aim of this research to develop the OM-based current sensor and address the factors limiting its responsivity, reliability and reproducibility. The work done and results achieved are now summarized.

The preliminary exploration involved the development of a compact thermometer capable of sliding along electrical wires to detect electrical arcing-induced hot spots. This was devised using a MCR coiled around a Teflon tube. The magnitude of the temperature-induced resonant wavelength shift can be tailored by the choice of materials, due to thermal expansion and thermo-optic effects. For the first time, MCRs were designed with such mobility so they can efficiently measure the temperature profile of a rod-like structure. This type of sensor can be potentially used in industrial applications to inspect insulated wires and cables for insulation defects, aiding the prevention of electrical fires.

The same physical arrangement of self-coupled OM coiled around a wire was subsequently established as a current sensor. Current-induced variations in the local magnetic field axial to the direction of light rotate the polarization azimuth via the Faraday Effect. The relatively short length of OMs allows short transit times of light, giving rise to potentially gigahertz detection bandwidth for fast current detection. The responsivity to current was linearly proportional to the number of OM turns.

A means to increase the current responsivity without being limited by the maximum producible OM length was investigated. It was subsequently demonstrated both theoretically and experimentally that resonantly enhanced Faraday rotation can be realized in MCRs, and it is a function of the ER. However, by increasing the OPL there is an unavoidable trade-off between the responsivity and the detection bandwidth.

The upmost-compact resonator configuration is achieved at the expense of temporal and wavelength instability. Thermal drifts and vibrations transfer from the ambient environment can modify the geometrical and optical properties of the MCR, thereby radically detuning the operating wavelength from the resonant condition and thus altering the Faraday rotation. This issue was solved using two different approaches, one being passive and the other active. The first approach involved optimizing the spatial arrangement of the OM turns with RI chirping to instigate a broadening of the lower region of the resonance shape such that its output transmittance is much more tolerant to resonant wavelength fluctuations. The second approach incorporated a PZC element inside the MCR package as a support rod, which can be actively tuned using feedback control to lock the resonance detuning.

Linear birefringence associated with packaged MCs and MCRs was another major concern. This characteristic is typical of devices operating with the Faraday Effect. Bend- and packaging-induced birefringence causes the differential phase between the eigenmodes in the two orthogonal axes to increase with OPL, resulting in alternating polarities of Faraday rotation that produce zero net rotation at half beat length intervals. The problem was solved by introducing a twist during the fabrication of hi-bi OMs to create the first reported SOMs. The magnitude of the intrinsic linear and circular birefringence can be optimized to deliver a good balance between resistance to external effects and responsivity.

Although SOMs are capable of delivering near-maximum performance for non-resonator sensor heads, resonantly enhanced OM devices would require further design optimizations due to their structural complexity. The exploration of OM resonator designs led to the investigation of MLRs. It was found that design optimizations are possible to host efficient Faraday rotation for both birefringent and

non-birefringent sensor heads. This study provided the groundwork for designing practical current sensors using MLR sensor heads with a high responsivity to current.

Going back to non-resonator sensor heads, an alternative to the SOM was proposed in the form of a novel post-fabrication technique for reversing the detrimental effect of linear birefringence in MC-based current sensors. By means of changing the local birefringence at the right positions along the fiber axis, the differential phase of light can be progressively optimized to deliver uni-directional Faraday rotation and thus maximum responsivity.

Diverging to the exploration of other sensing applications, a compact accelerometer based on a centrally supported FD overlaid with OM was modeled and demonstrated. Both the acceleration responsivity and detection bandwidth were influenced by the choice of disc material and geometry. There are several benefits from down-scaling the traditional accelerometer, including easier deployment, less intrusive and lower cost. Due to the large minimum bend radii of standard optical fibers, to achieve such small package sizes would result in severe PDL and depolarization. The excellent bend insensitivity of OMs enables very compact devices to be made without compromising their performance. Moreover, the responsivity scales with the length of OM and it can be potentially several orders of magnitude higher than conventional designs using standard optical fibers.

For a different purpose, a compact microphone based on an ABM coiled with OM was proposed and demonstrated. Both the acoustic responsivity and detection bandwidth were dependent on the material and geometry of the mandrel. Likewise, there are benefits with the compactness of the device, notably for defence applications. The microphone showed the potential for very high responsivity despite the miniaturization, which generates strong interest for future development. Another possible direction is the development of a hydrophone for underwater acoustic sensing.

Finally, the latest developments on a tapering rig specialized in manufacturing long fiber tapers were reported. The demand for very long OMs is driven by the objective of moving beyond the proof-of-concept stage to realize the full potential of OM technology.

7.2 Discussions

There have been many interesting developments in the various areas of MNF-based sensing. This section highlights the numerous advantages of MNF-based sensors over their traditional counterparts employing standard optical fibers, accompanied by an overview on the challenges ahead and the practical issues that need to be addressed.

7.2.1 Advantages of optical microfibers and nanofibers

By significantly reducing the size of sensors and their associated electronics with supporting hardware, miniaturization offers the possibility of complete portable micro-systems which can carry out many of the operations traditionally performed in a laboratory. The other benefits of high compactness due to the bend insensitivity of MNFs include easier deployment and minimal intrusion. The consequential reduction in weight also draws substantial interest, particularly from the aerospace industry.

It is widely recognized that for sensors responding to a mechanical stimulus, the better sensitivity associated with the higher responsivity resulting from the lower stiffness of MNFs grants a notable enhancement in the detection of weak signals of the measurand. In chemical and bio-chemical sensing, the superior sensitivity accompanying the higher responsivity resulting from the larger evanescent field of MNF waists gives rise to an improved detection of fewer atoms in its close vicinity. In addition, the greater selectiveness linked to the higher optical confinement of MNF tips allows the selection of fewer atoms to detect. As for current sensors based on the Faraday Effect, the higher detection bandwidth hosted by the shorter OPL resulting from the bend insensitivity of MNF coils enables the measurement of faster-changing current signals.

7.2.2 Challenges and practical issues (future work)

To compete with traditional fiber-optic sensors in terms of responsivity, some MNF-based sensors would require their tapered uniform waist region to be in excess of ~10 cm. Generally, the responsivity of non-resonator-type MNF-based sensors scales with the MNF length. However, the detection bandwidth associated with certain

sensing mechanisms such as the Faraday Effect decreases with longer OPLs. Hence, a trade-off must be considered for a good balance between responsivity and detection bandwidth.

The optical loss of MNFs is one of the key areas that need improvement. Although the theoretical minimum attenuation when embedded in polymers is very low [1], in practice it is usually not the case. Micro-bubbles in the polymer cladding cause scattering of the evanescent field [2], and contaminations of the polymer material introduce unwanted absorption. The average loss observed in packaged samples of OM ranged from 0.5–3 dB/cm. Therefore, to reach acceptable levels of loss (<0.1 dB/cm), a significant amount of work needs to be done to remove micro-bubbles from the polymer resin (e.g. vacuum pump) before UV-curing and to minimize contaminations (e.g. cleanroom conditions). Due to the availability of C-band laser sources, wavelengths around 1550 nm were used to excite the sensor heads described in this thesis. However, this wavelength region is known to exhibit relatively high absorption loss in polymers. At lower wavelengths such as 650 nm, light is more sensitive to scattering loss in polymers. Hence, it is better to operate somewhere in the middle, with the exception of water-absorption regions.

Another practical issue with MNF-based sensors is the dynamic temperature range, which is determined by the polymer material used for packaging. For the Efiron PC-373 AP, the polymer experiences significant evaporation in OH content around ~80 °C and noticeable deformation by ~120 °C. Apart from the physical deterioration of the material, thermal expansion and contraction can induce internal stresses in the embedded MNF, resulting in unpredictable loss and birefringence.

The life-time of each fabricated sensor head primarily depends on the curing state of the polymer coating. The UV-curing time of the polymer makes a profound impact on the long-term stability of the packaged device. A short duration tends to avoid the build-up of internal stresses that can modify the intended MNF geometry. On the other hand, the protective coating is more volatile and the geometrical stability of the embedded MNF is at risk from external perturbations. Hence, it is to be appreciated that ensuring long-term reliability is likely to be challenging. The aging process of the polymer itself was discovered at the time of writing to be slower in other variants, such as the now-discontinued Efiron PC-375 AP.

An alternative solution is suspended-core fibers, which exhibit the same optical properties of MNFs albeit in a mechanically stable arrangement. However, since the evanescent field is not accessible outside the optical fiber, they cannot be used for resonators that rely on self-coupling. In addition, suspended-core fibers are far bulkier than MNFs, which eliminates their advantages over standard optical fibers.

7.3 Conclusion

This thesis has researched new varieties of optical sensors based on OM technology to provide compact and high-performance solutions to well-known areas of sensing. The main achievements are:

- Developed a MCR-based thermometer for efficient probing of electrical wires to identify insulation faults [3].
- Analyzed issues relating to the detection bandwidth, pulse broadening and optical response of current sensors using the Faraday Effect [4].
- Overcame OM length limitation of the previously demonstrated MC-based current sensor by exploiting the resonance enhancement in MCRs [5].
- Envisaged both passive and active stabilization techniques to minimize the impact of external perturbations on MCR sensor heads [6].
- First reported fabrication of SOM to suppress bend- and packaging-induced birefringence in MC/MCRs, thereby maximizing the responsivity of the sensor heads [7].
- Design optimization of MLRs with birefringence for highly efficient resonance enhancement [8].
- Proposed a post-fabrication technique to revive non-ideal MC sensor heads with birefringence for high-performance current sensing [9].
- Theoretical and experimental demonstrations of a compact accelerometer consisting of a centrally supported FD overlaid with OM [10, 11].
- Demonstration of a compact microphone comprising of an ABM coiled with OM [12], potentially functional as a hydrophone.
- Development on a new tapering rig capable of delivering significantly longer lengths of OM.

Table 10 lists the key achievements in the core research area of current sensing:

Sensor type	Problem	Solution
Non-resonator	Bandwidth	Optical response correction
	Fiber length	Resonance enhancement

	Birefringence	Spun optical microfiber
	Birefringence	Birefringence modulation
Resonator	Birefringence	Spun optical microfiber
	Birefringence	Geometrical optimization
	Stability	Refractive index chirping
	Stability	Piezo-electric tuning

Table 10. Summary of contributions to current sensing using optical microfiber technology.

The results achieved in this thesis represent a significant advance in harnessing OM technology for sensing. It would be useful to combine the numerous techniques developed so far when engineering a sensing system to attain the best possible performance. Aside from achieving unprecedented high compactness, MC/MCR sensor heads have the potential to raise the detection bandwidth of traditional fiber-optic current sensors by at least one order of magnitude. Accelerometers and microphones employing OMs can expect a similar leap of improvement in their responsivity, which gives rise to enhanced sensitivity. Although the experiments were performed with relatively short OM lengths and a host of further scientific and more practical challenges remain, these results can be considered an important step towards demonstrating the feasibility of using OMs for sensing. While still in their infancy, these sensors promise a tremendous impact on a wide range of technological applications in industries such as biomedical, defence, navigation, oil & gas, process control and transportation. One should expect substantial activity in the rise of OM technology in the coming decade, and significant progress should be anticipated in the development of OM-based sensors as well as their outlook to establishing commercial interest.

7.4 References

1. G. Brambilla, V. Finazzi, and D. J. Richardson, "Ultra-low-loss optical fiber nanotapers", Opt. Express, vol. 12, no. 10, pp. 2258–2263, 2004.

2. S. Wang, X. Pan, and L. Tong, "Modeling of nanoparticle-induced Rayleigh–Gans scattering for nanofiber optical sensing", Opt. Commun., vol. 276, no. 2, pp. 293–297, 2007.

3. G. Y. Chen, G. Brambilla, and T. P. Newson, "Inspection of electrical wires for insulation faults and current surges using sliding temperature sensor based on optical microfibre coil resonator", Electron. Lett., vol. 49, no. 1, pp. 46–47, 2013.

4. G. Y. Chen and T. P. Newson, "Faraday Effect based fiber-optic current sensors: detection bandwidth, pulse broadening and optical response correction", Electron, Lett., *submitted*, 2014.

5. G. Y. Chen, T. Lee, R. Ismaeel, G. Brambilla, and T. P. Newson, "Resonantly enhanced Faraday rotation in an microcoil current sensor", IEEE Photonic. Tech. L., vol. 24, no. 10, pp. 860–862, 2012.

6. G. Y. Chen, X. Zhang, G. Brambilla, and T. P. Newson, "Temperature compensation techniques for resonantly enhanced sensors and devices based on optical microcoil resonators", Opt. Commun., vol. 285, no. 23, pp. 4677–4683, 2012.

7. G. Y. Chen, G. Brambilla, and T. P. Newson, "Spun optical microfiber", IEEE Photonic. Tech. L., vol. 24, no. 19, pp. 1663–1666, 2012.

8. G. Y. Chen, G. Brambilla, and T. P. Newson, "Efficient Faraday rotation in birefringent optical microfibre loop resonators for current sensing", Electron. Lett., vol. 48, no. 24, pp. 1547–1548, 2012.

9. G. Y. Chen, T. P. Newson, and G. Brambilla, "Birefringence treatment of non-ideal optical microfibre coils for continuous Faraday rotation", Electron. Lett., vol. 49, no. 11, pp. 714–715, 2013.

10. G. Y. Chen, X. Zhang, G. Brambilla, and T. P. Newson, "Theoretical and experimental demonstrations of a microfiber-based flexural disc accelerometer", Opt. Lett., vol. 36, no. 18, pp. 3669–3671, 2011.

11. G. Y. Chen, X. Zhang, G. Brambilla, and T. P. Newson, "Enhanced responsivity of a flexural disc acceleration sensor based on optical microfiber", Opt. Commun., vol. 285, no. 23, pp. 4709–4714, 2012.

12. G. Y. Chen, G. Brambilla, and T. P. Newson, "Compact acoustic sensor based on air-backed mandrel coiled with optical microfiber", Opt. Lett., vol. 37, no. 22, pp. 4720–4722, 2012.

Appendix A

List of publications

A.1 Journal publications

1. G. Y. Chen, C. A. Codemard, R. J. Lewis, L. Jankowski, J. S. Chan, P. M. Gorman, and M. N. Zervas, "Enhanced responsivity with skew mode excitation of transmission- and reflection-type refractometric sensors", **Optics Letters**, *submitted*, 2014.

2. G. Y. Chen and T. P. Newson, "The detection bandwidth of fiber-optic current sensors based on the Faraday Effect", **Electronics Letters**, vol. 50, no. 8, pp. 626–627, 2014.

3. G. Y. Chen, M. Ding, T. P. Newson, and G. Brambilla, "A review of micro- and nanofiber based optical sensors", **Open Optics Journal**, vol. 7, pp. 32–57, 2014. (invited paper)

4. G. Y. Chen, T. P. Newson, and G. Brambilla, "Optical microfibers for fast current sensing", **Optical Fiber Technology**, vol. 19, no. 6B, pp. 802–807, 2013. (invited paper)

5. G. Y. Chen, T. P. Newson, and G. Brambilla, "Birefringence treatment of non-ideal optical microfibre coils for continuous Faraday rotation", **Electronics Letters**, vol. 49, no. 11, pp. 714–715, 2013. (featured article)

6. G. Y. Chen, G. Brambilla, and T. P. Newson, "Inspection of electrical wires for insulation faults and current surges using sliding temperature sensor based on optical microfibre coil resonator", **Electronics Letters**, vol. 49, no. 1, pp. 46–47, 2013.

7. G. Y. Chen, G. Brambilla, and T. P. Newson, "Efficient Faraday rotation in birefringent optical microfibre loop resonators for current sensing", **Electronics Letters**, vol. 48, no. 24, pp. 1547–1548, 2012. (highlighted paper)

8. G. Y. Chen, G. Brambilla, and T. P. Newson, "Compact acoustic sensor based on air-backed mandrel coiled with optical microfiber", **Optics Letters**, vol. 37, no. 22, pp. 4720–4722, 2012.

9. G. Y. Chen, G. Brambilla, and T. P. Newson, "Spun optical microfiber", **IEEE Photonics Technology Letters**, vol. 24, no. 19, pp. 1663–1666, 2012.

10. G. Y. Chen, X. Zhang, G. Brambilla, and T. P. Newson, "Temperature compensation techniques for resonantly enhanced sensors and devices based on optical microcoil resonators", **Optics Communications**, vol. 285, no. 23, pp. 4677–4683, 2012. (invited paper)

11. G. Y. Chen, X. Zhang, G. Brambilla, and T. P. Newson, "Enhanced responsivity of a flexural disc acceleration sensor based on optical microfiber", **Optics Communications**, vol. 285, no. 23, pp. 4709–4714, 2012. (invited paper)

12. G. Y. Chen, T. Lee, R. Ismaeel, G. Brambilla, and T. P. Newson, "Resonantly enhanced Faraday rotation in an microcoil current sensor", **IEEE Photonics Technology Letters**, vol. 24, no. 10, pp. 860–862, 2012.

13. X. Zhang, M. Belal, G. Y. Chen, Z. Q. Song, G. Brambilla, and T. P. Newson, "Compact optical microfiber phase modulator", **Optics Letters**, vol. 37, no. 3, pp. 320–322, 2011.

14. G. Y. Chen, X. Zhang, G. Brambilla, and T. P. Newson, "Theoretical and experimental demonstrations of a microfiber-based flexural disc accelerometer", **Optics Letters**, vol. 36, no. 18, pp. 3669–3671, 2011.

A.2 Conference publications

1. G. Y. Chen "Recent progress in physical sensing with optical microfiber technology", **POEM**, *in press*, 2014. (invited paper)
2. G. S. Murugan, C. A. Codemard, M. N. M. Nasir, G. Y. Chen, A. Langner, H. Quarzglas, and M. N. Zervas, "Optical microstub resonator lasers", **SPIE Photonics West LASE**, pp. 8960-43, 2014.
3. G. Y. Chen, G. Brambilla, and T. P. Newson, "An optical microfiber acoustic sensor", **OSA Sensors**, pp. ST5B.2-1–2, 2013.
4. G. Y. Chen, X. Zhang, T. Lee, G. Brambilla, and T. P. Newson, "Compact flexural disc accelerometers based on optical microfiber", **OSA OFS-22**, pp. 84210U-1–4, 2012.
5. X. Zhang, G. Y. Chen, Z. Song, M. Belal, E. Koukharenkoc, G. Brambilla, and T. P. Newson, "Compact optical microfiber components based on small size piezoelectric ceramic transducer", **OSA OFS-22**, pp. 842112-1–4, 2012.
6. G. Y. Chen, T. Lee, R. Ismaeel, M. Belal, T. P. Newson, and G. Brambilla, "Optical microfiber sensors for the detection of current pulses", **OSA Sensors**, pp. JW2A.3-1–2, 2012. (invited paper)
7. M. Belal, X. Zhang, G. Y. Chen, Z. Song, G. Brambilla, and T. P. Newson, "A compact optical microfiber based PZT phase modulator", **CLEO**, pp. JW2A.78-1–2, 2012.
8. M. Ding, M. Belal, G. Y. Chen, R. Al-Azawi, T. Lee, Y. Jung, P. F. Wang, X. L. Zhang, Z. Q. Song, F. Xu, R. Lorenzi, T. P. Newson, and G. Brambilla, "Optical microfiber devices and sensors", **ACP**, pp. 83070Y-1–6, 2011.
9. G. Y. Chen, M. Belal, Y. Jung, G. Brambilla, and T. P. Newson, "High frequency current sensing using optical fiber micro-wire", **CLEO/Europe**, pp. CH6_4, 2011.
10. G. Y. Chen, T. Lee, Y. Jung, M. Belal, G. Brambilla, N. G. R. Broderick, and T. P. Newson, "Investigation of thermal effects on embedded microcoil resonators", **CLEO/Europe**, pp. CH2_2, 2011.

A.3 Book chapters

1. G. Y. Chen and G. Brambilla, "Optical microfiber physical sensors" in "Optical fiber sensors: advanced techniques and applications", CRS press, *in press*, 2014.